# DESIGN AND ANALYSIS OF AXIAL AND RADIAL FLUX MAGNETIC GEARS AND MAGNETICALLY GEARED MACHINES

A Dissertation

by

MATTHEW CHRISTOPHER JOHNSON

Submitted to the Office of Graduate and Professional Studies of
Texas A&M University
in partial fulfillment of the requirements for the degree of

DOCTOR OF PHILOSOPHY

| | |
|---|---|
| Chair of Committee, | Hamid A. Toliyat |
| Committee Members, | Prasad Enjeti |
| | Shankar Bhattacharyya |
| | Won-Jong Kim |
| Head of Department, | Miroslav Begovic |

May 2017

Major Subject: Electrical Engineering

# ABSTRACT

Over the last two decades, magnetic gears and magnetically geared machines gained interest as a promising technology for use in high torque, low speed applications. Magnetic gears accomplish the same task as mechanical gears, but they do so without mechanical contact between the moving components, instead relying on the modulated interaction between the flux generated by magnets on the rotors. Consequently, magnetic gears offer the potential to combine the compact size and cost effectiveness of mechanically geared systems with the reliability and quieter operation of larger direct drive machines.

This work focuses on the development of analysis and design techniques for axial and radial flux magnetic gears and magnetically geared machines. Prototypes of an axial flux magnetic gear, a new compact axial flux magnetically geared machine topology, and a large scale inner stator radial flux magnetically geared machine were constructed and tested to calibrate and validate the analysis tools and investigate the practical considerations associated with the technology. Despite conservative design practices, the largest of these machines achieved a torque density of 82.8 $kN \cdot m/m^3$. Additionally, a MATLAB-based infrastructure was developed for controlling various simulation models and analyzing their results. Specifically, parametric 2D and 3D finite element analysis (FEA) models were employed for most of the studies, including the designs of the magnetically geared machine prototypes. This system was also used to conduct other

simulation studies focused on a plethora of critical design trends and multi-faceted characterizations of the technology's potential.

Spurred on by the long simulation times required for FEA models, the later stages of the study describe the development and evaluation of generalized, parametric 2D and 3D magnetic equivalent circuit (MEC) magnetic gear models. These MEC models proved extremely accurate, matching the torque predictions of corresponding FEA models with an average error of less than 2%. The MEC models also achieved simulation speeds up to 300 times faster than those of corresponding FEA models.

Collectively, this work provides the tools and methodology for the systematic evaluation of radial and axial flux magnetic gears. It also characterizes design trends for both topologies and validates the results with experimental prototypes.

To my parents and my grandma.

Non nobis, Domine, non nobis, sed nomini tuo da gloriam.

# ACKNOWLEDGEMENTS

I want to express my deepest gratitude to everyone who helped me during my Ph.D. studies and my entire academic career.

First, I would like to thank my family, including my parents, grandma, sister, aunts, uncle, and cousin for their love and support. I would especially like to thank my parents and my grandma, everything I accomplish is because of them. I would not have made it this far without everything they did and sacrificed for me.

I would also like to thank my advisor, Dr. Hamid A. Toliyat, for his support, encouragement, and advice. He introduced me to this field of research and provided me with several invaluable opportunities to work on interesting and challenging projects related to the topic, as well as chances to gain classroom teaching experience. He afforded me the freedom to explore my own ideas and develop into an independent researcher and engineer. I am also very grateful to Dr. Prasad Enjeti, Dr. Shankar Bhattacharyya, and Dr. Won-Jong Kim for giving their valuable time to serve on my committee. They are all excellent professors and I enjoyed their classes and appreciated their feedback on my research.

Next, I want to thank Matthew Gardner, who served as my partner on many of the research projects described in this dissertation. He is brilliant, hard-working, and most importantly, simply a nice person. I greatly enjoyed brainstorming and working side-by-side with him, and I would not have accomplished nearly as much as I did without his

immeasurable contributions. I have no doubt that he will extend the research to even greater heights as he continues in the same field during his own Ph.D. studies.

I also sincerely appreciate my many graduate school colleagues. I am deeply grateful to Dr. Jae-Bum Park for allowing me to collaborate with him on his research during my first year in graduate school. I am greatly obliged to Dr. Siavash Pakdelian, Dr. Yateendra Deshpande, and Hussain Hussain for all of the advice that they offered me throughout my Ph.D. studies and thank them for their willingness to frequently serve as my sounding board for different ideas. I am indebted to Dr. Mahshid Amirabadi for her kindness and for patiently answering my questions about power electronics. I would also like to thank Dr. Vivek Sundaram and Morteza Moosavi for their continuous selflessness and help managing the lab throughout our Ph.D. studies. I am also grateful for the support and friendship of Dr. Robert Vartanian, Dr. Babak Farhangi, Dr. Khaled Ali Al Jaafari, Abdulkadir Bostanci, Esra Ozkentli, Yongqi Li, Bahar Anvari, Ajay Kumar Morya, Farid Naghavi, Amir Negahdari, Niloofar Torabi, Dr. Somasundaram Essakiappan, Dr. Harish Krishnamoorthy, Jorge Ramos-Ruiz, Jose Sandoval, and Dr. Michael Daniel.

I would also like to express my gratitude to the Texas A&M College of Engineering and the Department of Electrical and Computer Engineering for providing me with a world class education. Specifically thanks to Dr. Scott Miller, Tammy Carda, Jeanie Marshall, Wayne Matous, Melissa Sheldon, Katie Bryan, Henry Gongora, Enrique Terrazas, Anni Brunker, Sheryl Mallett, Rebecca Rice, Eugenia Costea, Nancy Reichart, and Omar Valenzuela for their help with the day-to-day aspects of graduate school and for all of the hard work that they put in to make the department run smoothly.

Next, I want like to thank Dr. Steven Englebretson, Dr. Wen Ouyang, Dr. Colin Tschida, and Dr. Alireza Shapoury for collaborating with me on some of the different research projects described in this dissertation. I deeply value the opportunities that they helped provide and appreciate having the chance to work with them. Additionally, I want to thank John Vilas and his team at Vilas Motor Works for all of their extremely skilled hard work on my prototype and testbed and for their immense kindness and patience with me.

Finally, I would like to extend a special thanks to Mrs. Albritton, Dr. Bailey, Mrs. Gordon, Mr. Laywell, and Mrs. Potticary who were all great role models and had a deep and lasting impact on me during my time in high school. These individuals helped foster a love of learning in me that carried me through my undergraduate and graduate studies.

# CONTRIBUTORS AND FUNDING SOURCES

## Contributors

This work was supervised by a dissertation committee consisting of Professor Hamid A. Toliyat, who served as the advisor, Professor Prasad Enjeti, and Professor Shankar Bhattacharyya of the Department of Electrical and Computer Engineering, as well as Professor Won-Jong Kim of the Department of Mechanical Engineering.

The work summarized in Section 3 was completed by the student in collaboration with Dr. Alireza Shapoury. The work presented in Sections 4 and 5 was completed by the student in collaboration with Matthew Gardner of the Department of Electrical and Computer Engineering and Dr. Steven Englebretson, Dr. Wen Ouyang, and Dr. Colin Tschida. The work discussed in Sections 6-10 was completed by the student in collaboration with Matthew Gardner of the Department of Electrical and Computer Engineering. All work for the dissertation was completed by the student under the advisement of Professor Hamid A. Toliyat of the Department of Electrical and Computer Engineering.

## Funding Sources

Graduate study was supported by the National Excellence Fellowship from the Dwight Look College of Engineering at Texas A&M University and the Thomas Powell Fellowship from the Department of Electrical and Computer Engineering. The work presented in the dissertation was made possible in part by funding from the United States Department of Energy under Award Number DE-EE0006400 and by funding from the

Office of Naval Research. Its contents are solely the responsibility of the authors and do not necessarily represent the official views of the Department of Energy or the Office of Naval Research.

TABLE OF CONTENTS

Page

Page

Page

LIST OF FIGURES

Page

Page

Page

Page

Page

Page

Page

Page

Page

LIST OF TABLES

Page

Page

# 1. INTRODUCTION

The weight and cost of a rotary electric machine are generally proportional to the amount of torque with which it must interact. In light of this scaling principle, there are two primary, conventional options for dealing with high torque, low speed loads (for motors) and inputs (for generators). The most traditional approach involves using a small high speed, low torque machine connected with a mechanical gearbox which effectively amplifies the motor or generator's torque rating. The second approach is to use a larger direct drive machine capable of directly supplying or handling the necessary torque. The problem with the first option is that mechanical gears require extensive maintenance and they are noisy and prone to failure. For example, they are generally one of the leading causes of failure in wind turbines. Alternatively, direct-drive machines are a more reliable solution, but, based on the aforementioned scaling principle, they become extremely large and expensive as the torque rating increases.

Over the last two decades magnetic gears have gradually gained interest as a promising technology for use in high torque, low speed applications and as a possible alternative to their mechanical counterparts [1-8]. Magnetic gears accomplish the same fundamental behavior as mechanical gears, scaling up and down the input and output torques and speeds, but they do so without any mechanical contact between the moving components, instead relying on the modulated interaction between the flux generated by magnets on the rotors. This contactless operation provides a plethora of potential advantages, such as reduced maintenance, inherent overload protection (no threat of gear

teeth breaking), improved reliability, decreased noise, and physical isolation between the input and output shafts. Furthermore, various magnetically geared machine (MGM) topologies integrate a magnetic gear with a conventional low torque, high speed motor or generator to produce a single device with the compact size and cost effectiveness of mechanically geared systems and the reliability and quieter, cleaner operation of larger direct drive machines [9-25]. Due to these promising characteristics, magnetic gears have attracted attention for possible use in several applications, including wind turbines [14, 26], wave energy generation [27, 28], tidal energy generation [29], electric vehicles [13, 23, 24], marine propulsion systems [30, 31], and oil and gas production [32].

This work focuses on the development of analysis and design techniques for axial and radial flux coaxial magnetic gears and magnetically geared machines, as well as the construction and evaluation of experimental prototypes of these devices. First, a brief overview of magnetic gears is presented, including a summary of the technology's history, most important performance metrics, key topologies, and fundamental operating principle. Next, the MATLAB-based analysis system developed throughout the course of this study is discussed along with the analytical models and finite element analysis (FEA) models that it was used to control. Then, the designs and experimental evaluations of the various magnetic gear and magnetically geared machine prototypes constructed throughout the study are described to validate the accuracy of the analysis tools and address various practical considerations associated with the technology. In particular, a patent was filed for the new compact axial flux magnetically geared machine topology invented and prototyped in this dissertation [33].

Following the discussions of the various prototypes, another simulation study compares neodymium iron boron (NdFeB) and ferrite radial flux magnetic gears. By characterizing the relative benefits and drawbacks of the two most common permanent magnet material options for magnetic gears and investigating their impacts on various critical design and performance trends, this study addresses a question frequently received from companies interested in commercializing the technology. Finally, spurred on by the relatively long simulation times required for the FEA models used throughout this work, the later stages of this study focus on the development and evaluation of generalized parametric 2D and 3D lumped parameter magnetic equivalent circuit (MEC) magnetic gear models as a faster, but still extremely accurate, alternative and supplementary analysis tool. Collectively, this work provides the tools, infrastructure, and methodology for the systematic evaluation of radial and axial flux magnetic gears, as well as a thorough characterization of design trends and practical considerations for both topologies.

## 1.1 Prominent Magnetic Gear Design and Performance Metrics

Before discussing the different magnetic gear topologies and the more conventional alternatives to the technology, it is useful to establish the key magnetic gear design quality and performance metrics, which include gear ratio, efficiency, torque ripple, volumetric torque density, gravimetric torque density, and cost. These metrics provide a means of comparison between different magnetic gear designs and the competing traditional solutions, such as mechanical gears and direct drive machines. In particular, active volumetric torque density (VTD), defined by (1) as the ratio of a design's maximum theoretical torque rating (known as its "stall torque" or "slip torque") to its

active volume, receives the most attention in the literature because it provides a normalized characterization of a design's size and compactness. A higher volumetric torque density indicates that a smaller magnetic gear volume is required for a given torque rating. Active gravimetric torque density (GTD), defined by (2) as the ratio of a design's stall torque to its active mass, is similar to volumetric torque density, but provides a normalized measure of gear mass instead of volume.

$$\text{Volumetric Torque Density} = \frac{\text{High Torque Rotor Stall Torque}}{\text{Active Volume}} \tag{1}$$

$$\text{Gravimetric Torque Density} = \frac{\text{High Torque Rotor Stall Torque}}{\text{Active Mass}} \tag{2}$$

Although most academic literature primarily concentrates on maximizing a magnetic gear's VTD and GTD in an effort to make the technology competitive with traditional mechanical gears from a size and weight standpoint, minimizing cost is also essential for the technology to achieve commercial success. In addition to providing extensive analysis of magnetic gear volumetric and gravimetric torque density design trends, this work also contains the first known detailed investigation into the active material cost (AMC) of magnetic gears, including a characterization of how this metric is impacted by using two different permanent magnet materials. In this study, and most other magnetic gear studies, VTD, GTD, and AMC are defined based on the magnetically "active" portion of the gear, which only includes the gear components that contribute to torque production and transmission (primarily the magnets and electrical steel or other ferrous material) and excludes the magnetically inactive components, such as the housing, bearings, and other structural materials.

## 1.2 Conventional Alternatives

In order to gain industrial market share, magnetic gears must compete against more conventional solutions based on mechanically geared systems and traditional direct drive machines. Therefore, before discussing the design trends and performance capabilities of magnetic gears, it is useful to briefly review the same characteristics for mechanical gears and direct drive machines. Table 1 provides a diverse sampling of commercial mechanical gears used for comparison in two prior studies on magnetic gears [34, 35].

Table 1. Mechanical Gear Examples Referenced in Prior Magnetic Gear Studies

| Topology | Stages | Type | Gear Ratio | High Speed (rpm) | Nominal Efficiency | Torque (N·m) | VTD (kN·m/m$^3$) | GTD (N·m/kg) | Reference(s) |
|---|---|---|---|---|---|---|---|---|---|
| Worm | 1 | Winsmith DB961 | 20 | 1450 | 90 | 3386 | 49 | 17 | [34, 36] |
| Worm | 1 | Winsmith DB961 | 100 | 1450 | 68 | 2588 | 38 | 13 | [34, 36] |
| Planetary | 1 | Neugart PLS90 HP | 5 | 500 | 98 | 110 | 132.5 | 25.6 | [34, 37] |
| Planetary | 2 | Neugart PLS90 HP | 20 | 2000 | 95 | 110 | 94.5 | 19.3 | [34, 37] |
| Planetary | 2 | Stober P812SPN1000 | 100 | 2000 | 95 | 800 | 128 | 25 | [34, 38] |
| Helical | 2 | Bonfiglioli C11 2P-4.9-P90 | 4.9 | 1400 | 95 | 48 | 16 | 6.9 | [34, 39] |
| Helical | 2 | Bonfiglioli C41 2P-44.8-P90 | 44.8 | 1400 | 95 | 500 | 51 | 17.2 | [34, 39] |
| Helical | 3 | Varvel RD03 | 324.4 | 1400 | 94 | 36 | 23 | 11.3 | [34, 40] |
| Harmonic | 1 | Harmonic Drive CSD-40-50-2UF | 50 | 3000 | 70 | 96 | 99.7 | 16.8 | [35, 41] |
| Harmonic | 1 | Harmonic Drive CSG-40-50-2UH | 50 | 3000 | 75 | 178 | 197.9 | 35.6 | [35, 42] |
| Harmonic | 1 | Harmonic Drive CSG-17-50-2UH | 50 | 3500 | 75 | 21 | 161.8 | 30.9 | [35, 42] |
| Cycloidal | 1 | Shimpo Drives 2C115 | 6 | 1135 | 95 | 1920 | 64 | N/A | [34] |
| Cycloidal | 1 | Sumitomo Drive Servo 110-Series | 11 | 1500 | N/A | 132 | 111 | 13.8 | [34, 43] |
| Cycloidal | 1 | Sumitomo Drive 6145 | 11 | 580 | N/A | 1288 | 195.1 | 34.6 | [35, 44] |
| Cycloidal | 1 | Shimpo Drives 2K225 | 87 | 1165 | 95 | 109,000 | 181 | N/A | [34] |

As suggested by the examples listed in Table 1, mechanical gear torque densities vary extensively depending on the topology and a plethora of other application and case

specific factors, including performance objectives, material selection, manufacturing precision, torque rating, operating speed, and gear ratio. When comparing different gears (including magnetic gears), these considerations must be accounted for in order to perform a fair and unbiased analysis. Consequently, the limited information in Table 1 is only intended to provide a general indication of reasonable torque density and efficiency values. In order to draw detailed conclusions, comparisons must be performed on a case-by-case basis.

It is critical to note that, based on the information available in public data sheets, the mechanical gear torque densities reported in Table 1 include the masses and volumes associated with the gear housings and other structural materials. In contrast, the magnetic gear torque densities discussed throughout this study do not account for the housing and include only the active components. Additionally, the efficiencies listed in Table 1 are generally nominal or best case operating point efficiencies reported in the manufacturer data sheets. Much like magnetic gear efficiencies, mechanical gear efficiencies depend heavily on the torque and speed operating point.

The findings of another study which performed a theoretical design comparison between mechanical and magnetic planetary gears also reinforce the importance of numerous design factors in determining feasible mechanical gear torque densities [45]. These results are summarized in part by the graphs in Figures 1(a) and 1(b), which illustrate that a mechanical planetary gear's theoretical torque density capability tends to decrease significantly as its gear ratio increases. Additionally, a comparison of the dramatically different torque densities in Figures 1(a) and 1(b) demonstrates the

importance of design safety factors in determining a mechanical gear's theoretical torque density limits. Figure 1(a) shows the theoretically achievable torque densities when using a high Hertz safety factor, while Figure 1(b) depicts the much higher set of achievable torque densities for the same mechanical planetary gears designed with lower Hertz safety factors [45]. The selection of these safety factor values is influenced by manufacturer experience, intended operating conditions, and desired gear life among other considerations.

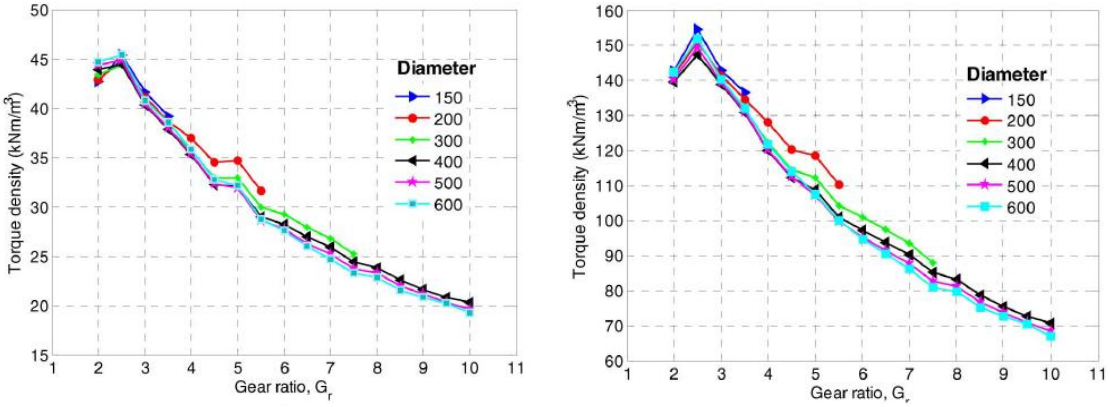


Figure 1. Torque Density Trends for (a) High and (b) Low Safety Factor Mechanical Planetary Gears © 2011 IEEE [45]

Much like mechanical gear torque densities, direct drive machine torque densities can also vary extensively based on different design considerations such as the cooling system, torque rating, and power rating. Within the literature on magnetic gears and magnetically geared machines, one commonly referenced set of typical direct drive machine torque densities is 10 kN·m/m$^3$ for naturally-cooled radial flux permanent magnet machines, 20 kN·m/m$^3$ for forced air-cooled radial flux permanent magnet machines, 30 kN·m/m$^3$ for liquid-cooled radial flux permanent magnet machines, and 40 – 80 kN·m/m$^3$

for liquid-cooled transverse flux machines [1, 10]. However, the higher torque densities of transverse flux direct drive machines come at the expense of lower power factors which necessitate the use of larger converters [10].

Table 2 provides three examples of direct drive machines referenced for comparison in a prior study on magnetically geared machines [13]. These machines all use liquid cooling and are all primarily intended for traction applications such as electric vehicles. The first two machines are axial flux permanent magnet machines and the third is a radial flux permanent magnet machine. The continuous volumetric torque densities for these machines vary from 20.5 – 40.8 kN·m/m$^3$; however, all three machines are capable of much higher peak volumetric torque densities ranging from 31.5 – 75.8 kN·m/m$^3$ for short term operation. Similarly, the continuous gravimetric torque densities for these machines vary from 6.3 – 19.1 N·m/kg and their short term peak gravimetric torque densities range from 9.8 – 29.4 N·m/kg. Larger scale machines are capable of even higher torque densities, with gravimetric torque densities on the order of 23.9 – 47.8 N·m/kg [46] and comparably higher volumetric torque densities [31] reported for electric ship direct drive propulsion motors. As illustrated by these ranges of values, direct drive machines must also be compared on a case-by-case basis, taking into account all relevant design considerations in order to draw fair and accurate conclusions.

Table 2. Examples of Direct Drive Machines Intended for Use in Electric Vehicles

| Model | Power (kW) | Continuous / Peak Torque (N·m) | Continuous / Peak VTD (kN·m/m$^3$) | Continuous / Peak GTD (N·m/kg) | References |
|---|---|---|---|---|---|
| GKN Driveline EVO AF-240 (Axial Flux PM) | 188 | 520 / 800 | 20.5 / 31.5 | 6.3 / 9.8 | [13, 47] |
| YASA Motors YASA 750 R (Axial Flux PM) | 70 | 400 / 790 | 38.4 / 75.8 | 12.1 / 23.9 | [13, 48] |
| Protean Electric PD18 (Radial Flux PM) | 54 | 650 / 1000 | 40.8 / 62.8 | 19.1 / 29.4 | [13, 49] |

## 1.3 Brief History of Magnetic Gears

The early history of magnetic gears is primarily composed of a diverse array of patents [32, 50-70], as summarized in prior studies on the subject [5, 34, 71-73]. In particular, the concept of magnetic gears dates back over 100 years to a set of three early U.S. patents by Armstrong in 1901 [50], Neuland in 1916 [51], and Faus in 1941 [52], whose respective designs are illustrated in Figure 2. Armstrong's design, shown in Figure 2(a), is the first known magnetic gear and essentially represents an electromagnetic analogue of a traditional mechanical spur gear. The device includes two parallel axis rotors, one with steel teeth on its perimeter and another with electromagnets formed by coils around steel teeth on its perimeter [50]. Neuland's magnetic gear, displayed in Figure 2(b), consists of three concentric bodies, including an outer rotor with steel teeth on its interior surface, an inner rotor with steel poles, and an intermediate structure of stationary cores wound with magnetizing coils. Notably, this is the first magnetic gear to employ the idea of flux modulation, a concept which is integral to the operating principle of the magnetic gears analyzed in this study [51]. Faus's apparatus, depicted in Figure 2(c), is also a magnetic spur consisting of two parallel axis rotors with permanent magnets attached to their perimeters and playing the role of the teeth in traditional mechanical spur gears. The permanent magnets on the two rotors "loosely intermesh" and the resulting repulsion forces transmit torque between the two rotors [52]. While this was the first magnetic gear to use permanent magnets, the intermeshing of the permanent magnet teeth means that if the device is overloaded, they will come into mechanical contact with each other and likely suffer damage or even break. This is not the case for Armstrong and

Neuland's designs in which the rotors will simply slip past each other without damage if the gear is overloaded.

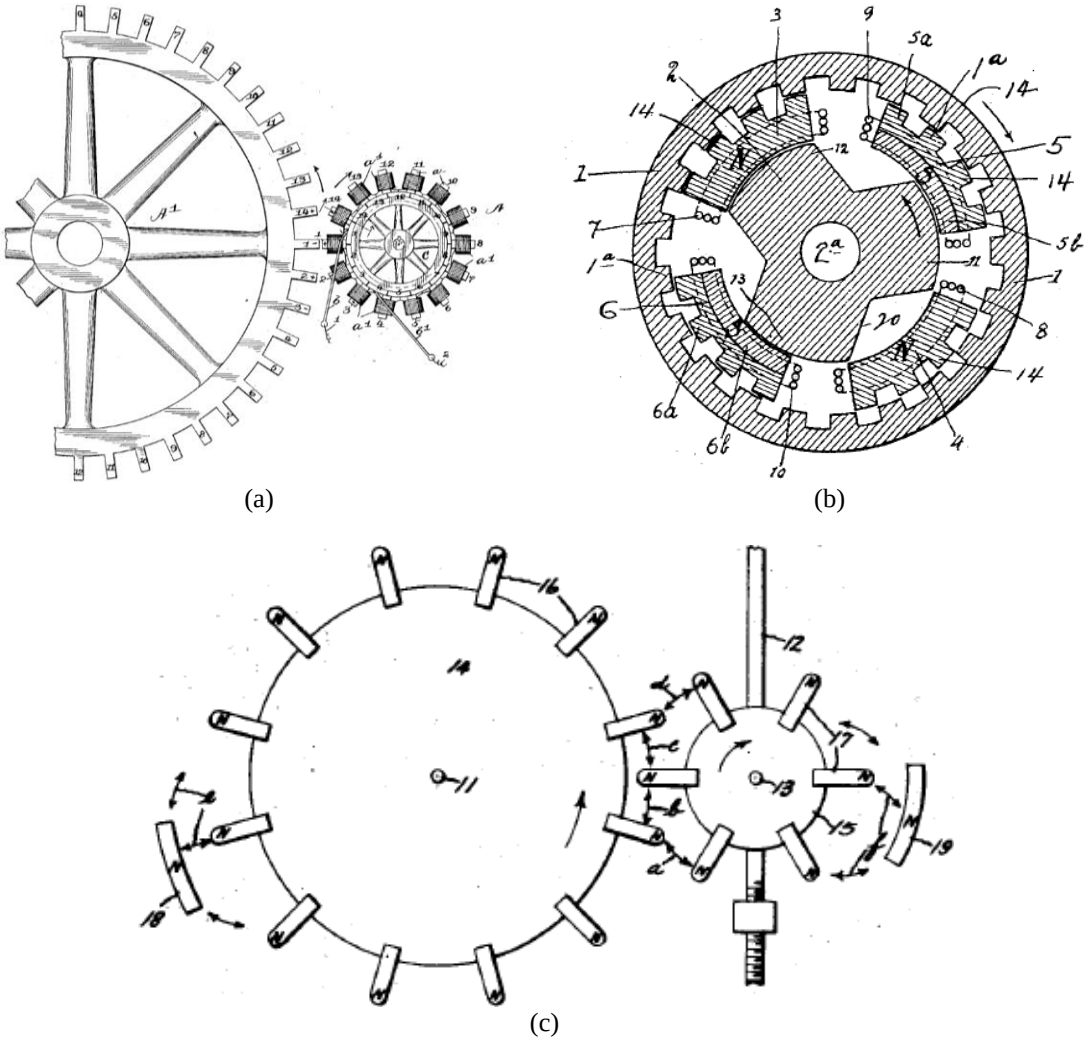

(a) (b) (c)

Figure 2. Early Magnetic Gear Patent Drawings by (a) Armstrong [50], (b) Neuland [51], and (c) Faus [52]

Unfortunately, despite the ingenuity of these inventors, magnetic gearing technology received minimal initial interest for two primary reasons: the limitations of the magnet materials available at the time and the poor performance of the sub-optimal topologies. During the early stages of magnetic gear development, the primary magnet

material was ferrite, which is considerably weaker than the rare earth magnets, such as neodymium iron boron (NdFeB), available for use in modern magnetic gears and electric machines. Additionally, because the permanent magnets available at the time were extremely weak, many early magnetic gears, such as the designs by Amstrong and Neuland, used electromagnets instead of permanent magnets. Due to thermal limitations, these electromagnets also create weaker magnetic fields than those produced by rare earth permanent magnets. Table 3 compares typical values for the key magnetic properties of ferrite and neodymium magnets. Neodymium magnets' higher coercivity ($H_c$) makes them more resistant to demagnetization and their larger remanence ($B_r$) and maximum energy density product ($BH_{max}$) allow them to produce significantly more compact designs. Although the permanent magnets in a magnetic gear do not necessarily operate at the points on the B-H curve corresponding to the remnant flux density or the maximum energy density product, a comparison of the relative values for these properties provides a rough indication of the differing impacts of the two materials. Accordingly, the discovery and development of rare earth permanent magnets, such as NdFeB, proved to be a crucial enabling advancement for magnetic gears and opened the possibility that they might achieve torque densities competitive with those of their mechanical counterparts, thus spawning a renewed interest in the field.

Table 3. Comparison of Typical Magnet Material Properties

| **Material** | **$H_c$ (kA/m)** | **$B_r$ (T)** | **$BH_{max}$ (MGOe)** |
|---|---|---|---|
| Ferrite | 143-286 | 0.22-0.46 | 1-5.6 |
| NdFeB | 836-1082 | 1.06-1.45 | 28-52 |

In addition to the issues caused by the limitations of the available magnet materials, early work on magnetic gears also struggled to gain traction because of the use of inherently poor topologies, such as the designs by Armstrong and Faus, as well as other magnetic pinion [74], worm [75] and spur [60, 76, 77] gear variations, including those shown in Figures 3(a) and 3(b). Most notably, these designs all suffer from poor magnet utilization. Only a small percentage of the permanent magnets or electromagnets used in these gears actually contributes to the torque production at any given position. This results in greater volume and material requirements for a given torque rating and larger, more expensive designs with relatively low torque densities. Even with the advent of rare earth magnets, magnetic gears did not reemerge as a potentially viable concept until new topologies were proposed with significantly higher magnet utilization.

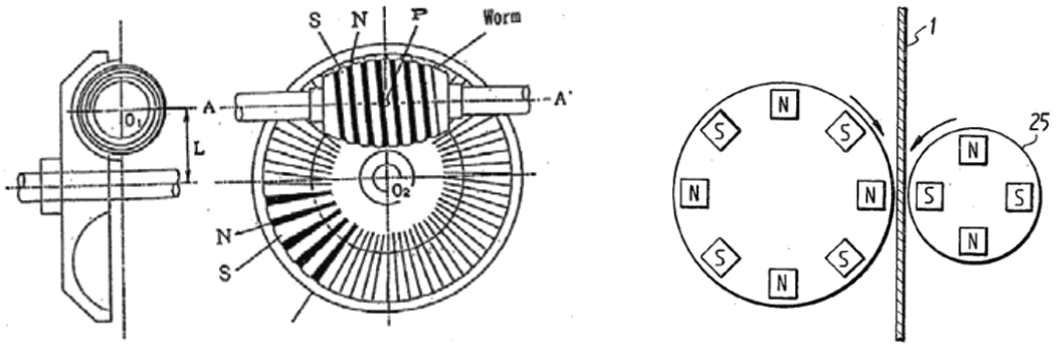


(a) (b)

Figure 3. Magnetic (a) Worm © 1993 IEEE [75] and (b) Spur [60] Gears

A quarter century after Faus's invention, two more patents were awarded to Reese and Martin for key designs in the evolution of magnetic gears. Reese's magnetic gear, patented in 1967 and shown in Figure 4(a), includes three concentric structures, an inner high speed rotor equipped with permanent magnets or electromagnets, an intermediate

low speed rotor with steel teeth, and an outer stator with steel teeth [54]. Martin's design, patented in 1968 and illustrated in Figure 4(b), also consists of three concentric assemblies and essentially represents the first embodiment of the modern concentric planetary radial flux magnetic gear analyzed in this study. The gear includes an inner high speed rotor with permanent magnets, an outer rotor with permanent magnets, and an intermediate rotor consisting of spaced iron segments. Martin provides some discussion of the configuration's operating principle and describes how it is analogous to that of mechanical planetary gears, with the inner rotor functioning as the sun gear, the intermediate rotor serving as the planet gear and carrier, and the outer rotor operating as the ring gear [55]. Further variations of the topology were also described in several ensuing patents which investigated the shape [58, 59], support, and positioning [65, 66] of the iron segments.

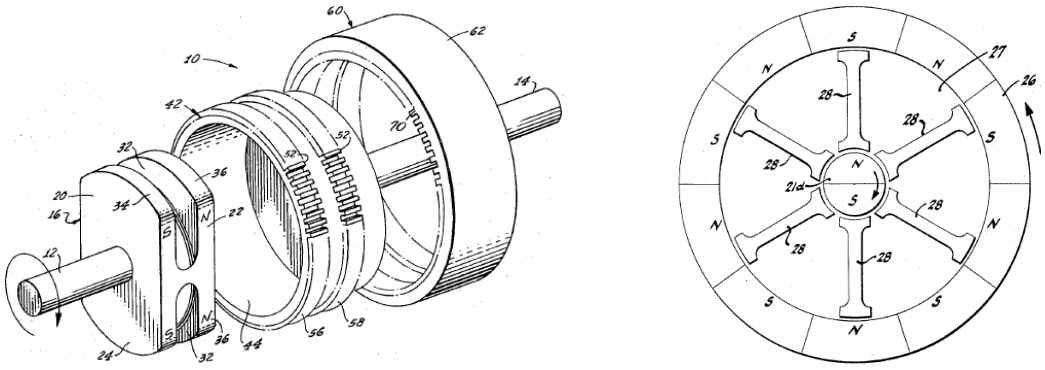


(a) (b)

Figure 4. Magnetic Gear Patent Drawings by (a) Reese [54] and (b) Martin [55]

## 1.4 Basic Modern Magnetic Gear Topologies and Their Operating Principle

The two basic modern magnetic gear topologies are the radial and axial flux coaxial magnetic gears shown in Figures 5 and 6. The radial flux concentric planetary magnetic gear depicted in Figure 5 is essentially the polished modern version of the

coaxial radial flux gears described in the preceding patent history. While several of the aforementioned inventors deserve credit for this topology's development, it did not receive significant interest until a critical study in 2001 provided a thorough explanation of its operating principle and a characterization of its potential for achieving high torque densities when using rare earth permanent magnets [1]. The axial flux coaxial magnetic gear illustrated in Figure 6 is the axial dual of the radial flux gear in Figure 5. The axial flux topology has a much briefer patent history [67] and its modern polished embodiment and operating principle were not described until 2006 [78].

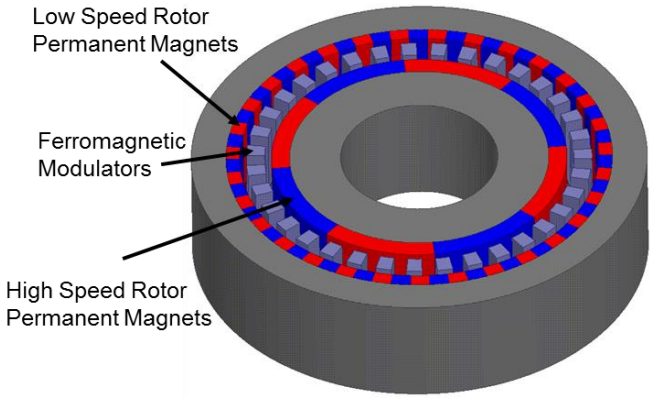


Figure 5. Radial Flux Coaxial Magnetic Gear with Surface Permanent Magnets

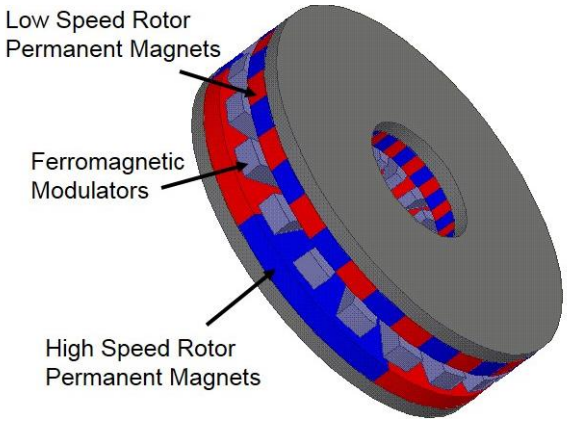


Figure 6. Axial Flux Coaxial Magnetic Gear with Surface Permanent Magnets

These two radial and axial flux magnetic gear topologies are the focus of this dissertation and although they have several key design trend differences, there are also many similarities between their structures and principles of operation. Both configurations consist of three rotors: a high speed permanent magnet rotor (HSR) with a relatively low number of permanent magnet pole pairs ($P_{HS}$) mounted on a ferromagnetic back-iron structure, a low speed permanent magnet rotor (LSR) with a higher number of permanent magnet pole pairs ($P_{LS}$) mounted on a ferromagnetic back-iron structure, and an intermediate modulator rotor consisting of an array of ferromagnetic segments separated by non-magnetic slots. These three rotors are separated by two air gaps, the high speed rotor air gap, between the HSR and the modulators, and the low speed rotor air gap, between the LSR and the modulators. The permanent magnets are depicted by the blue and red pieces in Figures 5 and 6, which indicate alternating north and south magnetic poles as seen by the gear air gaps. The radial flux magnetic gear's rotors are arranged in the form of concentric cylinders rotating about the same axis, while the axial flux magnetic gear's rotors are arranged in the form of disks facing each other and rotating about the same axis.

The ferromagnetic modulator segments in both topologies serve the same effective role: modulating the magnetic fields produced by the two sets of permanent magnets on the high and low speed rotors. When designed properly, this modulation effect creates the gearing action by allowing the two permanent magnet rotors to transmit non-zero average torques between each other at different mechanical speeds. Both the axial and the radial flux gears require the same fundamental relationship between the number of permanent

magnet pole pairs and the number of modulator poles ($Q_M$), given by (3), for proper optimum functionality. An example design illustration of this relationship is provided in Figure 7 with a radial flux magnetic gear using 4 pole pairs on the inner high speed rotor, 17 pole pairs on the outer low speed rotor, and 21 intermediate modulator segments.

$$Q_M = P_{HS} + P_{LS} \tag{3}$$

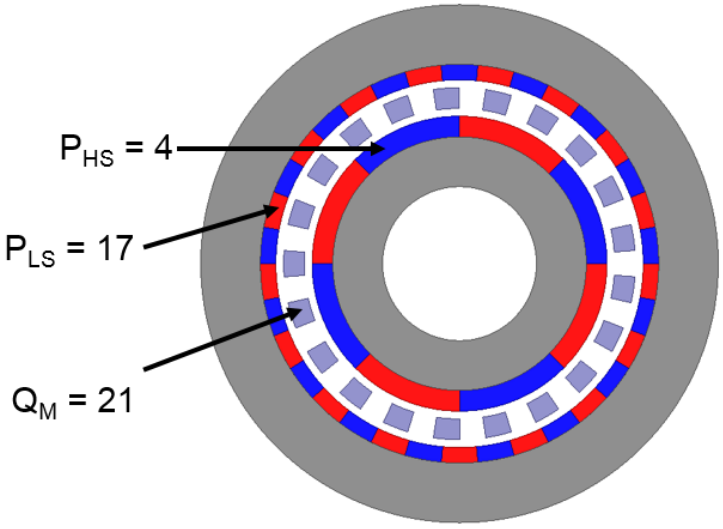


Figure 7. Radial Flux Magnetic Gear Design Example ($P_{HS} = 4$, $P_{LS} = 17$, $Q_M = 21$)

The explanation for the relationship defined in (3) can be understood through a simple idealized analysis of the basic operating principle which governs both axial and radial flux concentric planetary magnetic gears for steady-state HSR ($\omega_{HS}$), LSR ($\omega_{LS}$), and modulator ($\omega_M$) angular velocities [2]. Based on these conditions, the magnetomotive force (MMF) produced by the high speed rotor permanent magnets ($\mathcal{F}_{HS}$) is a function of the angular position ($\theta$) and can be represented by the Fourier series combination of its harmonic components ($\mathcal{F}_{HS,m}$), as shown in (4). Similarly, the MMF produced by the low

speed rotor permanent magnets ($\mathcal{F}_{LS}$) is also a function of θ and can be represented by the Fourier series combination of its harmonic components ($\mathcal{F}_{LS,n}$), as shown in (5). Due to the presence of the modulators, the radially or axially directed permeance seen by both MMFs ($\mathcal{P}$) is also a function of θ and can be represented as the Fourier series combination of its average value ($\mathcal{P}_0$) and its harmonic components ($\mathcal{P}_k$), as shown in (6). The useful magnetic flux resulting from either set of magnets can then ideally be determined from the product of the permeance function and the appropriate MMF function. This analysis reveals that the flux produced by either group of magnets contains a set of synchronous spatial harmonics which rotate at the same speed as the magnets themselves (the rotor's mechanical speed) and another set of asynchronous spatial harmonics which rotate at different speeds. These spatial harmonics and their associated angular velocities are summarized in Table 4. For simplicity, the preceding analysis neglects leakage flux and while this consideration does not impact the basic operating principle of magnetic gears, it does dramatically affect the performance of different designs.

$$\mathcal{F}_{HS}(\theta) = \sum_{m=1}^{\infty} \left\{ \mathcal{F}_{HS,m} \cdot \cos\left( (2m-1) \cdot P_{HS} \cdot \left( \theta - \omega_{HS} \cdot t - \theta_{HS,0} \right) \right) \right\} \tag{4}$$

$$\mathcal{F}_{LS}(\theta) = \sum_{n=1}^{\infty} \left\{ \mathcal{F}_{LS,n} \cdot \cos\left( (2n-1) \cdot P_{LS} \cdot \left( \theta - \omega_{LS} \cdot t - \theta_{LS,0} \right) \right) \right\} \tag{5}$$

$$\mathcal{P}(\theta) = \mathcal{P}_0 + \sum_{k=1}^{\infty} \left\{ \mathcal{P}_k \cdot \cos\left( k \cdot Q_M \cdot \left( \theta - \omega_M \cdot t - \theta_{M,0} \right) \right) \right\} \tag{6}$$

Table 4. Magnetic Gear Air Gap Flux Spatial Harmonics and Angular Velocities

| Term | Synchronous Harmonics | Asynchronous Harmonics |
|---|---|---|
| High Speed Magnet Flux Spatial Harmonics | $(2m-1)\cdot P_{HS}$ | $\lvert(2m\text{-}1)\cdot P_{HS} \pm k\cdot Q_M\rvert$ |
| Low Speed Magnet Flux Spatial Harmonics | $(2n-1)\cdot P_{LS}$ | $\lvert(2n\text{-}1)\cdot P_{LS} \pm k\cdot Q_M\rvert$ |
| High Speed Magnet Flux Angular Velocities | $\omega_{HS}$ | $\frac{(2m\text{-}1)\cdot P_{HS}\cdot\omega_{HS} \pm k\cdot Q_M\cdot\omega_M}{(2m\text{-}1)\cdot P_{HS} \pm k\cdot Q_M}$ |
| Low Speed Magnet Flux Angular Velocities | $\omega_{LS}$ | $\frac{(2n\text{-}1)\cdot P_{LS}\cdot\omega_{LS} \pm k\cdot Q_M\cdot\omega_M}{(2n\text{-}1)\cdot P_{LS} \pm k\cdot Q_M}$ |

In order for the gearing phenomenon to occur properly, a high speed magnet flux synchronous harmonic must couple to one of the low speed magnet flux asynchronous harmonics. Similarly, a low speed magnet flux synchronous harmonic must couple to one of the high speed magnet flux asynchronous harmonics. Any of the conditions described by (7) accomplishes this coupling; however, for optimal practical designs, the relationship specified by (3), which corresponds to m = 1, n = 1, and ±k = -1 in (4)-(6) and the expressions in Table 4, is used almost exclusively. Imposing the condition defined by (3) on the expressions in Table 4 yields the general relationship in (8) between the angular velocities of the three rotors.

$$k\cdot Q_M = (2n-1)\cdot P_{LS} \pm (2m-1)\cdot P_{HS} \tag{7}$$

$$Q_M\cdot\omega_M = P_{HS}\cdot\omega_{HS} + P_{LS}\cdot\omega_{LS} \tag{8}$$

Although (8) indicates that a variable gearing effect or power splitting operation can be achieved by allowing all three rotors to rotate simultaneously, this study focuses exclusively on the two more common operating modes in which one of the rotors is held stationary while the other two are allowed to rotate, thus achieving a constant gearing

behavior. In the first operating mode, the modulators are held stationary and the two permanent magnet rotors are allowed to rotate freely. The resulting gear ratio, which relates the HSR ($\omega_{HS}$) and LSR ($\omega_{LS}$) angular velocities, is given by (9), where the negative sign indicates that the rotors rotate in opposite directions. In the second operating mode, the low speed (high pole count) permanent magnet rotor is held stationary and the modulator assembly is allowed to rotate in its place. The resulting gear ratio, which relates the HSR ($\omega_{HS}$) and modulator ($\omega_{M}$) angular velocities, is given by (10), where the absence of a negative sign indicates that the rotors rotate in the same direction.

$$\text{Fixed Modulators Operation Gear Ratio} = \frac{\omega_{HS}}{\omega_{LS}} = \frac{-P_{LS}}{P_{HS}} \tag{9}$$

$$\text{Fixed LSR Operation Gear Ratio} = \frac{\omega_{HS}}{\omega_{M}} = \frac{Q_{M}}{P_{HS}} \tag{10}$$

The relationships in (3), (9), and (10) dictate that, for a given design, fixed LSR operation yields a gear ratio which is one greater than the absolute value of the gear ratio resulting from fixed modulators operation. Fixed LSR operation also ideally results in a proportional increase in stall torque relative to fixed modulators operation of the same gear. For the design in Figure 7, fixed modulators operation yields a gear ratio of -17:4 (or -4.25:1) and fixed LSR operation yields a gear ratio of 21:4 (or 5.25:1).

In lieu of the preceding mathematical derivation, a magnetic gear's operating principle can be explained by analogy to that of a traditional mechanical gear. In mechanical gears, different rotors rotate at different angular velocities, but the edges of each rotor move at the same tangential linear velocity due to the different radii of the rotors. A rotor with a larger radius rotates at a slower angular velocity than a rotor with a

smaller radius in order to achieve the same tangential linear velocity at its perimeter. Instead of having multiple rotors with matching tangential linear velocities at their perimeters, magnetic gears have multiple rotors with matching electromagnetic velocities. The electromagnetic angular velocity of a magnetic gear (or electric machine) rotor ($\omega_{emag}$) is related to its mechanical angular velocity ($\omega_{mech}$) based on its number of magnetic pole pairs (P) according to (11). This can be understood by considering that the electromagnetic field pattern produced by a rotor with P pole pairs (as seen at a fixed observation point) will repeat itself P times during one mechanical revolution. Thus, for a given mechanical angular velocity, a rotor with a larger number of pole pairs will have a higher electromagnetic angular velocity than another rotor with a lower number of pole pairs rotating at the same mechanical angular velocity. This is why the high speed rotor in a magnetic gear has a lower number of pole pairs than the low speed rotor.

$$\omega_{emag} = P \cdot \omega_{mech} \tag{11}$$

## 1.5 Additional More Complex Magnetic Gear Topologies

In addition to the axial and radial flux coaxial magnetic gears analyzed in this dissertation, there are several other more exotic magnetic gear topologies proposed throughout the literature. Some of the most noteworthy examples of these topologies are illustrated in Figures 8-10. Figure 8(a) shows a variation of the standard radial flux planetary gear in which the modulators are replaced with spinning magnetized cylinders [79] and Figure 8(b) depicts an alternate version of the magnetic planetary gear which is a more direct analogue of a traditional mechanical planetary gear [61, 80]. Figure 9(a) illustrates a radial flux cycloidal magnetic gear which uses eccentric rotation to create the

gearing effect instead of the modulator pieces [81], while Figure 9(b) shows an axial flux cycloidal magnetic gear [82]. Figure 10 depicts a magnetic harmonic gear which uses a flexible inner rotor to create the gearing effect [63, 83]. Several of these topologies exhibit the potential to achieve higher gear ratios or torque densities, but unfortunately, they are also extremely challenging to fabricate due to the need for additional moving parts, eccentric rotation, or a flexible rotor. As a result of this increased construction complexity, these configurations have primarily received limited interest for specific scenarios such as very high gear ratio applications. Other enhancements to the standard radial and axial flux coaxial magnetic gears, such as the use of Halbach arrays [84-87], flux focusing magnet configurations [27, 35, 71, 88-94], and various interior permanent magnet arrangements [4, 95] are also presented in the literature and many of them were analyzed during the course of this work, but they are not included in this study. Finally, in addition to these rotary-to-rotary magnetic gears, linear magnetic gears [96-98] and rotary-to-linear magnetic gears [28, 99-101] are also discussed throughout the existing literature.

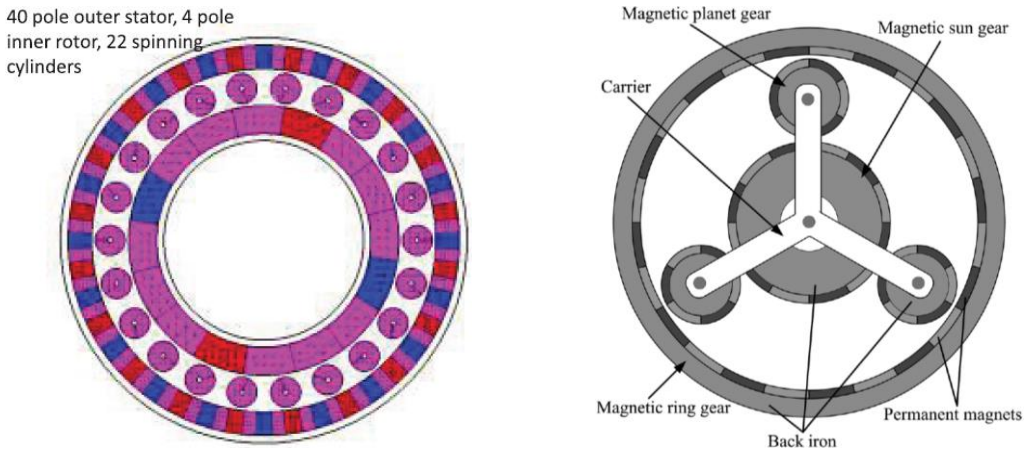


(a) (b)

Figure 8. (a) Rotating Cylinder Planetary Magnetic Gear © 2016 IEEE [79] and (b) Direct Magnetic Analogue of a Mechanical Planetary Gear © 2008 IEEE [80]

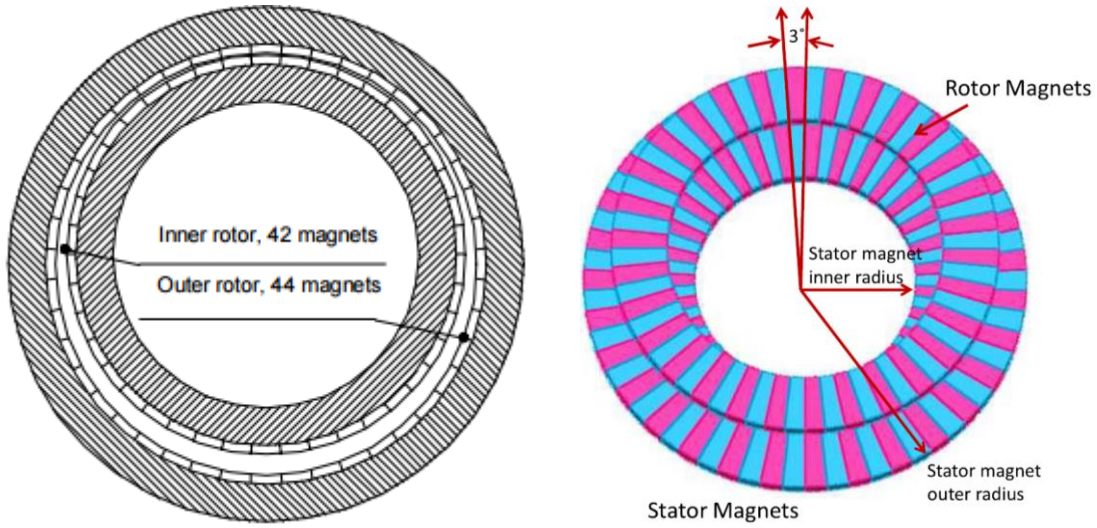


(a) (b)

Figure 9. (a) Radial © 2008 IEEE [81] and (b) Axial © 2014 IEEE [82] Flux Cycloidal Magnetic Gears

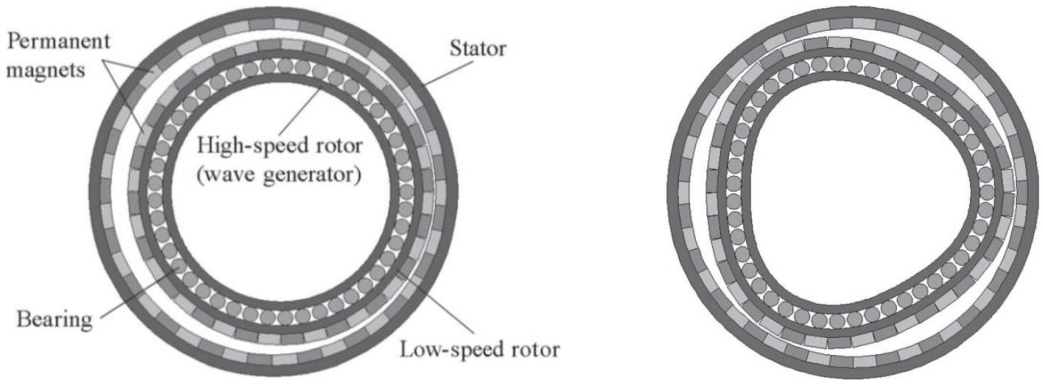


Figure 10. Magnetic Harmonic Gear © 2010 IEEE [83]

# 2. SIMULATION ANALYSIS SYSTEM

Although magnetic gears have garnered increasing interest over the last two decades, there is still a lack of detailed information on design methods and trends, especially when compared to other more traditional electromagnetic machines. This is particularly the case for axial flux gears which have not received nearly as much attention as radial flux gears. Because magnetic gears have entirely different numbers of magnetic pole pairs on the high and low speed permanent magnet rotors, there are significant harmonic and leakage flux considerations as well as limited symmetry (in good designs) which prevent the use or reduce the effectiveness of short-hand analysis techniques and fractional models employed for more conventional machines. These issues are further complicated by presence of the modulator assembly. This work aims to provide a thorough characterization of design trends and a systematic design methodology for both radial and axial flux magnetic gears. As a key step in this process, a modular MATLAB-based infrastructure was developed throughout the study to systematically control various simulation models and analyze their results. In particular, the primary analysis tools integrated into the MATLAB infrastructure included multiple commercial FEA software packages, analytical models implemented in MATLAB, and the lumped parameter magnetic equivalent circuit models developed at the end of this work.

## 2.1 Finite Element Analysis Models

Finite element analysis (FEA) is a numerical tool commonly used to evaluate and design electromagnetic devices. FEA is the most accurate and robust method of analyzing

magnetic gears because it can easily model non-linearities in the system and does not rely on any significant limiting approximations such as some other analysis techniques. Furthermore, although they require a significant amount of computational power and time, 3D models are essential tools for accurately predicting the performance characteristics of many magnetic gear designs, and most commercial FEA software programs have 3D modeling capabilities. Unfortunately, the majority of the existing magnetic gear literature published prior to this study only uses 2D FEA models and as a result, it is replete with wide discrepancies between the torque ratings predicted by simulations and the actual characteristics exhibited by experimental prototypes. In some cases, the simulated and experimental stall torques can differ by more than 30%.

Maxwell by ANSYS and MagNet by Infolytica are the two primary FEA software programs employed throughout this study. Although these two tools generally produce consistent answers, they each have certain strengths and weaknesses. Maxwell offers extremely flexible parameterization capabilities. In order to capitalize on this feature, fully parameterized Maxwell template models were developed for all evaluated systems and used in all 2D and 3D static simulations, as well as all 2D transient simulations. Unfortunately, at the time of this study, Maxwell does not allow multiple moving parts in 3D models, a feature which is absolutely essential for transient simulations of axial flux magnetic gears and also very useful for transient simulations of radial flux magnetic gears. Because MagNet does allow multiple moving parts in 3D models, it was used for all 3D transient simulations, including the loss analysis of the compact axial flux magnetically geared machine developed in this study.

## 2.2 MATLAB Simulation and Data Analysis Infrastructure

Throughout the course of this study, a modular MATLAB infrastructure was gradually developed to systematically control and automate these FEA models in order to save countless "human hours" of work and maximize the number of design cases that could be analyzed with the given amount of computational resources and time. The flowchart in Figure 11 illustrates the MATLAB system's operation. The user specifies the desired set of design points in a master Excel file. A high level MATLAB program reads the set of designs from the Excel file and creates the requested cases in the selected simulation software using fully parameterized magnetic gear template model files (in the case of Maxwell) or fully parametrized model creation MATLAB subroutines (in the case of MagNet). The MATLAB simulation manager program then automatically runs the existing pool of simulations and exports the results out of the simulation software and back into MATLAB. Finally, a MATLAB post-processing program performs several different data analysis calculations using the information extracted from the simulations. Additionally, the post-processing software offers a plethora of different methods for visualizing the data to identify and convey key trends. Based on these results, new simulations can then be added to the list in Excel by a human user or an optimization algorithm. Although, this software system was primarily employed to analyze axial and radial flux magnetic gears, it is extremely general and could easily be adapted to analyze any other type of electromagnetic device.

In order to enable extensive use of 3D FEA simulations, sensitivity analyses were performed on the meshing and convergence criteria. Loosening the FEA meshing and

convergence criteria allows the simulations to run faster, but it can also reduce their accuracy. The results of these sensitivity analyses were used to maximize the FEA system's simulation throughput without significantly compromising its accuracy. Detailed comparisons with experimental results demonstrating the accuracy of the FEA simulations are provided for each of the prototypes evaluated throughout this study.

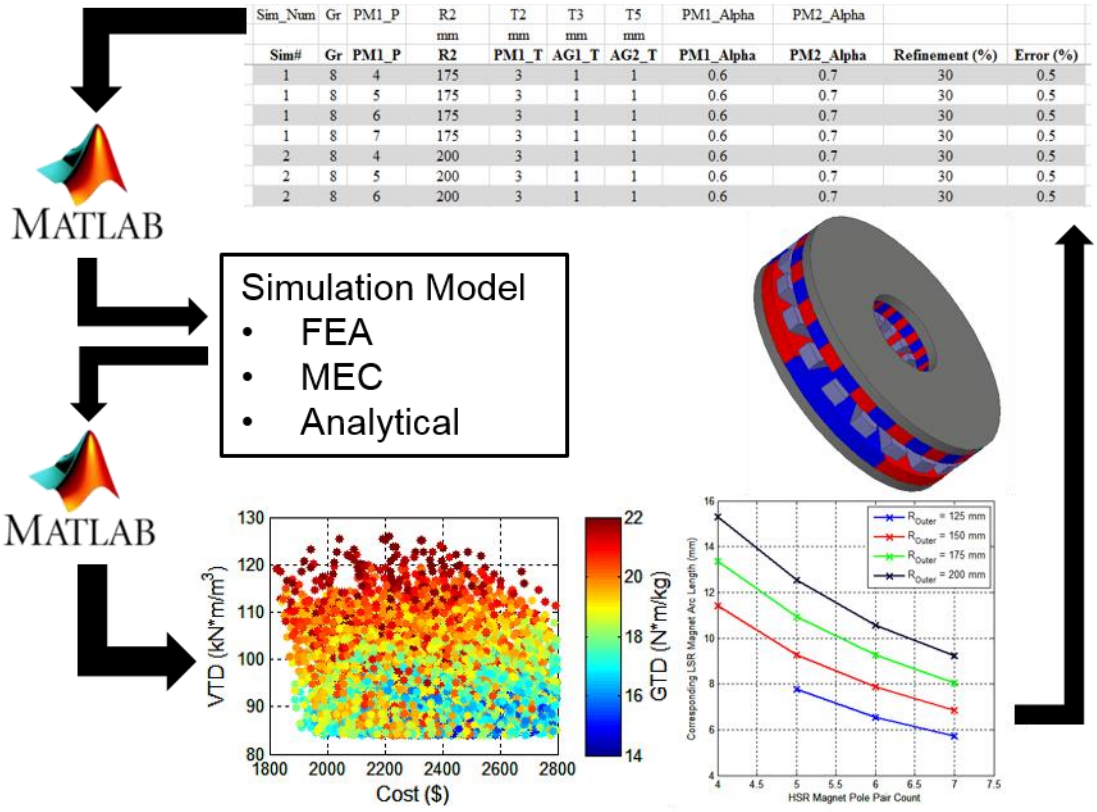


Figure 11. Flowchart for Operation of the MATLAB-Controlled Analysis System

## 2.3 Analytical Models

Analytical models are also frequently employed in the field of electric machines as a means of investigating and designing devices without relying on potentially computationally intensive and time consuming numerical techniques, such as FEA. At

the outset of this study, different researchers had already published 2D analytical models of radial and axial flux magnetic gears, but they were re-derived in this work and implemented in MATLAB, then integrated into the aforementioned MATLAB analysis system for use and evaluation [102-104]. An R-θ model is used for radial flux gears and a Z-θ model is used for axial flux gears. While the radial flux gear R-θ model is formed from a simple Z plane cross-section of the radial gear, such as the one illustrated in Figure 7, the axial flux gear Z-θ mode shown in Figure 12 is somewhat less intuitive and can be viewed as an "unrolled" radial slice of the 3D geometry, located at an equivalent radius ($R_{eq}$) which is either the average or the weighted average of the inner radius ($R_{In}$) and the outer radius ($R_{Out}$). Note that in this 2D model, boundary conditions are applied such that the left and right model boundaries mirror each other.

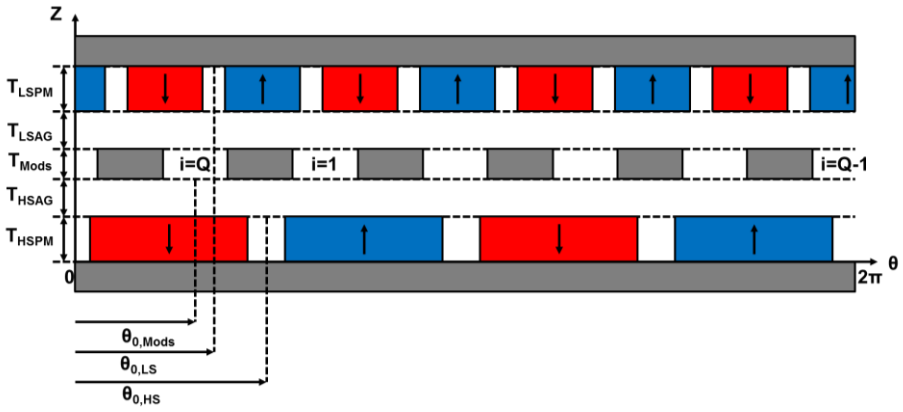


Figure 12. Axial Flux Magnetic Gear 2D Z-θ Model

These analytical models are based on the solution of Laplace and Poisson's equations for the magnetic vector potential (A) in the different gear regions (layers). The partial differential equations and boundary conditions defining the radial flux magnetic gear analytical model are summarized in Table 5, where $R_2$ – $R_7$ represent the radii of the

boundaries between the HSR back iron and HSR PMs, the HSR PMs and HSR air gap, the HSR air gap and modulators, the modulators and LSR air gap, the LSR air gap and LSR PMs, and the LSR PMs and LSR back iron, respectively. The partial differential equations and boundary conditions defining the axial flux magnetic gear analytical model are listed in Table 6, where $z_1 - z_6$ represent the z-coordinates of the analogous axial layer boundaries. Note that these models assume infinite permeability in the iron regions of the gears and no 3D effects (no Z directed field component and no Z dimension field dependency for the radial flux gear and no R directed field component and no R dimension field dependency for the axial flux gear). For the radial flux magnetic gear, the radial ($B_r$) and tangential ($B_\theta$) air gap flux density components can be calculated from the vector potential solution according to (12) and (13). Then, in turn, the torque on the HSR ($\tau_{HSR}$) and the torque on the LSR ($\tau_{LSR}$) can be computed for a unit stack length using Maxwell stress tensors according to (14) and (15), where $R_{HSAG}$ and $R_{LSAG}$ represent the radii of the integration paths in the high speed air gap and low speed air gap. The torque on the entire modulator structure, $\tau_{Mods}$, is then given by (16). Similarly, for the axial flux magnetic gear, the tangential ($B_\theta$) and axial ($B_z$) air gap flux density components can be calculated from the vector potential solution according to (17) and (18). Based on these results, the torque on the HSR ($\tau_{HSR}$) and the torque on the LSR ($\tau_{LSR}$) can be calculated using Maxwell stress tensors according to (19) and (20), where $Z_{HSAG}$ and $Z_{LSAG}$ represent the axial heights of the integration paths in the high speed air gap and low speed air gap. The torque on the entire modulator structure, $\tau_{Mods}$, is again given by (16).

Table 5. Radial Flux Magnetic Gear 2D Analytical Model Equations and Boundary Conditions

| Region | Vector Potential Equation | Boundary Conditions | Boundaries |
|---|---|---|---|
| High Speed Magnets | $\frac{\partial^2 A_1}{\partial r^2} + \frac{1}{r}\frac{\partial A_1}{\partial r} + \frac{1}{r^2}\frac{\partial^2 A_1}{\partial \theta^2} = \frac{\mu_0}{r}\frac{\partial M_{r,HSPM}}{\partial \theta}$ | $\left.\frac{\partial A_1}{\partial r}\right\|_{r=R_1} = 0$<br>$A_1(R_2,\theta) = A_2(R_2,\theta)$ | $R_2 \le r \le R_3$<br>$0 \le \theta \le 2\pi$ |
| High Speed Air Gap | $\frac{\partial^2 A_2}{\partial r^2} + \frac{1}{r}\frac{\partial A_2}{\partial r} + \frac{1}{r^2}\frac{\partial^2 A_2}{\partial \theta^2} = 0$ | $\left.\frac{\partial A_2}{\partial r}\right\|_{r=R_2} = \left.\frac{\partial A_1}{\partial r}\right\|_{r=R_2}$<br>$\left.\frac{\partial A_2}{\partial r}\right\|_{r=R_3} = \left.\frac{\partial A_3}{\partial r}\right\|_{r=R_3}$ | $R_3 \le r \le R_4$<br>$0 \le \theta \le 2\pi$ |
| $i^{th}$ Modulator Slot | $\frac{\partial^2 A_{3,i}}{\partial r} + \frac{1}{r}\frac{\partial A_{3,i}}{\partial r} + \frac{1}{r^2}\frac{\partial^2 A_{3,i}}{\partial \theta^2} = 0$ | $\left.\frac{\partial A_{3,i}}{\partial \theta}\right\|_{\theta=\theta_{0,i}} = 0$<br>$\left.\frac{\partial A_{3,i}}{\partial \theta}\right\|_{\theta=\theta_{0,i}+\beta} = 0$<br>$A_{3,i}(R_3,\theta) = A_2(R_3,\theta)$<br>$A_{3,i}(R_4,\theta) = A_4(R_4,\theta)$ | $R_4 \le r \le R_5$<br>$\theta_{0,i} \le \theta \le \theta_{0,i} + \beta$ |
| Low Speed Air Gap | $\frac{\partial^2 A_4}{\partial r^2} + \frac{1}{r}\frac{\partial A_4}{\partial r} + \frac{1}{r^2}\frac{\partial^2 A_4}{\partial \theta^2} = 0$ | $\left.\frac{\partial A_4}{\partial r}\right\|_{r=R_5} = \left.\frac{\partial A_3}{\partial r}\right\|_{r=R_5}$<br>$\left.\frac{\partial A_4}{\partial r}\right\|_{r=R_6} = \left.\frac{\partial A_5}{\partial r}\right\|_{r=R_6}$ | $R_5 \le r \le R_6$<br>$0 \le \theta \le 2\pi$ |
| Low Speed Magnets | $\frac{\partial^2 A_5}{\partial r^2} + \frac{1}{r}\frac{\partial A_5}{\partial r} + \frac{1}{r^2}\frac{\partial^2 A_5}{\partial \theta^2} = \frac{\mu_0}{r}\frac{\partial M_{r,LSPM}}{\partial \theta}$ | $\left.\frac{\partial A_5}{\partial r}\right\|_{r=R_7} = 0$<br>$A_5(R_6,\theta) = A_4(R_6,\theta)$ | $R_6 \le r \le R_7$<br>$0 \le \theta \le 2\pi$ |

$$B_r = \frac{1}{r}\frac{\partial A}{\partial \theta} \quad \text{(Radial Flux Gear)} \tag{12}$$

$$B_\theta = \frac{-\partial A}{\partial r} \quad \text{(Radial Flux Gear)} \tag{13}$$

$$\tau_{HSR} = \left(\frac{R_{HSAG}^2}{\mu_0}\right) \cdot \int_0^{2\pi} B_r(R_{HSAG},\theta) \cdot B_\theta(R_{HSAG},\theta) \cdot d\theta \quad \text{(Radial Flux Gear)} \tag{14}$$

$$\tau_{LSR} = -\left(\frac{R_{LSAG}^2}{\mu_0}\right) \cdot \int_0^{2\pi} B_r(R_{LSAG},\theta) \cdot B_\theta(R_{LSAG},\theta) \cdot d\theta \quad \text{(Radial Flux Gear)} \tag{15}$$

$$\tau_{Mods} = -(\tau_{HSR} + \tau_{LSR}) \quad \text{(Axial and Radial Flux Gears)} \tag{16}$$

Table 6. Axial Flux Magnetic Gear 2D Analytical Model Equations and Boundary Conditions

| Region | Vector Potential Equation | Boundary Condition(s) | Boundaries |
|---|---|---|---|
| High Speed Magnets | $\frac{1}{R_{eq}^2}\frac{\partial^2 A_1}{\partial\theta^2}+\frac{\partial^2 A_1}{\partial z^2}=\frac{-\mu_0}{R_{eq}}\frac{\partial M_{z,HSPM}}{\partial\theta}$ | $\left.\frac{\partial A_1}{\partial z}\right\|_{z=z_1}=0$<br>$A_1(\theta,z_2)=A_2(\theta,z_2)$ | $z_1\le r\le z_2$<br>$0\le\theta\le 2\pi$ |
| High Speed Air Gap | $\frac{1}{R_{eq}^2}\frac{\partial^2 A_2}{\partial\theta^2}+\frac{\partial^2 A_2}{\partial z^2}=0$ | $\left.\frac{\partial A_2}{\partial z}\right\|_{z=z_2}=\left.\frac{\partial A_1}{\partial z}\right\|_{z=z_2}$<br>$\left.\frac{\partial A_2}{\partial z}\right\|_{z=z_3}=\left.\frac{\partial A_3}{\partial z}\right\|_{z=z_3}$ | $z_2\le r\le z_3$<br>$0\le\theta\le 2\pi$ |
| $i^{th}$ Modulator Slot | $\frac{1}{R_{eq}^2}\frac{\partial^2 A_{3,i}}{\partial\theta^2}+\frac{\partial^2 A_{3,i}}{\partial z^2}=0$ | $\left.\frac{\partial A_{3,i}}{\partial\theta}\right\|_{\theta=\theta_{0,i}}=0$<br>$\left.\frac{\partial A_{3,i}}{\partial\theta}\right\|_{\theta=\theta_{0,i}+\beta}=0$<br>$A_{3,i}(\theta,z_3)=A_2(\theta,z_3)$<br>$A_{3,i}(\theta,z_4)=A_4(\theta,z_4)$ | $z_3\le r\le z_4$<br>$\theta_{0,i}\le\theta\le\theta_{0,i}+\beta$ |
| Low Speed Air Gap | $\frac{1}{R_{eq}^2}\frac{\partial^2 A_4}{\partial\theta^2}+\frac{\partial^2 A_4}{\partial z^2}=0$ | $\left.\frac{\partial A_4}{\partial z}\right\|_{z=z_4}=\left.\frac{\partial A_3}{\partial z}\right\|_{z=z_4}$<br>$\left.\frac{\partial A_4}{\partial z}\right\|_{z=z_5}=\left.\frac{\partial A_5}{\partial z}\right\|_{z=z_5}$ | $z_4\le r\le z_5$<br>$0\le\theta\le 2\pi$ |
| Low Speed Magnets | $\frac{1}{R_{eq}^2}\frac{\partial^2 A_5}{\partial\theta^2}+\frac{\partial^2 A_5}{\partial z^2}=\frac{-\mu_0}{R_{eq}}\frac{\partial M_{z,LSPM}}{\partial\theta}$ | $\left.\frac{\partial A_5}{\partial z}\right\|_{z=z_6}=0$<br>$A_5(\theta,z_5)=A_4(\theta,z_5)$ | $z_5\le r\le z_6$<br>$0\le\theta\le 2\pi$ |

$$B_\theta=\frac{\partial A}{\partial z}\quad\text{(Axial Flux Gear)}\tag{17}$$

$$B_z=\frac{-1}{R_{eq}}\frac{\partial A}{\partial\theta}\quad\text{(Axial Flux Gear)}\tag{18}$$

$$\tau_{HSR}=\frac{\left(R_{Out}^3-R_{In}^3\right)}{3\mu_0}\int_0^{2\pi}\left(B_\theta(\theta,Z_{HSAG})\cdot B_z(\theta,Z_{HSAG})\right)\cdot d\theta\quad\text{(Axial Flux Gear)}\tag{19}$$

$$\tau_{LSR}=\frac{-\left(R_{Out}^3-R_{In}^3\right)}{3\mu_0}\int_0^{2\pi}\left(B_\theta(\theta,Z_{LSAG})\cdot B_z(\theta,Z_{LSAG})\right)\cdot d\theta\quad\text{(Axial Flux Gear)}\tag{20}$$

Both of these analytical models were implemented in MATLAB and tested for accuracy. The radial flux magnetic gear analytical model proved reasonably accurate for

most basic designs and could serve as an acceptable first pass analysis tool. Although the model does assume infinite permeability in the iron, this is not a significant issue for most typical, ideal gear designs, because the permanent magnet and air gap reluctances are substantially larger than the nonlinear iron reluctances. However, this assumption does limit the model's ability to analyze designs with features, such as a modulator bridge, that increase the system's nonlinearity.

Unfortunately, unlike the radial flux magnetic gear analytical model, the axial flux magnetic gear analytical model is extremely inaccurate and inconsistent. This is due to the fact that axial flux magnetic gears have a significant amount of radial leakage flux which is completely neglected in the analytical model. Furthermore, each radial slice of an axial flux gear has different arc and path lengths, unlike the axial slices of a radial flux gear which are all identical to each other. Due to these issues, the axial flux magnetic gear analytical model was not used in this study.

One additional issue with both analytical models is that they are relatively inflexible. Both models were derived for specific geometric topologies and cannot be easily modified to represent other configurations without deriving new field solution expressions. Additionally, these analytical models cannot be easily extended to consider 3D effects without dramatically complicating the field solutions. While this may not be a significant issue for many electromechanical systems, 3D effects are fairly impactful for many magnetic gear designs and this limitation severely hinders the effectiveness of these analytical models.

## 2.4 Magnetic Equivalent Circuit Models

In addition to the FEA and analytical magnetic gear models, 2D and 3D lumped parameter magnetic equivalent circuit magnetic gear models were also developed and integrated into the MATLAB analysis system for evaluation at the end of this study. These models are discussed in Sections 7-10.

# 3. EVALUATION OF AN AXIAL FLUX MAGNETIC GEAR PROTOTYPE

The first experimental prototype evaluated in this dissertation is an axial flux magnetic gear, also referred to as AMTRAN (axial magnetic transmission), which was designed and constructed by a partner company through a project sponsored by the Office of Naval Research (ONR) [105]. This section focuses on the experimental evaluation of the prototype and the subsequent simulation analysis of the design using a 3D FEA model.

## 3.1 Axial Flux Magnetic Gear Prototype Design Details

Although the axial flux magnetic gear illustrated in Figure 6 was first proposed in 2006 [78], it has received much less attention than its radial counterpart. Prior to this work, the literature on axial flux gears was limited to the previously described analytical model [103], simulation analysis of a flux focusing variation of the topology [93], a prototype of an active axial flux magnetically geared generator [17, 18], and a prototype of a more complex axial flux cycloidal magnetic gear [82]. This dearth of literature on axial flux gears is primarily due to two challenges which do not apply its radial counterpart: the need for computationally intensive 3D models in order to accurately analyze the topology and the presence of strong axial forces which complicate the mechanical construction of prototypes. This study provides the first known experimental results for a prototype of the basic passive axial flux coaxial magnetic gear and compares them with 3D FEA simulation predictions to validate the accuracy of the model.

Figure 13 shows the axial flux magnetic gear prototype, while Table 7 lists its constituent materials and Table 8 summarizes its design dimensions. As this is believed to be the first physical prototype of the basic passive axial flux magnetic gear, the primary objective was simply to demonstrate tangible proof of the operating concept and validate the simulation models. With this goal in mind, large 5 mm air gaps, a single HSR magnetic pole pair, and solid back irons (no laminations) were used to simplify the construction process despite the fact that they yielded a significantly less than optimal performance. In particular, the large air gaps considerably lower the gear's stall torque rating, as demonstrated by the graph in Figure 14, which was produced by sweeping the air gaps of the prototype design in a parametric 3D FEA model.

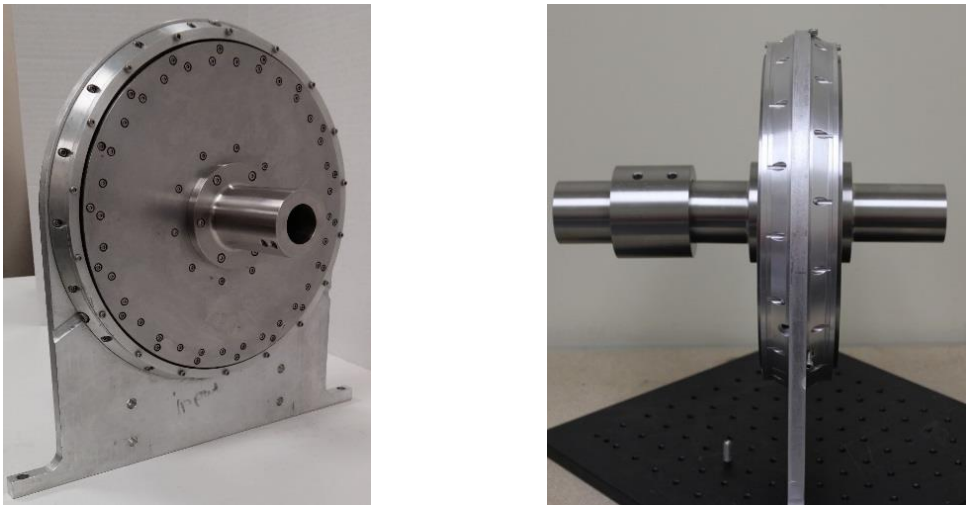

Figure 13. Axial Flux Magnetic Gear Experimental Prototype

Table 7. Axial Flux Magnetic Gear Prototype Materials

| Component | Material |
|---|---|
| Back Iron Disks | Stainless Steel 416 (Solid) |
| Permanent Magnets | NdFeB 42 |
| Modulators | Somaloy 700 3P |

Table 8. Axial Flux Magnetic Gear Prototype Dimensions

| Parameter | Value |
|---|---|
| High Speed Magnet Axial Thickness | 12.7 mm |
| High Speed Air Gap Axial Thickness | 5 mm |
| Modulators Axial Thickness | 6.35 mm |
| Low Speed Air Gap Axial Thickness | 5 mm |
| Low Speed Magnet Axial Thickness | 12.7 mm |
| Outer Radius | 102 mm |
| Inner Radius | 51 mm |
| High Speed Magnet Pole Pairs | 1 |
| Low Speed Magnet Pole Pairs | 8 |
| Modulator Pole Pieces | 9 |
| Gear Ratio | 8:1 |

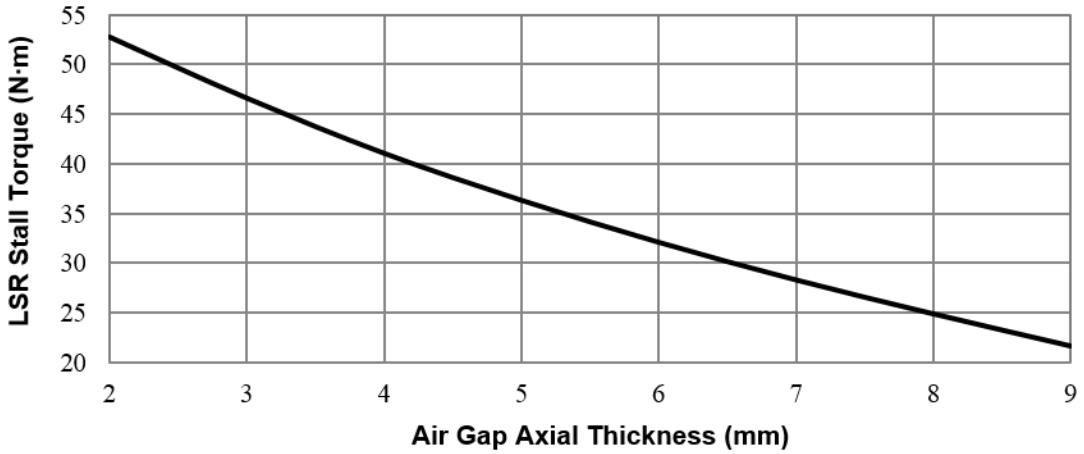


Figure 14. Simulated Variation of Axial Flux Magnetic Gear Prototype Design LSR Stall Torque with Air Gap Axial Thickness

### 3.2 Axial Flux Magnetic Gear Prototype Experimental Evaluation

AMTRAN's performance was examined through both static and dynamic tests using the setup shown in Figure 15. The static experiments consisted of a locked low speed rotor test and a locked high speed rotor test in which the appropriate rotor was "locked" in place while the other permanent magnet rotor was rotated to a set of specific

relative angular positions. The results of these locked rotor tests characterize the gear's torque transmission properties. The simulated and experimental torque values obtained from these locked rotor tests are very similar as demonstrated by the comparison "Torque vs Angle" graphs in Figures 16 and 17. These graphs demonstrate that the torque transmitted by a magnetic gear is approximately a sinusoidal function of the relative angle between the rotors. This relative angle is commonly referred to as the "torque angle" and the gear's peak torque transmission capability (known as its "stall torque" or "slip torque") ideally occurs at a torque angle of 90 electromagnetic degrees, which corresponds to 11.25 mechanical degrees of relative rotation of this prototype's low speed rotor (because of its 8 pole pairs) or 90 mechanical degrees of relative rotation of this prototype's high speed rotor (because of its 1 pole pair). If the driving torque or load torque applied to a magnetic gear exceeds this stall torque, then that will move the gear's operating point past the peak of its "Torque vs Angle" curve to an unstable operating region and the gear's rotors will lose synchronism and slip past each other.

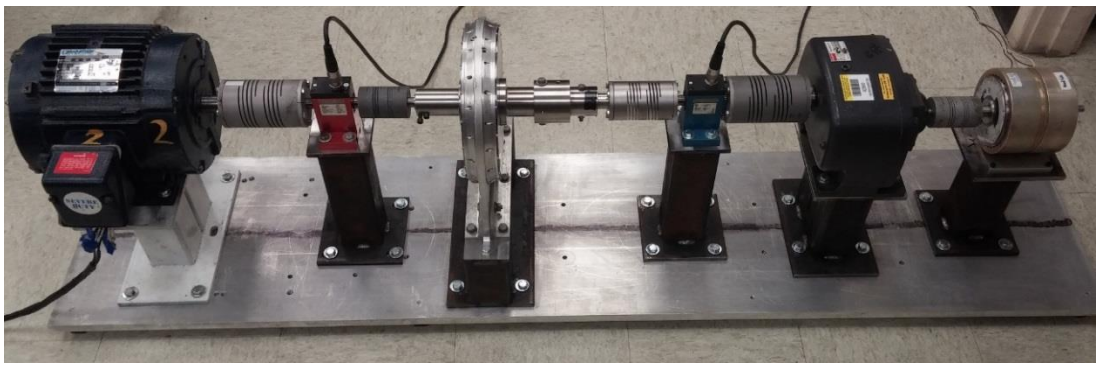

Figure 15. Axial Flux Magnetic Gear Prototype Experimental Testbed

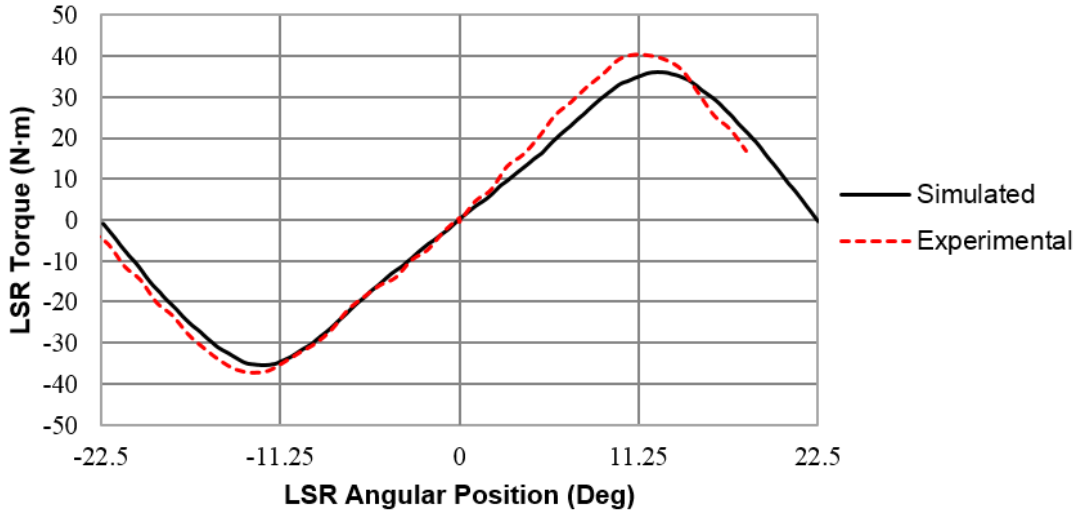


Figure 16. Axial Flux Magnetic Gear Prototype Simulated and Experimental Locked HSR Torque Transmission Characteristics

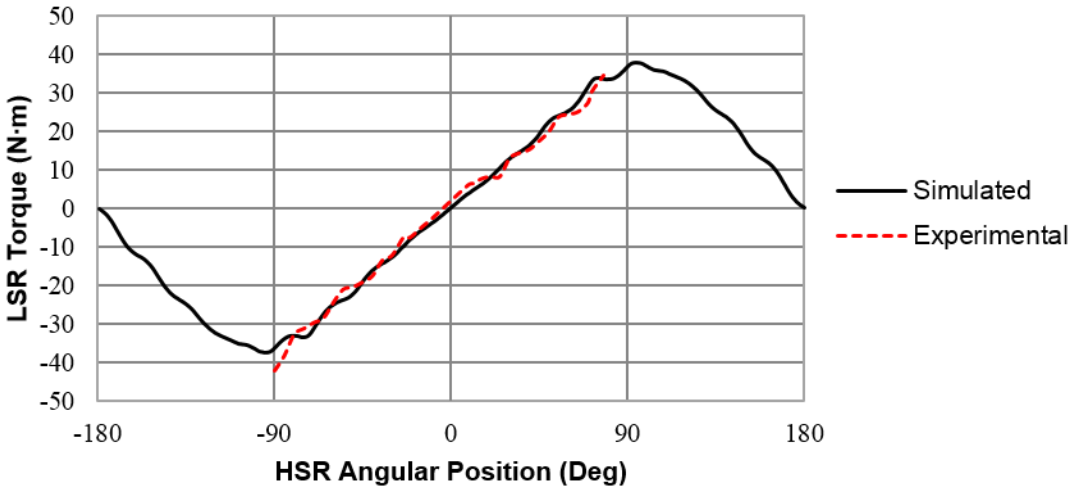


Figure 17. Axial Flux Magnetic Gear Prototype Simulated and Experimental Locked LSR Torque Transmission Characteristics

The experimental results indicate a stall torque of 40.2 N·m, which represents a slight 5.7% increase relative to the simulation value and results in a volumetric torque density of 22.4 kN·m/m$^3$. The relatively minor differences between the experimental and simulated data are primarily due to mechanical friction, issues with the bearings, and

discrepancies between the target and actual air gaps, which can be quite impactful, as indicated by the data in Figure 14. These inconsistencies could be further mitigated with an improved mechanical design and they are also expected to naturally decrease (from a per unit standpoint) for larger gears with higher torque ratings. In general, the close agreement between the simulated and experimental torque versus angular position curves provides strong evidence that the 3D FEA model accurately predicts the gear's torque transmission properties.

Dynamic tests were also conducted to characterize the prototype's losses. The input motor shown at the left in Figure 15 rotated the high speed rotor at different speeds while the hysteresis brake at the right applied different load torques to the low speed rotor. The no load losses were calculated by measuring the gear's input speed and power with the load disconnected and the results are shown in Figure 18. The no load losses represent the total combination of the gear's mechanical and magnetic losses. These losses are large in comparison to the gear's torque rating and this is primarily due to friction and other mechanical losses, as well as the use of solid back irons. Specifically, the gear's performance was hindered by issues with the bearings which contributed to excessive friction on both rotors. Additionally, the magnetic losses in the back irons were high because laminations were not employed in order to simplify the construction process and the use of a single magnetic pole pair on the high speed rotor gave rise to large harmonic flux components which produced significant eddy current losses and a large torque ripple. This high level of losses is not an inherent characteristic of the topology and the gear's efficiency could be significantly improved with the appropriate basic design changes.

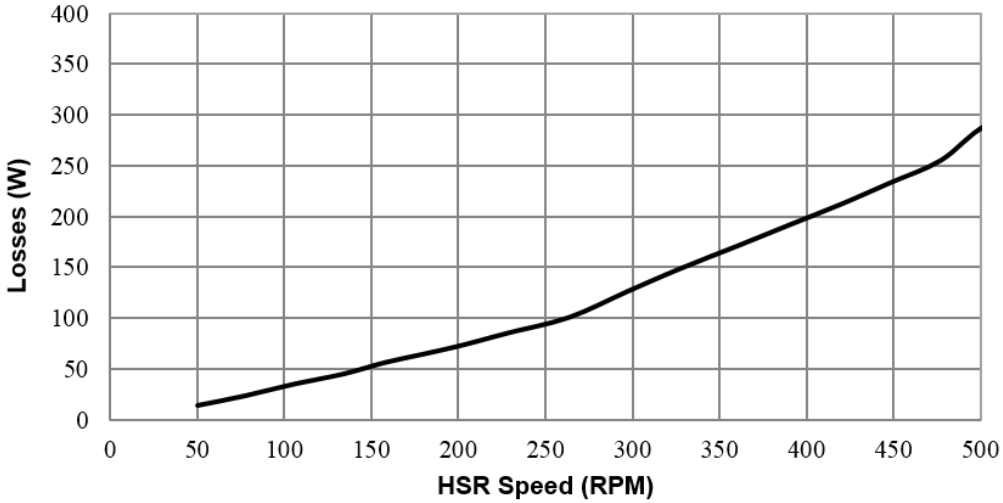


Figure 18. Axial Flux Magnetic Gear Prototype Experimental No Load Losses

Although the AMTRAN design is demonstrably sub-optimal due to several oversimplifications, it is the first known prototype of a passive axial flux coaxial magnetic gear and thus produced the first set of experimental data for the topology. The prototype's volumetric torque density of 22.4 $kN{\cdot}m/m^3$ is significantly lower than the results reported for various other magnetic gear designs and topologies. This low torque density is not an inherent property of axial flux magnetic gears, but rather a result of the sub-optimal design choices, most notably the use of large air gaps, a single HSR pole pair, and solid rotor back irons, which were intended to facilitate the development of a basic physical proof of concept prototype. Despite these shortcomings, the simulation analysis and experimental evaluation of the prototype did provide several useful outcomes. The comparison between the simulation torque predictions and the experimental results validated the accuracy of the 3D FEA models. Additionally, the process of constructing and testing the prototype provided a great deal of experience and information regarding the nature of the topology's mechanical and structural challenges.

# 4. DESIGN AND ANALYSIS OF AN AXIAL FLUX MAGNETICALLY GEARED GENERATOR

This section and the following section cover the design of two different magnetically geared machines developed as part of a Department of Energy (DOE) sponsored investigation into the use of the technology to harness wave energy and convert it into electrical energy. Wave energy is a largely untapped source of renewable energy with some intriguing attributes, including higher energy densities than wind and solar energy [106, 107]. Additionally, the amount of available wave energy is more consistent and easier to forecast than the amount of available wind or solar energy [106, 107]. Furthermore, the world's exploitable wave energy resources are on the order of 8000-80,0000 TWh/year, with some of the most promising regions including the coasts of Canada, the United States, and Western Europe. However, despite these positive qualities, harvesting wave energy presents significant challenges, most notably the fact that it naturally exists in the form of extremely low speed, high force motion. These challenges have led to a wide array of proposed wave energy converter technologies [106-109].

In particular, this project focused on the development of a magnetically geared generator for use with an Oscillating Wave Surge Converter (OWSC), which is one example of these technologies. The OWSC consists of a paddle anchored to the seabed and harnesses the waves to move this paddle back and forth. The motion of the paddle is

then used to generate electricity. The OWSC provides several advantages, such as elimination of mooring lines, protection from storms, and the use of minimal moving parts. However, because the waves move the paddle at a very low speed and with an extremely high torque, converting the mechanical energy to electrical energy is a significant challenge.

While a direct-drive generator is desirable for this application because of its high reliability, the requisite machine must be very large to harness the tremendous torque necessary to generate significant electrical power from such low speed motion. This dilemma is further compounded by the extreme variation between the peak and average wave power, which requires the generator to be sized for a power significantly greater than the average power that it will produce [106]. Magnetic gears are one recently proposed, promising alternative which could help address some of these issues in wave energy conversion systems [27, 28, 92, 98]. For wave energy conversion in particular, the inherent overload protection offered by magnetic gears provides significant benefits. First, the magnetic gear will not be damaged when exposed to torques exceeding its rated operating point. Second, the magnetic gear cannot transfer more torque than its stall torque, which protects the components connected to its high speed output. Thus, the gear and generator potentially do not need to be designed to accommodate the peak wave power; instead, they can be much smaller and less expensive without sacrificing the ability to capture most of the total wave energy.

In order to incrementally attack this challenge, the project was divided into three phases of increasing scale. The first phase targeted the development of a small scale 1

kW, 300 rpm magnetically geared machine. This section discusses the design, construction, analysis, and experimental evaluation of that machine. The second phase focused on the design of a large scale 10 kW, 30 rpm magnetically geared machine. Section 5 describes the design and experimental evaluation of that prototype. Finally, the third phase involved the development of a theoretical full scale design rated for 40 kW at 1.7 rpm, which are the operating conditions required for use with the OWSC.

Although the prototypes developed in this sequence of studies were part of a project investigating the use of magnetic gears for wave energy conversion, the contributions made throughout this work are primarily relevant to the general field of magnetic gears and magnetically geared machines and not necessarily unique to the objective of wave energy conversion. The extremely low speed and high torque requirements of the investigated wave energy system made this particular situation challenging and well suited to the use of magnetic gears and magnetically geared machines; however, the technology and innovations developed during this study are readily applicable to a host of other possible applications.

## 4.1 Theoretical Appeal of Axial Flux Magnetic Gear Topologies

Despite the mechanical challenges of constructing axial flux magnetic gears described in the previous section, one significant appeal of axial flux topologies can be observed through the simplistic theoretical analysis summarized in Table 9. For a radial flux topology with constant average air gap shear stress, torque increases with the square of the radius. This occurs because the air gap area increases linearly with radius, increasing the tangential forces linearly, and the torque arm of those tangential forces

increases linearly with radius. However, for an axial flux topology with constant average air gap shear stress, the torque increases with the cube of the radius. This occurs because the air gap area increases with the square of the radius and the average torque arm increases linearly with the radius. Since volume increases with the square of the radius, the axial field gear can theoretically achieve a torque density that increases linearly with the radius, while the radial field gear's torque density is ideally independent of the radius. This scaling principle causes axial field magnetic gears to favor designs with large outer diameters and short stack lengths. While these trends are subject to practical limiting concerns, such as the large axial forces and mechanical design challenges described throughout the discussion of AMTRAN in the previous section, the extremely limited amount of literature on experimental axial field magnetic gear and magnetically geared machine prototypes means that the implications of these issues are not well understood.

Table 9. Theoretical Comparison of Radial and Axial Flux Magnetic Gear Geometrical Scaling Properties

| Parameters | Radial Flux Gears | Axial Flux Gears |
|---|---|---|
| Air Gap Area | $\propto R \cdot H$ | $\propto R^2$ |
| Torque Arm | $\propto R$ | $\propto R$ |
| Torque | $\propto R^2 \cdot H$ | $\propto R^3$ |
| Volume | $\propto R^2 \cdot H$ | $\propto R^2 \cdot H$ |
| Torque Density | $\propto k$ | $\propto R/H$ |

## 4.2 Existing Magnetically Geared Machine Topologies

As a natural extension of a passive magnetic gear, a magnetically geared machine (MGM) directly integrates a magnetic gear with a conventional low torque, high speed electric machine, producing a single compact device which combines the benefits of a

magnetic gear and the simplicity of a traditional direct drive machine. The literature on magnetically geared machines is even more heavily tilted toward radial field systems [10-15] than the literature on passive magnetic gears. Section 5 provides a detailed discussion of the most promising of these radial flux magnetically geared machine (RFMGM) topologies, such as the inner stator configuration shown in Figure 19.

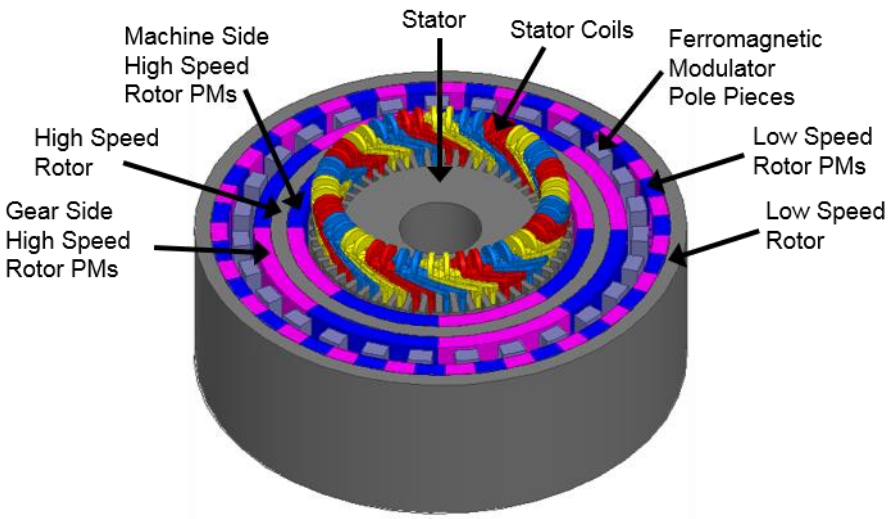


Figure 19. Magnetically Coupled Inner Stator Radial Flux Magnetically Geared Machine

In contrast to radial flux MGMs, only four known studies of axial flux magnetically geared machines (AFMGMs) have been published [17, 18, 110-112]. The first type suffers from an inherently low torque density because it replaces the high speed rotor magnets with stationary coils [110, 111]. The second topology, shown in Figure 20, appears to have much better potential despite the disappointing performance of the first prototype, which was caused by various mechanical and leakage flux issues [18]. However, while this topology does remove the need for a shaft connecting the electric machine to the magnetic gear, it is much closer to a series connection of the two devices than it is to the compact integration accomplished by the RFMGM topology shown in

Figure 19. Furthermore, because the axial field magnetic gear must transmit a much larger amount of torque than the axial machine, it requires a larger outer radius, which agrees with the results found in [17] and [18]. This consideration suggests that the axial field machine and axial field magnetic gear will tend to be mismatched in size.

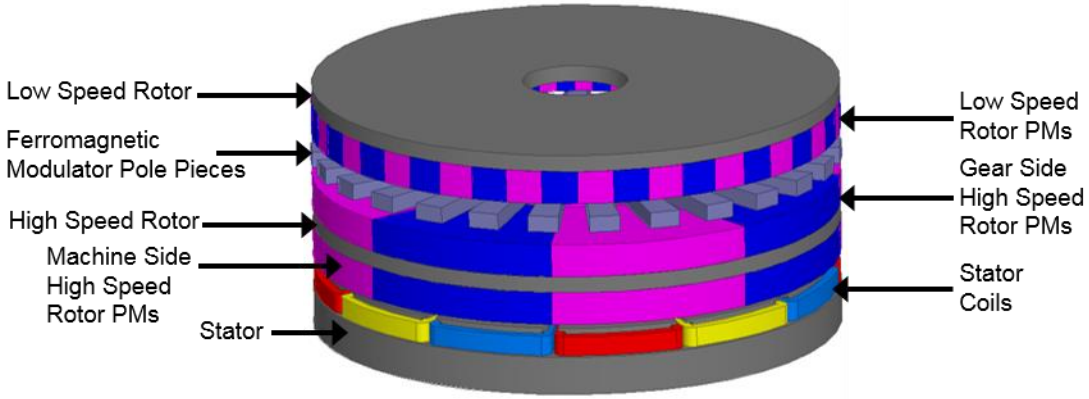


Figure 20. Series Connected Axial Flux Magnetically Geared Machine

On top of the size matching issues, the series connected AFMGM topology in Figure 20 has the undesirable characteristic that the addition of the axial field machine increases the overall size of the device, unlike the RFMGM topology in Figure 19. The significance of this is evidenced by the fact that [17] reports a volumetric torque density of 105 kN·m/m$^3$ for the topology, based only on the gear volume; unfortunately, if the generator volume (not including end windings) is also considered, then the torque density decreases by about 50% [18].

### 4.3 Proposed Topology

Drawing on the experience gained from evaluating the axial flux magnetic gear prototype described in the previous section, this work continues to fill the void of experimental results for axial field magnetically geared systems by proposing,

constructing, and analyzing the new compact AFMGM topology illustrated in Figures 21 and 22. This design consists of an axial flux permanent magnet machine located concentrically in the radial bore of an axial flux magnetic gear. The high speed rotors of both the electrical machine and the gear are connected together to form a single mechanical structure, as depicted in Figure 22. The relationship between the high speed rotor permanent magnet pole pair count ($P_{HS}$), low speed rotor permanent magnet pole pair count ($P_{LS}$), and modulator pole pieces count ($Q_M$), as well as the resulting gearing ratio, are still described by (3) and (9), respectively. The axial flux permanent magnet generator pole count can be selected independently of the gear pole counts, provided that there is a large enough radial gap between the two subsystems to ensure magnetic isolation.

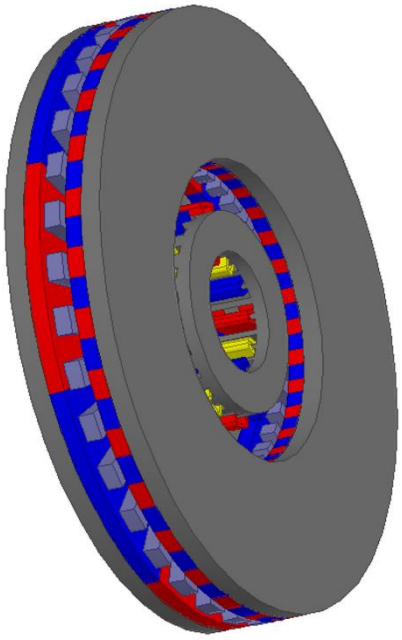

Figure 21. Proposed Compact Axial Flux Magnetically Geared Machine Topology

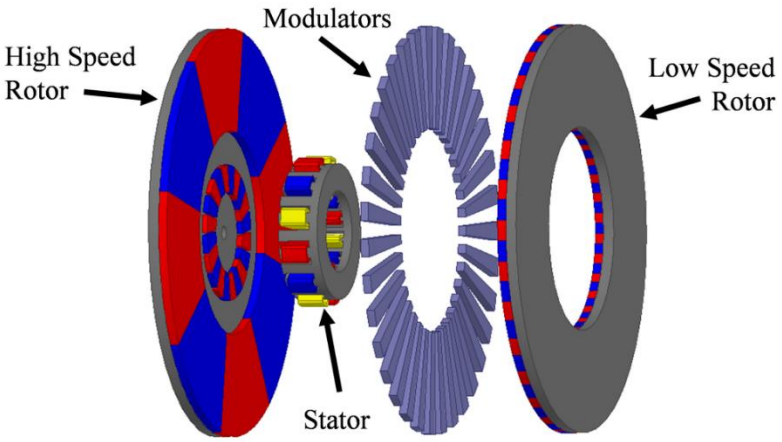


Figure 22. Exploded View of the Proposed Compact AFMGM

When the compact AFMGM is operated as a generator, the external motion source turns the gear's LSR. The LSR magnets then interact with the HSR magnets through the modulators to produce motion in the HSR according to the gear ratio given by (9). Because the gear's HSR and the generator's rotor are a single mechanical structure, the torque exerted on the gear HSR also rotates the generator magnets. The motion of the generator magnets then electrically excites the stator windings. As with conventional machines, the system can also be driven in the inverse configuration as a motor.

Placing the axial field generator inside the bore of the gear prevents the increase in volume caused by the series connection of the generator to the gear in the original topology. This makes use of the empty space inside of the axial gear which is unused or poorly used in the original topology. As a result of this change, the total volume consumed by the compact AFMGM is identical to that required for the corresponding passive axial field gear (although additional limitations are now placed on the inner radius of the gear). The compact topology also allows the generator to inherently use a smaller outer radius than the magnetic gear, which is consistent with their natural design points since the

generator is a low torque, high speed machine and the gear is high torque, low speed device. Another small, but potentially significant advantage of this topology is that the HSR back iron can be thinner than in the original magnetically decoupled version of the series connected design, because it no longer has to isolate or accommodate flux from magnets on both sides. All of these benefits are independent of whether the high magnet pole count disk or the modulators are allowed to rotate.

### 4.4 Electromagnetic Design of the Prototype

In order to experimentally evaluate the proposed topology, a small scale prototype was designed and fabricated. Due to time and cost constraints, the rotor and tape wound laminated stator from a commercially available axial field PM machine were used as the integrated generator in the compact AFMGM. This repurposed machine, which is shown in Figure 23, is rated for 3.4 N·m at a speed of 2800 rpm (a power of 1 kW). While this machine is suboptimal for use in the magnetically geared machine topology, hindering the performance of the AFMGM, it does not prevent the prototype from being useful for addressing magnetic and mechanical design considerations and for experimental evaluation of the proposed topology and magnetically geared machines in general.

(a) (b)

Figure 23. (a) Tape Wound Stator and (b) Rotor of Axial Flux PM Machine

Due to time and cost considerations, the magnetic gear portion of the prototype was intentionally designed for ease of fabrication and for low cost rather than for optimal performance. Future work could be performed to create an optimized version of the topology; however, the parametric study defined in Table 10 was conducted using 3D finite element analysis in ANSYS Maxwell to develop a conservative gear prototype and illustrate key design trends. In this sweep, the derived parameter, $G_r$, represents the approximate (nearest integer) desired gear ratio and relates the number of low speed rotor pole pairs to the number of high speed rotor pole pairs according to (21). This maintains a high least common multiple between $P_{HS}$ and $P_{LS}$, which reduces the gear's torque ripple [26]. A second derived parameter, $K_R$, relates the gear's inner radius to its outer radius according to (22). Furthermore, the LSR magnet thickness is limited to not exceed the HSR magnet thickness to ensure that most of the magnet material is placed on the rotor with fewer poles and less leakage flux. Similarly, the LSR back iron thickness is limited to not exceed the HSR back iron thickness. For all designs, demagnetization was analyzed in the static simulations by evaluating the percentage of the magnet bodies operating at flux densities below the knee point of their demagnetization curves at 20 °C. While this neither comprehensively quantifies the full extent of demagnetization during operation nor addresses demagnetization's temperature dependence, it does indicate which designs are most susceptible to demagnetization. To that end, the 153 designs with more than 1% of the magnet volume operating below the knee point were removed from the population of 6480 designs. For most reasonable designs, this is typically not a significant issue at

normal operating temperatures due to the reluctance of the two air gaps and the high coercivity of NdFeB magnets.

$$P_{LS} = G_r \times P_{HS} + 1 \tag{21}$$

$$R_{in} = K_R \times R_{out} \tag{22}$$

Table 10. Axial Field Magnetic Gear Parametric Design Sweep

| Name | Description | Values | Units |
|---|---|---|---|
| $G_r$ | Nearest integer gear ratio | 6, 9, 12 | |
| $P_{HS}$ | HSR pole pairs | 2, 3, 4, 5 | |
| $R_{out}$ | Outer radius | 70, 90, … 150 | mm |
| $K_R$ | Ratio of inner and outer radii | 0.5, 0.625, 0.75 | |
| $T_{HSBI}$ | HSR back iron thickness | 5, 10, 20 | mm |
| $T_{HSPM}$ | HSR magnet thickness | 3.18, 6.35, 12.7 | mm |
| $T_{AG}$ | Air gap thicknesses | 3 | mm |
| $T_{Mods}$ | Modulator thickness | 6 | mm |
| $T_{LSPM}$ | LSR magnet thickness<br>For $T_{HSPM}$ = 3.18 mm<br>For $T_{HSPM}$ = 6.35 mm<br>For $T_{HSPM}$ = 12.7 mm | <br>3.18<br>3.18, 6.35<br>3.18, 6.35, 12.7 | mm |
| $T_{LSBI}$ | LSR back iron thickness<br>For $T_{HSBI}$ = 5 mm<br>For $T_{HSBI}$ = 10 mm<br>For $T_{HSBI}$ = 20 mm | <br>5<br>5, 10<br>5, 10, 20 | mm |

Figure 24 shows the variation of the maximum volumetric torque density (within this parametric sweep) with the gear ratio for different HSR magnet thicknesses. This demonstrates that within the evaluated design space the maximum achievable volumetric torque density of the gear decreases as the gear ratio increases beyond approximately 6. While the use of a larger gear ratio increases the necessary volume of the gear, it decreases the integrated machine size by lowering its torque requirement. Thus, a true system level

optimization must involve varying the design of both the integrated machine and the gear as the gear ratio changes. Figure 24 also illustrates that increasing the magnet thicknesses increases the torque density, but with diminishing returns.

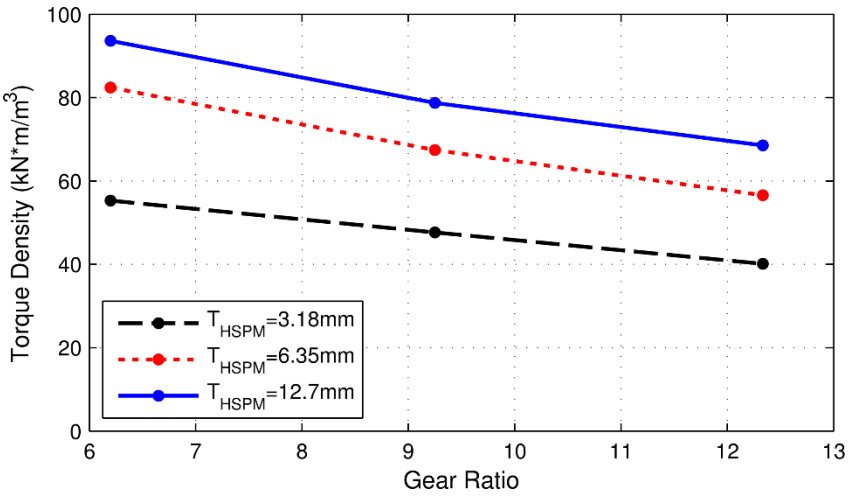


Figure 24. Maximum Volumetric Torque Density vs. Gear Ratio for Different Magnet Thicknesses

Another important design parameter is the back iron thickness, which impacts the containment of magnetic flux, the torque rating (and torque density), and the efficiency. Figure 25 illustrates the effects of pole count and the ratio of back iron to magnet thicknesses on the leakage flux density axially beyond the back irons. Flux leakage on both the HSR and LSR sides is heavily influenced by the HSR pole count and HSR magnet thickness. This occurs because the HSR magnets' lower order spatial flux harmonics span longer paths than the higher order harmonics from the LSR magnets. Also, higher pole counts decrease the span of the flux paths, decreasing leakage flux for a given back iron thickness. Figure 26 shows the effect of the HSR back iron thickness on torque density. While a thicker back iron increases the torque by accommodating more flux, it also

increases the active volume. Thus, oversizing the back iron beyond the thickness necessary to accommodate most of the flux actually decreases the torque density.

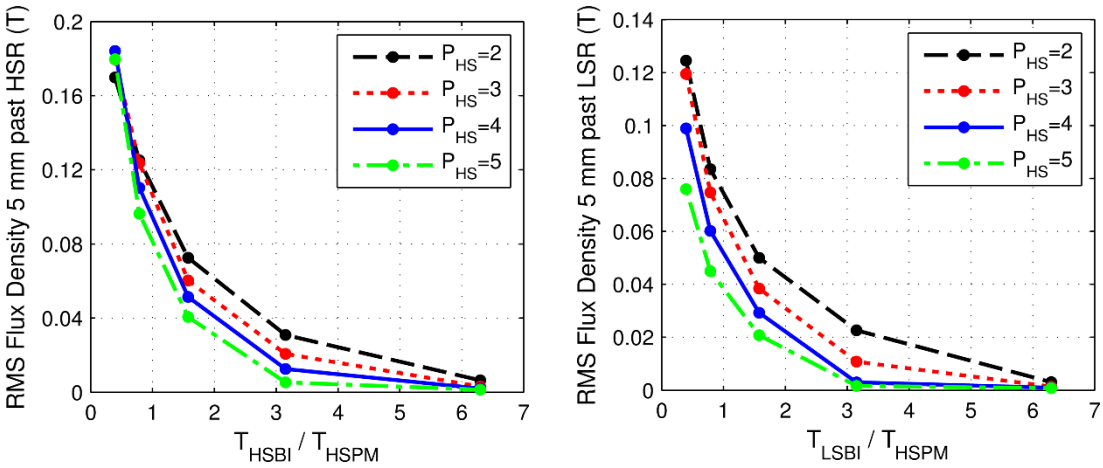


Figure 25. Worst Case Leakage Flux Density Variation with HSR Pole Pairs, (a) HSR Back Iron to HSR Magnet Thicknesses Ratio, and (b) LSR Back Iron to HSR Magnet Thicknesses Ratio with an LSR Magnet Thickness of 3.18 mm

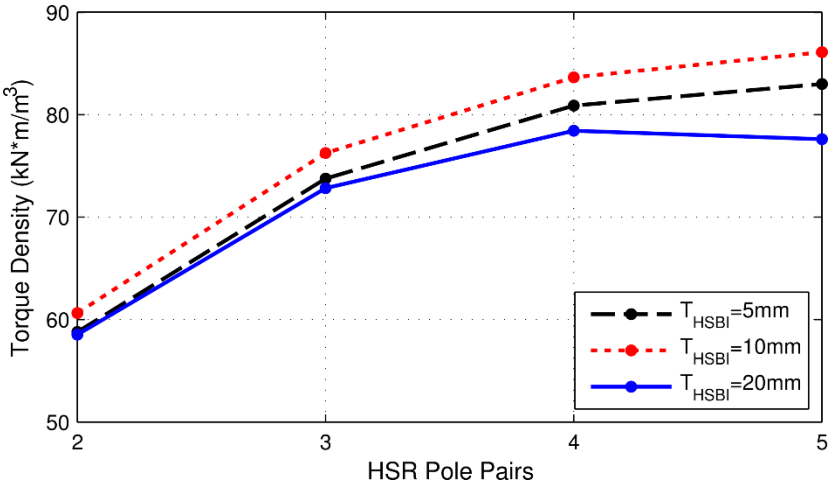


Figure 26. Impact of HSR Pole Pair Count and Back Iron Thickness on Maximum Volumetric Torque Density

Figure 27 shows the volumetric torque density for the set of parametric design points versus the corresponding low speed rotor stall torque. This illustrates that the

maximum achievable torque density increases as the radius and torque increase, which is in accordance with the axial field magnetic gear scaling principles presented at the beginning of this section. It also implies that applications requiring higher torques can expect to achieve even higher volumetric torque densities. This is an important principle to consider when comparing different axial field magnetic gears presented in the literature.

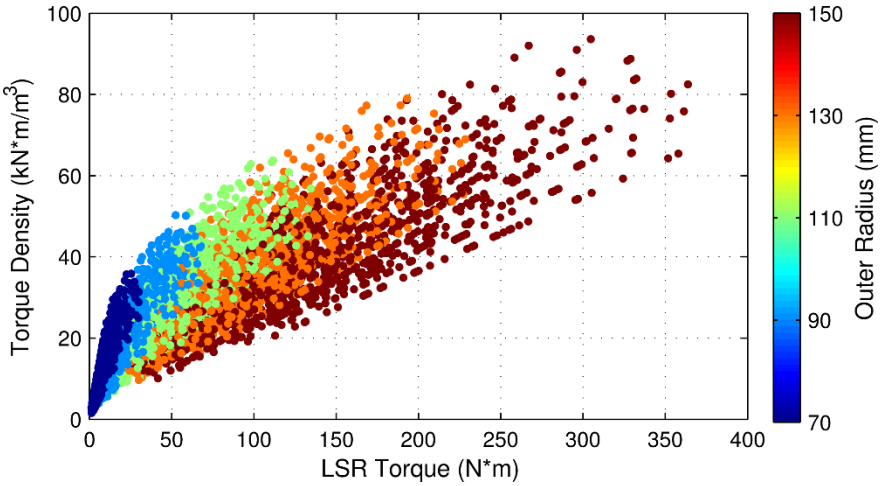


Figure 27. Volumetric Torque Density vs. Torque Rating

As noted in the previous section, axial forces are a concern for axial field machines, especially magnetic gears. Figure 28 shows the axial forces on the two rotors for different potential design points, and Figure 29 shows the axial forces on the modulators. From Figure 28, it is evident that the axial forces on the two rotors tend to increase with the required torque. However, because the axial force on the modulators is the difference between the axial forces on the two rotors (in accordance with Newton's 3rd law), designs with small total axial forces on the modulators can be achieved even for high torques, as illustrated in Figure 29. This approach can be used to simplify the mechanical requirements of the support structure which holds the modulators in place.

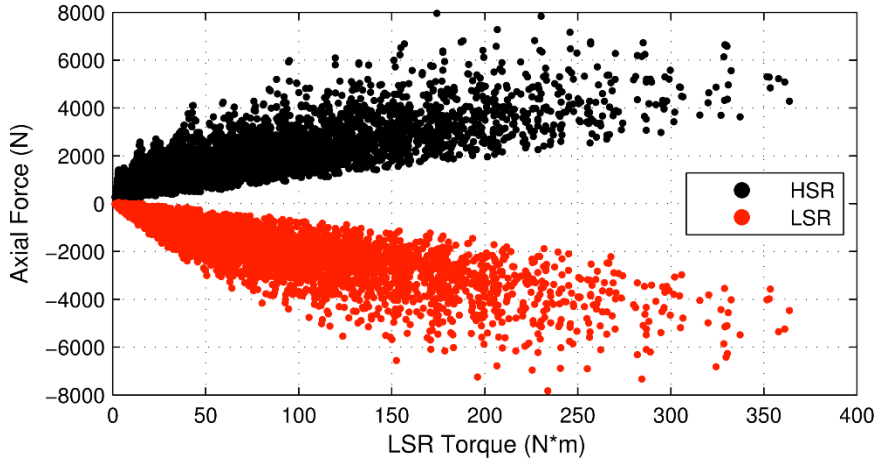


Figure 28. Axial Forces on Rotors vs. LSR Torque at Maximum Torque Angle

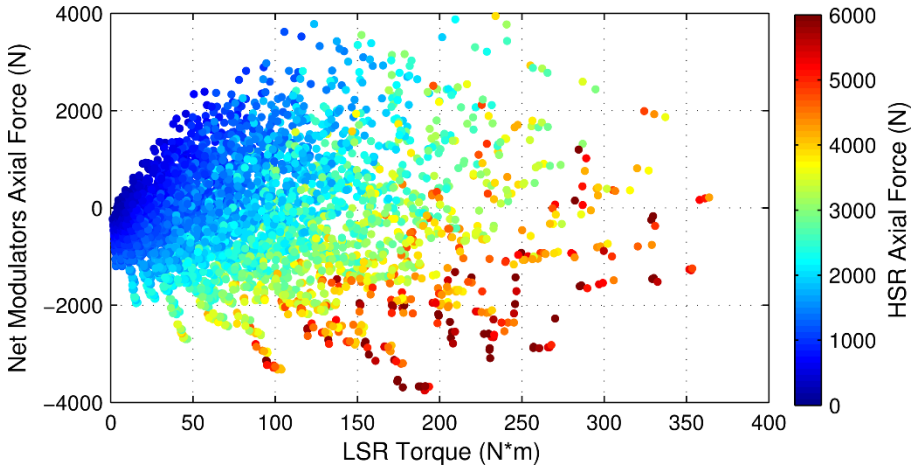


Figure 29. Axial Force on Modulators vs. LSR Torque at Maximum Torque Angle

The axial force data presented in Figures 28 and 29 represents the forces corresponding to the maximum torque angle position. Figures 30 and 31 illustrate the variation of the simulated torques and axial forces on the different gear bodies with the torque angle for the conservative prototype design. These graphs demonstrate that the maximum torque angle corresponds to intermediate axial force values. Thus, while Figures 28 and 29 do not indicate the maximum axial forces on the bodies, they do indicate the general force trends.

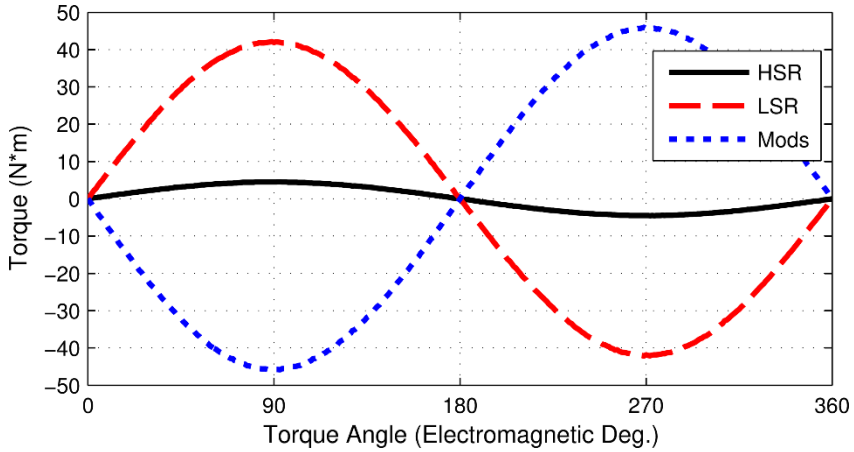


Figure 30. AFMGM Prototype Simulated Torque Characteristics Curves

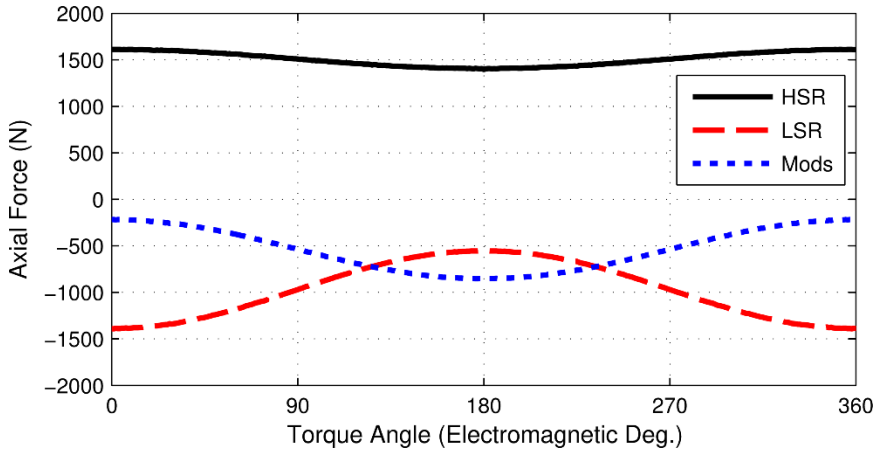


Figure 31. AFMGM Prototype Simulated Axial Force Characteristics Curves

In addition to the experimental prototype, a more competitive theoretical magnetic gear design was simulated using a 3D FEA model to demonstrate the high torque densities that can be achieved by the topology. The differences between the prototype and the higher torque density design are simply intended to realistically reflect the superior manufacturing capabilities available in an industrial setting. This less conservative design is based on using the same commercially available stator and rotor for the integrated machine and still achieves the necessary magnetic isolation between the integrated

machine and the magnetic gear. Table 11 shows the design parameters and ratings for both the fabricated prototype and the more aggressive design. Note that the dimensions of the integrated machine constrain the dimensions of the magnetic gear and that the torque rating of the integrated machine limits the volumetric torque density of the AFMGM. Significant additional improvements could be achieved with the freedom to perform system level optimization of both the magnetic gear and the integrated machine.

Table 11. Design Parameters and Ratings for AFMGM Designs

| **Parameters and Ratings** | **Prototyped Design** | **Simulated Design** |
|---|---|---|
| Gear Ratio | 9.33 | 30.33 |
| Stator Outer Diameter | 100 mm | 100 mm |
| End Winding Outer Diameter | 120 mm | 120 mm |
| Stator Stack Length | 30 mm | 30 mm |
| Integrated Machine Air Gap | 2 mm | 1 mm |
| Integrated Machine PM Thickness | 4 mm | 4 mm |
| Integrated Machine Back Iron Thickness | 3 mm | 3 mm |
| Stator Tooth Count | 24 | 24 |
| Integrated Machine Pole Pairs | 10 | 10 |
| Stator Current Density | 6.3 $A_{RMS}/mm^2$ | 4.7 $A_{RMS}/mm^2$ |
| Gear Inner Diameter | 195 mm | 160 mm |
| Gear Outer Diameter | 260 mm | 239 mm |
| HSR Pole Pairs | 3 | 3 |
| HSR Back Iron Thickness | 20 mm | 12 mm |
| HSR Magnet Thickness | 6.35 mm | 8 mm |
| Modulator Thickness | 18 mm | 6 mm |
| LSR Magnet Thickness | 3.175 mm | 4 mm |
| LSR Back Iron Thickness | 20 mm | 6 mm |
| Gear High Speed Side Air Gap | 4.8 mm | 1 mm |
| Gear Low Speed Side Air Gap | 3.9 mm | 1 mm |
| Gear Magnet Grade | NdFeB N42 | NdFeB N42 |
| LSR Pullout Torque | 42.2 N·m | 105.9 N·m |
| Rated LSR Speed | 300 rpm | 92 rpm |
| AFMGM Power | 1 kW | 1 kW |
| AFMGM Volumetric Torque Density | 7.8 $kN·m/m^3$ | 60.6 $kN·m/m^3$ |
| Gear Volumetric Torque Density | 10.4 $kN·m/m^3$ | 62.2 $kN·m/m^3$ |

## 4.5 Mechanical Design of the Prototype

In order to quickly produce a working prototype for this novel topology, ease of fabrication and assembly was prioritized over performance. This approach is reflected in part by the large size of the air gaps, thickness of the modulators, common sizing of the back irons, and the large radial gap between the magnetic gear and the integrated machine, all of which are summarized in Table 11. Additionally, the magnetic design was selected to reduce the axial load on the modulators structure. Throughout the mechanical design process, an ANSYS 3D mechanical FEA model was used with the forces from Maxwell 3D electromagnetic simulations to verify that static deformations were within acceptable tolerances. A cutaway view of the resulting prototype is displayed in Figure 32, and an exploded view is provided in Figure 33. The completed prototype is shown in Figure 34 on its testbed with the LSR connected to a DC motor, which was used as a prime mover.

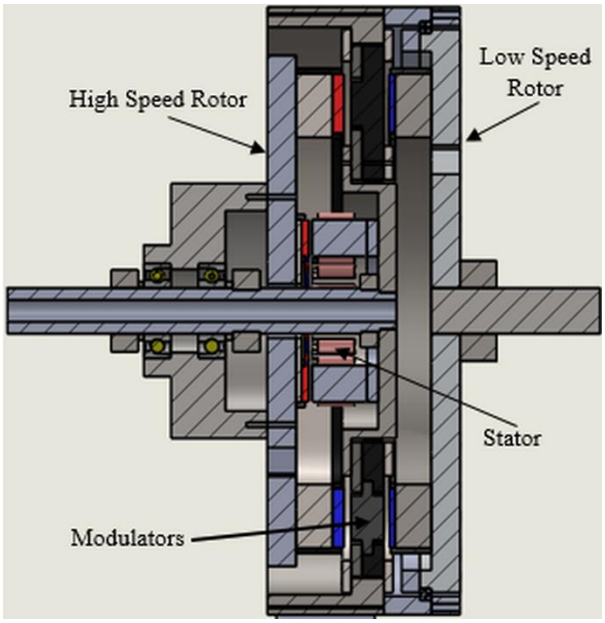


Figure 32. Cutaway View of AFMGM Prototype

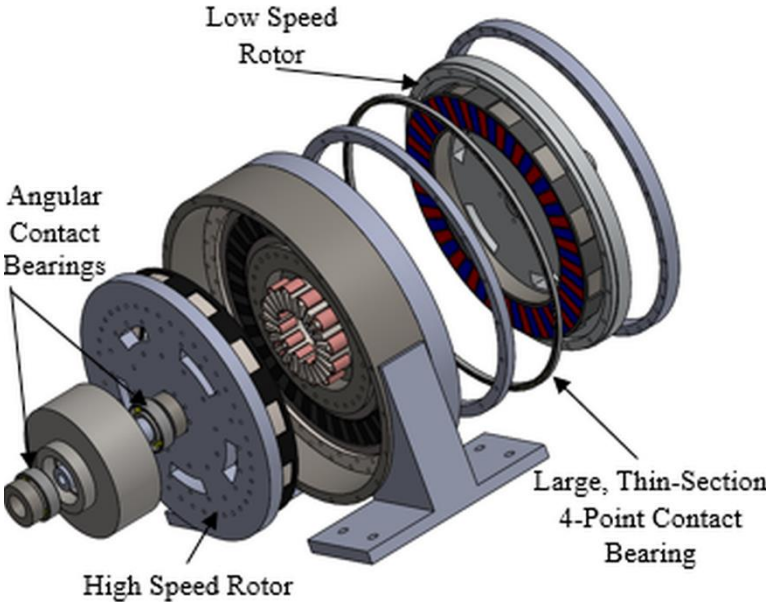


Figure 33. Exploded View of AFMGM Prototype

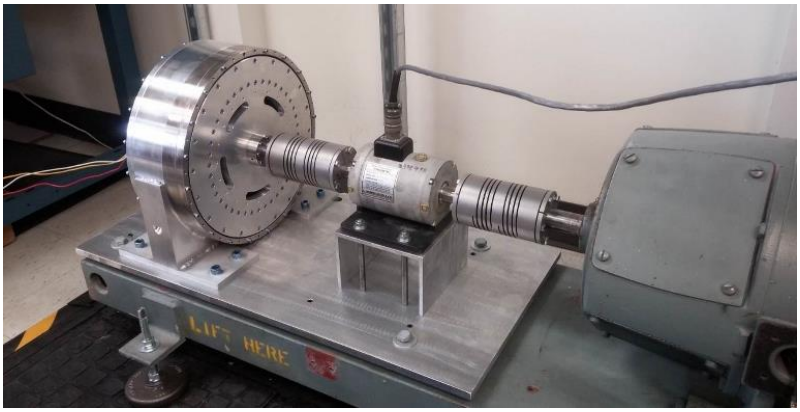


Figure 34. AFMGM Prototype on Testbed

As indicated in Figure 33, two angular contact ball bearings were used to support the high speed rotor. The bearings were oriented in opposite directions to handle axial forces in either direction. While the HSR is always attracted toward the LSR in normal operation, forces in the opposite direction could be experienced during assembly or

handling. A single large diameter, thin-section four-point contact ball bearing was used to support the low speed rotor.

## 4.6 Simulated and Experimental Results

In order to characterize the torque transmission properties of the axial field magnetic gear in the AFMGM prototype, a locked HSR test was conducted by fixing the HSR in place and rotating the LSR to different angular positions. The resulting LSR torques are shown in Figure 35 as a function of the relative electromagnetic angle (or torque angle) between the LSR and the HSR. The corresponding simulated torque characteristics obtained from static 3D FEA simulations at different torque angles are also shown in the same graph. This clearly proves that the 3D FEA model accurately predicts the gear's torque transmission capability, as the simulated and experimental results indicate a stall torque of 42.1 N·m and 42.2 N·m, respectively.

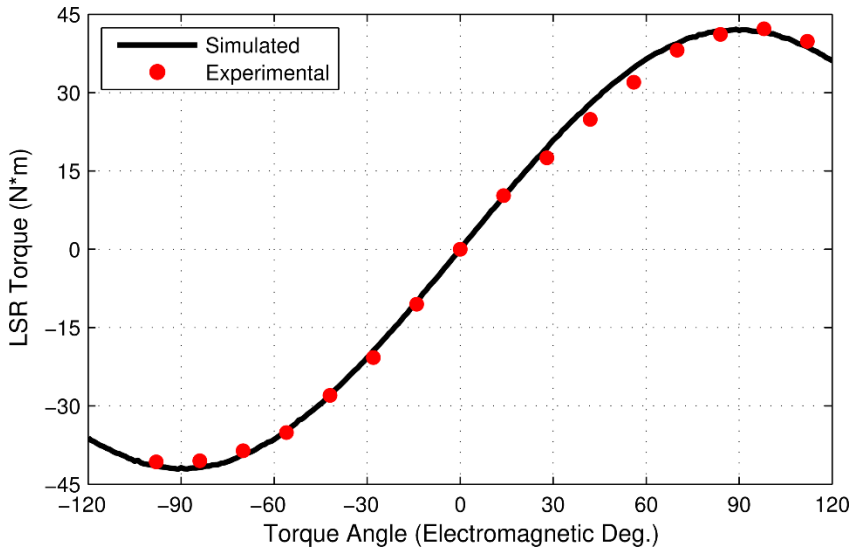


Figure 35. AFMGM Prototype LSR Static Torque Characteristics Curve

The AFMGM prototype's internal gear ratio was verified by recording the HSR speed at different LSR input speeds under the no load condition. The measurements are summarized in Figure 36 and demonstrate a consistent gear ratio of 9.33 which matches the theoretically anticipated results based on the 28:3 pole pair combination on the rotors.

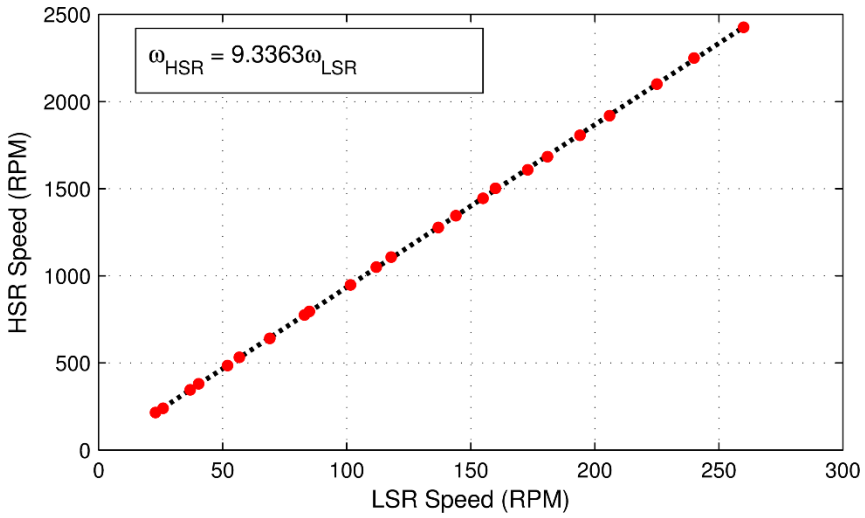


Figure 36. AFMGM Gear Ratio Measurements

The no load, open circuit back EMF produced by the AFMGM's integrated machine was measured at several different speeds and the results are summarized by the graph in Figure 37. The same graph also depicts the simulated back EMF amplitude characteristics obtained from a 3D FEA model. The data illustrates a high degree of consistency between the simulated and experimental results, and the relatively small deviations are likely due to a very minor difference between the actual generator air gap size and the designed size. Additional 3D FEA simulations suggest that the differences in predicted and measured back EMF amplitudes could be accounted for by less than 0.2 mm of variation in the generator air gap, which is less than 10% of the 2 mm design value.

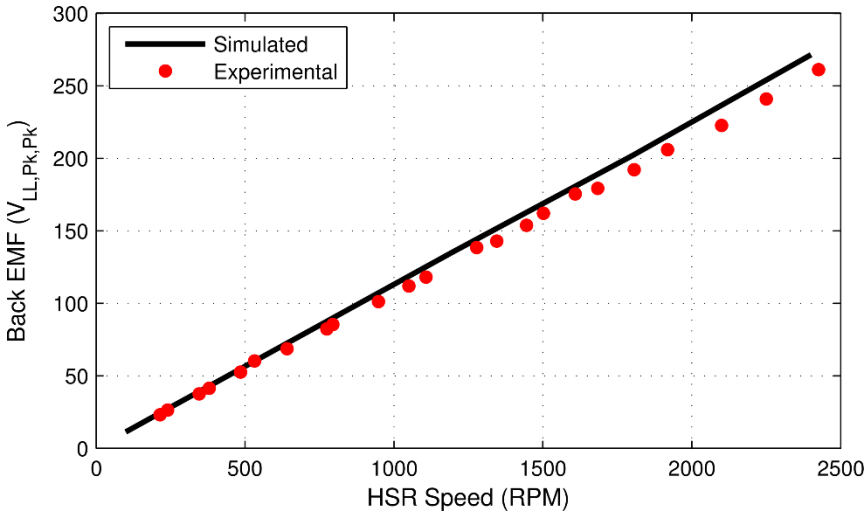


Figure 37. Experimental and Simulated AFMGM No Load Back EMF Amplitude Characteristics

The experimental and simulated no load, open circuit back EMF waveforms produced at an HSR speed of 1800 rpm are shown in Figure 38. Not only are the simulated and experimental waveforms a good match for each other, but they are also very smooth sine waves with negligible harmonic content. This observation is important for two reasons, first and most importantly, it demonstrates that the AFMGM's magnetic gear and integrated generator are magnetically isolated as desired. If the two were not isolated, the EMF would contain harmonic content from the three pole pairs of the magnetic gear HSR. Second, the quality of the sine wave indicates how smoothly the HSR was rotating. This smooth operation is due in part to the lack of direct mechanical contact between the HSR and the LSR, as well as the AFMGM's low cogging torque. The HSR peak to peak torque ripple is a mere 3.5% of the HSR stall torque, while the LSR peak to peak torque ripple is only 1.3% of the LSR stall torque. These minor torque ripples are easily damped out by the machine's inertia.

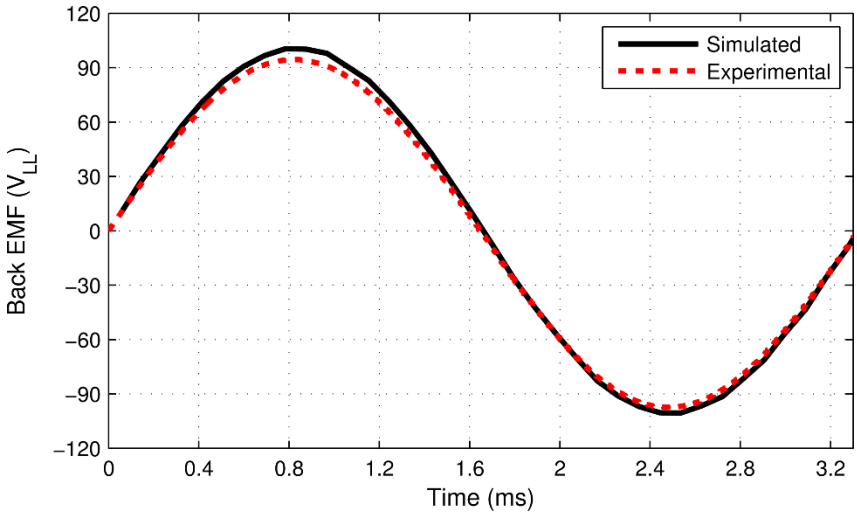


Figure 38. Simulated and Experimental No Load Back EMF Waveforms at an HSR Speed of 1800 rpm

The AFMGM prototype's no load losses were recorded at several different LSR input speeds, and the information is shown in Figure 39 along with the magnetic loss predictions obtained from transient 3D FEA simulations in Infolytica MagNet. This graph demonstrates that the experimental losses are significantly higher than the simulated losses. The additional losses experienced in the experimental prototype are believed to be a result of the large diameter, thin-section four-point contact bearing used on the LSR. This hypothesis is based on rotation of the individual rotors before the prototype was fully assembled. Although the strong magnetic axial forces do place a significant thrust load on both the HSR and LSR bearings, these losses are not believed to be an intrinsic characteristic of the topology, but instead an issue with this specific LSR bearing solution. In light of these findings, a modified LSR bearing arrangement was developed, and it is anticipated that this redesign would alleviate this issue.

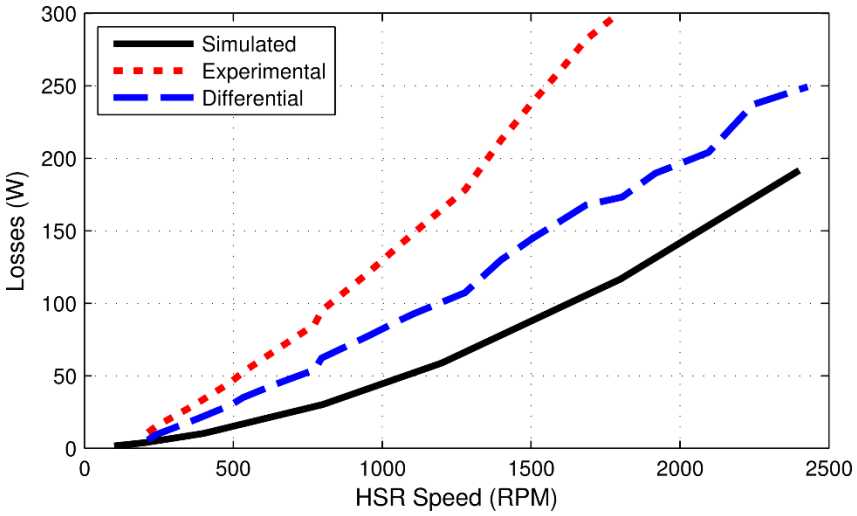


Figure 39. Experimental and Simulated No Load AFMGM Losses

A breakdown of the simulated no load and full load electromagnetic loss components is provided in Figure 40. This data demonstrates that the full load and no load magnetic losses are very similar except for the iron core losses. In particular, that variation is due to the losses in the integrated generator rotor back iron, which was the only non-laminated back iron in the AFMGM. These findings suggest that with the appropriate design, the no load and full load magnetic losses should be very similar with the only significant remaining differences being the copper and mechanical losses.

The loss components breakdown in Figure 40 also indicates that one of the largest magnetic loss components is eddy current losses produced by leakage flux in some of the structural aluminum. This was a known potential issue during the prototype development process and is primarily associated with aluminum structural reinforcement components that were added due to concerns over the large axial forces in accordance with a very conservative design approach. Based on insight gained during the prototype's

construction and experimental operation, along with information from 3D mechanical FEA models, this aluminum is unnecessary and can be eliminated from future designs.

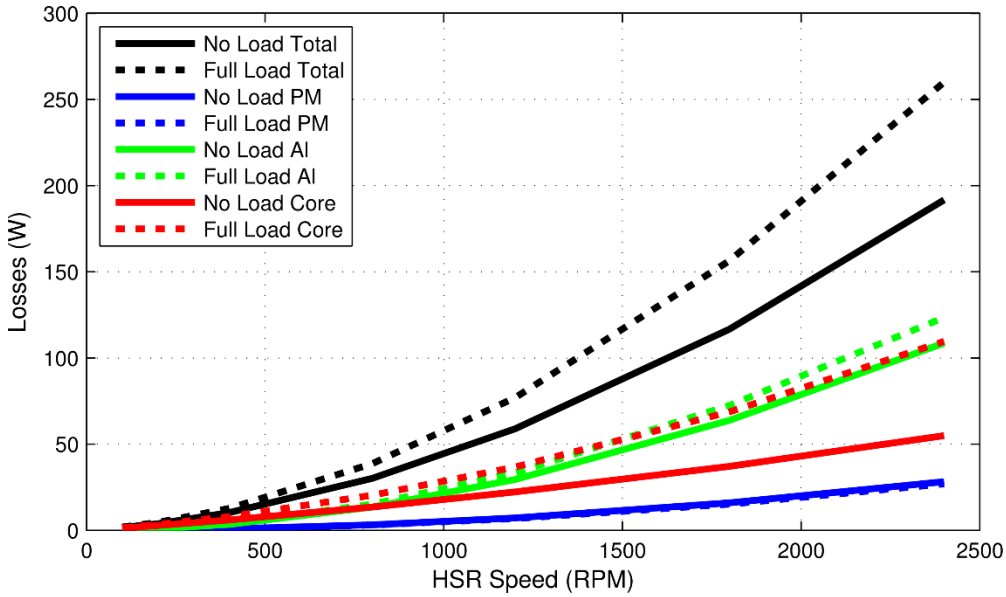


Figure 40. Simulated No Load and Full Load Magnetic Loss Components

## 4.7 Conclusion

A new compact axial flux magnetically geared machine topology was proposed, analyzed, prototyped, and evaluated. This AFMGM topology integrates an axial field permanent magnet machine into the bore of an axial field magnetic gear instead of connecting the two in series as was done in a previously proposed topology. Inserting the axial field machine into the bore of the axial field magnetic gear allows the two sub-systems to be optimally sized for operation with each other. This provides the potential to develop a significantly more compact AFMGM in which both the integrated machine and the magnetic gear are fully utilized to the proper extent of their individual maximum ratings. Furthermore, this integration method allows the AFMGM to have the same

volume as its axial field magnetic gear, as opposed to the series combination method in which the addition of the axial field machine to the magnetic gear increases the volume of the AFMGM.

A small scale proof of concept prototype of the proposed compact AFMGM topology was developed for experimental evaluation of the device's magnetic and mechanical design and operation. The prototype AFMGM's performance was handicapped by the use of a sub-optimal commercially available axial field machine as the integrated generator and a very conservative design of the axial field magnetic gear, resulting in a low torque density of 7.8 $kN{\cdot}m/m^3$. However, the axial field gear in the AFMGM demonstrated nearly identical torque characteristics to those predicted by 3D FEA simulations, which verifies that the modeling methods used in the design process provide an accurate means of sizing the device. Additionally, EMF data from the AFMGM's internal generator provides strong evidence that the desired magnetic isolation between the gear and the generator was achieved, as predicted by FEA simulations.

A less conservative design of the topology was simulated using the same sub-optimal integrated generator and resulting in a much improved torque density of 60.6 $kN{\cdot}m/m^3$. Although that theoretical performance is already competitive with some RFMGM designs reported in the literature, it could be further improved by redesigning both the integrated machine and axial field magnetic gear using a system level optimization. Moreover, based on the theoretical principle that the torque of an axial field magnetic gear scales with the cube of its outer radius, while its active volume only scales with the square of its outer radius, it is anticipated that higher torque densities are

attainable at larger scale design points. This principle is reinforced by the 3D FEA simulation data provided in Figure 27.

Experimental no load testing of the AFMGM prototype revealed that the device exhibited larger than anticipated no load losses. These additional losses are believed to be caused by the thin-section four-point contact bearing used on the LSR; however, this lossy bearing can be avoided in future variations of the design.

Although the prototype presented in this study exhibited a low torque density, it demonstrated the viability of the topology. Simulation results suggest that more ambitious yet still feasible designs can achieve extremely promising results. Further prototypes and experimental work are necessary to continue to refine the mechanical design and bearing arrangement and to fully characterize the scaling characteristics of the device's support structure.

# 5. DESIGN AND ANALYSIS OF A LARGE SCALE INNER STATOR RADIAL FLUX MAGNETICALLY GEARED GENERATOR

The second phase of the aforementioned DOE project involved the development of a large scale 10 kW, 30 rpm magnetically geared machine, which represented a hundredfold increase in scale relative to the torque rating of the compact AFMGM prototype described in Section 4. Due to this large torque requirement and various full scale OWSC system integration considerations, a radial flux magnetically geared machine topology was selected for this phase of the project to simplify the already challenging mechanical construction of the prototype as much as possible.

## 5.1 Existing Radial Flux Magnetically Geared Machine Topologies

As noted in Section 4, several different MGM topologies have been proposed [10, 11, 14, 17, 25], but the inner stator radial flux MGM (IS-RFMGM) [11, 14], shown in Figure 41, and the outer stator radial flux MGM (OS-RFMGM) [10] have received the most attention to this point and appear to be the two most promising radial flux configurations with respect to a combination of practical and theoretical considerations. One design study comparison of the IS-RFMGM and the OS-RFMGM found that the IS-RFMGM is capable of achieving a higher torque density [113] and that conclusion is consistent with a general comparison of the results reported throughout the literature. The IS-RFMGM topology can be further sub-divided into designs in which the magnetic gear and integrated machine are magnetically coupled and other designs in which the magnetic gear and integrated machine are magnetically decoupled. Magnetically coupled IS-

RFMGMs allow for the use of much thinner (and in some cases essentially non-existent [15]) HSR back-irons between the integrated machine magnets and the gear HSR magnets, but they require the use of the same pole counts for the integrated machine and the gear HSR. Alternatively, magnetically decoupled IS-RFMGMs require thicker HSR back-irons to decouple the fluxes of the integrated machine and the gear, but they allow for independent optimization of the integrated machine and gear HSR pole counts.

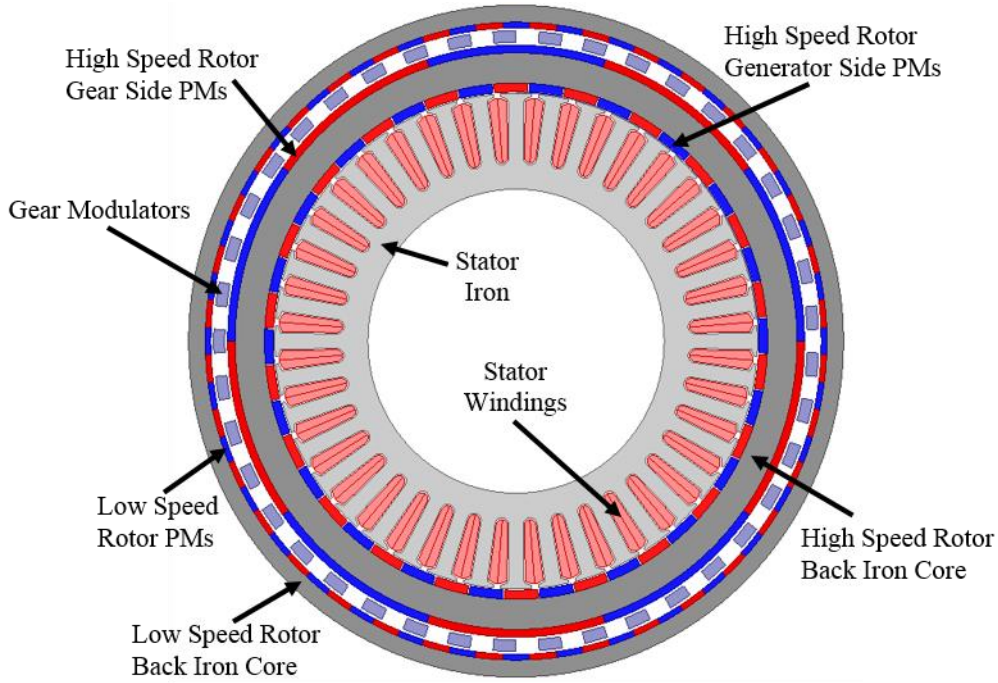


Figure 41. Inner Stator Radial Flux Magnetically Geared Machine

The vast majority of the existing detailed literature on magnetic gear and magnetically geared machine prototypes focuses on relatively small scale designs with stall torques of less than 150 N·m and, although there are some cursory claims of larger scale MGMs [114], there are no known detailed descriptions of prototypes with stall torques of 1000 N·m or more in the existing literature at the time of this study. The

primary objective of the second phase of the DOE project was to experimentally demonstrate the technology's feasibility at a much larger scale. This work accomplishes that by describing the design, fabrication, and evaluation of a large scale magnetically decoupled IS-RFMGM prototype for wave energy conversion with an OWSC. Although the prototype is not full scale relative to the tremendous torque requirements (225 kN·m) for operation with a full scale 40 kW, 1.7 rpm OWSC, its experimental stall torque of 3870 N·m is believed to be by far the largest ever achieved by any MGM prototype described in the existing literature at the time of this study.

## 5.2 Design Methodology

In a magnetically geared machine, the design of the magnetic gear and the design of the integrated machine are heavily interdependent. First, the gear ratio relates the torque and speed of the integrated machine to those of the prime mover. Second, because the machine is placed in the bore of the magnetic gear, the outer radius of the machine is tied to the inner radius of the magnetic gear. Third, the integrated machine should be rated for the same operating torque as the magnetic gear HSR. Finally, to make optimal use of volume and maximize torque density, the stack length of the integrated machine should be approximately equal to the stack length of the magnetic gear, but sufficiently shorter to accommodate the additional space consumed by the end-windings.

Because the magnetic gear was assumed to be magnetically decoupled from the integrated machine, the two subsystems were simulated separately. This assumption was later verified for the final design. In order to design this prototype, the 102,060 magnetic gear parametric design variations summarized in Table 12 were each simulated and the

results are used to illustrate important design trends and tradeoffs. Because the primary objective of the study was to demonstrate the large scale viability of MGMs, several conservative design choices were made to simplify the construction of the prototype and further optimization could be performed to develop a more aggressive design with a higher torque density. Due to the strong interdependencies between design parameters, some derived variables were used. Because the LSR has more magnetic poles than the HSR, there is significantly more flux leakage between adjacent poles on the LSR than on the HSR. Therefore, it is prudent to concentrate most of the magnet material on the HSR. However, if the LSR magnets are too thin in relation to the HSR magnets, then the LSR magnets may become demagnetized. Thus, the radial thickness of the LSR magnets, $T_{LSPM}$, is determined by the radial thickness of the HSR magnets, $T_{HSPM}$, and a derived parameter, $k_{PM}$, as shown in (23). A second derived parameter, $G_r$, represents the approximate (nearest integer) desired gear ratio, and it is used, along with $P_{HS}$, to determine $P_{LS}$, as described in (24). This improved approach keeps the number of modulators even, which results in symmetrical cancellation of the net forces on each rotor. Additionally, this approach still maintains a relatively high least common multiple (LCM) between $P_{HS}$ and $P_{LS}$, which reduces the gear's torque ripple [26]. A third derived parameter, $k_{Mods}$, relates the angular fill factor of the modulators at their outer edges, $\alpha_{Mods,Out}$, to the angular fill factor of the modulators at their inner edges, $\alpha_{Mods,In}$, according to (25). As shown in Figure 42, the modulator poles are trapezoidal wedge shaped structures and, because there are more poles on the outer rotor (the LSR) than there are on

the inner rotor (the HSR), it is generally beneficial to use a smaller angular fill factor on the outer edges of the modulators to reduce leakage flux.

$$T_{LSPM} = T_{HSPM} \cdot k_{PM} \tag{23}$$

$$P_{LS} = \begin{cases} G_r \cdot P_{HS} + 1 & \text{for } (G_r+1) \cdot P_{HS} \text{ odd} \\ G_r \cdot P_{HS} + 2 & \text{for } (G_r+1) \cdot P_{HS} \text{ even} \end{cases} \tag{24}$$

$$\alpha_{Mods,Out} = \alpha_{Mods,In} \cdot k_{Mods} \tag{25}$$

Table 12. Magnetic Gear Parametric Design Study Ranges

| Name | Description | Values | Units |
|---|---|---|---|
| $G_r$ | Nearest integer gear ratio | 7, 11, 15 | |
| $P_{HS}$ | HSR pole pairs<br>For $G_r = 7$<br>For $G_r = 11$<br>For $G_r = 15$ | <br>3, 4, 5, … 10<br>3, 4, 5, … 8<br>3, 4, 5, 6 | |
| $R_{Out}$ | Gear's active outer radius | 300, 400 | mm |
| $T_{HSBI}$ | HSR back iron thickness | 10, 30, 50 | mm |
| $T_{HSPM}$ | HSR magnet thickness | 10, 12.5, … 20 | mm |
| $T_{AG}$ | Air gap thickness | 3 | mm |
| $T_{Mods}$ | Modulator thickness | 10, 15, 20 | mm |
| $T_{Bridge}$ | Modulator bridge thickness | 3 | mm |
| $k_{PM}$ | LSR magnet thickness ratio | 0.5, 0.75, 1 | |
| $T_{LSBI}$ | LSR back iron thickness<br>For $T_{HSBI}$ = 10 mm<br>For $T_{HSBI}$ = 30 mm, 50 mm | <br>10<br>10, 20, 30 | mm |
| $\alpha_{Mods,In}$ | Modulator inner angular fill factor | 0.5, 0.625, 0.75 | |
| $k_{Mods}$ | Modulator angular fill factor ratio | 0.6, 0.8, 1 | |

The construction and support of the modulator poles is one of the most challenging mechanical design features of a magnetic gear. As illustrated in Figure 42 and specified in Table 12, all designs evaluated in this parametric sweep included a 3 mm thick bridge connecting adjacent modulators on the inner edge of the modulator annulus. This

strengthens the entire modulator structure and is similar to the approaches described in multiple previous magnetic gear studies [4, 11, 15, 16, 115]. Further discussion of the modulator bridge's impact on the magnetic gear's electromagnetic performance is included with the simulation results.

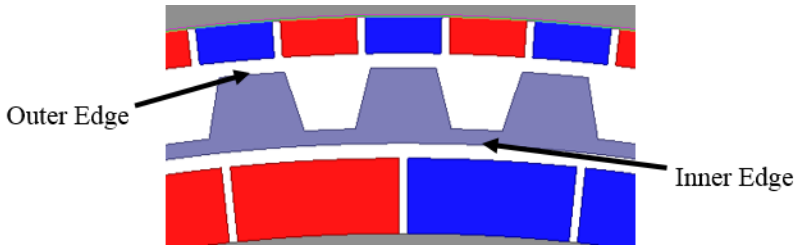


Figure 42. Modulators with Inner Bridge

Each design specified in Table 12 was evaluated using static 2D FEA at its stall torque position. Table 13 shows the key properties of the MGM active materials. The magnetic gear stack length necessary to achieve an LSR stall torque of 4200 N·m was determined for each design based on the simulated torque. Additionally, for each design, the size of the required integrated machine was determined from the machine's design curves based on the gear ratio and the magnetic gear's inner radius (the integrated machine's outer radius). This information was then used to calculate the overall volume and mass of the magnetically geared generator and its constituent active materials for each parametric design case. Throughout the design process, three key metrics (in addition to efficiency) were employed to evaluate the quality of each design variation: volumetric torque density (VTD), gravimetric torque density (GTD), and active material cost (AMC). VTD is the LSR stall torque divided by the total volume enclosed by the active materials (including the bore), as indicated in (26). Using the maximum of the gear axial stack

length ($L_{Gear}$) and the integrated machine axial stack length ($L_{Machine}$) for the active volume calculation in the denominator of (26) inherently drives the two stack lengths to match for maximum VTD designs. GTD is simply the LSR stall torque divided by the total mass of the active materials. The AMC is calculated according to (27), based on the simplifying assumption that the material price rates are fixed at the values listed in Table 13. Section 6 provides additional discussion of this AMC calculation methodology.

Table 13. Characteristics of MGM Active Materials

| Material | Density | $B_r$ | Cost Rate |
|---|---|---|---|
| N42 NdFeB | 7400 kg/m$^3$ | 1.3 T | \$50/kg |
| M19 Steel (29 Gauge) | 7870 kg/m$^3$ | N/A | \$2/kg |
| Copper | 8933 kg/m$^3$ | N/A | \$10/kg |

$$\text{VTD} = \frac{\text{LSR Stall Torque}}{\pi \cdot R_{Out}^2 \cdot \max(L_{Gear}, L_{Machine})} \tag{26}$$

$$\begin{aligned}\text{AMC} = &(\text{PM Mass}) \cdot (\text{PM Rate}) + (\text{Steel Mass}) \cdot (\text{Steel Rate}) \\ &+ (\text{Copper Mass}) \cdot (\text{Copper Rate})\end{aligned} \tag{27}$$

Based on the results of the static 2D FEA simulations, static 3D FEA simulations were performed to more accurately analyze the magnetic gear designs with the best system-level performances. These 3D simulations were conducted with each gear design scaled to the height predicted by the corresponding 2D simulation result and were used to determine the impact of end-effects on the torque of each design. Based on these 3D simulation results, the stack lengths were linearly rescaled to match the target torque. Finally, 2D transient simulations were performed for the best gear designs to determine their electromagnetic losses at full load at the nominal rated LSR speed of 30 rpm. These

cross-sectional losses were linearly scaled by the requisite stack lengths predicted by the 3D simulations and used to compute the ideal electromagnetic efficiency of each gear design.

### 5.3 Design Trends

Several critical MGM design trends are illustrated by the graphs in Figures 43-46 using the results of the parametric FEA simulation study defined in Table 12. Figure 43(a) displays the active material costs, volumetric torque densities, and gravimetric torque densities of the evaluated MGM parametric designs based on the 2D FEA results, while Figure 43(b) shows the same metrics for the highest performing designs based on 3D FEA results. Both graphs demonstrate a significant tradeoff between VTD and AMC, with the highest VTD design achieving a VTD 34.9% higher than that of the lowest AMC design but requiring an AMC 67.6% higher than that of the lowest AMC design, based on the 3D FEA results.

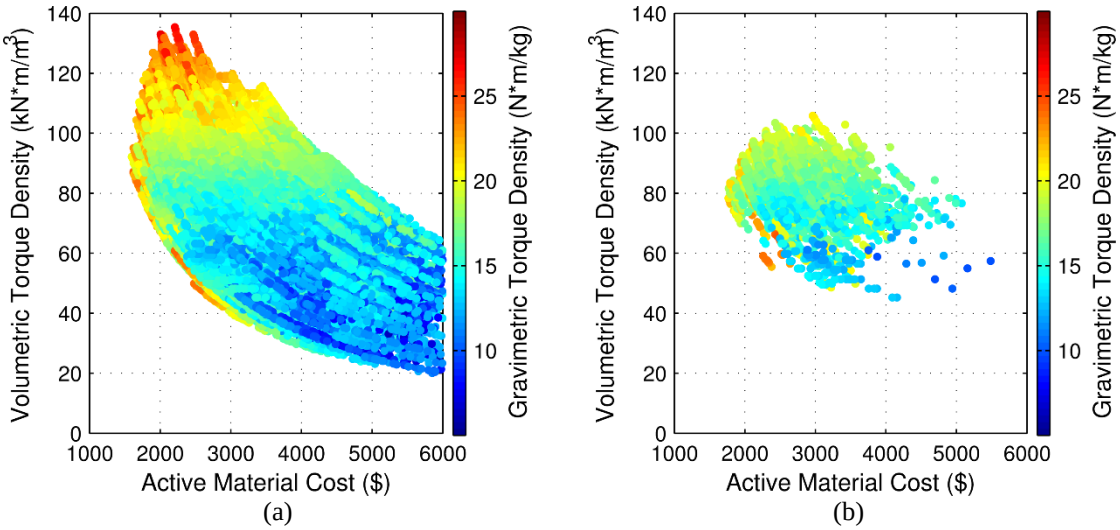


Figure 43. Active Material Costs, Volumetric Torque Densities, and Gravimetric Torque Densities for the Evaluated MGM Designs Based on (a) 2D and (b) 3D FEA Simulations

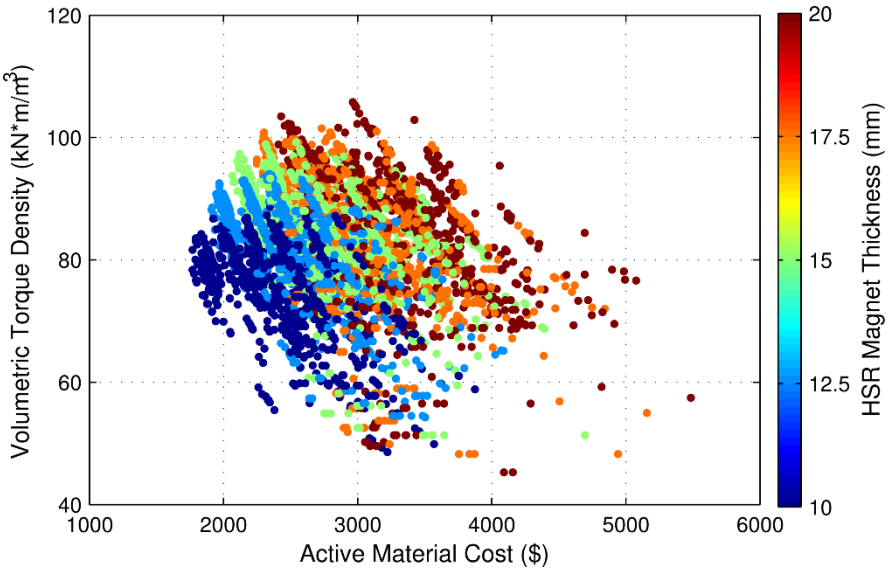


Figure 44. Impact of Gear HSR Magnet Thickness on the Tradeoff between MGM Volumetric Torque Density and Active Material Cost

Figure 44 illustrates that the selection of magnet thickness plays a large role in the tradeoff between VTD and AMC. Designs with thicker magnets tend to achieve higher torque densities at the expense of elevated AMCs. This is due in part to the fact that increasing the magnet thickness offers diminishing torque density returns, because, in addition to increasing the source of MMF in the magnetic gear's equivalent magnetic circuit, increasing the magnet thickness also increases the effective air gap size and thereby the reluctance of the primary radial flux path. Additionally, designs with thicker magnets generally require shorter stack lengths for a fixed outer radius, which also leads to more substantial 3D effects. Figure 43(b) depicts the significant performance reducing impact of 3D effects on the design set. In particular, the maximum VTD designs typically suffer the most from 3D effects because, for a given radius, they have the shortest stack lengths and generally have the thickest magnets [116, 117]. Additionally, if the gear's

stack length is greater than that of the generator, extending the gear's stack length to compensate for 3D effects directly impacts the entire system VTD based on the calculation approach defined in (26); however, it only affects the AMC of the gear and not that of the generator, so it has a less significant impact on the AMC of the whole MGM system. Within this design set, the maximum achievable VTD falls from 135.4 $kN{\cdot}m/m^3$ based on 2D FEA results to 105.8 $kN{\cdot}m/m^3$ based on 3D FEA results, a decrease of 21.9%. In contrast, the minimum achievable AMC rises from \$1598 based on 2D FEA results to \$1769 based on 3D FEA results, an increase of only 10.7%.

Figure 45(a) depicts the variation of the gear's maximum achievable VTD with gear ratio and magnet thickness, while Figure 45(b) illustrates the variation of the full MGM system's maximum achievable VTD with gear ratio and magnet thickness. It is clear that, within the range considered, thicker magnets and a lower gear ratio allow the gear to achieve a higher VTD; however, the design trends for the full MGM system are more complex. For a fixed outer radius, increasing the gear magnet thickness decreases the gear inner radius (which is the integrated generator outer radius), especially if the back irons must be thickened to accommodate the increased flux, and this necessitates an increase in the integrated generator stack length. At the higher end of the gear ratio range, the generator is relatively small compared to the gear and the gear stack length dictates the system stack length; therefore, increasing the magnet thickness decreases the gear and MGM system stack length, which leads to higher MGM system VTDs. However, at the lower end of the gear ratio range, the generator volume is bigger and the gear volume is smaller, so the generator stack length is generally comparable to the gear stack length. For

these low gear ratio designs, increasing the gear magnet thickness in the lower end of the considered range does help decrease the gear and system stack length (and thus increase the system VTD); however, beyond a certain point, the integrated generator stack length becomes dominant and increasing the gear magnet thickness further actually increases the generator stack length as previously described, which leads to a decrease in the system VTD as defined in (26).

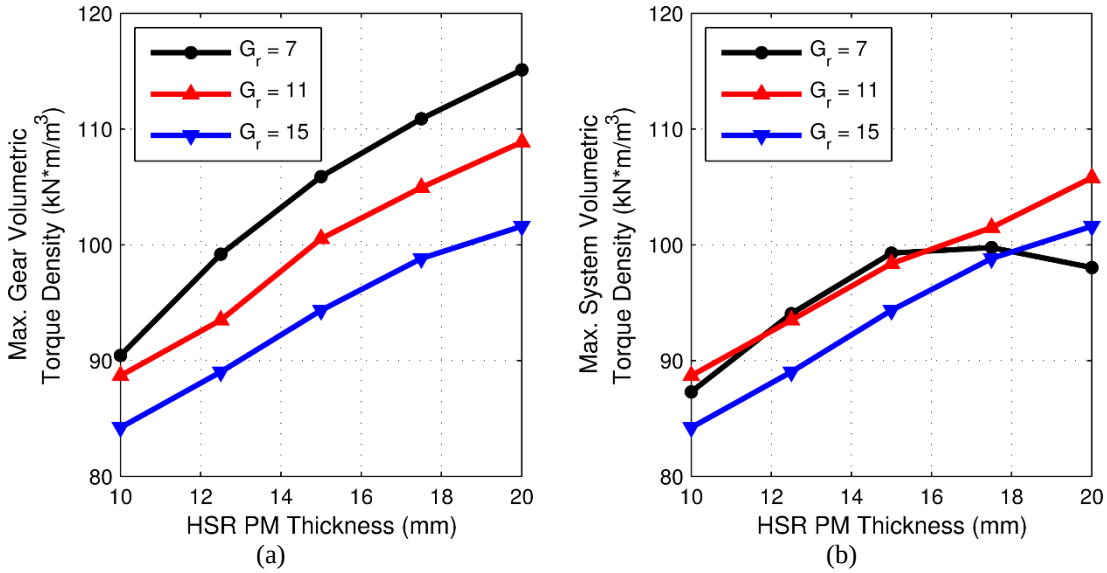


Figure 45. Variation of Maximum (a) Gear and (b) System Volumetric Torque Density with HSR Magnet Thickness for Different Gear Ratios

Figure 46 shows additional MGM system design tradeoffs involved in the selection of the gear ratio. Figure 46(a) illustrates the mass breakdowns of the designs achieving the minimum active mass for each gear ratio. Similarly, Figure 46(b) depicts the AMC breakdowns of the designs achieving the minimum AMC for each gear ratio. Increasing the gear ratio decreases the generator's active mass and AMC, but it increases the gear's active mass and AMC. For the evaluated design space, the reductions in active mass and

AMC of the generator achieved by increasing the gear ratio from 7 to 11 outweigh the corresponding increases in the active mass and AMC of the gear to yield net MGM system improvements. However, the reductions in active mass and AMC of the generator attained by further increasing the gear ratio from 11 to 15 are essentially counterbalanced by the associated increases in the same quantities for the gear and the net system improvements are negligible. For this design scenario, increasing the gear ratio to even higher values would yield a net negative effect on the MGM system design, resulting in increased total active mass and AMC. In general, the overall system level optimum design for any MGM is achieved in part by selecting the gear ratio that strikes the appropriate balance between these two sub-systems. Based on the tradeoffs illustrated in Figures 45 and 46 and practical design considerations, a gear ratio of approximately 11 was selected for the prototype design.

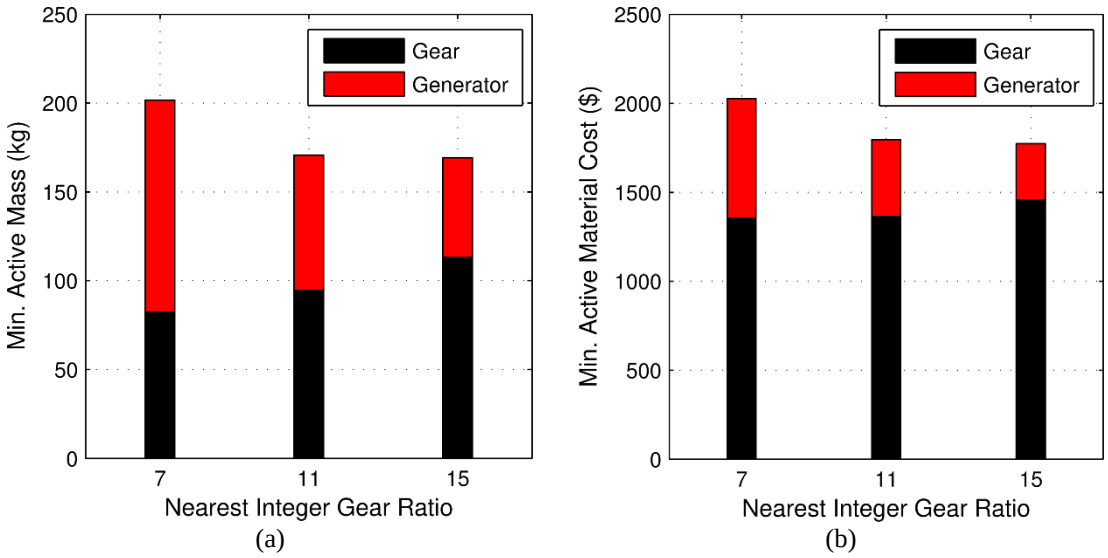


Figure 46. Variation of Minimum MGM System Active (a) Mass and (b) Material Cost with Gear Ratio

## 5.4 Final Prototype Design

A prototype design was selected based on the parametric design study results. However, several parameters were adjusted to facilitate fabrication of the prototype. Table 14 summarizes the final prototype design details and Figure 47 provides a cross-sectional view of the final design. The most significant changes were made to the modulator. The modulator shape was slightly adjusted to make it easier to retain potting between each pole. Additionally, 4.8 mm diameter holes were added in each modulator to allow the insertion of tension rods for both alignment and strengthening purposes. Another notable change from the parametric design study was the use of rectangular magnets instead of ideal arc-shaped magnets. Collectively, these changes reduced the final simulated LSR stall torque from 4200 N·m to 3905 N·m.

Table 14. Prototype RFMGM Final Design Specifications

| Parameter | Value |
|---|---|
| LSR PM Pieces per Pole | 1 |
| LSR Pole Pairs | 68 |
| Number of Modulators | 74 |
| Gear HSR PM Pieces per Pole | 5 |
| Gear HSR Pole Pairs | 6 |
| Gear Ratio | 11.33:1 |
| Outer Radius (mm) | 400 |
| LSR Back Iron Thickness (mm) | 31.6 |
| LSR PM Thickness (mm) | 7.5 |
| LSR PM Width (mm) | 15.2 |
| Gear Air Gap Thicknesses (mm) | 3 |
| Modulators Thickness (mm) | 15 |
| Gear HSR PM Thickness (mm) | 15 |
| Gear HSR PM Width (mm) | 32.3 |
| Back Iron Thickness (mm) | 74.1 |

| Parameter | Value |
|---|---|
| Modulators Outer Angular Fill Factor | 0.43 |
| Modulators Inner Angular Fill Factor | 0.71 |
| Gear Stack Length (mm) | 93 |
| Generator Pole Pairs | 20 |
| Stator Slots | 48 |
| Stator Winding Turns/Coil | 45 |
| Generator Phases | 6 |
| Stator Winding Connection | YY |
| HSR Back Iron Inner Radius (mm) | 250.2 |
| Generator PM Thickness (mm) | 7.6 |
| Generator PM Width (mm) | 29.3 |
| Generator Air Gap Thickness (mm) | 2.5 |
| Stator Bore Radius (mm) | 110 |
| Generator Stack Length (mm) | 53 |

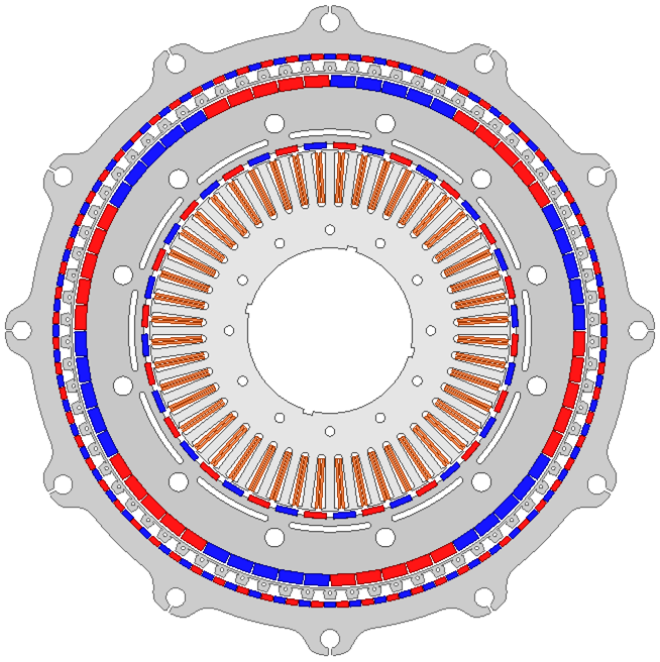

Figure 47. Cross-Sectional View of the Prototype RFMGM Final Design

Figure 48 shows a cutaway view of the prototype RFMGM design. The LSR, modulators, and HSR are each supported by stainless steel end bells, which are in turn supported by the central stationary shaft. A non-magnetic and non-conductive buffer of G11 glass reinforced epoxy laminate separates the magnetically active portion of the magnetic gear from each of the end bells to prevent axially escaping magnetic fields from inducing eddy current losses in the end bells. This is an important issue which has plagued multiple prior magnetic gear and MGM prototypes, causing them to achieve significantly lower experimental efficiencies than the theoretically predicted values [3, 115, 118, 119]. Figure 49 shows the prototype's stator, HSR, modulators, and LSR, while Figure 50 provides multiple views of the fully assembled prototype mounted on its testbed. As depicted in Figure 50, the prototype was driven by an induction machine connected to a mechanical gear in order to provide the necessary input torque to the MGM LSR.

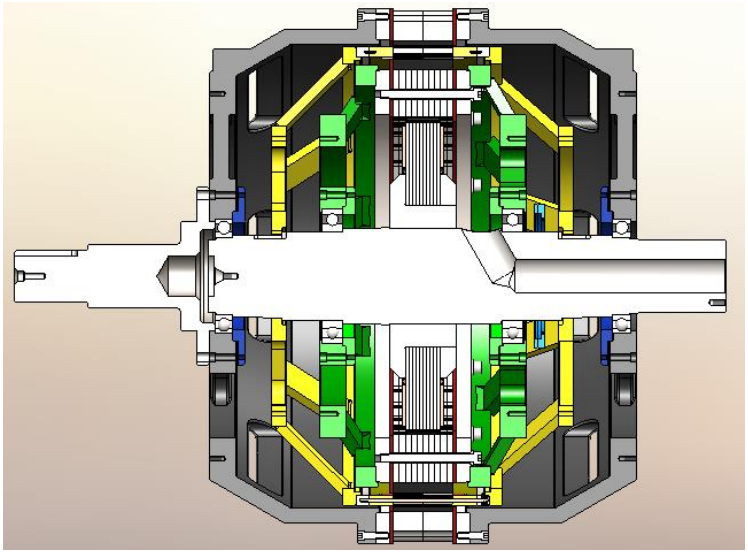

Figure 48. Cutaway View of the RFMGM Prototype

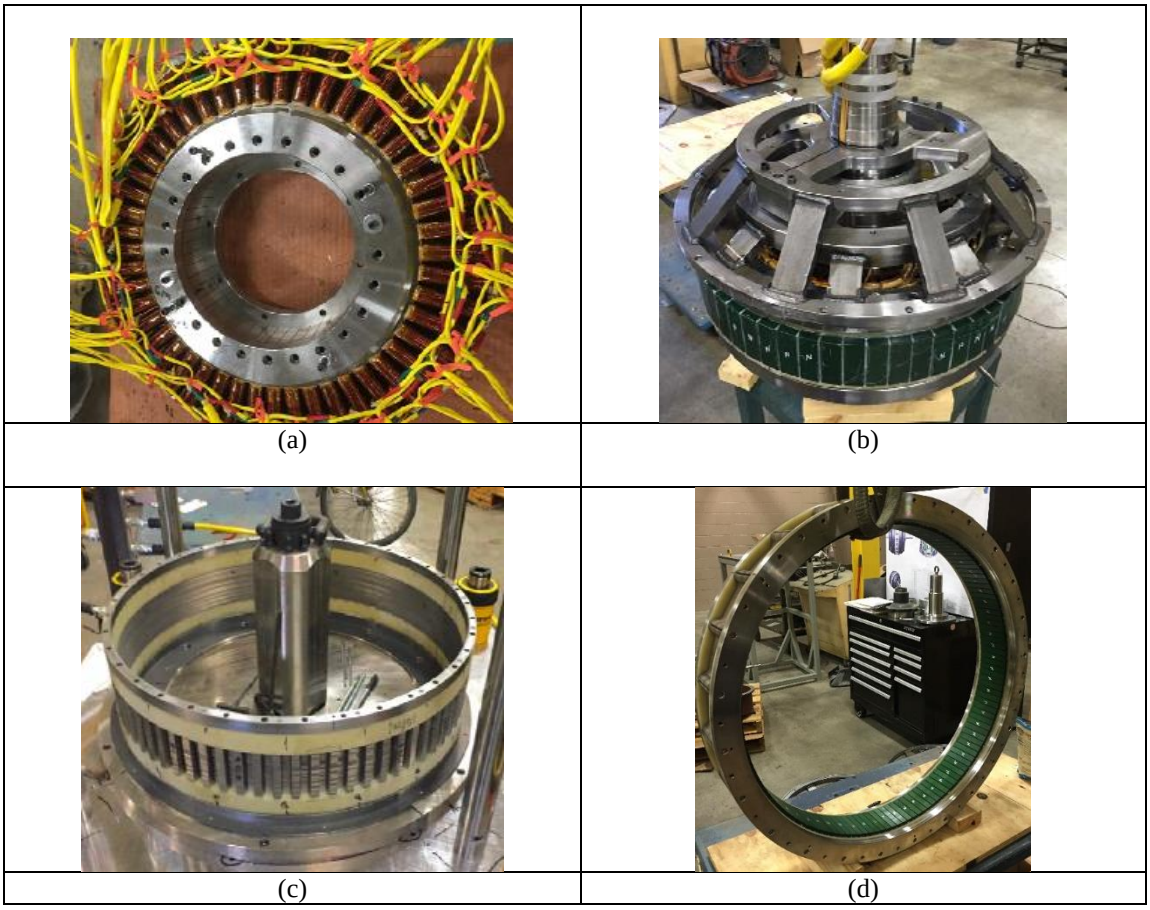

(a) (b) (c) (d)

Figure 49. RFMGM Prototype (a) Stator, (b) High Speed Rotor, (c) Modulator Assembly, and (d) Low Speed Rotor

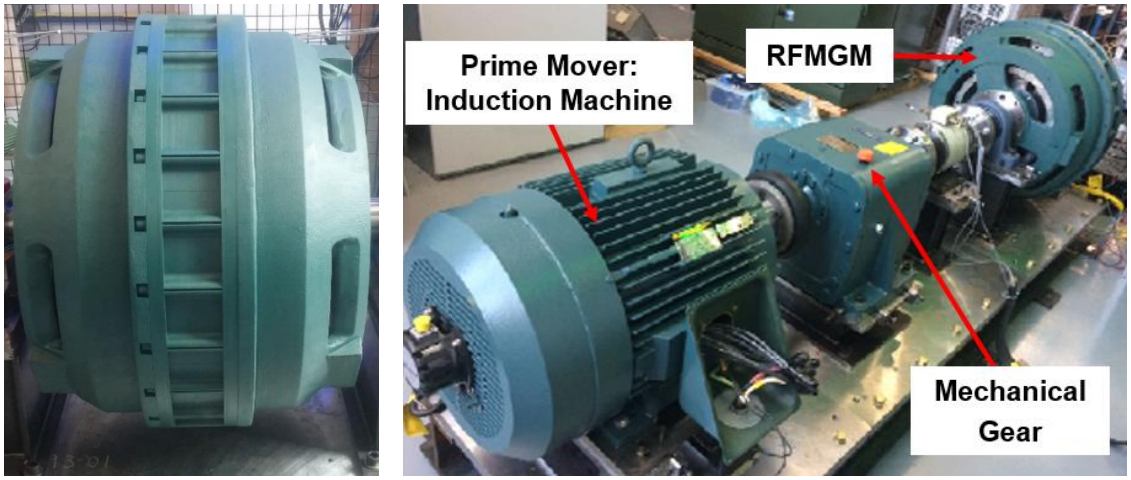


(a) (b)

Figure 50. RFMGM Prototype (a) Standalone Side View and (b) Mounted on Testbed

## 5.5 Key Magneto-Mechanical Design Considerations

There are strong interrelations between the magnetic and mechanical design aspects of the magnetic gear. First, the selection of the air gap thicknesses has major ramifications both magnetically and mechanically. Increasing the air gap thicknesses increases the reluctance of the magnetic flux paths and decreases the torque density. Thus, in addition to adjusting the optimum design point with respect to considerations such as pole count, the stack length, outer radius, or magnet thickness must be increased to achieve the same torque requirement. Any of these changes will impact the mechanical stresses on the gear. From the mechanical perspective, the air gap must be large enough to adequately accommodate both tolerances involved in fabrication and any deflection that occurs. Significant deflection can occur in the modulators because they experience large magnetic forces which makes them challenging to support [90]. After a preliminary

analysis of tolerances and modulator deflection, conservative air gaps of 3 mm were selected for the magnetic gear.

Another major magneto-mechanical concern involves magnetic flux extending axially beyond the magnetically active portion of the gear [117]. As previously noted, this axially escaping magnetic flux can cause significant losses in conductive structural material located axially beyond the magnetically active portion of the gear [3, 115, 118, 119]. Figure 51 shows the prototype's simulated axial leakage flux density in the region axially beyond the modulators, where it is the strongest. To mitigate any losses in the stainless steel end bells, 36 mm axially thick non-conductive G11 standoffs were placed between the magnetically active portion of the gear and the end bells.

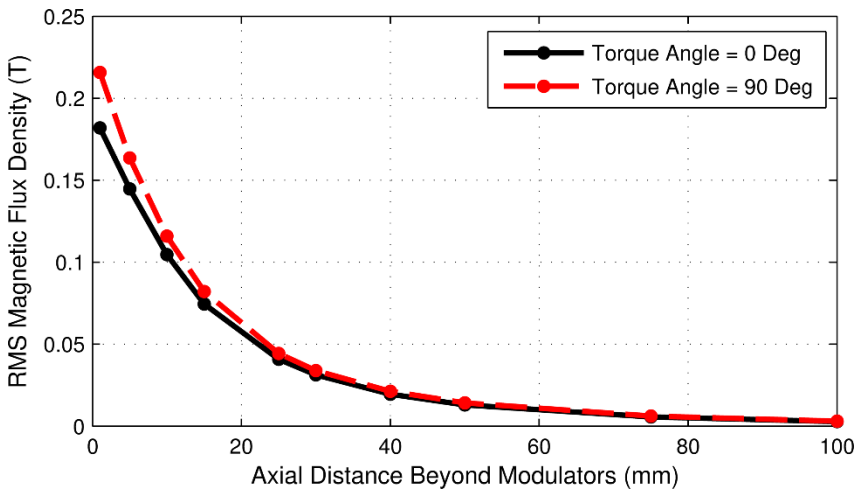


Figure 51. Decline of Axial Leakage Flux Density with Axial Distance Beyond the Modulators

A third magneto-mechanical consideration is the thickness of the bridge between the modulators. While increasing the bridge thickness improves the modulators' mechanical strength, rigidity, and ease of handling, it also decreases the magnetic gear's

stall torque, as indicated by the simulation trends shown in Figure 52. The results in Figure 52 are based on simulated variations of the bridge thickness and position in the final MGM prototype design, where the bridge position indicates the radial location of the bridge, with 0 corresponding to the inner radial edge of the modulators and 1 corresponding to their outer radial edge. Figure 52 clearly indicates that the decrease in stall torque resulting from the modulator bridge is minimized by placing the bridge on the radially inner edge of the modulators and making it as thin as mechanically permissible, which is consistent with the conclusions of prior studies [4]. This occurs because the bridge provides a leakage path for the magnetic flux. Increasing the bridge thickness decreases the reluctance of this path, which increases the leakage flux. Additionally, because the LSR has many more poles than the HSR, moving the bridge toward the LSR significantly increases the leakage flux and, within the range considered, the bridge position is generally more impactful than the bridge thickness.

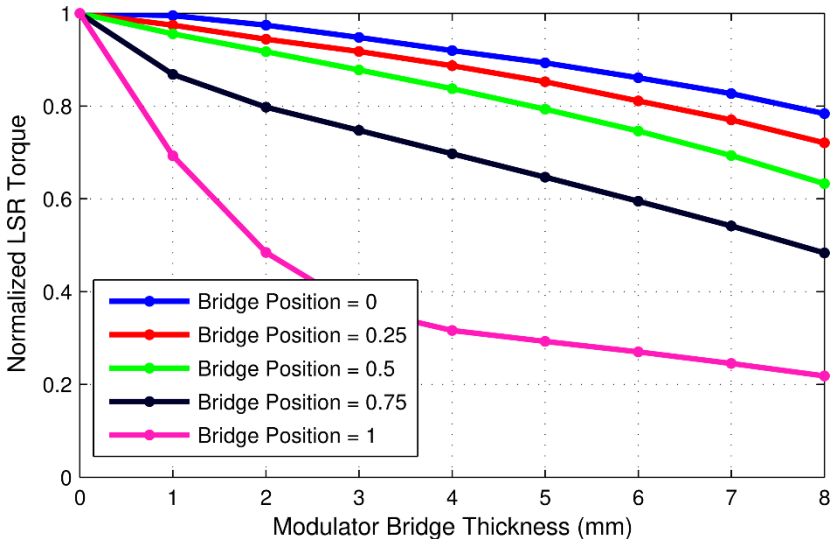


Figure 52. Simulated Variation of Stall Torque with Modulator Bridge Thickness and Position for the Final MGM Prototype Design

One advantage of the bridge leakage path is that it affects higher order spatial flux harmonics more significantly than lower order harmonics. This filters out some of these unwanted harmonics, which can reduce losses and improve efficiency [115]. Figure 53 shows the simulated loss breakdown for the prototype magnetic gear design as the bridge thickness changes with the bridge position fixed to the inner edge of the modulators. As the bridge thickness increases, the losses in the HSR decrease significantly due to the bridge's filtering effect. However, as the bridge thickness increases, the stack length of the design increases to maintain the target LSR stall torque and the resulting growth in gear volume eventually leads to a rise in total losses once the bridge thickness crosses a certain point. Additionally, there are also core losses in the bridge itself which contribute to the overall increase in modulator losses that occurs as the bridge thickness increases.

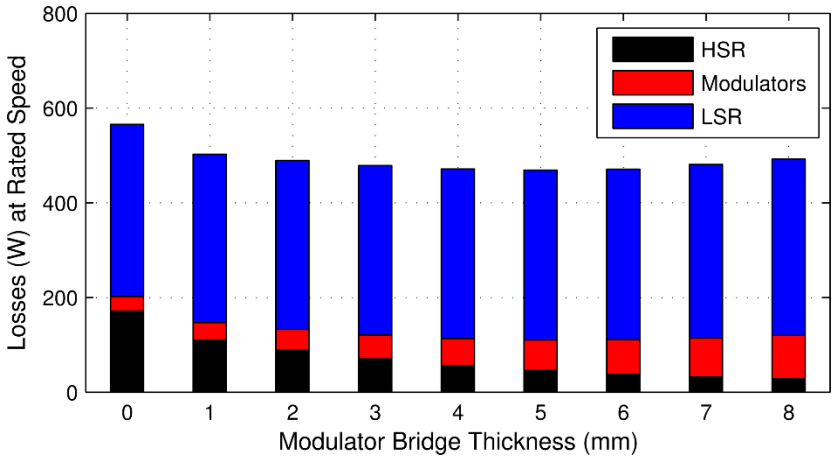


Figure 53. Effect of Modulator Bridge Thickness on Simulated Electromagnetic Gear Losses for the Final MGM Prototype Design

## 5.6 Simulated and Experimental Results

Figure 54 shows a comparison of the RFMGM prototype's simulated and measured LSR torque angle curves. The measurements were obtained by locking the HSR

and using a dial indicator to measure the LSR position. Because the large torque on the HSR caused it to deflect slightly, even when locked, a second dial indicator was used to measure this deflection. Dial indicators were employed because of the relatively small mechanical angular displacements involved in the measurements and the high accuracy required. The torque angle is calculated according to (28) based on the positions of both the HSR, $\theta_{HS}$, and the LSR, $\theta_{LS}$, relative to the resting equilibrium alignment. Figure 54 shows an excellent match between the 3D FEA simulation results and the experimental measurements. The simulated stall torque was 3905 N·m, and the measured stall torque was 3870 N·m, yielding a 99.1% match between the simulated and experimental results. Based on the experimental stall torque, the prototype achieved a volumetric torque density of 82.8 kN·m/m$^3$ and a gravimetric torque density of 14.5 N·m/kg with an ideal active material cost of $2274.

$$\theta_{Torque} = P_{HS} \cdot \theta_{HS} + P_{LS} \cdot \theta_{LS} \tag{28}$$

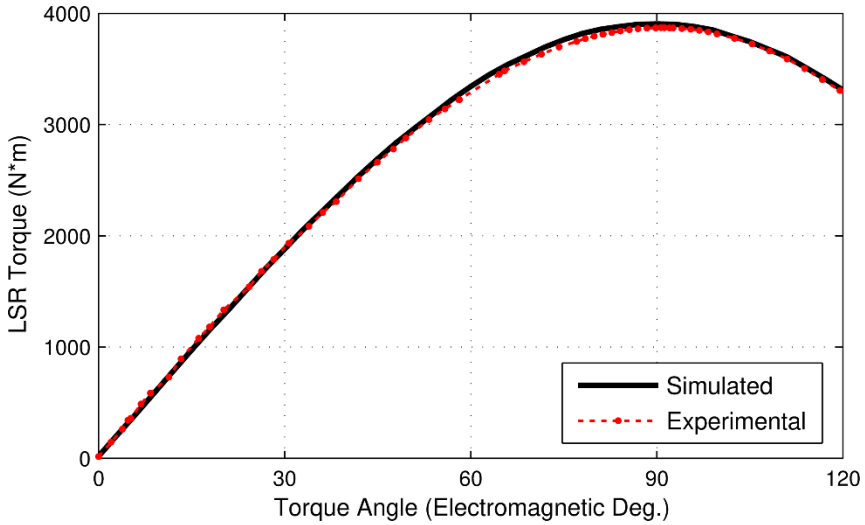


Figure 54. Simulated and Experimental Magnetic Gear LSR Torque Angle Curves

Figures 55 and 56 illustrate the simulated electromagnetic losses characteristics for the magnetic gear subsystem based on transient 2D FEA. The nearly vertical contour lines in Figure 55(a) show that the magnetic gear's electromagnetic losses do not vary significantly based on the torque loading and are almost exclusively dependent on speed. This load independence of the losses leads to higher electromagnetic efficiencies at higher loads as depicted in Figure 55(b). Additionally, because certain loss components, most notably eddy current losses, scale superlinearly with the gear's operating speed and the output power only increases linearly with speed, the gear's efficiency decreases as the operating speed increases. Figure 56 provides a breakdown of the magnetic gear's various electromagnetic loss components at different speeds under the no load operating condition. Due to the modulator bridge, there are negligible losses in the HSR and most of the losses occur in the LSR, especially at higher speeds where the eddy current losses in the LSR PMs become dominant.

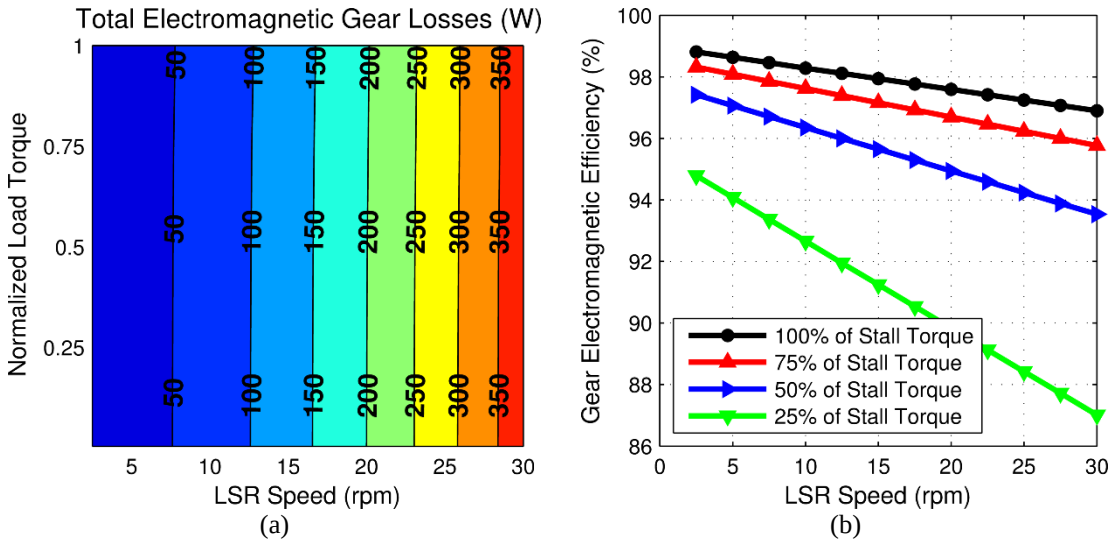


Figure 55. Simulated Electromagnetic (a) Losses and (b) Efficiency for Operation of the Prototype Magnetic Gear Design at Different Loads and Speeds

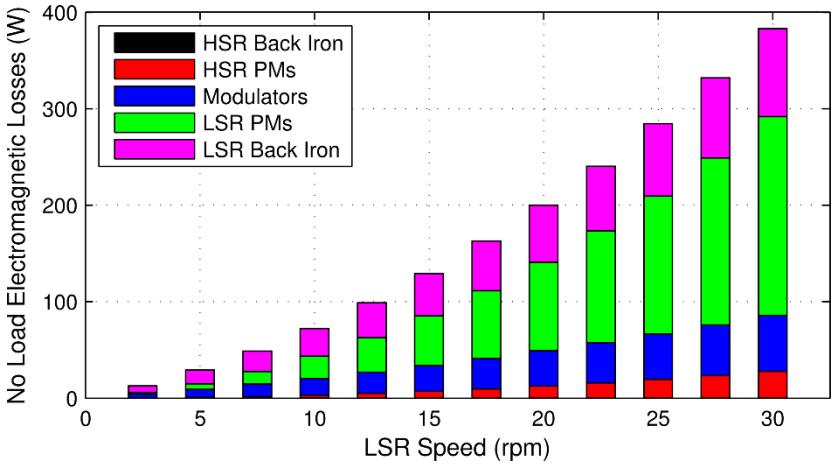


Figure 56. Simulated Electromagnetic No Load Loss Component Breakdown for Operation of the Prototype Magnetic Gear Design at Different Speeds

The RFMGM prototype's steady-state performance was characterized at different fixed speeds using multiple YY-connected resistive loads. Figure 57 compares the simulated and experimental steady-state performances of the prototype under the different operating conditions. Figure 57(a) indicates that the prototype achieves the rated 10 kW output at the rated 30 rpm LSR input speed with an 18.8 Ω resistive load. With the smaller resistances, the prototype achieves the rated torque at lower speeds. The data in Figure 57(b) reveals that the MGM prototype experienced higher experimental losses than the losses predicted by simulation results. The discrepancy between the simulated and experimental losses is due in part to the fact that the simulation loss data does not include the mechanical losses associated with the bearings, windage, etc.; however, further work is required to determine the exact sources of these differences. Due to the aforementioned precautions with the non-magnetic, non-conductive G11 buffers, it is not anticipated that there are appreciable electromagnetic losses in the end bells and the other inactive material outside of the active MGM stack. Despite these differences, Figure 57(c) illustrates that

the MGM prototype still achieves an experimental efficiency of approximately 90% over much of its operating range.

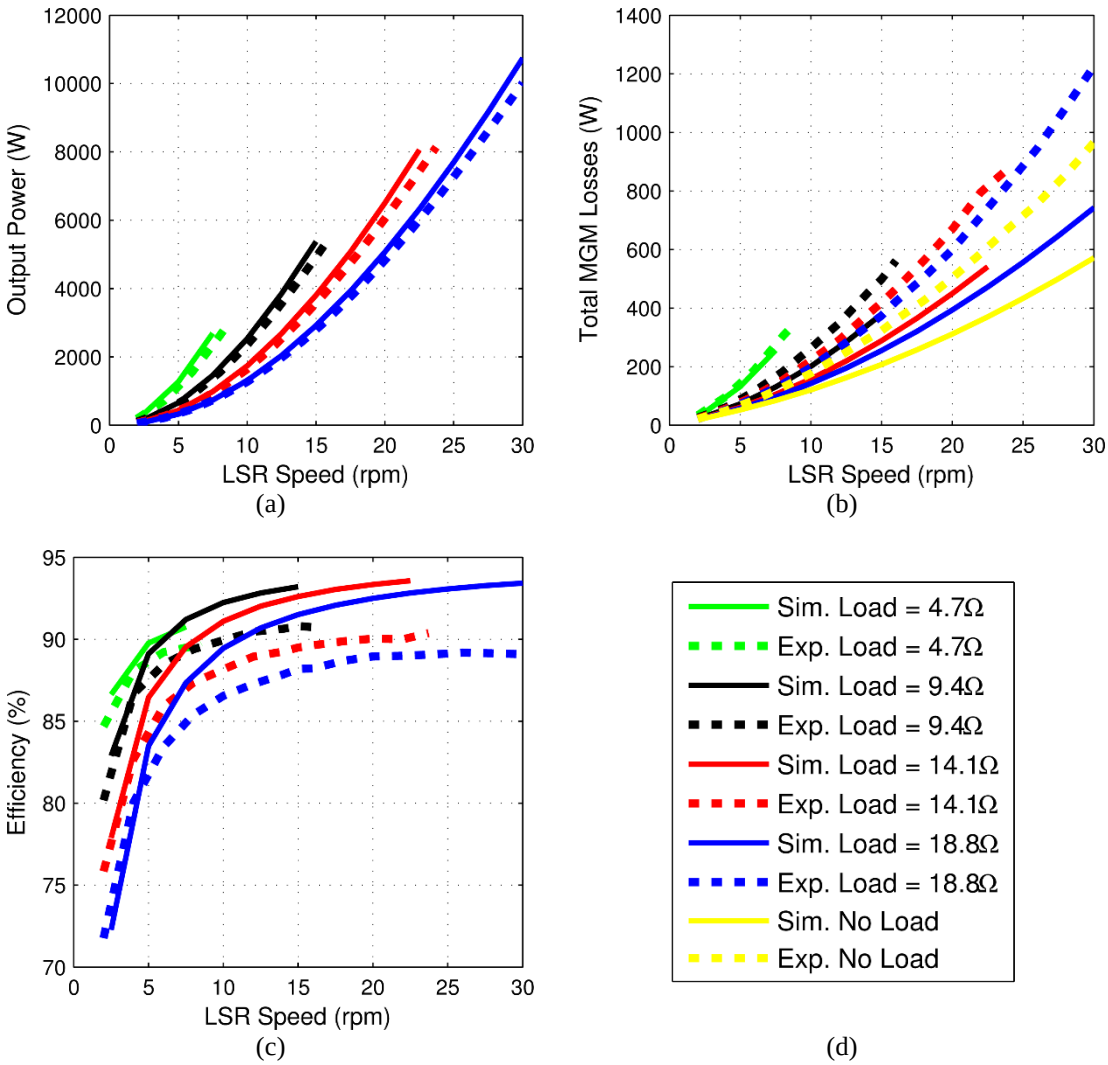


Figure 57. Simulated and Experimental MGM (a) Output Power, (b) Total Losses, and (c) Efficiency at Different Speeds and (d) Resistive Loads

## 5.7 Conclusion

This study describes the design, construction, analysis, and experimental evaluation of a magnetically-decoupled inner stator radial flux magnetically geared

machine prototype. Most notably, the study demonstrates the technology's feasibility at a much larger scale than ever before. This is evidenced by the fact that the MGM prototype achieved an experimental stall torque of 3870 N·m, while all other known prior MGM prototypes described in detail throughout the existing literature were limited to much smaller stall torques of less than 1000 N·m. This experimental stall torque represents a 99.1% match with the simulated 3D FEA stall torque and corresponds to a volumetric torque density of 82.8 $kN{\cdot}m/m^3$ and a gravimetric torque density of 14.5 N·m/kg with an active material cost of $2274. Additionally, the prototype also achieved an efficiency of nearly 90% over much of its steady-state operating range. These characteristics demonstrate the technology's tremendous potential for high torque, low speed applications, such as wave and wind energy harvesting, traction, and oil and gas production.

Nevertheless, there is still significant work required to further develop the technology and realize its commercial potential. For wave energy conversion in particular, future studies must also investigate the prototype's performance with an oscillating input motion source analogous to what would be provided by the actual OWSC, including transient overload torques which exceed the MGM's stall torque. Additionally, the prototype must also be tested with an active converter load capable of maximizing the power that the MGM extracts from the waves and managing the loss of synchronism between the MGM's rotors caused by overload input torques. Despite this remaining work, this study provides a clear, tangible demonstration of the MGM technology's immense promise for use in large scale high torque applications.

# 6. DESIGN COMPARISON OF NEODYMIUM AND FERRITE RADIAL FLUX MAGNETIC GEARS

Most literature on magnetic gears focuses on maximizing their torque density to make them competitive in size with mechanical gears [87, 91], but minimizing cost is also essential for the technology to achieve commercial success. One of the first decisions in the design of a magnetic gear is the selection of the magnet material. In an effort to reduce magnet costs, some literature suggests using weaker, but less expensive ferrite magnets instead of NdFeB magnets [27, 120]. This tactic is further motivated by the volatility of rare earth magnet prices, as shown in Figure 58 [121], which makes many manufacturers leery of relying on rare earth magnets.

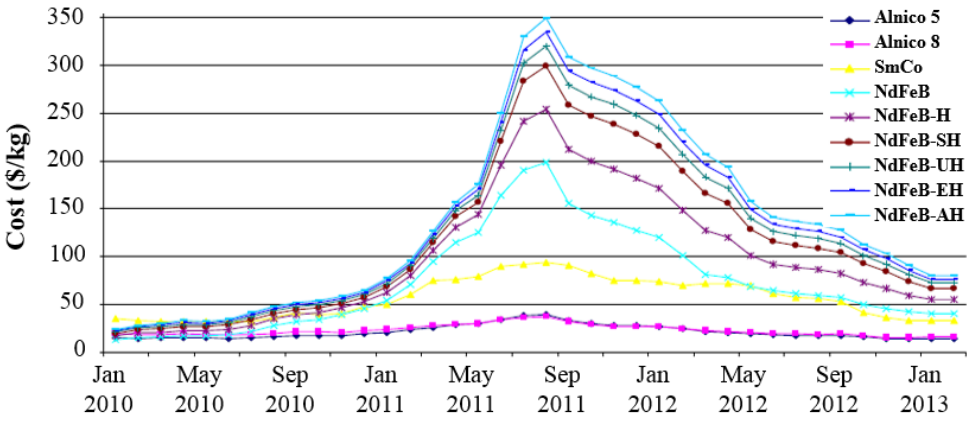


Figure 58. Rare Earth Permanent Magnet Cost Trends [121]

Some studies have evaluated the torque density of NdFeB and ferrite magnetic gears on the basis of limited parametric sweeps [91] or the permanent magnet costs for the

same single design with different magnet materials [120]. However, while thorough magnet material cost studies have been performed for conventional machines [122, 123], there is no known comprehensive comparison for individually optimized magnetic gears using the different materials and illustrating their divergent impacts on trends. Because the ferrite and NdFeB magnets result in different optimum designs, it is crucial to consider the best design for each material to perform a proper comparison for a given objective.

## 6.1 Design Study Methodology

The study in this section analyzes the coaxial radial flux magnetic gear topology with surface mounted permanent magnets shown in Figures 5 and 7 and examines the impact of using ferrite or NdFeB magnets on various design trends. In particular, tradeoffs between active material cost minimization and torque density maximization are characterized to highlight the effects of the magnet materials. As indicated by the material properties listed in Table 15, a relatively strong grade of ferrite was selected for use in the comparison analysis.

Table 15. Characteristics of Magnetic Gear Materials

| Material | Density | $B_r$ | Cost Rate |
|---|---|---|---|
| N42 NdFeB | 7400 kg/m$^3$ | 1.3 T | \$50/kg |
| Hitachi NMF-12F Ferrite | 4800 kg/m$^3$ | 0.46 T | \$10/kg |
| M47 Steel (26 Gauge) | 7870 kg/m$^3$ | N/A | \$3/kg |

This study assumes the use of fixed modulator operation and calculates the torque densities and gear sizing requirements based on the LSR stall torque. If fixed LSR operation is used instead, this would slightly increase the gear ratio and torque rating of each design, but it would not change any optimization patterns.

This study focuses only on active material cost and torque density and neglects factors such as structural material (housing, bearings, etc.), manufacturing considerations (such as the impact of varying the radius on achievable air gap sizes), and assembly costs. In particular, the cost of each gear design is evaluated based on the assumption that its constituent materials, listed in Table 15, each have a fixed price per unit mass, independent of the necessary component sizes and shapes. This is the same approach used in Section 5 and it is a simplification with respect to the reality that smaller, more complex sizes and shapes could increase the effective material prices and manufacturing costs. Thus, for the purposes of this analysis, the cost of a given design can be calculated by determining the requisite amounts of steel (used to form the rotor back irons and modulators) and permanent magnet material (either NdFeB or ferrite) and applying (29). The costs in Table 15 are used to demonstrate design trends and optimization patterns. However, because these patterns will vary slightly with the cost of the materials and because the dramatic volatility of NdFeB prices illustrated in Figure 58 is a primary motivation for this investigation, the last part of the study provides an analysis of the impact of NdFeB, ferrite, and steel cost rate variations on optimal costs and torque densities.

$$\text{Cost} = (\text{PM Mass})\cdot(\text{PM Rate}) + (\text{Steel Mass})\cdot(\text{Steel Rate}) \tag{29}$$

To characterize the different design trends for both NdFeB and ferrite magnetic gears, several critical geometric gear parameters were swept over the ranges of values specified in Table 16. As described in Section 5, because there are strong interdependencies between the effects of different dimensions, the values of certain variables were coupled through derived parameters, which are included in Table 16. First,

the radial thickness of the LSR magnets, $T_{LSPM}$, is determined by the radial thickness of the HSR magnets, $T_{HSPM}$, and a ratio, $k_{PM}$, as indicated in (23), which is repeated below. This relationship is employed because the LSR has more magnetic poles than the HSR, which leads to increased flux leakage, so it is cost effective to keep the LSR magnets thinner than the HSR magnets. Thus, $k_{PM}$ is swept over a range of values not exceeding 1. The second derived parameter, $G_r$, represents the approximate (nearest integer) desired gear ratio, and it is used, along with $P_{HS}$, to determine $P_{LS}$, as described in (24), which is repeated below. This keeps the number of modulators even, which results in symmetrical cancellation of the net forces on each rotor. Additionally, this approach still maintains a relatively high least common multiple (LCM) between $P_{HS}$ and $P_{LS}$, which reduces the gear's torque ripple [26].

$$T_{LSPM} = T_{HSPM} \cdot k_{PM} \tag{23}$$

$$P_{LS} = \begin{cases} G_r \cdot P_{HS} + 1 & \text{for } (G_r+1) \cdot P_{HS} \text{ odd} \\ G_r \cdot P_{HS} + 2 & \text{for } (G_r+1) \cdot P_{HS} \text{ even} \end{cases} \tag{24}$$

Table 16. Parametric Design Study Ranges

| Name | Description | Values | Units |
|---|---|---|---|
| $G_r$ | Nearest integer gear ratio | 4, 8, 16 | |
| $P_{HS}$ | HSR pole pairs | | |
| | For $G_r = 4$ | 3, 4, 5, … 18 | |
| | For $G_r = 8$ | 3, 4, 5, … 13 | |
| | For $G_r = 16$ | 3, 4, 5, … 8 | |
| $R_{Out}$ | Gear's active outer radius | 100, 125, 150 | mm |
| $T_{HSBI}$ | HSR back iron thickness | 5, 10, 20 | mm |
| $T_{HSPM}$ | HSR magnet thickness | 3, 5, 7, 9, 11, 13 | mm |
| $T_{AG}$ | Air gap thickness | 1 | mm |
| $T_{Mods}$ | Modulator thickness | 8, 11, 14 | mm |
| $k_{PM}$ | LSR magnet thickness ratio | 0.5, 0.75, 1 | |
| $T_{LSBI}$ | LSR back iron thickness | 5, 10, 20 | mm |

In addition to the design parameters specified in Table 16, all permanent magnet pole arcs were set equal to the corresponding pole pitches, as shown in Figures 5 and 7, resulting in 100% angular fill factors for each magnet pole. All modulator pole arcs were set equal to half of the corresponding modulator pole pitches, as shown in Figures 5 and 7, resulting in equally distributed modulator pieces and modulator slots.

All 48,114 designs specified by the combinations of parameter values in Table 16 were evaluated for both ferrite and NdFeB gears using static 2D FEA simulations at the stall torque alignment. Additionally, because several studies report significant discrepancies between the magnetic gear performance results predicted by 2D and 3D FEA simulations, due to axial leakage flux, more accurate 3D simulation models were used in this investigation where necessary (further explanation is provided in the following subsection). Although there is already a good analysis of the key trends related to these 3D effects [117], this study provides additional insight into their relative significance for a wider array of designs. Based on these 2D and 3D simulations, each gear design case was linearly scaled to the stack length required to achieve a stall torque of 250 N·m on the LSR. For each case, this stack length and the cross-sectional design were used to determine the gear volume and constituent material masses for torque density and active material cost calculations. In practice, a magnetic gear must be operated below its stall torque, but this will not change optimization trends.

Two additional considerations, demagnetization and magnetic flux containment, were addressed by analyzing the results and removing designs from the population set if they did not meet certain criteria with respect to these issues. Demagnetization was

handled based on the static simulation results by evaluating the percentage of the magnet bodies operating at flux densities below the knee point of their demagnetization curves at 20 °C. Although this does not comprehensively quantify the full extent of the demagnetization that will occur during operation, nor does it address the temperature dependent nature of this phenomenon, it does indicate which designs are most susceptible to demagnetization. To that end, designs with more than 1% of the magnet volume operating below the knee point were removed from the population. Adequate magnetic flux containment was ensured by eliminating designs with an RMS flux density of greater than 10 mT on either the circular path 1 mm inside of the HSR back iron or the circular path 1 mm outside of the LSR back iron. This filtration process also served as one means of determining the acceptable back iron thicknesses for a given design. The other primary performance issues affected by the back iron sizing are the gear's cost, torque density, and efficiency. Cost and torque density were addressed simply by calculating these values for each design and selecting the best results that were not eliminated due to demagnetization or magnetic containment issues. Efficiency was considered for the most cost effective and torque dense designs by performing 2D transient simulations to evaluate their full load losses at an LSR operating speed of 100 rpm.

## 6.2 Results

The analysis of the simulation results is separated into three parts. The first set of graphs is based on the fixed cost rates provided in Table 15 and contains large sets of design points to simply illustrate general performance capabilities and trends, such as cost, torque density, mass, 3D effects, and efficiency, for various design subsets. The second

set of graphs is also based on the fixed component cost rates provided in Table 15 and depicts detailed optimization patterns with respect to key design parameters for both NdFeB and ferrite gears. Finally, the third set of plots demonstrates the impact of material cost rate variations on the design optimization results.

### *6.2.1 Overview of Results*

Figure 59 displays the active material costs and volumetric torque densities of the most cost effective NdFeB and ferrite gear designs based on 2D FEA results, excluding those that suffered from poor magnetic containment or susceptibility to demagnetization. Similarly, Figure 60 shows the active material costs and active masses of the best NdFeB and ferrite gear designs based on 2D FEA results. The data in these plots verifies the well-known facts that NdFeB magnetic gears can achieve significantly higher torque densities and much lower active masses than ferrite magnetic gears. Additionally, the graphs illustrate the previously unestablished conclusion that optimally designed NdFeB magnetic gears also have lower active material costs than optimally designed ferrite gears (based on the cost rates in Table 15). Furthermore, these results indicate that the NdFeB gear designs with the lowest active material costs do not have the highest torque densities and vice versa. The highest torque density for any NdFeB design is 200 $kN{\cdot}m/m^3$ with an active material cost of \$110. However, the most cost effective NdFeB design has an active material cost of \$65 with a torque density of only 93 $kN{\cdot}m/m^3$. This divergence in optimization trends is primarily due to the fact that maximizing torque density requires using thicker magnets, but minimizing the active material cost of NdFeB designs requires using thinner permanent magnets. The same divergence is also present to a lesser extent

in the ferrite gear data set. The most compact ferrite design achieves a torque density of 26 kN·m/m$^3$ at an active material cost of $153, while the most cost effective ferrite gear design has an active material cost of $121 and a torque density of 21 kN·m/m$^3$. The difference between the optimization extremes is smaller for the ferrite data set because the ratio of the ferrite to steel costs is smaller than the ratio of NdFeB to steel costs, and thus the overall cost is not simply minimized by using the thinnest acceptable ferrite magnets.

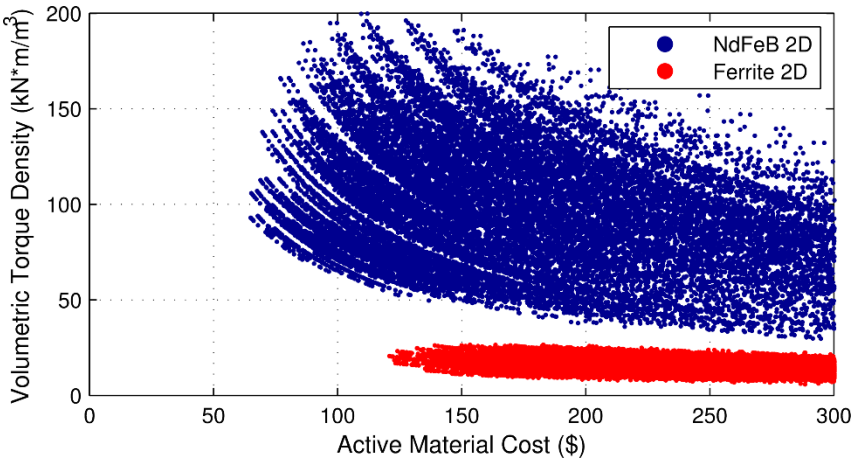


Figure 59. Torque Density and Cost for the Best Designs based on 2D Simulations

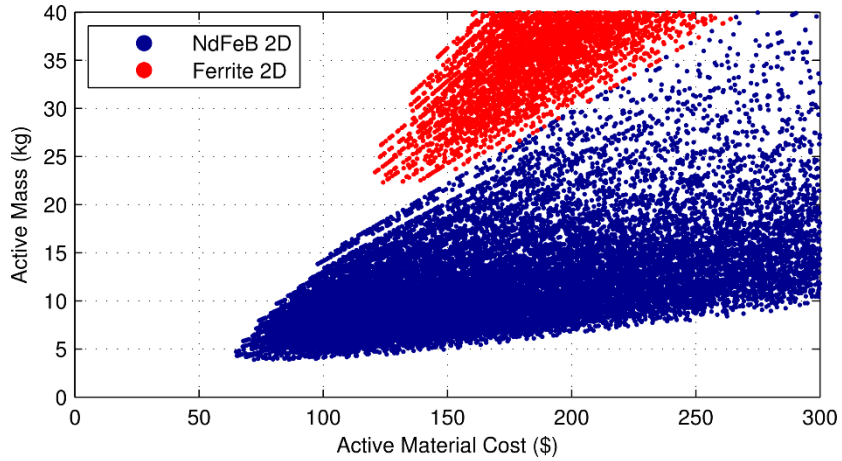


Figure 60. Active Mass and Cost for the Best Designs based on 2D Simulations

As noted earlier, magnetic gear designs can suffer from significant end effects due to axially escaping leakage flux not accounted for in 2D models. To address this issue, a subset of the most cost effective and torque dense NdFeB designs were re-simulated using 3D models at the stack lengths predicted by the 2D models and the corresponding active material cost, torque density, and active mass results are again shown in Figures 61 and 62 along with the 2D ferrite design results. As indicated by their lower torque densities, the ferrite designs require much longer stack lengths than the NdFeB designs and, as result, they experience less significant 3D effects. Thus, 3D ferrite gear simulations were only conducted for the optimization design trends presented in the final results subsection. Due to the impact of the 3D effects, the maximum NdFeB design torque density decreased from 200 kN·m/m$^3$ to 143 kN·m/m$^3$ and the minimum NdFeB design active material cost increased from \$65 to \$74, both of which are still superior to the corresponding optimum ferrite gear designs. Note that the impact of these 3D effects would decrease if the target gear torque rating was increased (assuming the same set of radii).

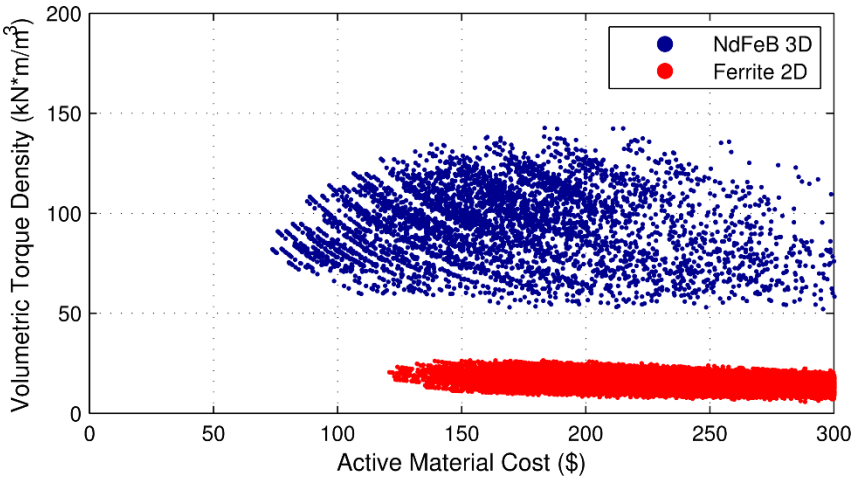


Figure 61. Torque Density and Cost for the Best Designs based on 3D NdFeB and 2D Ferrite Simulations

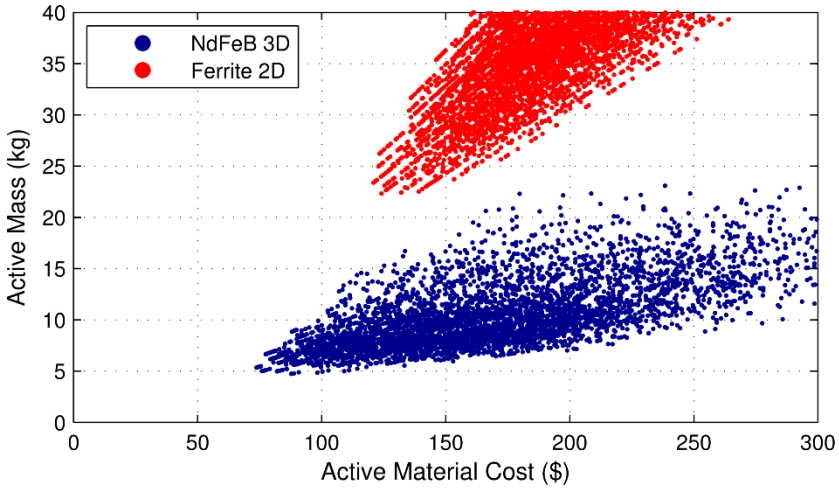


Figure 62. Active Mass and Cost for the Best Designs based on 3D NdFeB and 2D Ferrite Simulations

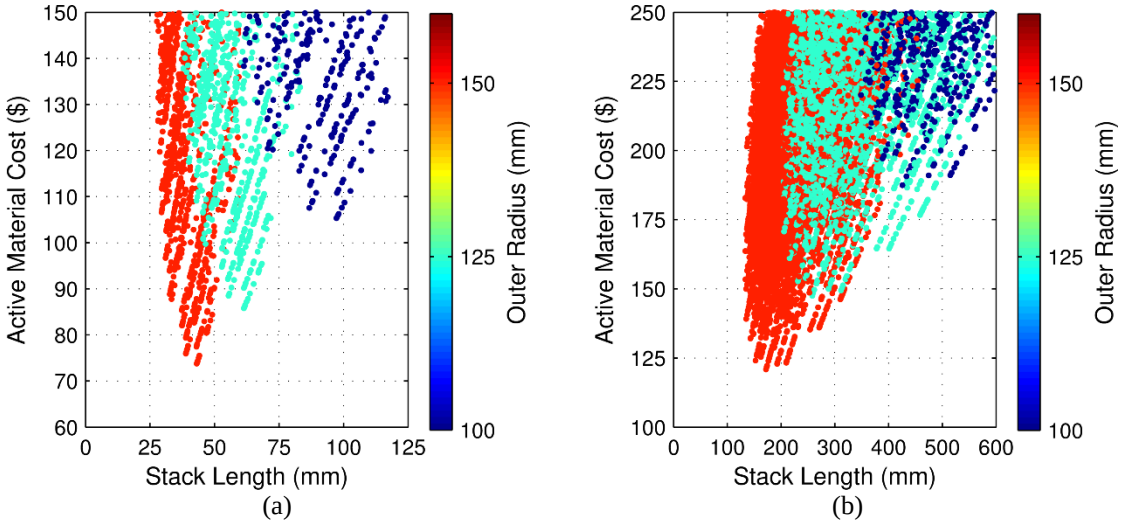


Figure 63. Relationship between Stack Length, Active Material Cost, and Outer Radius for (a) 3D NdFeB and (b) 2D Ferrite Magnetic Gear Simulations

Figures 63(a) and 63(b) show the relationship between stack length, active material cost, and outer radius for 3D NdFeB and 2D ferrite magnetic gear simulations. As the outer radius increases, the stack lengths and active material costs of the best designs decrease (although practical designs would likely require larger air gaps at larger radial

design points, which would slightly blunt this trend). As indicated by Figure 63(a), this trend remains true, albeit slightly less significant, even when 3D effects are considered. A comparison of Figures 63(a) and 63(b) demonstrates that the optimal ferrite gear designs require significantly longer stack lengths than the optimal NdFeB gear designs at the same radius. As noted earlier, these longer stack lengths reduce the impact of 3D effects on the ferrite designs.

Figure 64 demonstrates the relative impact of 3D effects on NdFeB gear designs with different form factors. As illustrated by the data in Figure 64, for a fixed torque rating, optimally designed gears with a larger outer radius, and thus a shorter stack length, tend to suffer a more significant reduction in torque, as compared to their 2D model projections. However, despite this consideration, the larger outer radius designs still generally achieve the lowest active material costs.

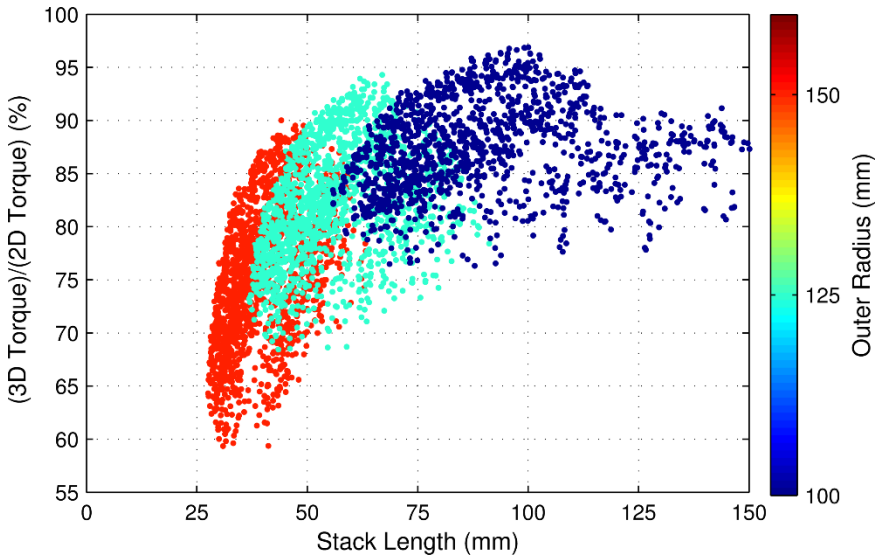


Figure 64. Impact of Outer Radius on 3D Effects for NdFeB Gear Designs at Different Stack Lengths

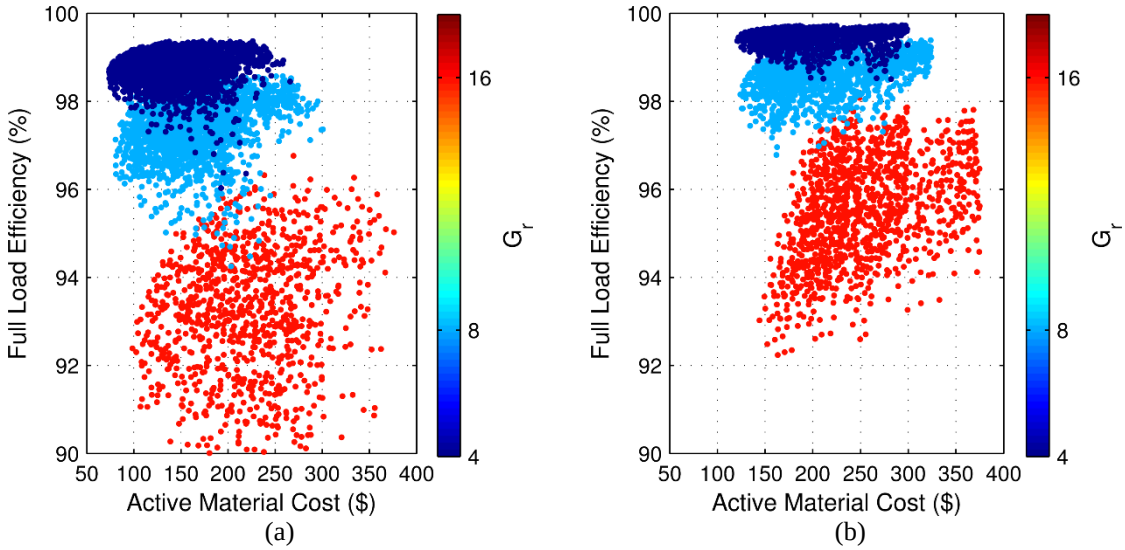


Figure 65. Efficiencies for the Best (a) NdFeB and (b) Ferrite Gear Designs

Figure 65 shows the simulated efficiencies of the most cost-effective and torque dense designs. These efficiencies only include the electromagnetic losses (eddy losses in the magnets and core losses in the steel) for operation at the LSR stall torque and an LSR speed of 100 rpm. The losses are determined from 2D transient simulations and linearly scaled to the necessary stack lengths. Figure 65(a) shows the efficiencies of NdFeB designs at each of the gear ratios based on the stack lengths determined by 3D static simulations, and Figure 65(b) illustrates the efficiencies of ferrite designs at each of the gear ratios based on the stack lengths determined by 2D static simulations. In both cases, the lower gear ratios achieve higher efficiencies due in part to the fact that the HSR rotates faster for higher gear ratios, which increases the electromagnetic frequencies present in the gear and leads to higher losses. There is also a tradeoff between cost and efficiency, which is primarily related to the selection of pole pair counts and back iron thicknesses. Additionally, despite being larger, the ferrite designs can achieve higher efficiencies than

the NdFeB designs because the ferrite designs have lower flux densities, which lead to lower steel core loss densities, and because ferrite's resistivity eliminates magnet eddy current losses.

### *6.2.2 Design Optimization Trends*

In order to demonstrate important design trends and tradeoffs, the effects of several of the design parameters are considered for designs using NdFeB magnets and designs using ferrite magnets at each of the different gear ratios. One key source of the differences in optimization trends for NdFeB and ferrite gears is the difference in the percentage of the active material cost associated directly with the magnet material as indicated in Figure 66. Trends are evaluated for the NdFeB designs using both 2D and 3D simulation results and for the ferrite designs using 3D simulation results. Figure 67 provides a legend describing the significance of each of the curves in Figures 68 and 69, which demonstrate the impact of different design parameters.

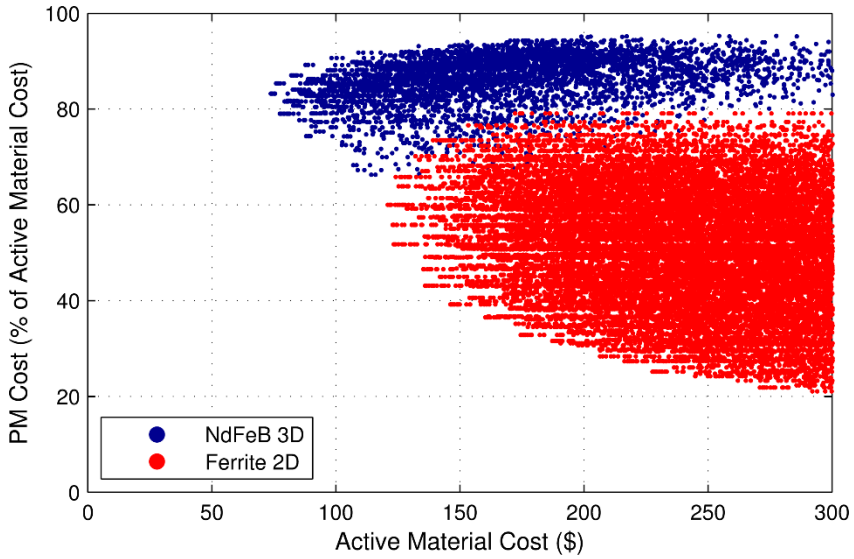


Figure 66. Percentage of Total Active Material Cost from Magnet Material for NdFeB and Ferrite Designs

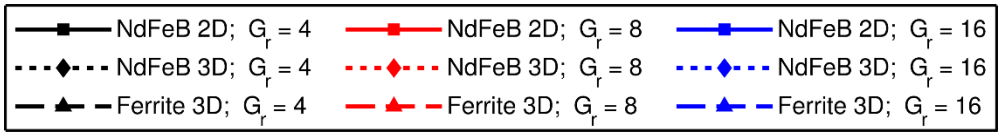


Figure 67. Legend for Design Optimization Trend Plots in Figures 68 and 69

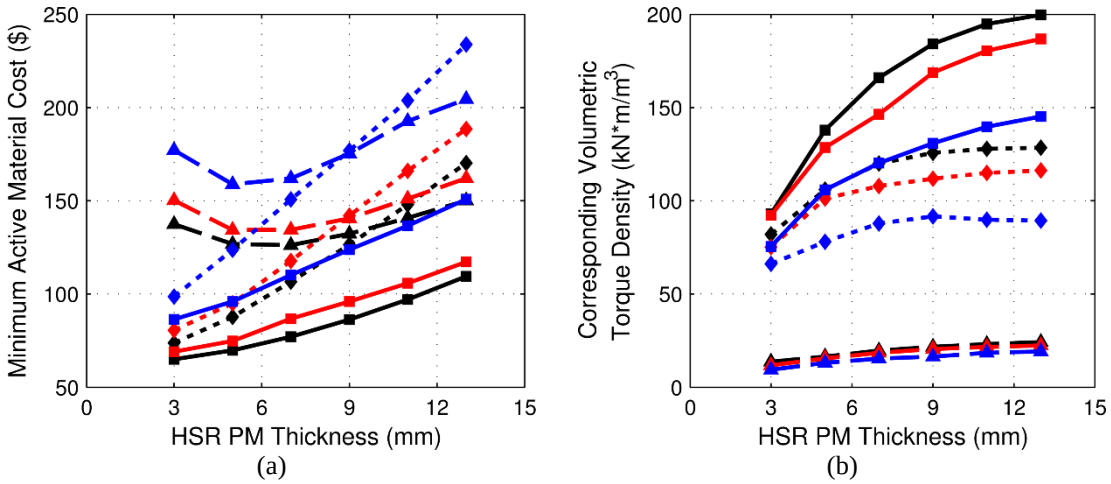


Figure 68. Impact of HSR Magnet Thickness on (a) the Minimum Active Material Cost and (b) the Corresponding Torque Density

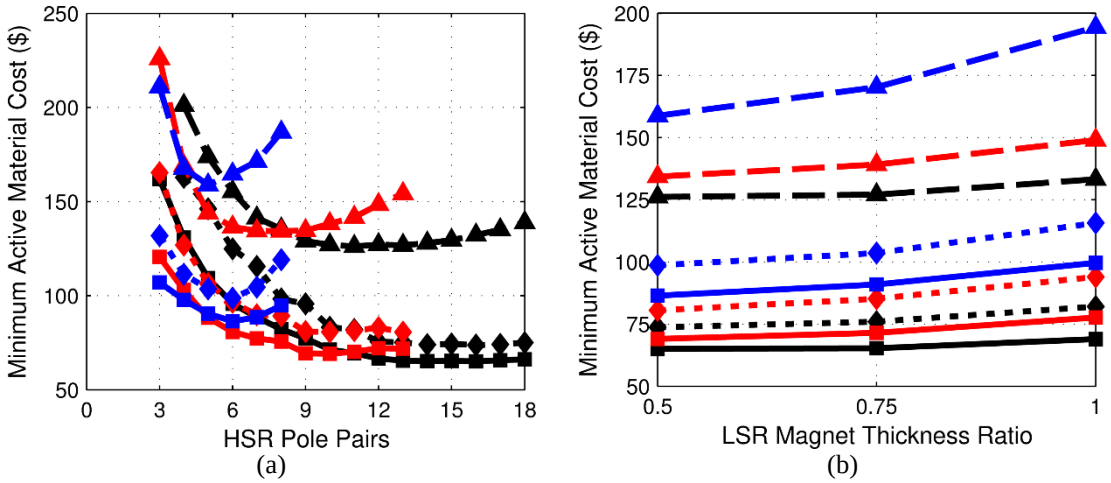


Figure 69. Impact of (a) HSR Pole Pairs and (b) the LSR Magnet Thickness Ratio on the Minimum Active Material Cost

Figure 68(a) illustrates the minimum active material costs that can be achieved with HSR magnets of various thicknesses, and Figure 68(b) provides the corresponding

torque densities of these same minimum cost designs. Figure 68(a) indicates that the minimum material cost for the NdFeB designs of each gear ratio can be achieved by using the thinnest magnets allowed in the simulation sweep. However, the minimum cost ferrite designs are achieved with thicker magnets. Because the magnet thickness contributes to the effective air gap, increasing the magnet thickness provides diminishing torque returns. Due to the relatively high cost of NdFeB magnets, the optimal NdFeB designs use magnet material almost as efficiently as possible, resulting in relatively thin magnets. However, the cost of iron is more significant in the ferrite designs, as shown in Figure 66, creating a more significant tradeoff between magnet usage and steel usage. This leads to the optimal ferrite designs having thicker magnets than the optimal NdFeB designs. Figure 68(b) shows that the torque density of the optimal designs increases with the magnet thickness. However, the 3D simulations reveal less of an increase in torque density than the 2D simulations because the end-effects penalty increases as the increased magnet thickness decreases the stack length.

Figure 69(a) shows the effects of varying the HSR pole pair count on the minimum material cost. Higher gear ratios favor lower HSR pole pair counts because the gear ratio affects the tradeoff between optimizing the HSR and LSR pole pair counts. Additionally, ferrite designs tend to favor lower HSR pole pair counts than NdFeB designs because the thicker magnets favored by ferrite increase the effective air gap and, thus, the leakage flux per pole. Decreasing the number of poles counteracts this increase in leakage flux.

Figure 69(b) illustrates the effect of varying $k_{PM}$, the ratio of the LSR magnet thickness to the HSR magnet thickness. Because the higher number of poles on the LSR

leads to more leakage flux on the LSR, it is cost effective to concentrate most of the magnet material on the HSR. As the gear ratio increases, the difference between the LSR and HSR pole counts increases, leading to a greater improvement achieved by reducing $k_{PM}$. However, in addition to the practical limitations on producing extremely thin magnets for the LSR, decreasing $k_{PM}$ too far can increase the LSR magnets' susceptibility to demagnetization by the HSR magnets.

### *6.2.3 Impact of Material Cost Variation*

The previous graphs and analysis are all based on the fixed costs provided in Table 15; however, all of the materials, especially NdFeB, have some level of cost variability, which will impact the optimum designs and minimum achievable active material costs. Figures 70 and 71 characterize the impact of this variation in NdFeB and ferrite price rates on the minimum costs of the different designs, based on 3D simulation results. Figure 70 shows the impact of NdFeB price variation on the minimum active material costs of the NdFeB designs relative to the fixed minimum costs of ferrite designs at the nominal ferrite price rate of $10/kg. Figure 71 shows the impact of ferrite price variation on the minimum active material costs of the ferrite designs relative to the fixed minimum costs of NdFeB designs at the nominal NdFeB price rate of $50/kg. This data shows that, for surface mounted radial flux magnetic gears, relatively high NdFeB prices or low ferrite prices are required before ferrite gears become cost competitive. Under the assumed constraints, relative to the fixed minimum active material costs of the ferrite designs based on a ferrite cost of $10/kg, NdFeB designs with a gear ratio of ~4 require NdFeB to cost at least $93/kg before ferrite is cost competitive, while designs with gear ratios of ~8 and ~16 require

NdFeB rates of $92/kg and $91/kg, respectively. Alternatively, relative to the fixed minimum active material costs of the NdFeB designs based on a cost of $50/kg for NdFeB, ferrite designs with a gear ratio of ~4 require ferrite to cost $3.3/kg or lower for ferrite to be cost competitive, while designs with gear ratios of ~8 and ~16 require a rate of $3.5/kg or lower. Regardless of active material cost, NdFeB designs are still significantly smaller.

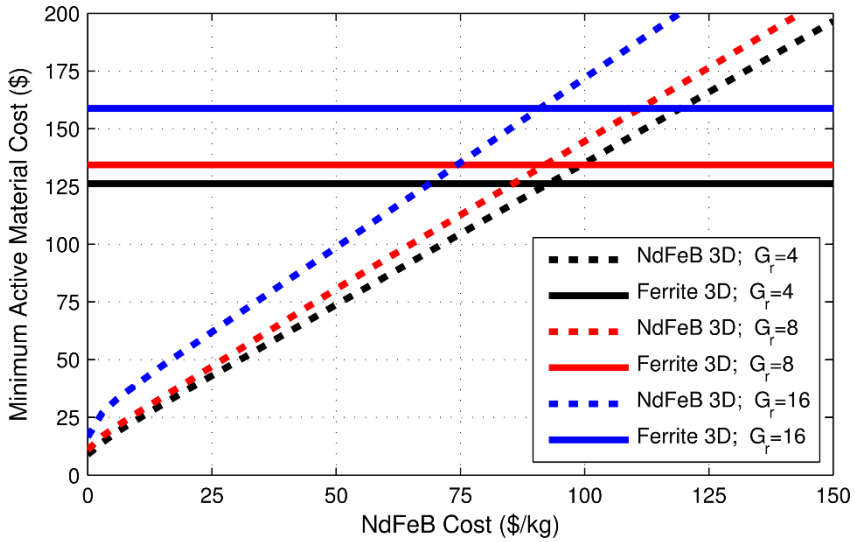


Figure 70. Impact of NdFeB Cost Variation on Minimum Active Material Cost

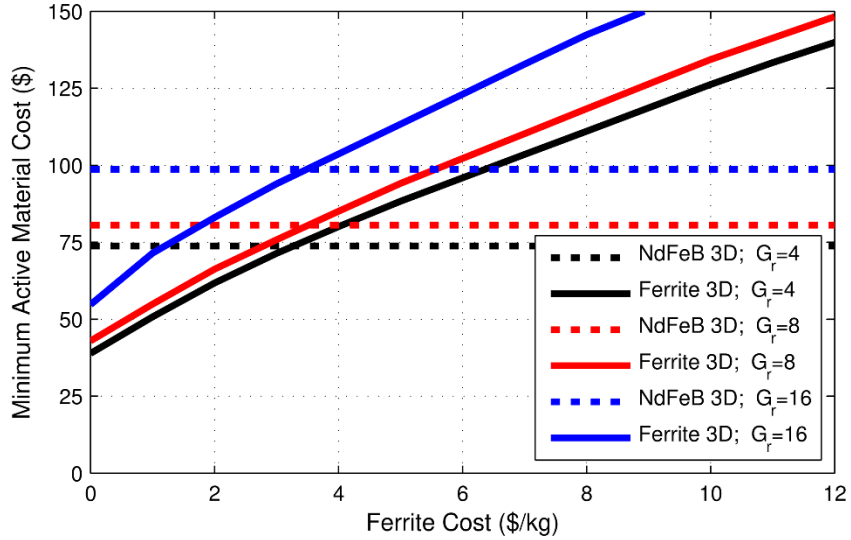


Figure 71. Impact of Ferrite Cost Variation on Minimum Active Material Cost

Figures 70 and 71 describe the impact of magnet material prices on the minimum achievable active material costs for the two sets of magnetic gear designs; however, Figure 66 reveals that, while the active material costs of NdFeB designs are dominated by the cost of the magnets themselves, the cost of the steel is a non-negligible component of the ferrite gear costs. Thus, a range of costs for all three materials are considered for a gear ratio of ~4 in the analysis provided in Figure 72, based on 3D simulation results. Figure 72(a) shows the impact of the steel and NdFeB price rates on the minimum achievable active material cost for the NdFeB designs, where the different colors and contour lines indicate the variation in this minimum cost. Similarly, Figure 72(b) shows the impact of the steel and ferrite price rates on the minimum achievable active material cost for the ferrite designs. Figure 72(c) illustrates the corresponding torque densities of these same minimum active material cost ferrite designs whose costs are characterized in Figure 72(b). The trends in Figures 70-72 display some curvature as prices vary, indicating that the optimal design changes as the material cost rates vary. As the ratio of magnet price to steel price increases, the optimal design increasingly favors thinner, more effectively utilized magnets, decreasing the torque density of the minimum active material cost design, as illustrated in Figure 72(c).

These results demonstrate that, for most reasonable combinations of NdFeB, ferrite, and steel cost rates, the increased energy density of NdFeB relative to ferrite offsets its higher cost per unit mass, making it the most cost effective magnet material to use in this magnetic gear topology.

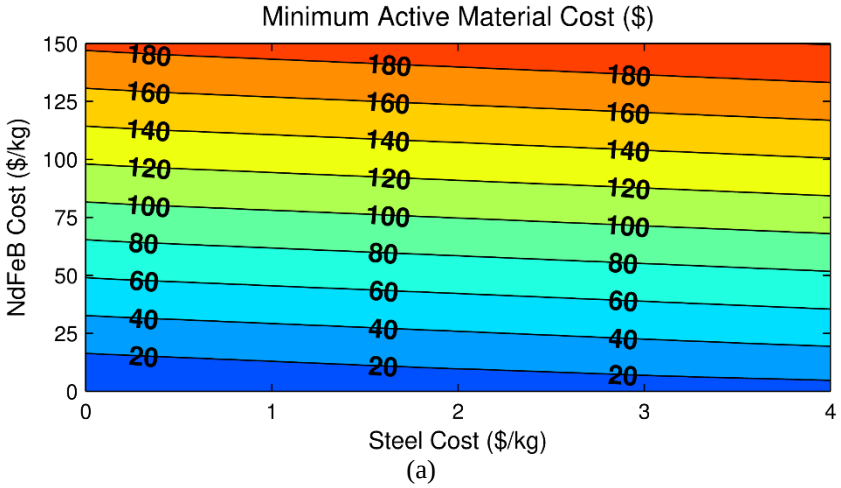


(a)

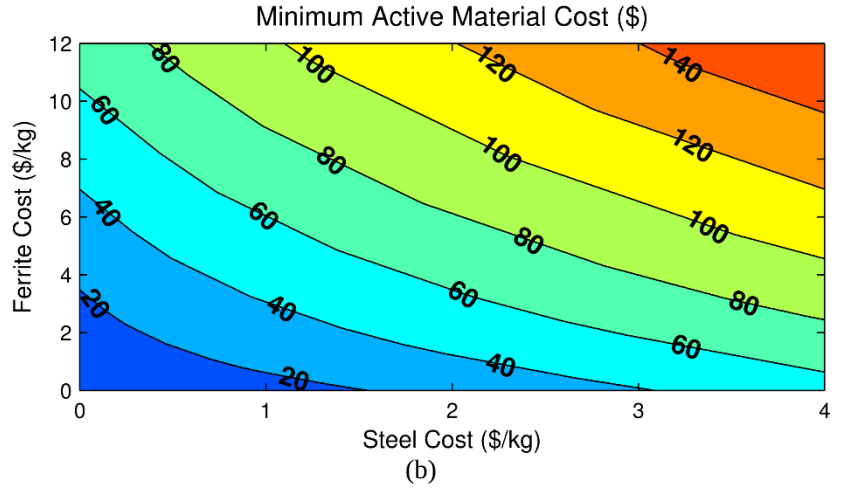


(b)

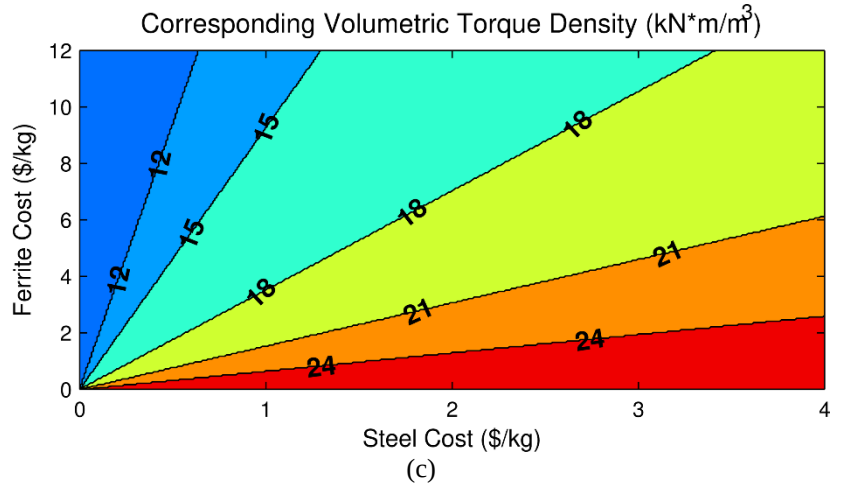


(c)

Figure 72. Effect of Steel and Magnet Costs on (a) Minimum Active Material Cost of NdFeB Designs, (b) Minimum Active Material Cost of Ferrite Designs, and (c) the Corresponding Torque Density of the Minimum Active Material Cost Ferrite Designs

## 6.3 Conclusion

In this section, both NdFeB and ferrite radial flux magnetic gears with surface mounted permanent magnets were parametrically evaluated using 2D and 3D FEA to demonstrate various design trends and performance capabilities with the two different magnet materials. The results reveal that, under the assumed cost scenario of Table 15, the optimal NdFeB designs are significantly more cost-effective than the optimal ferrite designs. Under the assumed design constraints, relative to the nominal ferrite cost of $10/kg, a gear with a gear ratio of ~4 requires NdFeB to cost at least $93/kg before ferrite is cost competitive, while designs with gear ratios of ~8 and ~16 require NdFeB rates of $92/kg and $91/kg, respectively. Alternatively, relative to the nominal NdFeB cost of $50/kg, a ferrite design with a gear ratio of ~4 requires ferrite to cost at most $3.3/kg for ferrite to be cost competitive, while designs with gear ratios of ~8 and ~16 require a ferrite rate of $3.5/kg.

Additionally, the minimum active material cost was evaluated for NdFeB and ferrite gear designs across a range of combinations of different magnet material and steel cost rates to illustrate the minimum active material costs that could be achieved for each cost scenario. This analysis demonstrated that for most historical price combination scenarios, NdFeB gear designs are still capable of achieving lower active material costs than ferrite gear designs. Furthermore, the results in Figure 72 indicate that the prices of ferrite magnetic gear designs are significantly more dependent on the price of magnetic steel, as compared to the prices of NdFeB designs. Ferrite designs become increasingly cost-competitive at lower steel prices. Thus, the ratio of all three material cost rates is

crucial for determining the best permanent magnet material to use for a given application. Additionally, the ratio of the material cost rates significantly impacts the optimal design parameters for ferrite magnetic gears. In all cases, regardless of material cost rates, the optimal NdFeB designs achieve significantly lower sizes and masses than the optimal ferrite designs. In addition to being generally undesirable, the higher size and mass of the ferrite designs will incur some additional cost penalties, such as increased housing material expenses. However, the ferrite designs are able to achieve slightly higher efficiencies than the NdFeB designs.

Based on these observations, it is evident that NdFeB magnets are generally preferable for use in radial flux magnetic gears with surface mounted permanent magnets. Flux focusing topologies have been proposed for ferrite, due to their ability to increase the air gap flux density, but these topologies suffer from increased complexity, poor magnetic containment, and increased susceptibility to demagnetization. However, these topologies could disproportionately improve the performance of ferrite designs relative to NdFeB designs. For simplicity, flux focusing gears were not considered in this analysis. Future studies should evaluate the relative effectiveness of NdFeB and ferrite flux focusing magnetic gear designs to determine how the different topology impacts design and performance trends.

# 7. DEVELOPMENT OF A 2D MAGNETIC EQUIVALENT CIRCUIT MODEL FOR RADIAL FLUX MAGNETIC GEARS

Despite all of their promising attributes, magnetic gears still struggle to compete with their mechanical counterparts and achieve parity or superiority with respect to crucial fundamental considerations such as size, weight, and cost [45]. Thorough, design-specific parametric optimizations, such as the studies described in the previous sections, are essential in order for the technology to bridge this gap and realize the full extent of its potential advantages. This in turn necessitates the development of fast and accurate analysis tools capable of characterizing the performance of a large number of parametric design variations.

The basic tools commonly used for evaluation of electromechanical devices include FEA, analytical models, winding function theory, and magnetic equivalent circuit (MEC) models, all of which can be applied to magnetic gears. As evidenced by the prior sections, FEA models are the overwhelmingly most popular choice for analysis of magnetic gears due to their broad commercial availability, ease of use, and high degree of accuracy, including the ability to characterize 3D and nonlinear effects. However, these benefits come at the expense of high computational intensity and long simulation run times which severely limit the number of parametric design variations that can be assessed. This is a particularly significant issue for magnetic gears, because the different permanent magnet pole counts on the two rotors and the intermediate set of modulators produce numerous significant spatial harmonics in the field distribution, as well as substantial

leakage flux in multiple regions, particularly in the slots between the modulators. These issues, combined with the presence of two air gaps, necessitate the use of numerous small mesh elements to accurately determine the field solution. Furthermore, as indicated in the previous sections, good designs have limited symmetry to decrease torque ripple, which mitigates the extent to which fractional models can reduce mesh element counts and expedite analysis [26]. Finally, these issues are all exacerbated by the fact that many magnetic gear designs suffer from more significant 3D effects than most traditional electrical machines, as shown in the design of the large scale inner stator radial flux magnetically geared machine in Section 5 and the simulation study comparing NdFeB and ferrite magnetic gears in Section 6. This compels the use of 3D models to accurately characterize the torque rating of a given design and thus dramatically increases the required simulation time and further reduces the number of parametric design cases that can be evaluated.

In an effort to bypass the long FEA simulation times, analytical models, such as those described in Section 2, have also been developed for certain magnetic gear topologies, and, while they are significantly faster than FEA models with proper implementation, they are typically based on simplifying assumptions and either severely limited or completely lacking in ability to model 3D effects and nonlinear considerations such as iron saturation [102, 103]. Furthermore, as noted in Section 2, analytical models are relatively inflexible and limited to a very specific topology. Based on similar motivation for a faster, less computationally intense model, winding function theory has also been employed to analyze magnetic gears with reasonably accurate results

demonstrated for a single design case [5]. However, the underlying assumptions used in winding function theory prevent it from accurately characterizing the high levels of leakage and fringing flux present in many magnetic gear designs. Additionally, basic winding function theory is also incapable of modeling 3D and nonlinear effects. As a result of these shortcomings, analytical models and winding function theory models are useful quick first pass analysis tools, but they are not directly suitable for detailed, extensive magnetic gear design optimization studies. Motivated by the limitations of these models and the excessive simulation times required to perform the various FEA-based parametric optimization studies described in the previous sections, the later stages of this dissertation focus on the development and evaluation of generalized parametric 2D and 3D lumped parameter magnetic equivalent circuit (MEC) magnetic gear models as faster, but still extremely accurate alternative and supplementary analysis and design tools.

## 7.1 Introduction to Magnetic Equivalent Circuits

MECs, also referred to as reluctance networks, are an alternative modeling tool which represents a compromise between less accurate, but extremely fast analytical models and extremely accurate, but relatively slow and computationally intense FEA models. The basic concept of an MEC is to decompose a physical electromagnetic system into individual pieces known as flux tubes (defined paths through which magnetic flux flows) and represent each tube using lumped reluctances, magnetomotive force (MMF) sources, and flux sources to collectively form a lumped parameter magnetic equivalent circuit which is directly analogous to a traditional lumped parameter electrical circuit and can be solved using the same set of analysis techniques. Just as Kirchhoff's current and

voltage laws define the system of equations for an electrical circuit, Gauss's law for magnetism and Ampere's circuital law define the corresponding system of equations for MECs.

Although MEC and FEA models both analyze a system by breaking it up into pieces of varying sizes, there are some critical differences between the two approaches. The most significant distinction is that flux flow directions are predetermined in MEC models (excluding the sign of the direction) by the definition of the flux tubes, but in FEA models the flux orientation in each element is unrestricted and determined as a result of the model solution. This is highlighted by the fact that MEC models typically, although not universally, use scalar quantities such as MMFs (scalar magnetic potentials) or scalar fluxes as the unknown state variables, whereas FEA models commonly use vector quantities, such as vector magnetic potentials, as the unknown state variables. Additionally, MEC models traditionally rely heavily on prior empirical knowledge of system behavior and use significantly less elements than FEA models; however, this difference is not necessarily an intrinsic characteristic of the two approaches.

The concepts of a magnetic circuit and reluctance (meaning the magnetic dual of electrical resistance) date back well into the 1800s [124]. Furthermore, Hopkinson's Law, given by (30), was formulated by 1886 and relates the scalar magnetic potential or MMF, $\mathcal{F}$, drop across a flux tube to the magnetic flux, $\Phi$, flowing through the flux tube and the reluctance, $\mathcal{R}$, of the flux tube. MEC techniques were extended to analysis of ac electromechanical systems in the 1960s [125, 126]. Ostovic published several instrumental papers applying MECs to the analysis of induction and PM synchronous

machines in the 1980s [127-130]. Since that time, there have been several additional studies demonstrating the ability of MEC models to analyze both induction motors and various synchronous machines with better accuracy than simplified analytical models and significantly faster simulation run times than corresponding FEA models [131-137]. A few works have also established that MEC analysis techniques are well suited for adaptation to 3D models, with their advantages of reduced computational intensity and faster simulation times becoming even more pronounced as compared to 3D FEA models [138-140].

$$\mathcal{F} = \mathcal{R}\Phi \tag{30}$$

This study focuses on the development of a generalized, parametric linear magnetic equivalent circuit model for analysis of the coaxial radial flux magnetic gear topology with surface mounted permanent magnets shown in Figure 5. Although MECs have been used extensively to model various types of electric machines, there are only a few instances in which the concept has been applied to the analysis of rotary magnetic gears and magnetically geared machines [141-143] and one other study in which an MEC was used to model a linear magnetic gear [97]. Furthermore, while [141-143] do demonstrate the potential for MEC models to evaluate a gear design much more rapidly than FEA models, they use coarse reluctance networks with very few elements included in the MEC, and provide minimal analysis of the MEC discretization's impact on its accuracy nor much indication of how the MEC's accuracy varies with different design parameters. Additionally, only the work in [142] offers limited discussion of a 3D MEC model with a very small number of elements to account for axial leakage flux.

This study uses an approach more in line with the MEC models developed in [131, 132, 135, 137-140], in the sense that it systematically creates a fully parameterized flux tube mesh by breaking the magnetic gear up into pieces, referred to as node cells. The levels of discretization in different regions of the gear are parameterized so that more mesh elements can be added to the areas that need high resolution for accuracy and less elements can be used in the other regions to minimize simulation run times. Moreover, in Section 9, this study also details how the 2D model can be easily extended into a full 3D model with parameterized axial meshing resolution for extremely fast and accurate analysis of 3D effects. Finally, whereas [143] develops a fully nonlinear model, using nonlinear B-H curves for all steel regions and [97, 141, 142] use non-linear B-H curves for the modulator material and assume infinite permeability for the back irons, this work employs a fully linear MEC model that assumes a constant relative permeability for both the modulators and the back irons. The data obtained from this linear model demonstrates that, as suggested by the results in [97], it is still extremely accurate for analysis of the torque capabilities of most reasonable ideal designs, because the large linear reluctances associated with the two sets of magnets and the two air gaps in the primary flux paths dominate the much smaller nonlinear reluctances of the ferromagnetic modulators and the HSR and LSR back irons, even in many cases where they experience significant saturation. The linear model allows for tremendously fast calculation of a design's torque capabilities. Furthermore, the MEC implementation, which is described in the following subsection, is well suited for extension to a nonlinear model using an iterative approach such as the one described in [136]. This extension to a nonlinear model is necessary for

analysis of additional considerations, such as losses or flux densities in the air regions beyond the rotor back irons. It is also essential for analysis of designs which include features, such as a modulator bridge, that significantly increase the system's nonlinearity.

## 7.2 Geometry Discretization

The 2D MEC mesh is systematically formed by dividing the magnetic gear cross-section into radial and circumferential (tangential or angular) layers as illustrated by the simple example shown in Figure 73, which depicts a source free annular region in the θ-r plane, divided into 3 radial layers (RL) along the r dimension and 4 angular layers (AL) along the θ dimension. Each intersection of a radial layer and an angular layer defines an annular sector, referred to as a 2D node cell. Every 2D node cell consists of two radially directed reluctances and two tangentially directed reluctances, each of which is connected to the center node of the cell and one of the cell's radial or tangential boundaries as shown in Figure 73. Each of these lumped reluctances corresponds to a flux tube oriented along the same direction, which allows flux to flow in a positive or negative direction along the specified linear path. In this analysis, the MEC model is solved using node MMF analysis techniques (analogous to node voltage analysis in electrical circuits), based on Gauss's law for magnetism, in which the scalar magnetic potentials at each node represent the unknown state variables. Because of this approach, it is more appropriate to speak of lumped permeances (the multiplicative inverses of the reluctances) rather than lumped reluctances. An alternate 2D MEC model implementation based on mesh flux analysis techniques derived from Ampere's circuital law was also developed using fluxes as the unknown state variables, but the node MMF approach was ultimately selected for ease of

extension to a 3D model. However, while the two approaches are equivalent for a linear model, it may prove computationally advantageous to use the mesh flux methodology when extending the MEC to a nonlinear model [144].

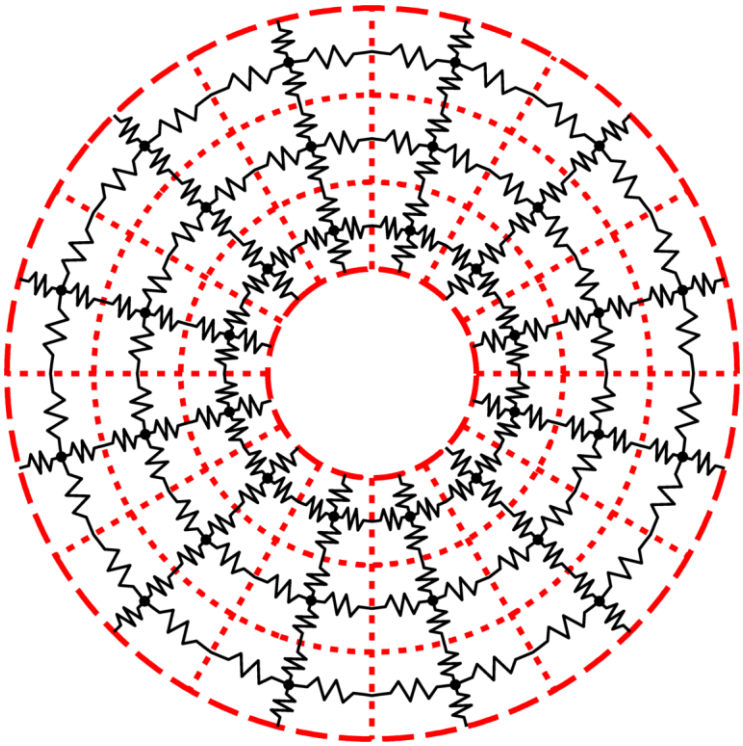

Figure 73. Definition of Mesh Node Cells Based on Intersection of Radial and Angular Layers

The lumped reluctance of a uniform flux tube is given by the well-established expression in (31), where A represents the cross-sectional area of the flux tube surface normal to the flux path, μ is the permeability of the physical material that comprises the flux tube, and *l* is the total length of the flux tube flux path. The lumped permeance of the flux tube is given by the inverse expression in (32). Using these relationships, the permeance of each radially directed flux tube ($\mathcal{P}_{rad}$) and each tangentially directed flux

tube ($\mathcal{P}_{tan}$) in the reluctance network mesh can be calculated according to (33) and (34), respectively. Conceptual illustrations of a radially oriented flux tube and a tangentially oriented flux tube are provided in Figures 74(a) and 74(b), respectively. Note that each radially directed flux tube corresponds to one radial half of its node cell, the full angular width of its node cell, and the full axial height of its node cell. The expression in (33) effectively uses integration to calculate the total lumped radial permeance by combining the reluctances of series connected differential radial slivers of the flux tube. Similarly, each tangentially directed flux tube corresponds to the full radial width of its node cell, one angular half of its node cell, and the full axial height of its node cell. The expression in (34) effectively uses integration to combine the permeances of parallel connected differential radial slivers of the flux tube. In each of these equations, $R_{in}$ indicates the inner radius of the flux tube, $R_{out}$ denotes the outer radius of the flux tube, $\Delta\theta$ is the uniform angular width of the flux tube (in radians), $\Delta z$ is the uniform axial height of the flux tube (which corresponds to the full axial height of the system in a 2D model or the axial height of the axial layer in a 3D model), and $\mu$ is the permeability of the flux tube material. In the event that a flux tube overlaps with two different materials, the flux tube is further subdivided into two different flux tubes, one for each material region, and the lumped permeances for each individual flux tube are calculated and combined in series or parallel in accordance with the relationships of the two paths, using the same formulas employed for combining series or parallel conductances in lumped electrical circuits.

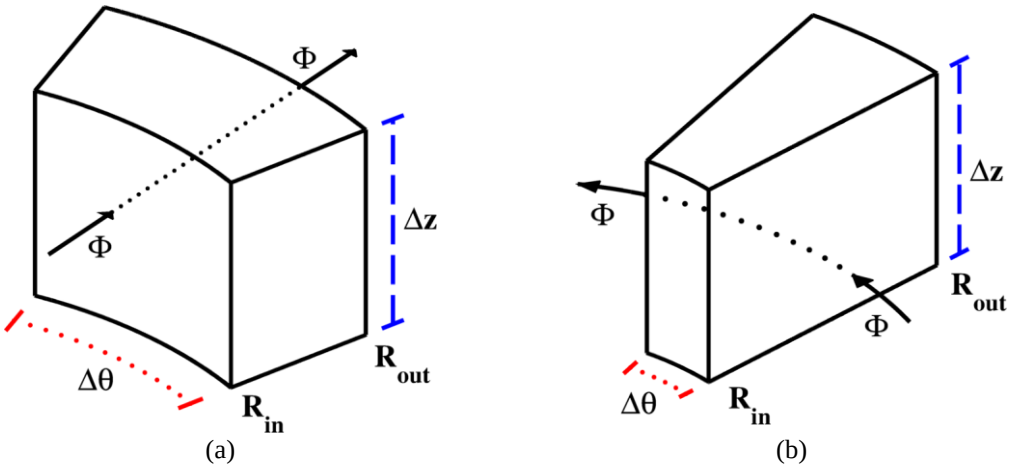


Figure 74. Conceptual Illustrations of (a) Radially and (b) Tangentially Oriented Flux Tubes

$$\mathcal{R} = \frac{l}{\mu \cdot A} \tag{31}$$

$$\mathcal{P} = \frac{1}{\mathcal{R}} = \frac{\mu \cdot A}{l} \tag{32}$$

$$\mathcal{P}_{rad} = \left( \int_{R_{in}}^{R_{out}} \frac{dr}{\mu \cdot \Delta z \cdot (r \cdot \Delta\theta)} \right)^{-1} = \frac{\mu \cdot \Delta z \cdot \Delta\theta}{\ln\left(\frac{R_{out}}{R_{in}}\right)} \tag{33}$$

$$\mathcal{P}_{tan} = \int_{R_{in}}^{R_{out}} \frac{\mu \cdot \Delta z \cdot dr}{(\Delta\theta \cdot r)} = \left(\frac{\mu \cdot \Delta z}{\Delta\theta}\right) \cdot \ln\left(\frac{R_{out}}{R_{in}}\right) \tag{34}$$

The appropriate lumped parameter representations of flux tubes corresponding to permanent magnets can be derived by analyzing the linear 2nd quadrant permanent magnet B-H curve shown in Figure 75 and the corresponding linear equation provided in (35), where $B_{PM}$ is the magnetic flux density in the permanent magnet, $H_{PM}$ is the magnetic field strength in the permanent magnet, $B_r$ is its remanence or residual flux density, $H_c$ is its coercivity, and $\mu_{PM}$ is its recoil permeability as defined in (36). Only radially magnetized permanent magnets, and thus only radially oriented flux tubes within permanent magnets,

are considered in this analysis; however, the same process can easily be extended to permanent magnets with tangential or axial magnetization components for analysis of other magnet configurations such as Halbach arrays or axially oriented systems. Rearranging (35) to express $H_{PM}$ as a function of $B_{PM}$ and substituting in (37), which describes the permanent magnet flux density at radius r within the flux tube in terms of the flux flowing in the tube, $\Phi_{PM}$, and the cross-sectional area of the tube at radius r, $A_{PM}(r)$, yields the relationship in (38). Integrating the expression in (38) along the flux path produces the result in (39) which defines the MMF drop across the length of the flux tube; however, the integral term on the right side of (39) is merely the radial reluctance of the flux tube as defined in (31) and (33), and the final term on the right side of (39) is the "injected" MMF ($\mathcal{F}_{inj}$) associated with the permanent magnet magnetization as defined in (40). Thus, the permanent magnet flux tube MMF drop defined in (39) can be compactly expressed in terms of the flux flowing through the tube, the reluctance of the tube, and the injected MMF associated with the permanent magnet magnetization as shown in (41). This expression corresponds to a circuit realization comprised of an MMF source connected in series with a reluctance, as shown in Figure 76(a). This circuit representation is analogous to a Thevenin equivalent circuit traditionally used in lumped electrical circuits. The expression in (41) can also be rearranged into the formulation in (42), which describes the flux flowing through the permanent magnet flux tube in terms of the MMF drop across the tube, the reluctance of the tube, and the injected flux associated with the permanent magnet magnetization as defined in (43). This expression corresponds to a circuit realization comprised of a flux source connected in parallel with a reluctance, as

shown in Figure 76(b). This circuit representation is analogous to a Norton equivalent circuit traditionally used in lumped electrical circuits. If a flux tube path overlaps with multiple permanent magnets, then a weighted algebraic average of the relevant permanent magnet magnetizations is used to determine the value of the corresponding injected MMF or flux source.

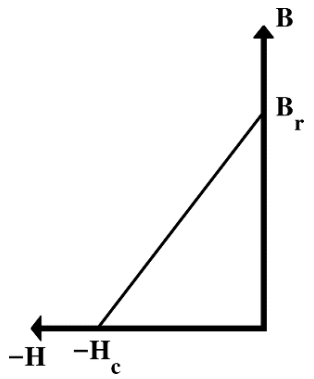


Figure 75. Linear 2nd Quadrant Permanent Magnet B-H Curve

$$B_{PM} = \mu_{PM} \cdot H_{PM} + B_r \tag{35}$$

$$\mu_{PM} = \frac{B_r}{H_c} \tag{36}$$

$$B_{PM}(r) = \frac{\Phi_{PM}}{A_{PM}(r)} \tag{37}$$

$$H_{PM}(r) = \frac{\Phi_{PM}}{\mu_{PM} \cdot A_{PM}(r)} - \frac{B_r}{\mu_{PM}} \tag{38}$$

$$\mathcal{F}_{PM} = \int_{R_{in}}^{R_{out}} H_{PM}(r) \cdot dr = \Phi_{PM} \cdot \int_{R_{in}}^{R_{out}} \left( \frac{dr}{\mu_{PM} \cdot A_{PM}(r)} \right) - \frac{B_r}{\mu_{PM}} \cdot (R_{out} - R_{in}) \tag{39}$$

$$\mathcal{F}_{inj} = -\frac{B_r}{\mu_{PM}} \cdot (R_{out} - R_{in}) \tag{40}$$

$$\mathcal{F}_{PM} = \Phi_{PM} \cdot \mathcal{R}_{rad} + \mathcal{F}_{inj} \tag{41}$$

$$\Phi_{PM} = \frac{\mathcal{F}_{PM}}{\mathcal{R}_{rad}} + \Phi_{inj} \tag{42}$$

$$\Phi_{inj} = \frac{\mathcal{F}_{inj}}{\mathcal{R}_{rad}} \tag{43}$$

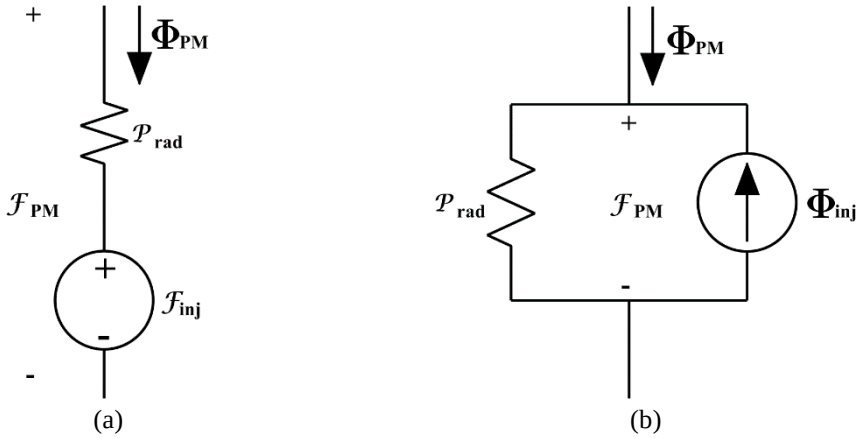


Figure 76. (a) Thevenin and (b) Norton Equivalent Circuit Representations of Radially Oriented Permanent Magnet Flux Tubes

## 7.3 Formation of the System of Equations

In a similar fashion to the use of Kirchhoff's current law in node voltage analysis of electrical circuits, application of Gauss's law for magnetism to each node cell in the MEC, such as the one shown in Figure 77, yields a node MMF equation of the form given in (44). For generality, Figure 77 and the node MMF equation in (44) describe a permanent magnet node cell; however, the flux source terms are simply set to zero in node cells that do not correspond to permanent magnets. The node MMF equation in (44) was developed using the reference definition of positive flux flow corresponding to flux flowing outward from the node. The first term on the left side is simply the product of the

sum of all permeances attached to the target node (node "x") and the MMF of the target node ($\mathcal{F}_x$). This term describes the effect of the target node's MMF in its own node MMF equation and it is has a positive permeance coefficient because it corresponds to flux flowing out of the target node. The subsequent terms on the left side of (44) correspond to each of the nodes in the MEC that are adjacent to the target node. Each of these terms is simply the product of the permeance connecting the corresponding adjacent node to the target node and the MMF of the adjacent node. These terms all have negative permeance coefficients because they correspond to flux flowing into the target node. The terms on the right side correspond to the algebraic sum of the injected flux sources flowing into the target node.

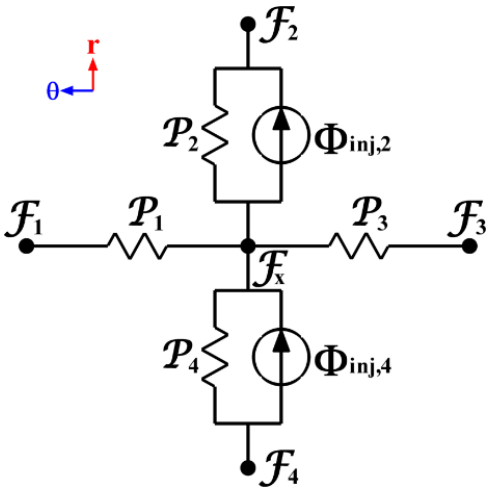


Figure 77. Annotated 2D Node Cell Schematic

$$(\mathcal{P}_1 + \mathcal{P}_2 + \mathcal{P}_3 + \mathcal{P}_4)\cdot\mathcal{F}_x - \mathcal{P}_1\cdot\mathcal{F}_1 - \mathcal{P}_2\cdot\mathcal{F}_2 - \mathcal{P}_3\cdot\mathcal{F}_3 - \mathcal{P}_4\cdot\mathcal{F}_4 = -\Phi_{inj,2} + \Phi_{inj,4} \quad (44)$$

In light of the analysis of a single 2D node cell, consider the MEC mesh distribution throughout the entire radial flux magnetic gear 2D cross-section. The radial

flux magnetic gear geometry shown in Figure 5 consists of 7 distinct annular radial regions: the HSR back iron, the HSR permanent magnets, the inner HSR air gap, the modulators, the outer LSR air gap, the LSR permanent magnets, and the LSR back iron. Each of these radial regions is meshed according to the previously described methodology depicted in Figure 73. The entire gear (each radial region) is divided into the same number of angular layers and each radial region is divided into an independently specified number of radial layers. The number of angular layers used throughout the gear, $N_{AL}$, and the number of radial layers used in each radial region ($N_{RL,HSBI}$, $N_{RL,HSPM}$, $N_{RL,HSAG}$, $N_{RL,Mods}$, $N_{RL,LSAG}$, $N_{RL,LSPM}$, and $N_{RL,LSBI}$) are all independent user controlled parameters, resulting in a total of 8 mesh discretization parameters for a 2D MEC model. Figure 78 illustrates the flux path network resulting from the application of a relatively coarse 2D MEC mesh to the full magnetic gear geometry, with 96 angular layers, 2 radial layers in the HSR back iron, 3 radial layers in the HSR permanent magnets, 2 radial layers in the HSR air gap, 4 radial layers in the modulators, 2 radial layers in the LSR air gap, 3 radial layers in the LSR permanent magnets, and 2 radial layers in the LSR back iron. The resulting nodes for this mesh distribution are indicated by the black dots in Figure 78. Figure 79 shows an example of the ladder MEC network resulting from an even coarser mesh overlaid on top of an unrolled linear representation of an overly simplistic magnetic gear geometry with $P_{HS} = 1$, $P_{LS} = 2$, and $Q_M = 3$ in the $\theta$-r plane. The corresponding nodes on the left and right edges of Figure 79 are connected by "wrap around" flux paths in accordance with the circular nature of the actual physical geometry and the MEC model implementation.

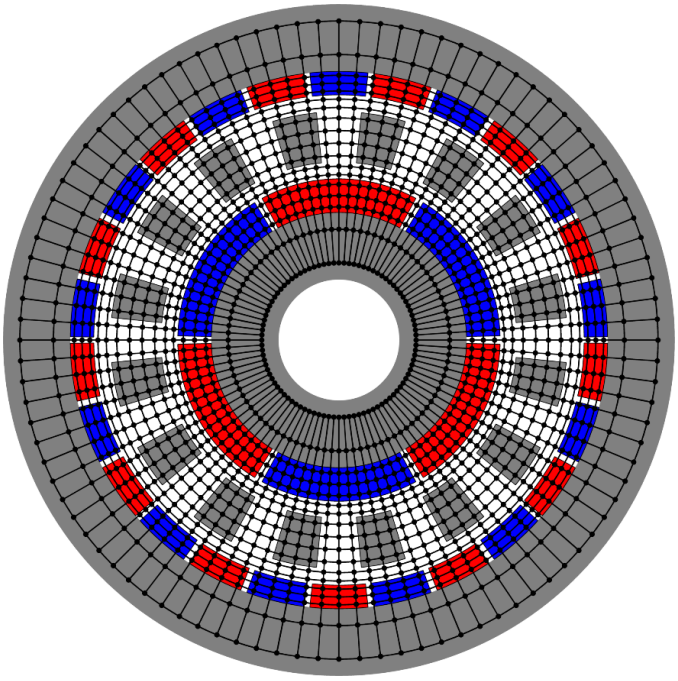

Figure 78. Example Radial Flux Magnetic Gear MEC Flux Path Network

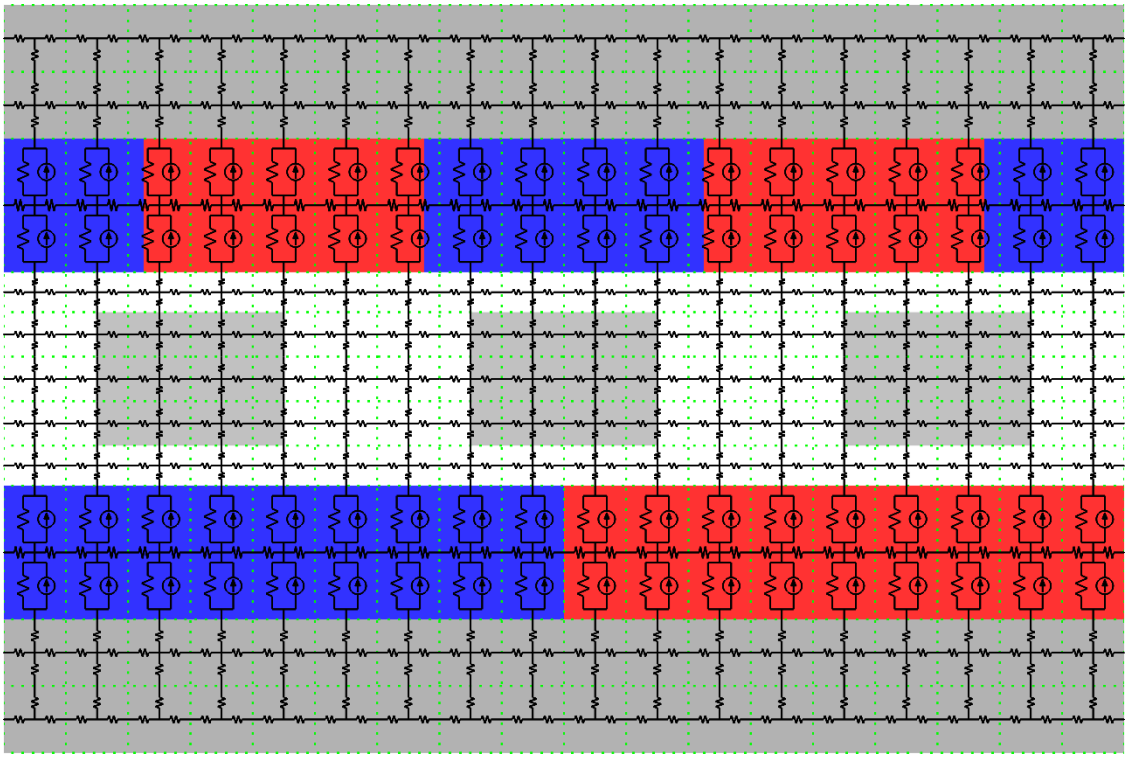

Figure 79. Example 2D MEC Schematic Overlay on Unrolled Radial Flux Magnetic Gear Geometry

Each node in the MEC corresponds to a node MMF equation of the same basic form as the one shown in (44) and there are $N_{2D}$ total nodes in a 2D MEC model, where $N_{2D}$ is the product of the number of angular layers, $N_{AL}$, and the total number of radial layers, $N_{RL}$, as indicated in (45) and (46). Thus, the resulting system of linear equations for the full 2D MEC model can be expressed in matrix form according to (47), where $\mathcal{P}_{2D}$ is the ($N_{2D}$ x $N_{2D}$) 2D system permeance matrix, $\mathcal{F}_{2D}$ is the ($N_{2D}$ x 1) column vector of unknown MMFs for each corresponding node in the 2D MEC, and $\Phi_{2D}$ is the ($N_{2D}$ x 1) column vector of the algebraic sums of the injected fluxes entering each corresponding node in the 2D MEC. The $i^{th}$ row in $\mathcal{P}_{2D}$ corresponds to the $i^{th}$ node in the MEC and contains the permeance coefficients for that node's MMF equation, such as those shown on the left side of (44). The $j^{th}$ column in $\mathcal{P}_{2D}$ also corresponds to the $j^{th}$ node in the MEC. Entry $\mathcal{P}_{2D(i,j)}$ in $\mathcal{P}_{2D}$ contains the permeance coefficient which describes the impact of the $j^{th}$ node's MMF on the $i^{th}$ node's MMF equation. Each diagonal entry $\mathcal{P}_{2D(i,i)}$ in $\mathcal{P}_{2D}$ contains the positive sum of all equivalent permeances attached directly to node i. The permeance coefficient of $\mathcal{F}_x$ in (44) is an example of what would become a diagonal entry in the matrix representation of the system of equations. These diagonal entries indicate the impact of the corresponding node's MMF on its own node MMF equation. Each off-diagonal entry $\mathcal{P}_{2D(i,j)}$ in $\mathcal{P}_{2D}$ (entries where $i \neq j$) contains the negative value of the equivalent permeance directly connecting nodes i and j. If there is no direct connection between nodes i and j (a permeance path that does not go through another node), then the corresponding entry in $\mathcal{P}_{2D}$ is zero. The permeance coefficients of $\mathcal{F}_1$, $\mathcal{F}_2$, $\mathcal{F}_3$, and $\mathcal{F}_4$ in

(44) are examples of what would become off-diagonal entries in the matrix representation of the system of equations.

$$N_{2D} = N_{AL} \cdot N_{RL} \tag{45}$$

$$N_{RL} = N_{RL,HSBI}+N_{RL,HSPM}+N_{RL,HSAG}+N_{RL,Mods}+N_{RL,LSAG}+N_{RL,LSPM}+N_{RL,LSBI} \tag{46}$$

$$\mathcal{P}_{2D}\mathcal{F}_{2D} = \Phi_{2D} \tag{47}$$

The overall 2D MEC permeance matrix, $\mathcal{P}_{2D}$, can be constructed in a general form with its constituent submatrices as shown in (48)-(50). The arrangement of these matrices is based on node numbering system used in the MEC model, in which the first $N_{AL}$ rows and the first $N_{AL}$ columns in $\mathcal{P}_{2D}$ correspond to nodes in the first radial layer, and the next $N_{AL}$ rows and the next $N_{AL}$ columns correspond to nodes in the second radial layer, and so on. The ($N_{AL}$ x $N_{AL}$) matrix $\mathcal{P}_{RL(k:k)}$ defined in (48) contains the permeance coefficients corresponding to nodes in the $k^{th}$ radial layer. Each diagonal entry $\mathcal{P}_{(k:k),(i:i)}$ in $\mathcal{P}_{RL(k:k)}$ contains the positive sum of all equivalent permeances attached directly to the node formed by the intersection of the $k^{th}$ radial layer and the $i^{th}$ angular layer. As indicated by (50), the diagonal entries in $\mathcal{P}_{RL(k:k)}$ are also the aforementioned diagonal entries of $\mathcal{P}_{2D}$. Each off-diagonal entry $\mathcal{P}_{(k:k),(i:j)}$ in $\mathcal{P}_{RL(k:k),}$ (entries where $i \neq j$) contains the negative value of the equivalent permeance directly connecting the node formed by the intersection of the $k^{th}$ radial layer and the $i^{th}$ angular layer and the node formed by the intersection of the $k^{th}$ radial layer and the $j^{th}$ angular layer. Because all permeances in the MEC are bidirectional, entry $\mathcal{P}_{(k:k),(i:j)}$ is always equal to entry $\mathcal{P}_{(k:k),(j:i)}$, thus each matrix $\mathcal{P}_{RL(k:k)}$ is symmetric.

$$\mathcal{P}_{RL(k:k)} = \begin{bmatrix} \mathcal{P}_{(k:k),(1:1)} & -\mathcal{P}_{(k:k),(1:2)} & 0 & \cdots & 0 & -\mathcal{P}_{(k:k),(1:N_{AL})} \\ -\mathcal{P}_{(k:k),(2:1)} & \mathcal{P}_{(k:k),(2:2)} & -\mathcal{P}_{(k:k),(2:3)} & 0 & \cdots & 0 \\ 0 & -\mathcal{P}_{(k:k),(3:2)} & \ddots & \ddots & \ddots & \vdots \\ \vdots & 0 & \ddots & \ddots & \ddots & 0 \\ 0 & \vdots & \ddots & \ddots & \ddots & -\mathcal{P}_{(k:k),(N_{AL}-1:N_{AL})} \\ -\mathcal{P}_{(k:k),(N_{AL}:1)} & 0 & \cdots & 0 & -\mathcal{P}_{(k:k),(N_{AL}:N_{AL}-1)} & \mathcal{P}_{(k:k),(N_{AL}:N_{AL})} \end{bmatrix} \tag{48}$$

$$\mathcal{P}_{RL(k:k-1)} = \mathcal{P}_{RL(k-1:k)} = \begin{bmatrix} \mathcal{P}_{(k:k-1),(1:1)} & 0 & \cdots & 0 \\ 0 & \mathcal{P}_{(k:k-1),(2:2)} & \ddots & \vdots \\ \vdots & \ddots & \ddots & 0 \\ 0 & \cdots & 0 & \mathcal{P}_{(k:k-1),(N_{AL}:N_{AL})} \end{bmatrix} \tag{49}$$

$$\mathcal{P}_{2D} = \begin{bmatrix} \mathcal{P}_{RL(1:1)} & -\mathcal{P}_{RL(1:2)} & 0 & \cdots & 0 \\ -\mathcal{P}_{RL(2:1)} & \mathcal{P}_{RL(2:2)} & -\mathcal{P}_{RL(2:3)} & \ddots & \vdots \\ 0 & -\mathcal{P}_{RL(3:2)} & \ddots & \ddots & 0 \\ \vdots & \ddots & \ddots & \ddots & -\mathcal{P}_{RL(N_{RL}-1:N_{RL})} \\ 0 & \cdots & 0 & -\mathcal{P}_{RL(N_{RL}:N_{RL}-1)} & \mathcal{P}_{RL(N_{RL}:N_{RL})} \end{bmatrix} \tag{50}$$

The ($N_{AL}$ x $N_{AL}$) matrix $\mathcal{P}_{RL(k:k-1)}$ defined in (49) contains the permeances corresponding to paths directly connecting nodes in the $k^{th}$ radial layer to adjacent nodes

in radial layer k-1. Each diagonal entry $\mathcal{P}_{(k:k-1),(i:i)}$ in $\mathcal{P}_{RL(k:k-1)}$ contains the equivalent permeance directly connecting the $i^{th}$ node in the $k^{th}$ radial layer (which is the node formed by the intersection of the $k^{th}$ radial layer and the $i^{th}$ angular layer) to the $i^{th}$ node in radial layer k-1. All other entries in $\mathcal{P}_{RL(k:k-1)}$ are zero. Because all permeances in the MEC are bidirectional, the matrix $\mathcal{P}_{RL(k-1:k)}$ is always equal to the matrix $\mathcal{P}_{RL(k:k-1)}$. $\mathcal{P}_{2D}$, is then constructed from these constituent submatrices, as shown in (50). Additionally, because each matrix $\mathcal{P}_{RL(k:k)}$ is symmetric, and each diagonal matrix $\mathcal{P}_{RL(k-1:k)}$ is always equal to the matrix $\mathcal{P}_{RL(k:k-1)}$, the matrix $\mathcal{P}_{2D}$ is always symmetric.

Each node in the 2D MEC has four adjacent nodes: one on the radial inside, one on the radial outside, one on the clockwise circumferential side, and one on the counterclockwise circumferential side. The only exceptions to this rule are the nodes in the innermost radial layer, which do not have any adjacent nodes on the radial inside, and the nodes in the outermost radial layer, which do not have any adjacent nodes on the radial outside. In light of this observation and close inspection of the matrices defined in (48)-(50), it is evident that each row in $\mathcal{P}_{2D}$ corresponding to a node in the first or last radial layers has four non-zero entries and all other rows corresponding to intermediate radial layer nodes have five non-zero entries, one for each adjacent node, as well as the diagonal entry in each row. Thus, $N_{NZ2D}$, the total number of non-zero entries in $\mathcal{P}_{2D}$, is given by (51) and the sparseness of $\mathcal{P}_{2D}$ (the percentage of its entries which are zeros) can be calculated according to (52). This expression indicates that MEC models with reasonable mesh resolutions correspond to extremely sparse permeance matrices; therefore, the

MATLAB implementation of the MEC model stores $\mathcal{P}_{2D}$ as a sparse matrix in order to dramatically reduce the requisite amount of memory used by the program.

$$N_{NZ2D} = N_{AL} \cdot (5 \cdot N_{RL} - 2) \tag{51}$$

$$\text{Sparseness of } \mathcal{P}_{2D} = \left(1 - \frac{N_{NZ2D}}{N_{2D}^2}\right) \cdot 100\% \tag{52}$$

### 7.4 Solution of the System of Equations

The 2D MEC model is "solved" by solving the linear system of equations given in (47) for the $N_{2D}$ unknown node MMFs in the column vector $\mathcal{F}_{2D}$. If the 2D MEC model has symmetry, then it can be analyzed by solving the subset of equations corresponding to nodes in a symmetrical fraction of the model and extending that solution to the remaining symmetrical fraction(s). Additionally, because MMF values represent scalar potentials with respect to a reference node, in full 2D MEC models or fractional models with even symmetry, the first node is defined as the zero potential reference for the rest of the system. This makes the first node equation redundant, allowing the first row of $\mathcal{P}_{2D}$ and $\Phi_{2D}$ to be eliminated. Furthermore, because the first node has zero potential, the first column of $\mathcal{P}_{2D}$ is eliminated, and the remaining system can be solved. However, for models with odd symmetry, it is desirable for corresponding nodes in adjacent fractions of the model to have potentials with the same magnitudes and opposite signs. This choice effectively determines the zero potential reference, which may not correspond to any of the nodes. Thus, for models with odd symmetry, the first row of $\mathcal{P}_{2D}$ and $\Phi_{2D}$ and the first column of $\mathcal{P}_{2D}$ must not be eliminated before the system is solved.

In theory, the textbook solution to the system can be obtained by inverting the appropriate part of the system permeance matrix, $\mathcal{P}_{2D}$', as shown in (53), where $\mathcal{P}_{2D}$', $\mathcal{F}_{2D}$', and $\Phi_{2D}$' represent the relevant portions of $\mathcal{P}_{2D}$, $\mathcal{F}_{2D}$, and $\Phi_{2D}$ based on the application of the preceding discussion of symmetry and the reference node. However, most practical MEC models with adequate mesh resolution result in system permeance matrices which would require a relatively enormous amount of time and memory to invert; therefore, the MATLAB implementation of the MEC model solves the system by factorizing $\mathcal{P}_{2D}$' and solving the corresponding triangular systems as described in [145]. The use of sparse matrices and an optimal factorization method dramatically decreases the amount of memory and simulation run time required to solve an MEC model.

$$\mathcal{F}_{2D}' = (\mathcal{P}_{2D}')^{-1}\Phi_{2D}' \tag{53}$$

Once an MEC model has been "solved" for the vector of node MMFs, this information can be used along with the reluctances of the flux tubes to calculate various other quantities of interest, such as the flux in any flux tube and the flux density at any position in the gear. Due to their coarse flux tube distributions, many of the other MEC models described in the literature, including most of the few prior magnetic gear MEC studies [97, 141-143], use the virtual work (co-energy) method to calculate torque; however, this implementation uses Maxwell stress tensors for torque calculations from the more detailed solutions provided by its higher resolution flux tube distributions. In particular, the torque on the HSR, $\tau_{HSR}$, and the torque on the LSR, $\tau_{LSR}$, are calculated using Maxwell stress tensors according to (14) and (15), which are listed again below for

convenience. $R_{HSAG}$ and $R_{LSAG}$ represent the radii of the integration paths in the high speed air gap and low speed air gap, while $B_r$ and $B_\theta$ represent the radial and tangential components of the magnetic flux density, which are both functions of the position in the gear. The torque on the entire modulator structure, $\tau_{Mods}$ is then given by (16).

$$\tau_{HSR} = \left(\frac{R_{HSAG}^2}{\mu_0}\right) \cdot \int_0^{2\pi} B_r(R_{HSAG},\theta) \cdot B_\theta(R_{HSAG},\theta) \cdot d\theta \tag{14}$$

$$\tau_{LSR} = -\left(\frac{R_{LSAG}^2}{\mu_0}\right) \cdot \int_0^{2\pi} B_r(R_{LSAG},\theta) \cdot B_\theta(R_{LSAG},\theta) \cdot d\theta \tag{15}$$

$$\tau_{Mods} = -(\tau_{HSR} + \tau_{LSR}) \tag{16}$$

# 8. EVALUATION OF THE RADIAL FLUX MAGNETIC GEAR 2D MAGNETIC EQUIVALENT CIRCUIT MODEL

## 8.1 Impact of Non-Linearity and Discretization

The radial flux magnetic gear 2D MEC model implementation presented in the previous section introduced 8 different independent discretization parameters which are summarized in Table 17, as well as the fundamental simplifying assumption of linear, fixed permeability B-H characteristics in the modulators and rotor back irons. Before applying the MEC to design problems, it is critical to characterize the impact of the linearity assumption and various mesh discretization parameters on the model accuracy. This step is neglected in many MEC studies which rely on a fixed, coarse lumped element distribution as opposed to a fully parameterized network of lumped elements. Table 18 summarizes three different magnetic gear "base designs" selected for this analysis. All gear designs evaluated in this section use NdFeB N42 magnets and M47 electrical steel for the modulators and back irons. As discussed in Sections 5 and 6, $G_r$ represents the approximate (nearest integer) desired gear ratio, assuming that the modulators are fixed and the low speed rotor rotates. The values of $G_r$ and $P_{HS}$ set the value of $P_{LS}$ according to (24). This keeps the number of modulators even, which results in symmetrical cancellation of the net forces on each rotor and maintains a relatively high LCM between $P_{HS}$ and $P_{LS}$, thus reducing the gear's torque ripple [26]. In addition to the parameters specified in Table 18, all permanent magnet pole arcs were set equal to the corresponding pole pitches, resulting in 100% angular fill factors for each magnet pole. All modulator

pole arcs were set equal to half of the corresponding modulator pole pitches, resulting in 50% angular fill factors, or equally distributed modulator pieces and modulator slots. Figures 5 and 7 illustrate these additional design conditions. The base designs listed in Table 18 were specifically chosen to provide a relatively broad and diverse, albeit limited sampling of somewhat reasonable gear configurations in order not to bias the results. Furthermore, these designs are not necessarily intended to be optimal in any way.

Table 17. Radial Flux Magnetic Gear 2D MEC Discretization Parameters

| Parameter | Description |
|---|---|
| $N_{AL}$ | Number of angular layers |
| $N_{RL,HSBI}$ | Number of radial layers in the high speed rotor back iron |
| $N_{RL,HSPM}$ | Number of radial layers in the high speed rotor magnets |
| $N_{RL,HSAG}$ | Number of radial layers in the high speed rotor air gap |
| $N_{RL,Mods}$ | Number of radial layers in the modulators |
| $N_{RL,LSAG}$ | Number of radial layers in the low speed rotor air gap |
| $N_{RL,LSPM}$ | Number of radial layers in the low speed rotor magnets |
| $N_{RL,LSBI}$ | Number of radial layers in the low speed rotor back iron |

Table 18. Radial Flux Magnetic Gear Base Designs for MEC Model Evaluation

| Parameter | Description | Base Design 1 | Base Design 2 | Base Design 3 | Units |
|---|---|---|---|---|---|
| $G_r$ | Nearest integer gear ratio | 4 | 8 | 16 | |
| $P_{HS}$ | HSR pole pairs | 11 | 4 | 6 | |
| $R_{Out}$ | Gear active outer radius | 150 | 175 | 200 | mm |
| $T_{HSBI}$ | HSR back iron thickness | 20 | 35 | 40 | mm |
| $T_{HSPM}$ | HSR magnet thickness | 9 | 5 | 13 | mm |
| $T_{HSAG}$ | HSR air gap thickness | 0.5 | 2 | 1 | mm |
| $T_{Mods}$ | Modulator thickness | 11 | 17 | 14 | mm |
| $T_{LSAG}$ | LSR air gap thickness | 0.5 | 2 | 1 | mm |
| $T_{LSPM}$ | LSR magnet thickness | 7 | 5 | 7 | mm |
| $T_{LSBI}$ | LSR back iron thickness | 20 | 30 | 25 | mm |

$$P_{LS} = \begin{cases} G_r \cdot P_{HS} + 1 & \text{for } (G_r+1)\cdot P_{HS} \text{ odd} \\ G_r \cdot P_{HS} + 2 & \text{for } (G_r+1)\cdot P_{HS} \text{ even} \end{cases} \quad (24)$$

Before addressing the effects of the discretization parameters, the impact of the linear ferromagnetic material assumption was evaluated by sweeping the constant relative permeability of the material (used in both rotor back irons and the modulators) from 10 to 4000 and evaluating the resulting LSR stall torque predicted by the MEC model at each point for all three of the base designs. Unless otherwise specified, all results used in the evaluation of the MEC model are based on the LSR stall torque; however, the modulator assembly stall torque could also be used and the trends would be identical with proportionally higher torque and torque density values. Each simulation case in the permeability sweep was evaluated using the same extremely tight (and extremely inefficient) mesh for all base designs, with 4000 angular layers and 30 radial layers in each of the 7 radial regions. The results of the permeability sweep study are illustrated in Figure 80, which shows the variation in the percentage match between the LSR stall torque predicted by the MEC model at each constant permeability setting and the LSR stall torque predicted for the corresponding base design by an ANSYS Maxwell FEA model using nonlinear M47 steel B-H characteristics for the modulators and both rotor back irons.

The data depicted in Figure 80 suggests two key results. First, the approximation of linearity is valid for the three base designs. Second, as long as the value selected for the relative permeability of the ferromagnetic material is above a certain minimum setting (in this case approximately 500), it has little bearing on the torque rating predicted by the MEC model. As previously suggested, this is true because the linear reluctances of the two sets of permanent magnets and the two air gaps dwarf the non-linear reluctances of the back irons and modulators for most practical ideal designs. Based on this information,

the relative permeability of the ferromagnetic material was set to 3000 for all following MEC model studies. The results in Figure 80 also indicate that the MEC model is extremely accurate for the three base designs with the selected discretization settings. As the relative permeability increases, the MEC model asymptotically approaches torque prediction matches of 101%, 99.95%, and 99.8% for each of these designs. These accuracies are well within the margins of error for FEA modeling tools and the uncertainties resulting from realistic manufacturing practices.

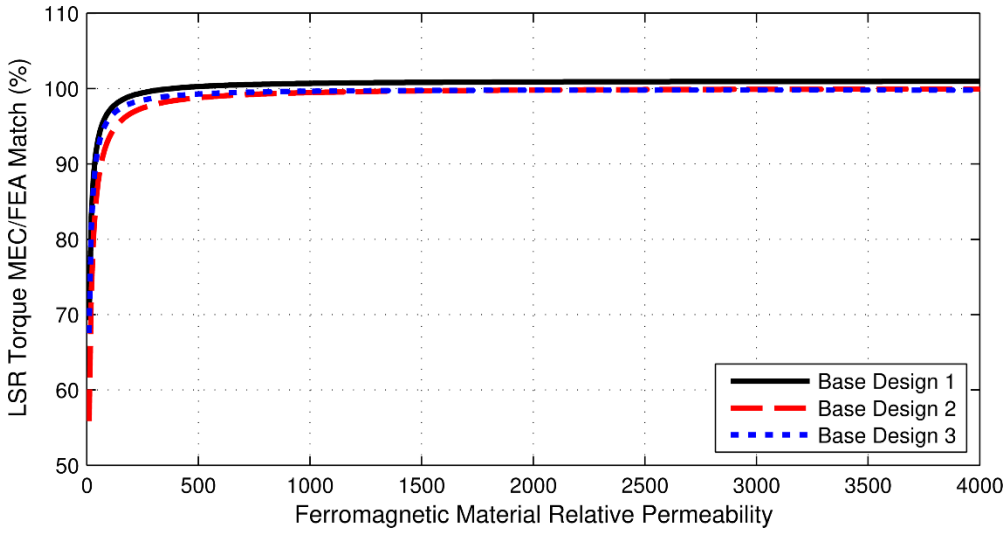


Figure 80. Impact of Linear Ferromagnetic Material Relative Permeability on the MEC Model Accuracy

In an ideal model, the eight discretization parameters summarized in Table 17 would all be set to infinitely high values, resulting in infinitely small MEC node cells which accurately capture every detail (except for any nonlinearity) of a given design. Unfortunately, this is obviously impractical as it would also result in infinitely long simulation run times which require an infinite amount of computational power. As a result, it is necessary to study the impact of each discretization parameter and determine

the appropriate set of values to use for each of these variables in order to achieve the optimal tradeoff between model accuracy and speed.

The first discretization parameter considered in this analysis is the number of angular layers. In order to evaluate the impact of this variable on the MEC model's accuracy, the number of angular layers was swept from 50 to 8000 in steps of 25 and the MEC torque prediction was evaluated at each setting for each base design. Each simulation case in the angular layer sweep used a relatively tight (and again extremely inefficient) mesh of 18 radial layers in each of the gear's 7 radial regions. Figure 81(a) shows the results of the angular layer sweep. This information indicates that the MEC converges to an extremely accurate torque prediction for each of the three base designs, asymptotically approaching matches of 101%, 100.2%, and 100.7%, respectively.

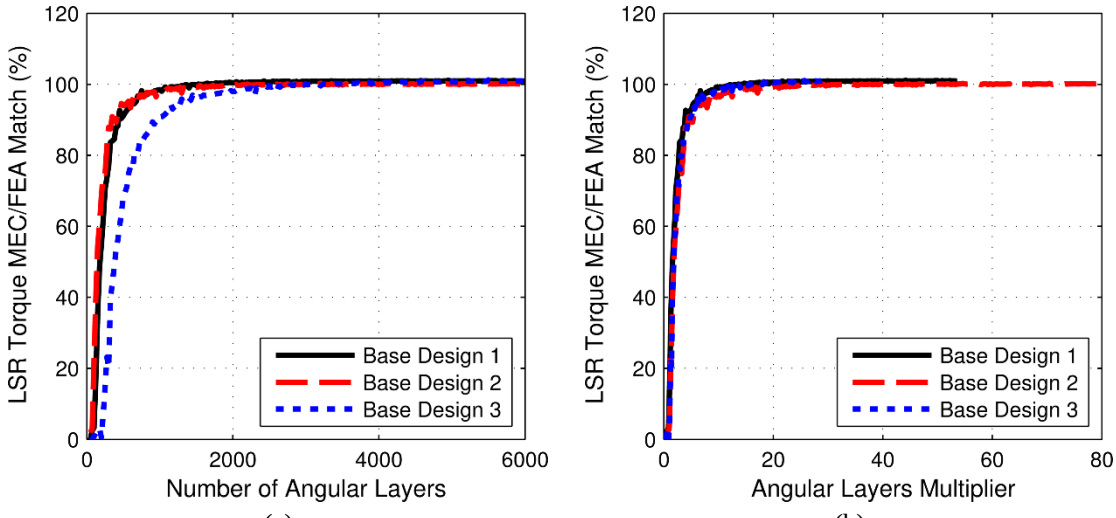


Figure 81. Variation of MEC Model Accuracy with (a) the Number of Angular Layers and (b) the Angular Layers Multiplier

The data in Figure 81(a) also illustrates that the torque predicted by the MEC model increases as the number of angular layers increases. A much wider set of designs

were evaluated during the MEC model development and this pattern remained true in every case. In general, the variation of the MEC model's torque prediction with changes in discretization settings is related to changes in how accurately the different settings capture the harmonic field content and leakage flux for a given design. The exact natures of the changes are dictated by the relative significances of each of these characteristics for a given design.

Unfortunately, the results in Figure 81(a) also indicate that the torque predictions for the different designs converge to the correct values at widely varying angular layer counts. This is an undesirable characteristic, because using a fixed number of angular layers to evaluate a wide range of designs may bias the results toward a certain subset of designs. One way to overcome this problem is to use a large constant number of angular layers for all designs, but this approach is not ideal as it will result in excessive amounts of angular layers for many designs and unnecessarily slower simulation run times. An alternate strategy employed in this study is to set the number of angular layers used in the MEC model based on the number of modulators in a given design. This is accomplished by using the angular layers multiplier (ALM), defined in (54), which is the number of angular layers per modulator-slot pair. This approach was selected because the modulators are the features with the smallest tangential width in every design and the number of modulators is the sum of the number of pole pairs on both rotors. Figure 81(b) shows the same information as Figure 81(a), but the horizontal axis indicates the angular layers multiplier value for each point instead of the number of angular layers. This graph demonstrates that the MEC model torque predictions for all three base designs converge

to the correct values at approximately the same rate with respect to angular layers multiplier values, which is the desired effect. During the MEC model development, this trend was evaluated over a much larger design set and proved to be very consistent, although there is some small variation in the necessary angular layers multiplier based on other design features besides the number of modulators. Furthermore, the angular layers multiplier convergence trends proved to be largely independent, within reason, of the number of radial layers used in each radial region.

$$ALM = \frac{N_{AL}}{2 \cdot Q_M} \tag{54}$$

In order to evaluate the relative impacts of the number of radial layers in each radial region, each of these 7 discretization parameters was independently swept from 1 to 40 radial layers while all other radial layer parameters were each fixed at 12 radial layers. An angular layers multiplier of 20 was used for each simulation case. The results for all radial layer parameters are shown for each base design in Figures 82(a), 82(b), and 82(c), respectively. The different curves in each graph correspond to the different radial layer parameters (the different radial regions) and the horizontal axis indicates the number of radial layers used in the specified radial region. For all three designs, the number of radial layers in the LSR magnets and the modulators are easily the most important parameters. Additionally, the number of HSR PM layers can also have a less significant, but still notable impact for some designs. The number of radial layers in either air gap consistently has an extremely limited impact and the number of layers in either back iron region has essentially no impact, which is not surprising given the trends in Figure 80.

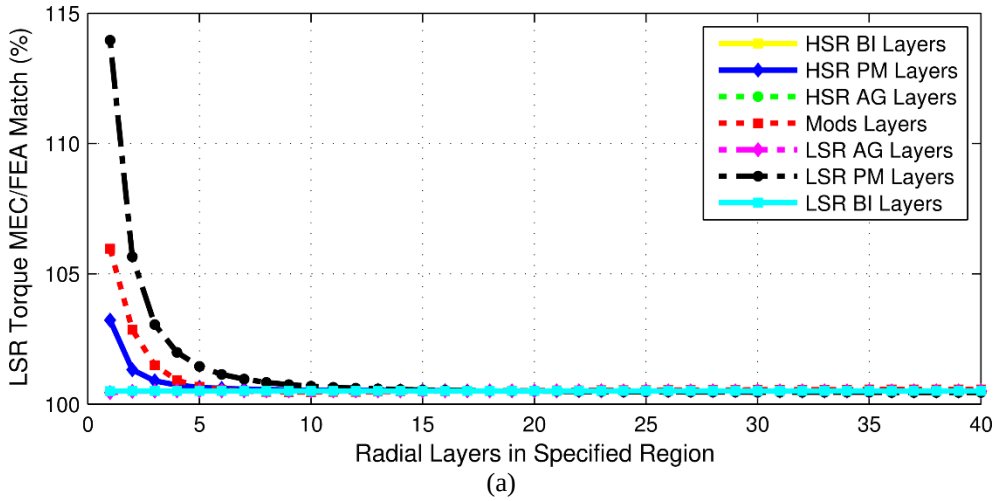


(a)

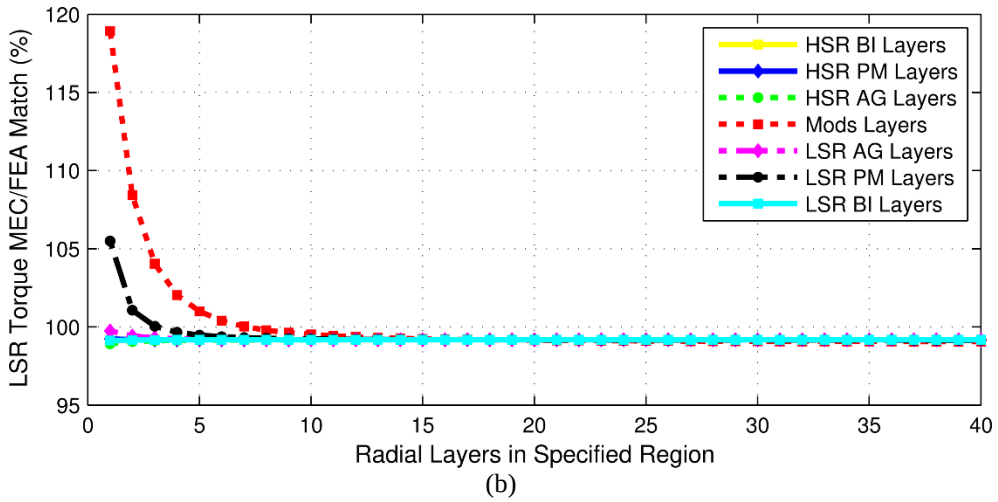


(b)

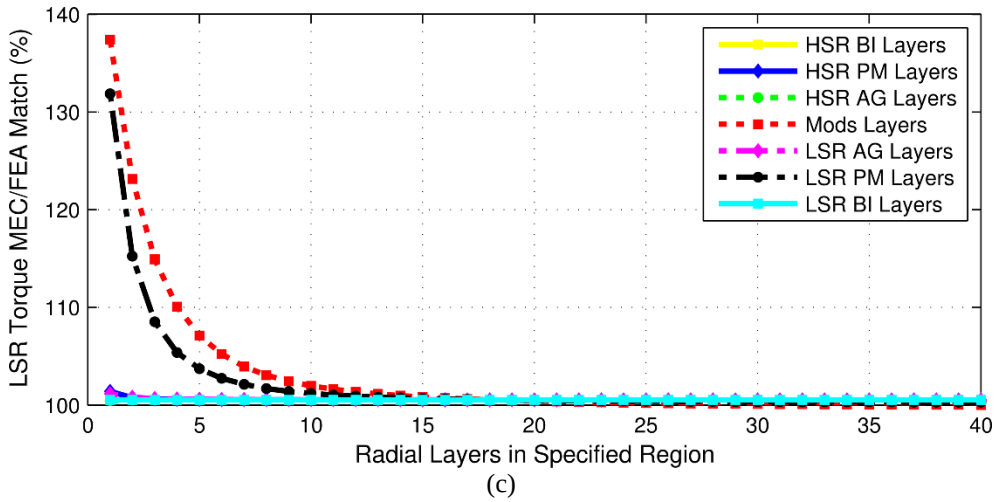


(c)

Figure 82. Variation of MEC Model Accuracy with the Number of Radial Layers in Each Radial Region for (a) Base Design 1, (b) Base Design 2, and (c) Base Design 3

All of the data shown in Figure 82 indicates that increasing the number of radial layers tends to decrease the model's torque predictions, and this is likely due to corresponding increases in the accuracy of the model's leakage flux characterizations. However, there are some designs for which increasing the number of radial layers in certain regions, such as the modulators, actually raises the torque predictions slightly. The exact effect of changing any of the discretization parameter values depends heavily on the relative significances of a plethora different factors in any given design.

Just as the torque predictions for the models of the different base designs converge to the correct answers at different angular layer settings, the data in Figure 82 demonstrates that they also converge to the correct answers at different radial layer settings. The graph in Figure 83(a) shows the impact of the LSR permanent magnet radial layers on the MEC torque prediction for all 3 base designs to further highlight these differences. Note that the torque values for each point in any one curve are normalized by the torque value associated with the last point in that curve to appropriately scale the graph and determine the values at which further increasing the number of radial layers ceases to cause a significant change in the model's torque predictions. In order to eliminate the issue of these differing convergence rates, the LSR permanent magnet radial layers multiplier, $RLM_{LSPM,}$ defined in (55), was developed to select the number of LSR permanent magnet region radial layers based on the pole arc and radial thickness of the magnets. Decreasing the LSR magnet pole arc and increasing the LSR magnet radial thickness both tend to increase the amount of leakage flux in this region of the gear, which also means that more radial layers are required in this region to accurately characterize the field solution. Using

the relationship defined in (55) with a fixed LSR permanent magnet radial layers multiplier value overcomes these differing convergence rates. Figure 83(b) shows the same information as Figure 83(a), but the horizontal axis indicates the LSR permanent magnet radial layers multiplier value for each point instead of the number of LSR permanent magnet radial layers. This graph demonstrates that the MEC model torque predictions for all three base designs converge to the correct values at approximately the same rate with respect to LSR permanent magnet radial layers multiplier values, which is the desired effect. During the MEC model development, this trend was also evaluated over a much larger design set and proved to be very consistent.

$$RLM_{LSPM} = \frac{\text{LSR PM Average Pole Arc}}{\text{LSR PM Radial Layer Thickness}} = \frac{\text{LSR PM Average Pole Arc}}{\left(\frac{T_{LSPM}}{N_{RL,LSPM}}\right)} \qquad (55)$$

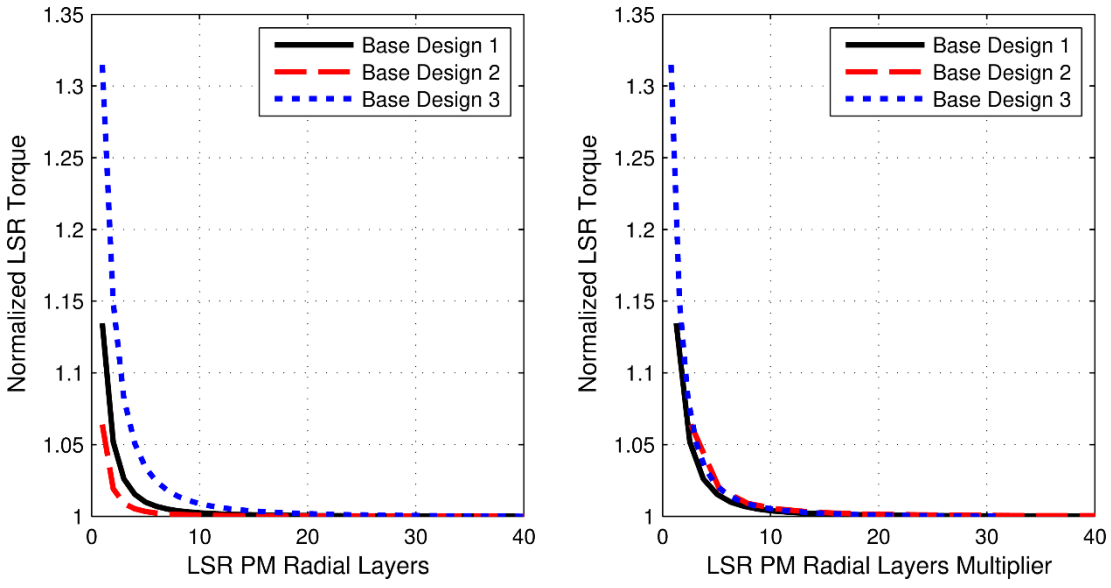


(a) (b)

Figure 83. Variation of the MEC Model Accuracy with (a) the Number of LSR PM Radial Layers and (b) the LSR PM Radial Layers Multiplier

A modulators radial layers multiplier, $RLM_{Mods}$, and an HSR permanent magnet radial layers multiplier, $RLM_{HSPM}$, are also similarly defined for their respective regions in (56) and (57). The graph in Figure 84(a) shows the normalized MEC model torque predictions for the 3 base designs as functions of the number of radial layers in the modulator region, while the graph in Figure 84(b) depicts the same normalized torque predictions as functions of the modulators radial layers multiplier. A comparison of these two graphs demonstrates that the while the modulators radial layers multiplier is not as effective of a discretization control parameter as the LSR permanent magnet radial layers multiplier, it is an improvement over simply using a constant number of radial layers in the modulator region. Finally, Figures 85(a) and 85(b) show the corresponding set of graphs for the radial layers in the HSR permanent magnet region and the HSR permanent magnet radial layers multiplier. Although the amount of radial layers used in the HSR permanent magnet region does not have as large of an effect on the MEC model's torque predictions as the amounts of layers in the LSR permanent magnets and the modulators, the HSR permanent magnet radial layers multiplier clearly serves as an effective uniform means of controlling the discretization setting in this region.

$$RLM_{Mods} = \frac{\text{Modulator Average Pole Arc}}{\left(\frac{T_{Mods}}{N_{RL,Mods}}\right)} \tag{56}$$

$$RLM_{HSPM} = \frac{\text{HSR PM Average Pole Arc}}{\left(\frac{T_{HSPM}}{N_{RL,HSPM}}\right)} \tag{57}$$

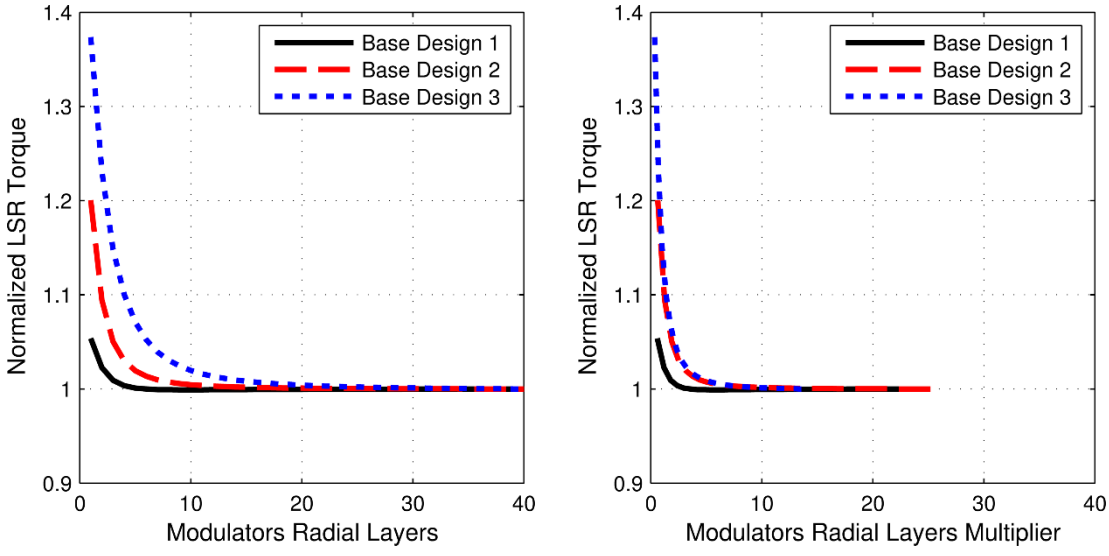


Figure 84. Variation of the MEC Model Accuracy with (a) the Number of Modulators Radial Layers and (b) the Modulators Radial Layers Multiplier

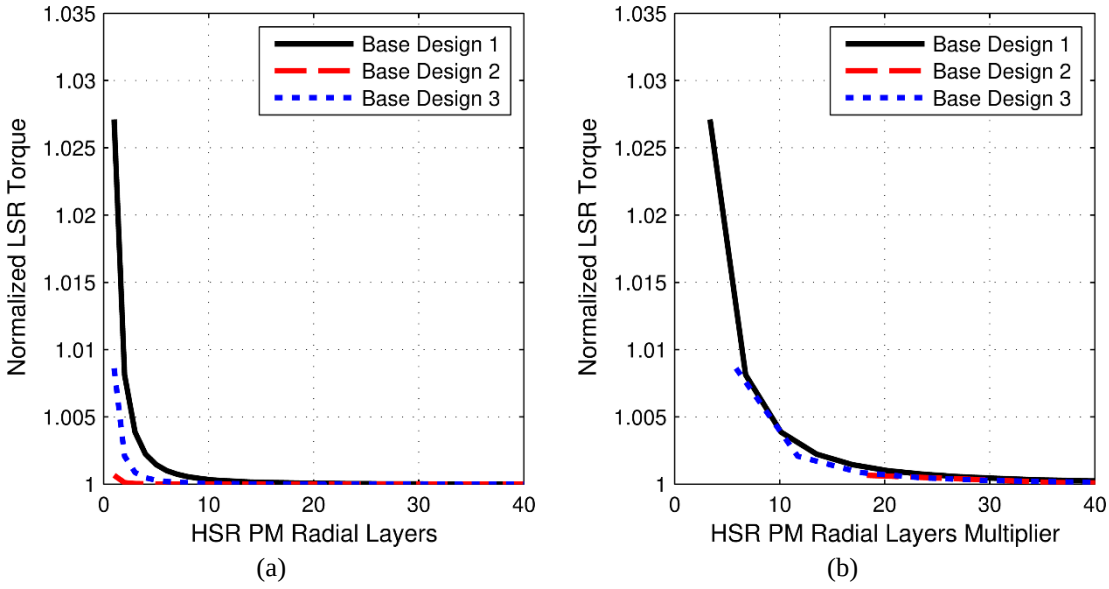


Figure 85. Variation of the MEC Model Accuracy with (a) the Number of HSR PM Radial Layers and (b) the HSR PM Radial Layers Multiplier

Despite the limited impact of the amount of radial layers in the air gaps, an HSR air gap radial layers multiplier, $RLM_{HSAG}$, and an LSR air gap radial layers multiplier,

$RLM_{LSAG}$, are also defined in (58) and (59), respectively. Because the amounts of radial layers in the back irons have essentially no impact on the torque predicted by the MEC model for most designs, simple constant small amounts of radial layers are used in these regions.

$$RLM_{HSAG} = \frac{\text{HSR PM Pole Arc in HSR Air Gap}}{\left(\frac{T_{HSAG}}{N_{RL,HSAG}}\right)} \tag{58}$$

$$RLM_{LSPM} = \frac{\text{LSR PM Pole Arc in LSR Air Gap}}{\left(\frac{T_{LSAG}}{N_{RL,LSAG}}\right)} \tag{59}$$

## 8.2 Comparison of MEC and FEA Model Flux Density Predictions

The preceding section evaluated the accuracy of the MEC model based solely on the accuracy of its torque predictions relative to those of the nonlinear FEA model. It is also beneficial to compare the flux density distributions predicted by the two models. Figures 86-92 show the radial flux density distributions predicted by the FEA and MEC models along circular paths in the radial middle of each of the 7 radial regions in the gear for all 3 base designs. Similarly, Figures 93-99 show the tangential flux density distributions predicted by the FEA and MEC models along the same paths for all 3 base designs. These results demonstrate that the MEC model also produces extremely accurate flux density distributions which correctly characterize the magnetic gear's rich spatial flux harmonic content in all regions except for the rotor back irons. Even in the rotor back irons, the flux density distributions are still fairly accurate for these base designs despite the assumption of linear ferromagnetic material B-H characteristics.

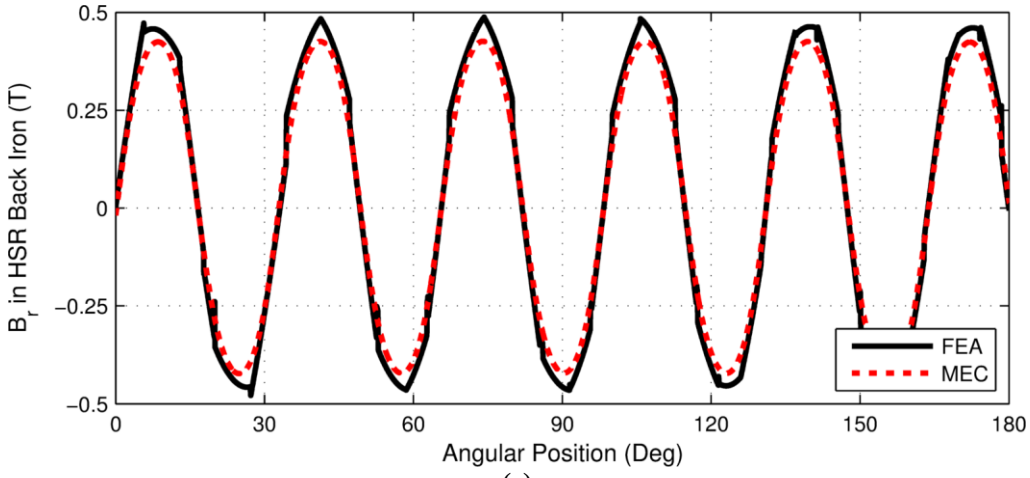


(a)

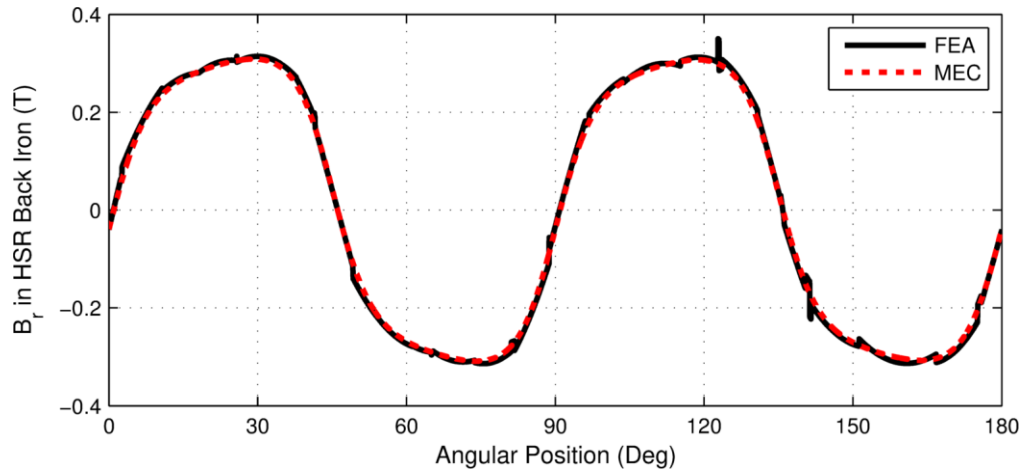


(b)

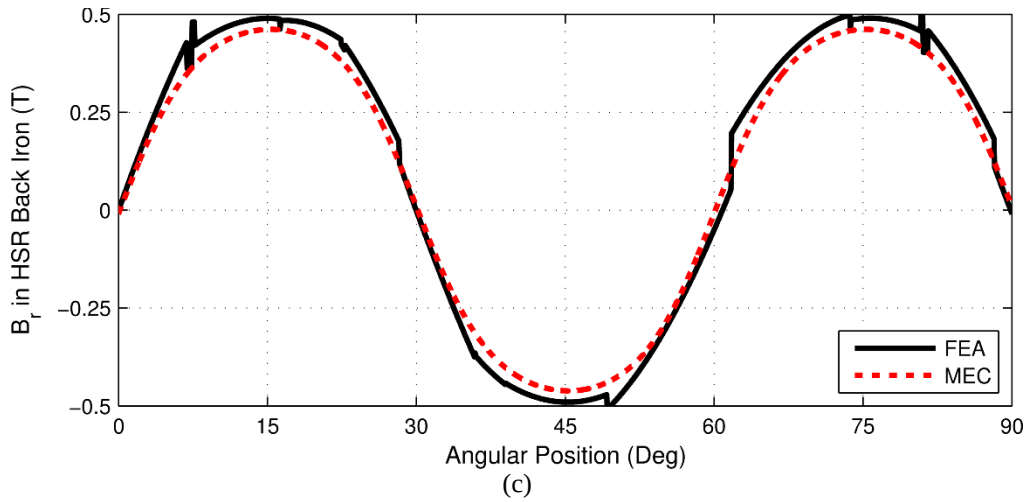


(c)

Figure 86. Radial Flux Density Along a Circular Path in the Radial Middle of the HSR Back Iron of (a) Base Design 1, (b) Base Design 2, and (c) Base Design 3

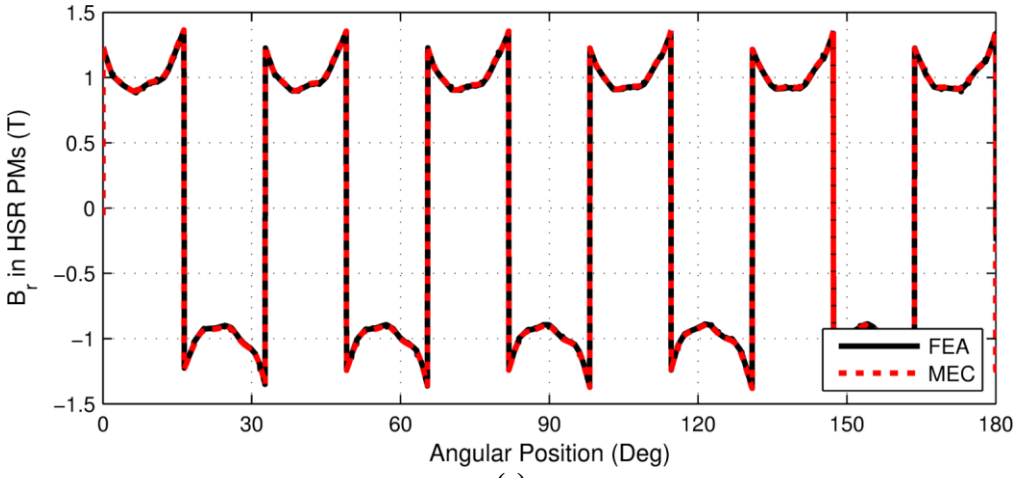


(a)

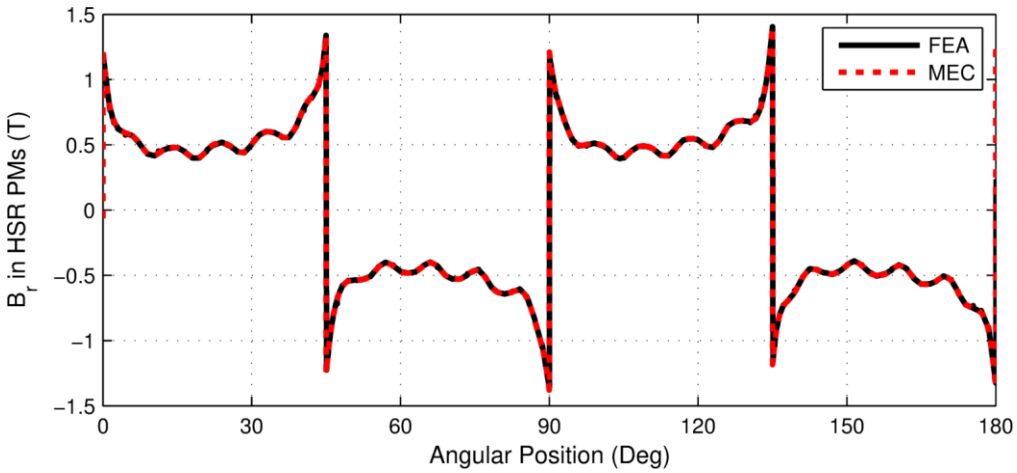


(b)

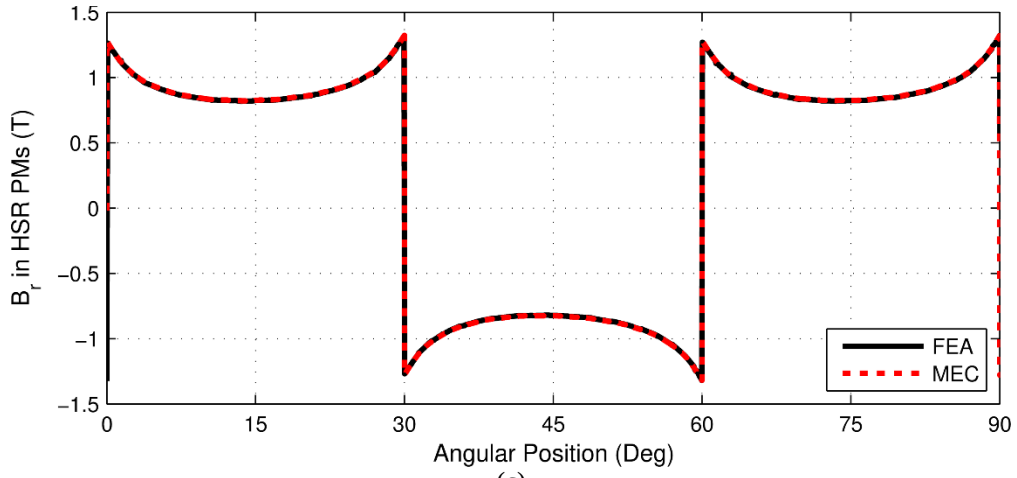


(c)

Figure 87. Radial Flux Density Along a Circular Path in the Radial Middle of the HSR Permanent Magnets of (a) Base Design 1, (b) Base Design 2, and (c) Base Design 3

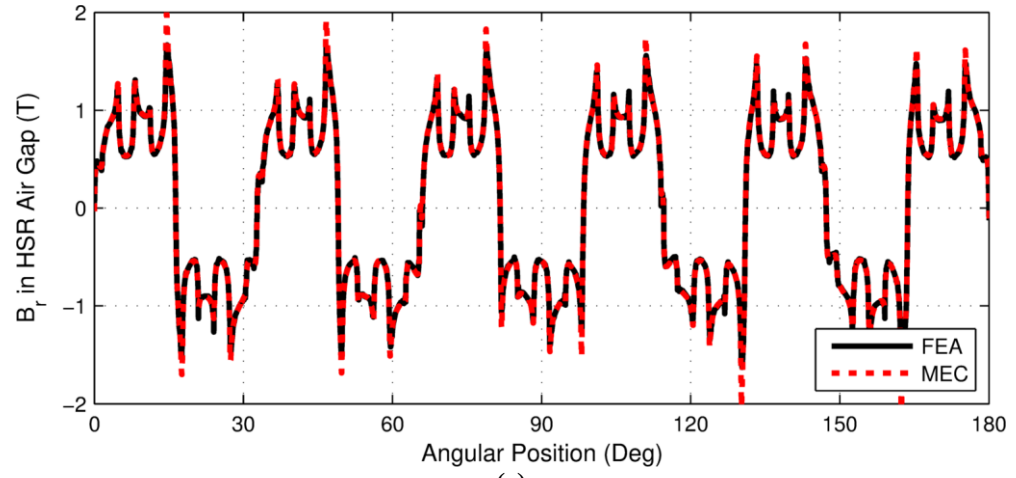


(a)

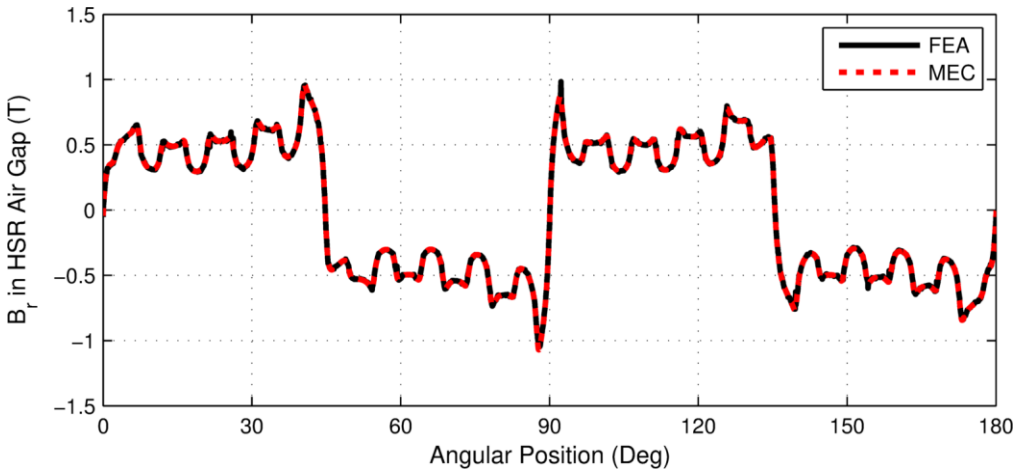


(b)

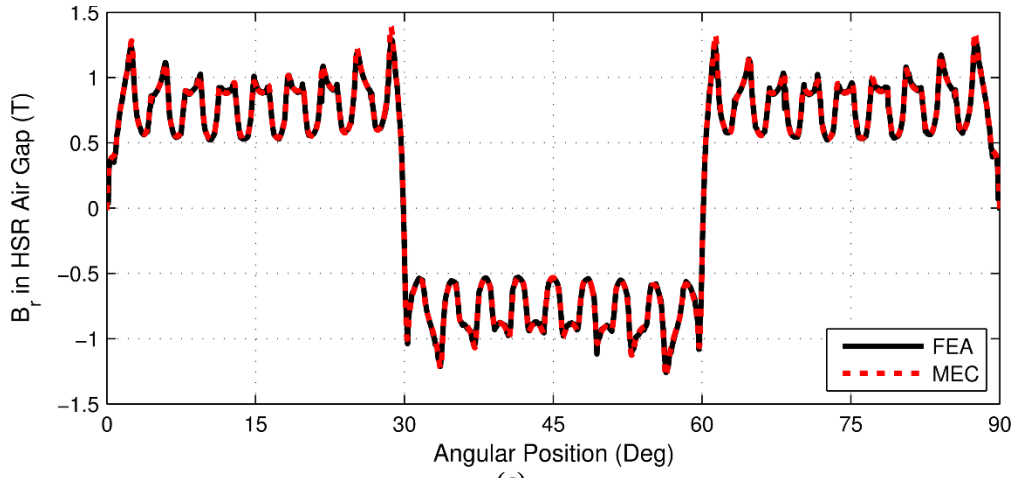


(c)

Figure 88. Radial Flux Density Along a Circular Path in the Radial Middle of the HSR Air Gap of (a) Base Design 1, (b) Base Design 2, and (c) Base Design 3

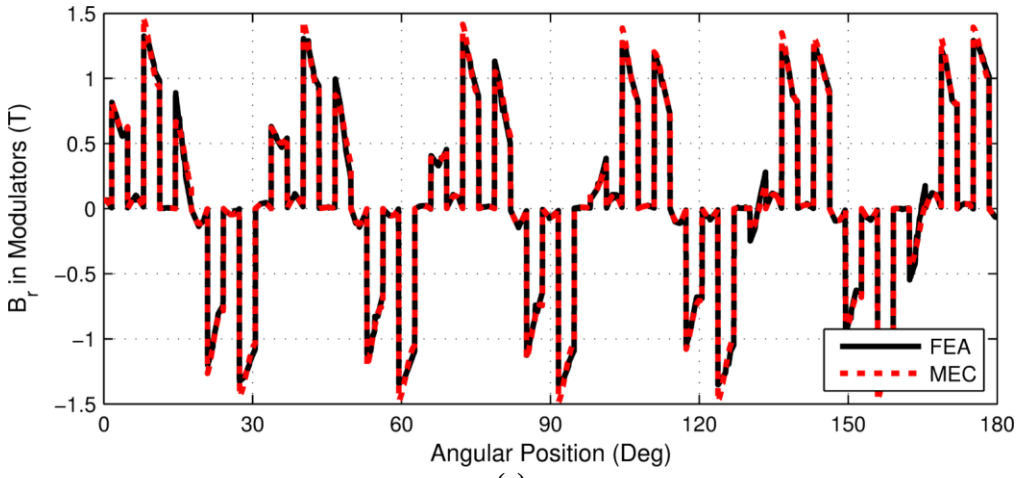


(a)

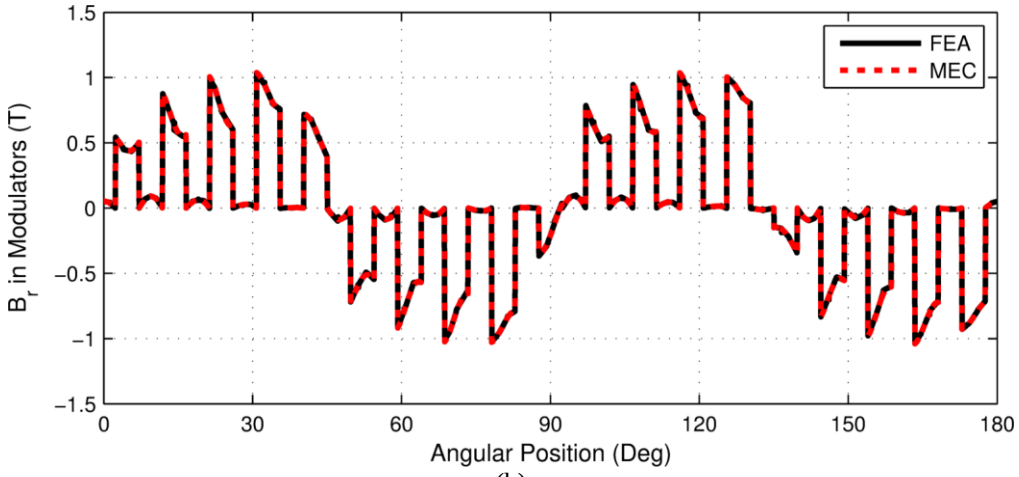


(b)

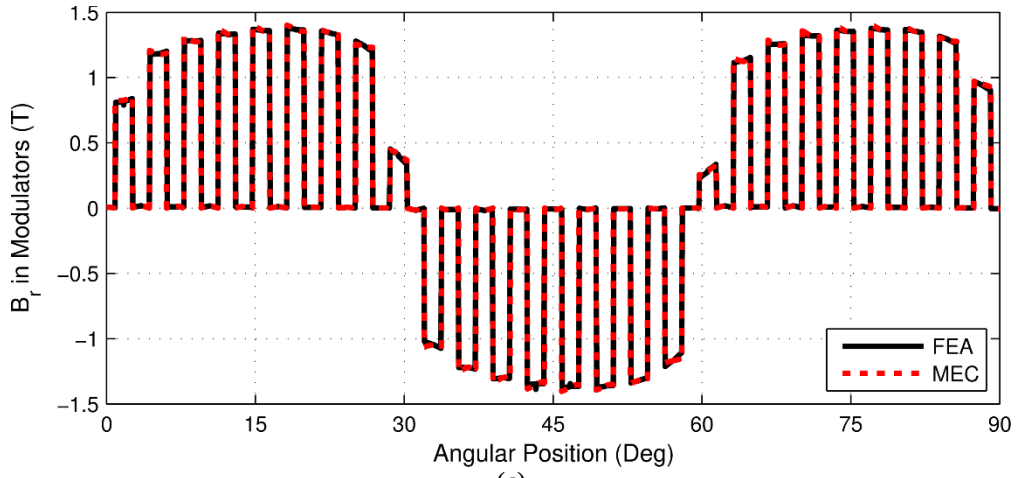


(c)

Figure 89. Radial Flux Density Along a Circular Path in the Radial Middle of the Modulators and Slots of (a) Base Design 1, (b) Base Design 2, and (c) Base Design 3

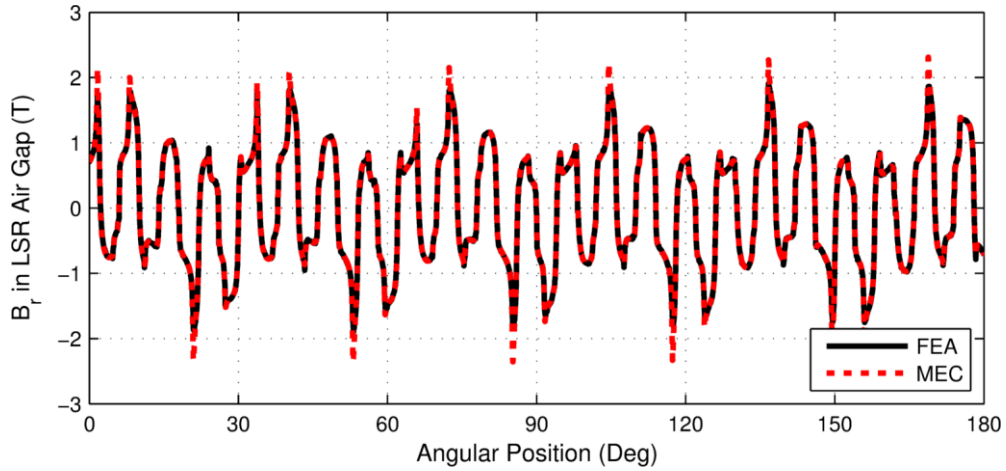


(a)

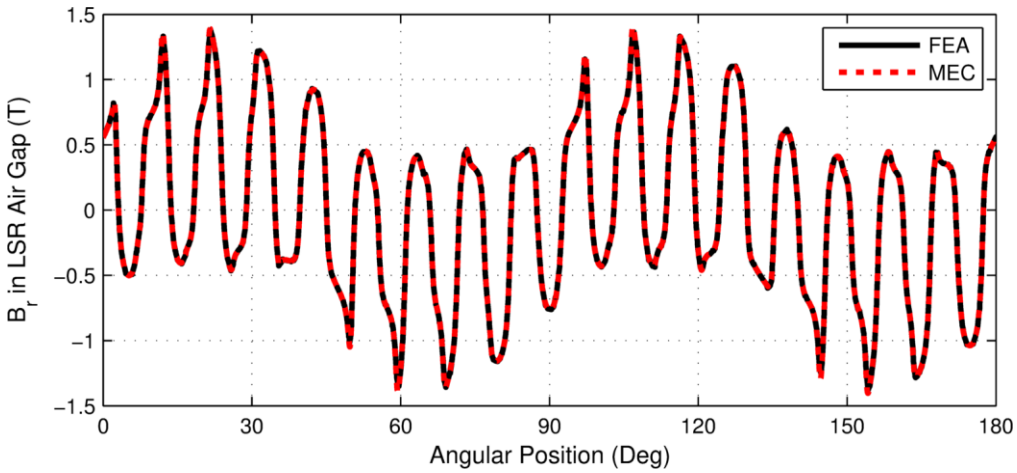


(b)

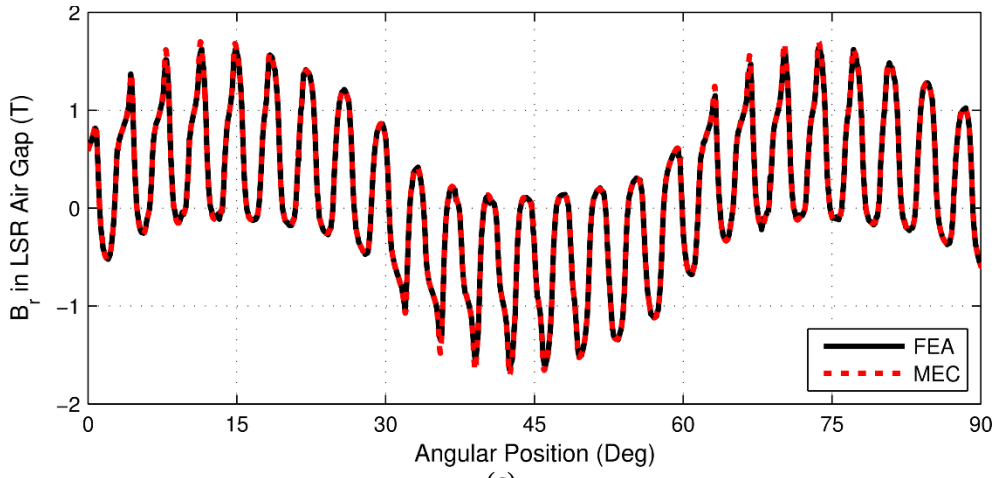


(c)

Figure 90. Radial Flux Density Along a Circular Path in the Radial Middle of the LSR Air Gap of (a) Base Design 1, (b) Base Design 2, and (c) Base Design 3

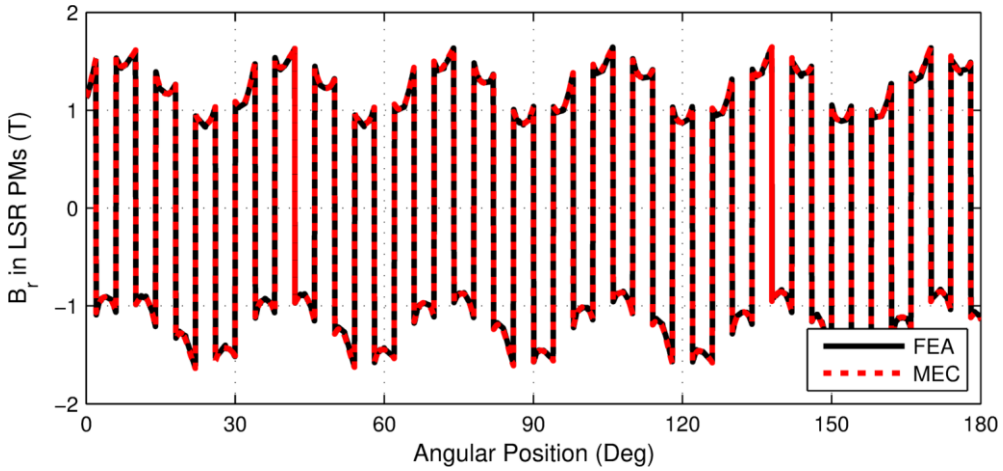


(a)

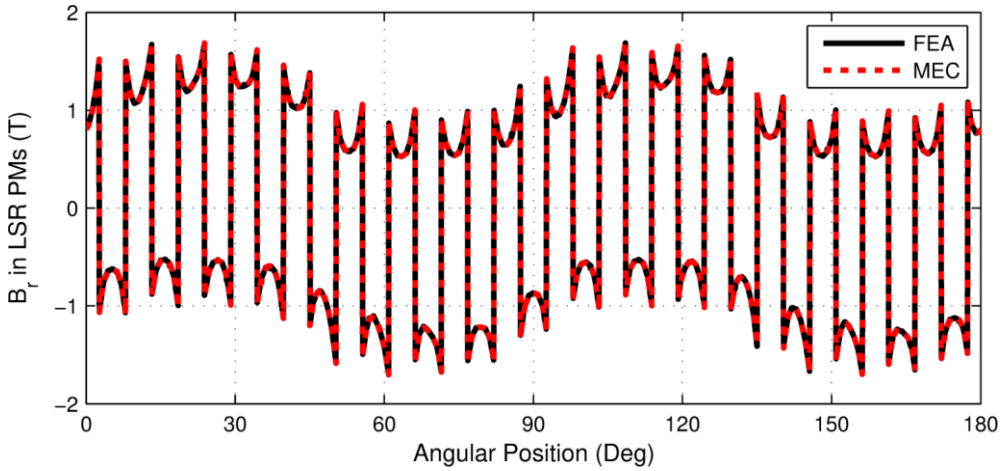


(b)

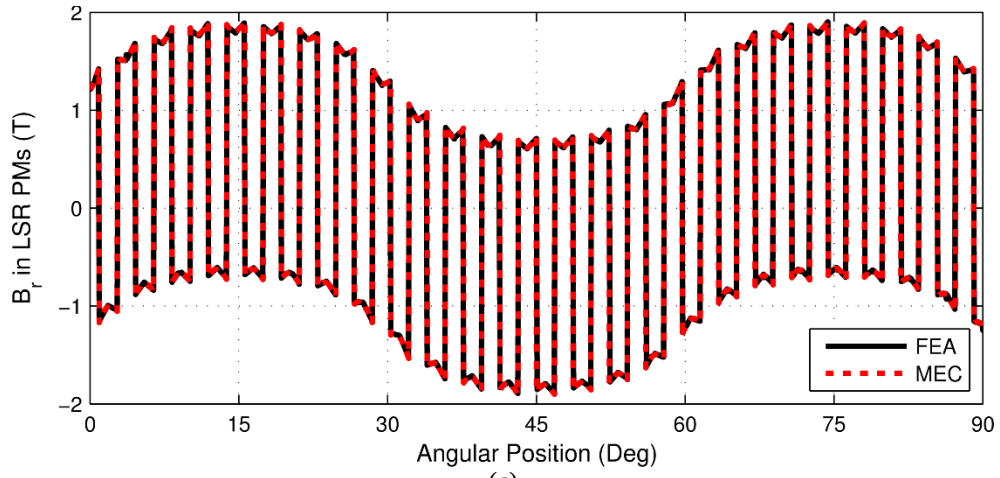


(c)

Figure 91. Radial Flux Density Along a Circular Path in the Radial Middle of the LSR Permanent Magnets of (a) Base Design 1, (b) Base Design 2, and (c) Base Design 3

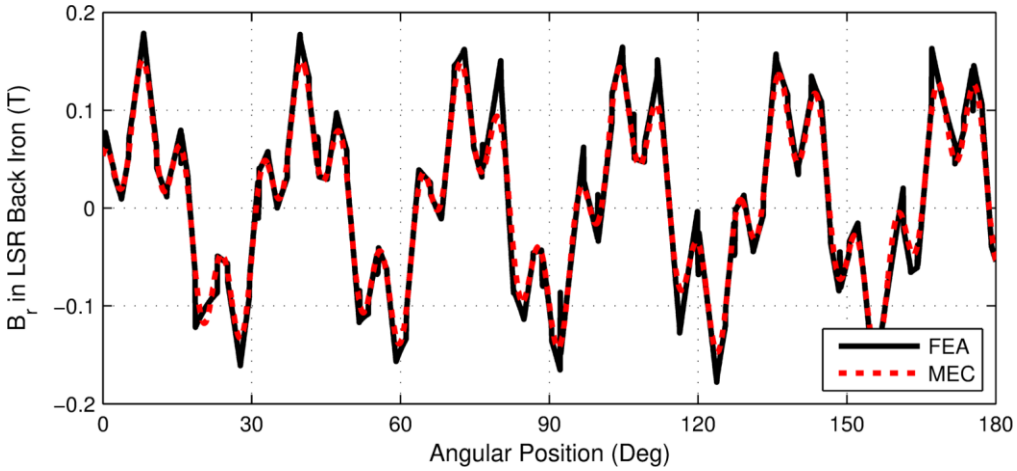


(a)

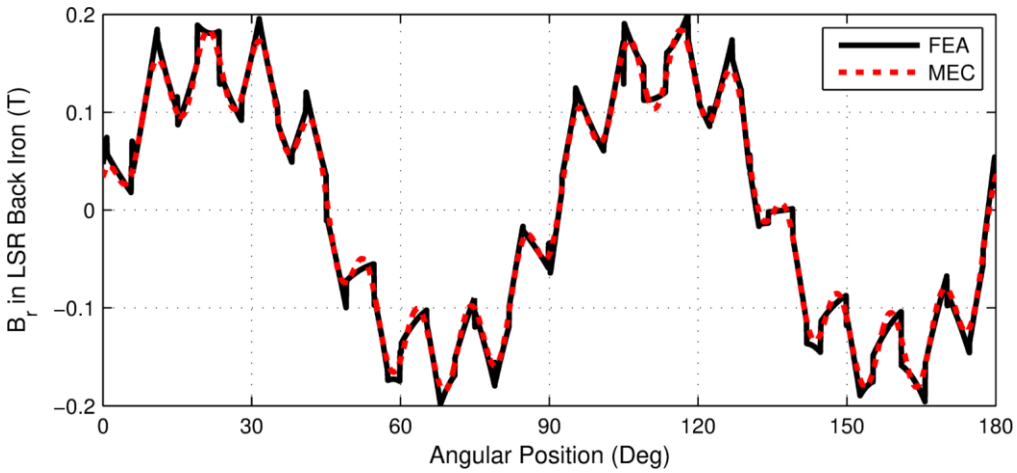


(b)

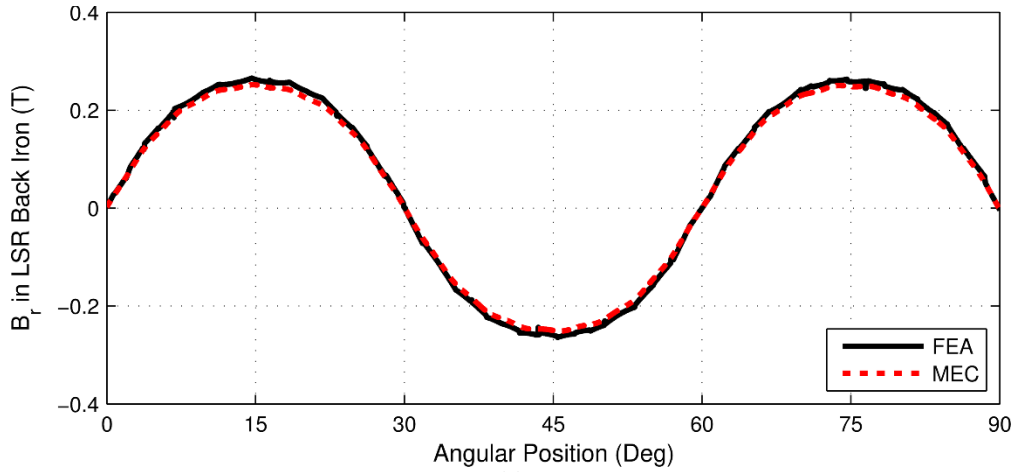


(c)

Figure 92. Radial Flux Density Along a Circular Path in the Radial Middle of the LSR Back Iron of (a) Base Design 1, (b) Base Design 2, and (c) Base Design 3

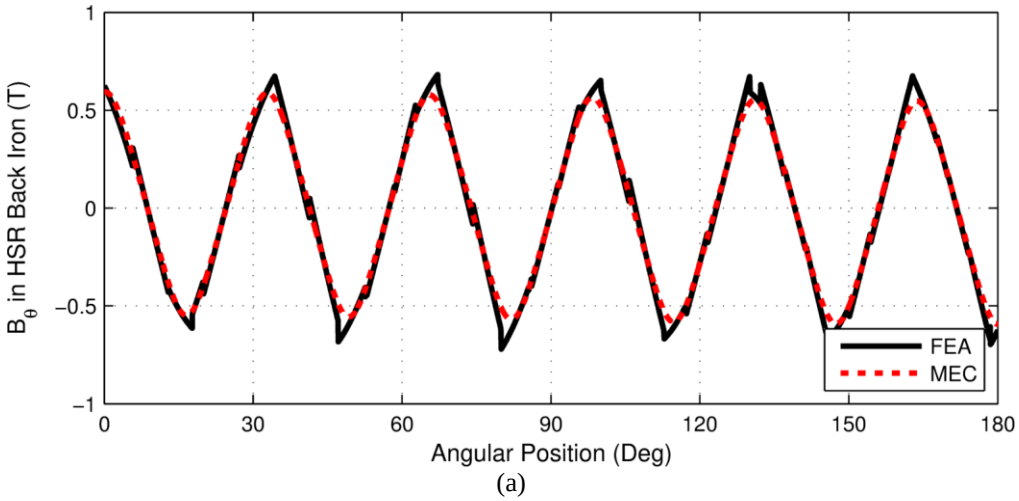


(a)

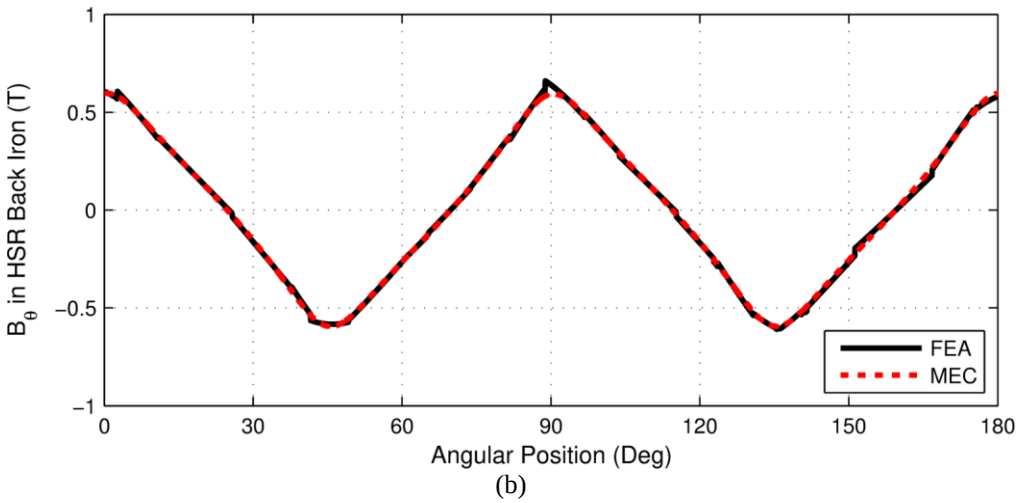


(b)

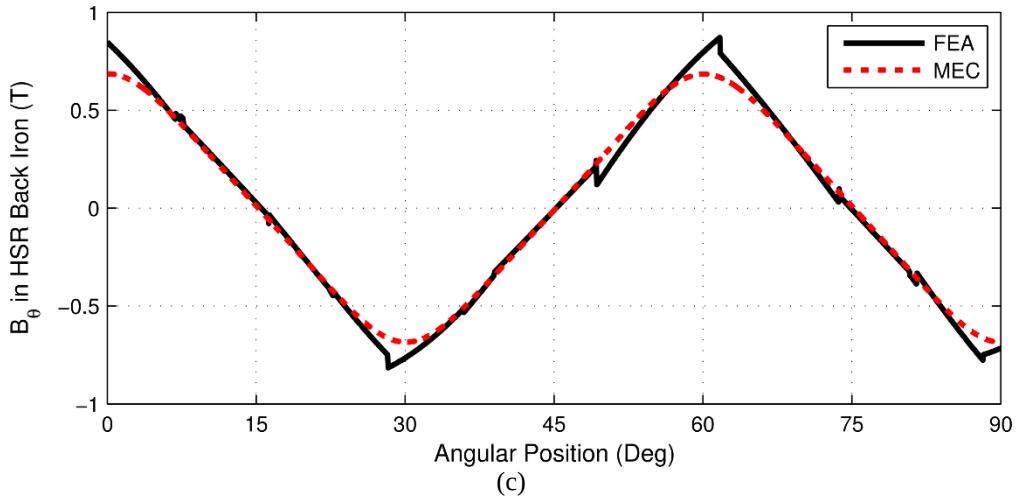


(c)

Figure 93. Tangential Flux Density Along a Circular Path in the Radial Middle of the HSR Back Iron of (a) Base Design 1, (b) Base Design 2, and (c) Base Design 3

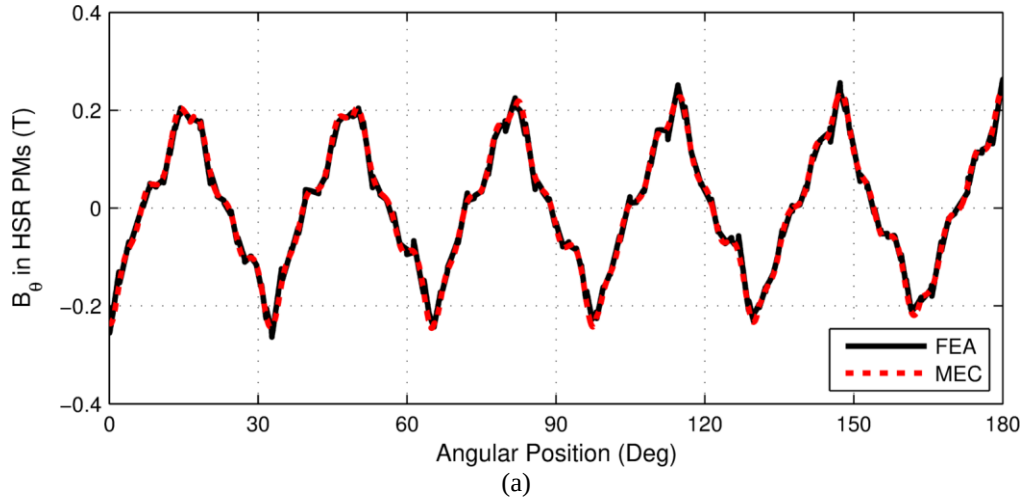


(a)

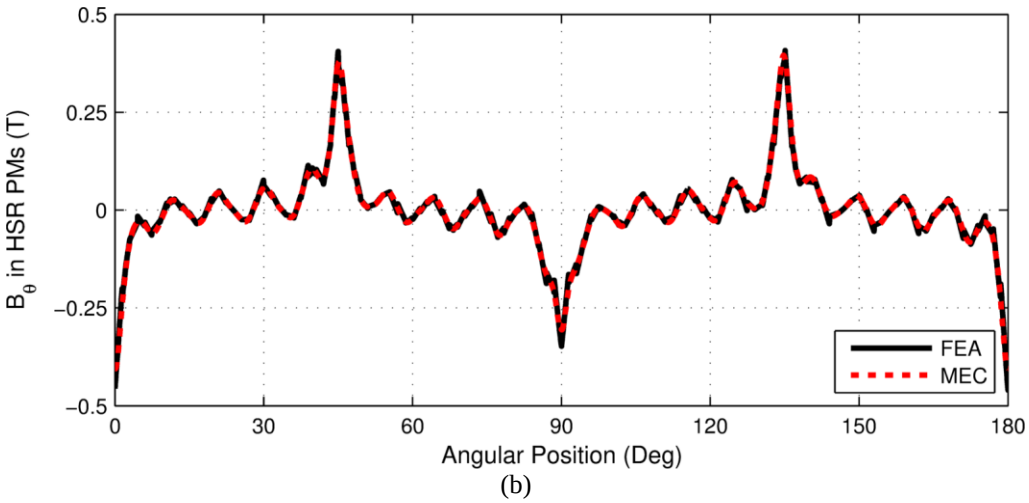


(b)

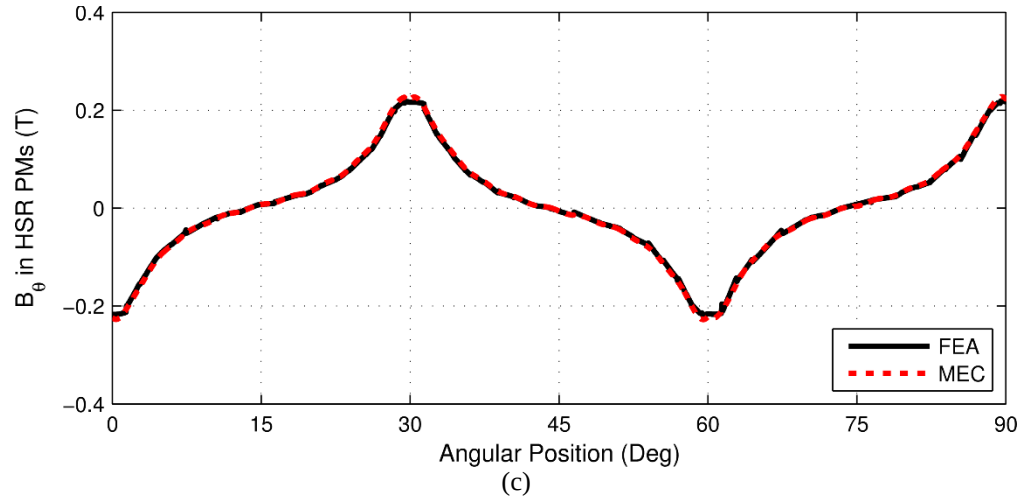


(c)

Figure 94. Tangential Flux Density Along a Circular Path in the Radial Middle of the HSR Permanent Magnets of (a) Base Design 1, (b) Base Design 2, and (c) Base Design 3

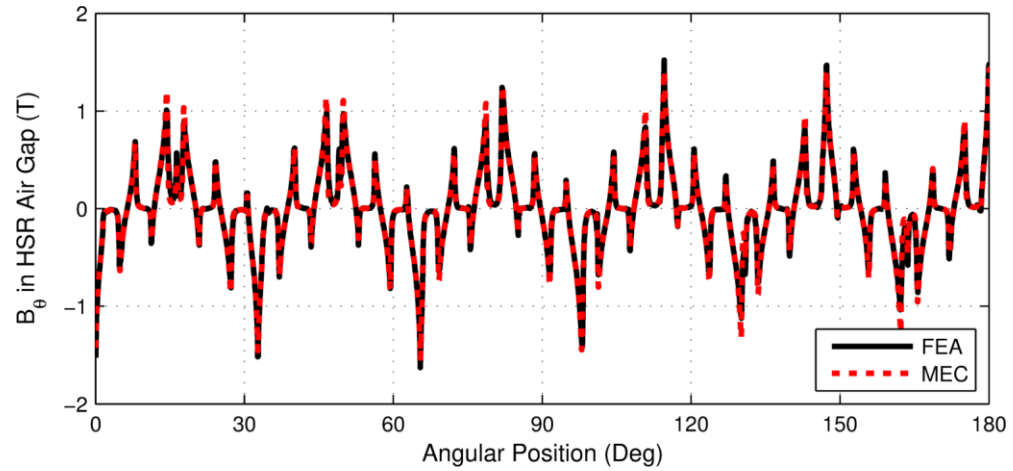


(a)

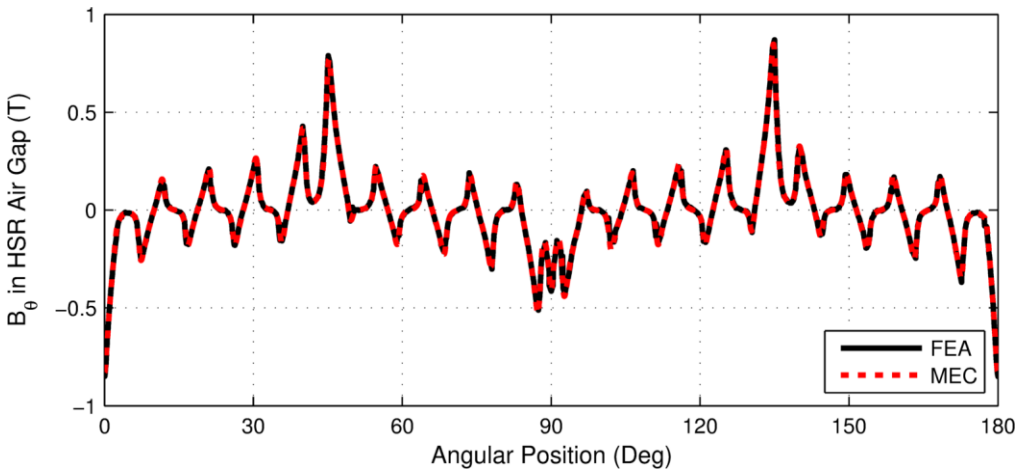


(b)

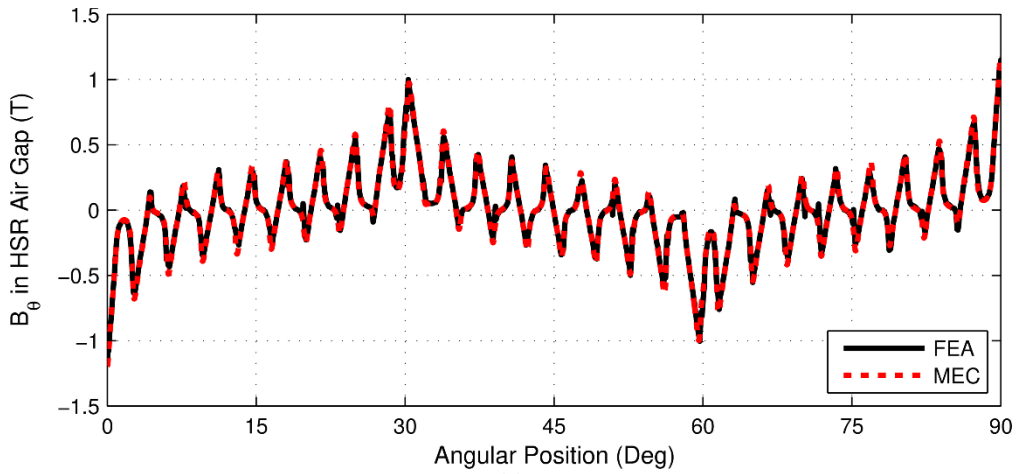


(c)

Figure 95. Tangential Flux Density Along a Circular Path in the Radial Middle of the HSR Air Gap of (a) Base Design 1, (b) Base Design 2, and (c) Base Design 3

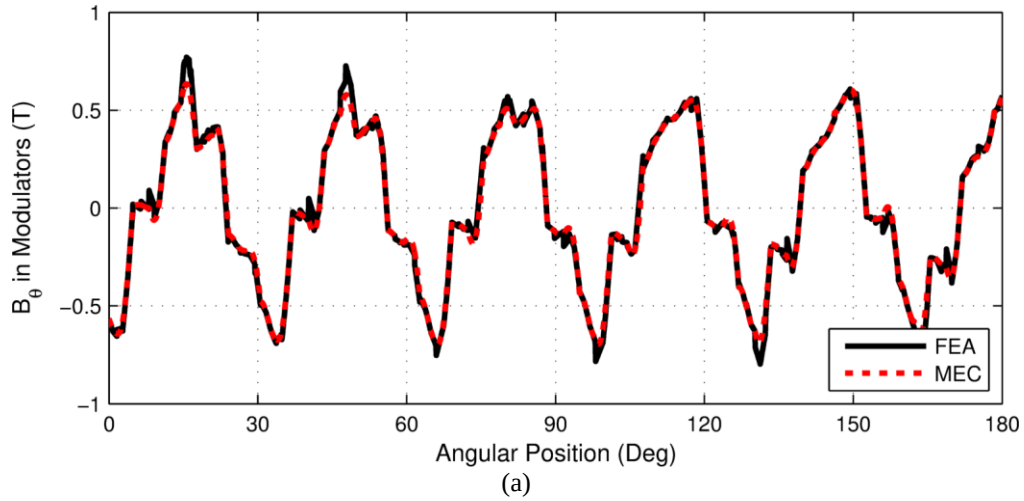


(a)

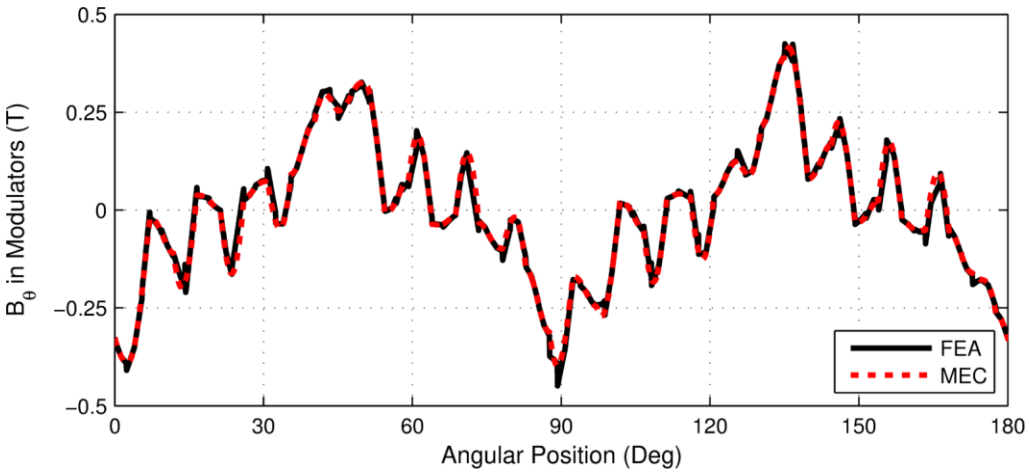


(b)

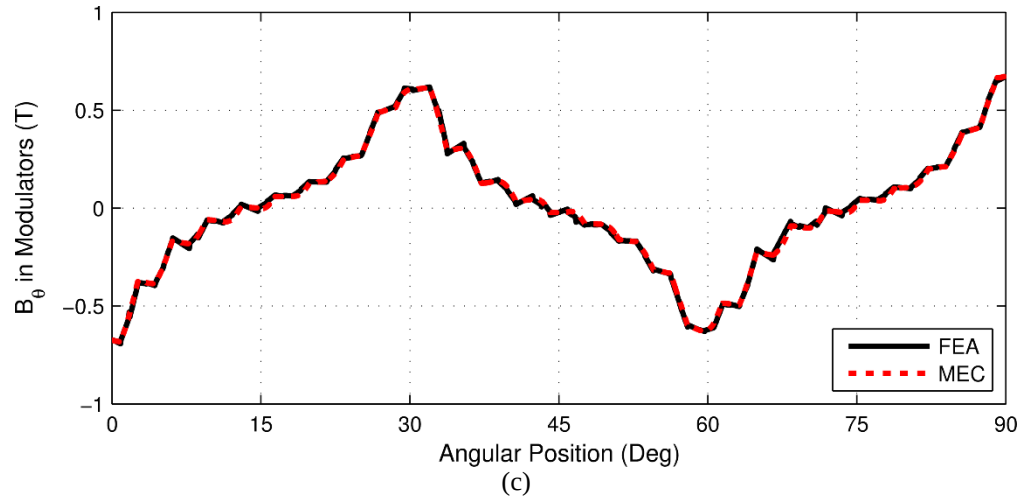


(c)

Figure 96. Tangential Flux Density Along a Circular Path in the Radial Middle of the Modulators and Slots of (a) Base Design 1, (b) Base Design 2, and (c) Base Design 3

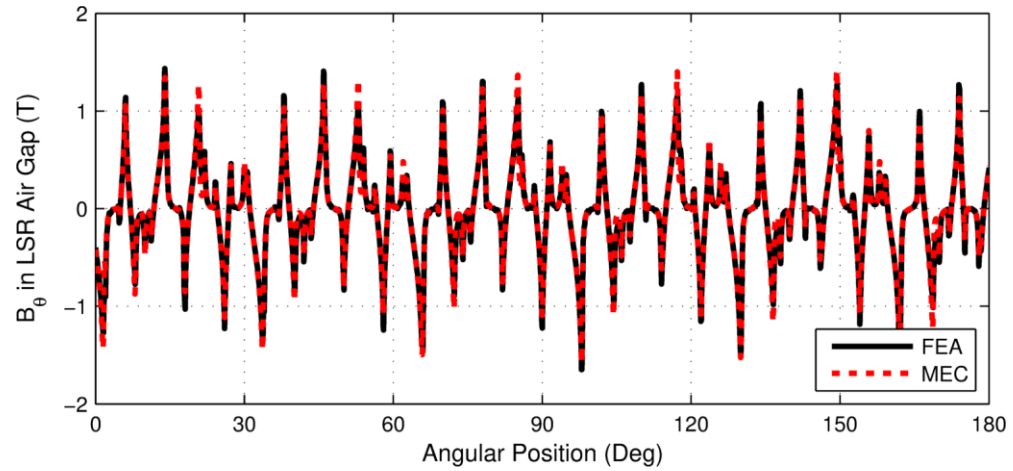


(a)

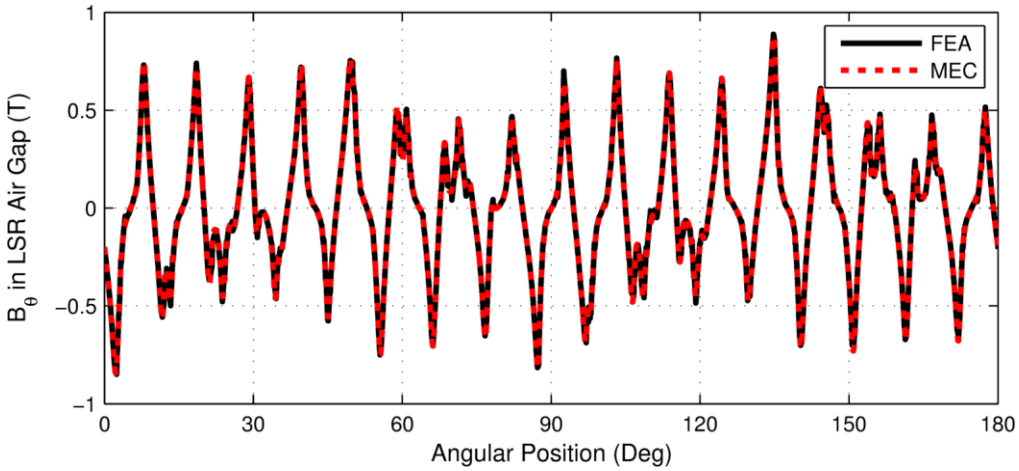


(b)

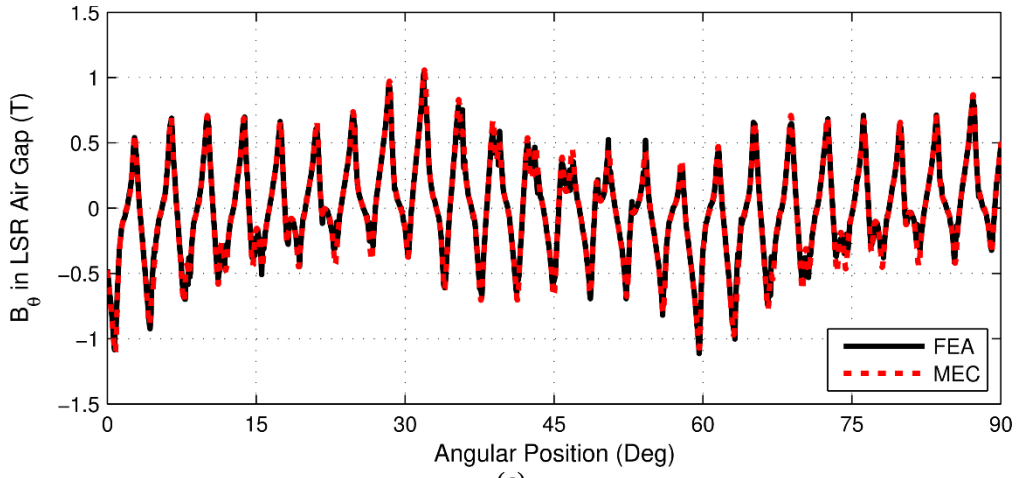


(c)

Figure 97. Tangential Flux Density Along a Circular Path in the Radial Middle of the LSR Air Gap of (a) Base Design 1, (b) Base Design 2, and (c) Base Design 3

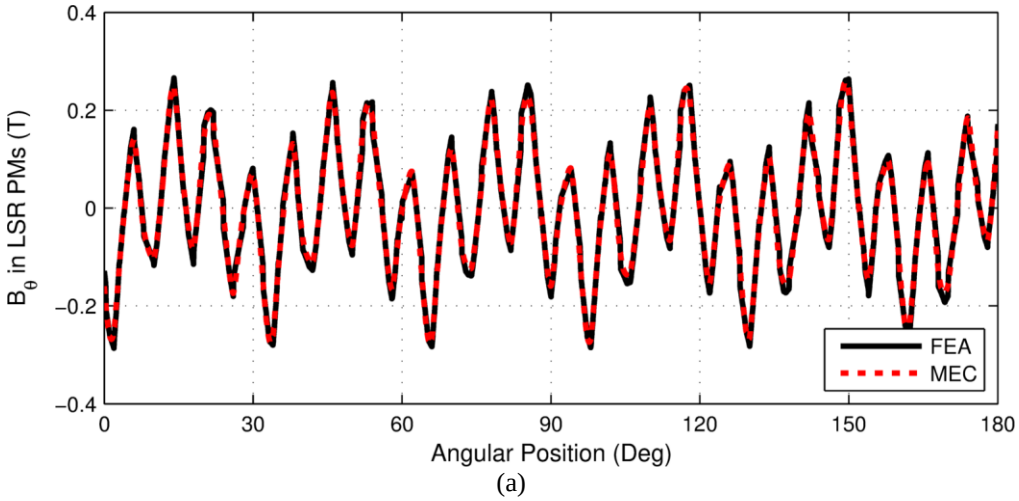


(a)

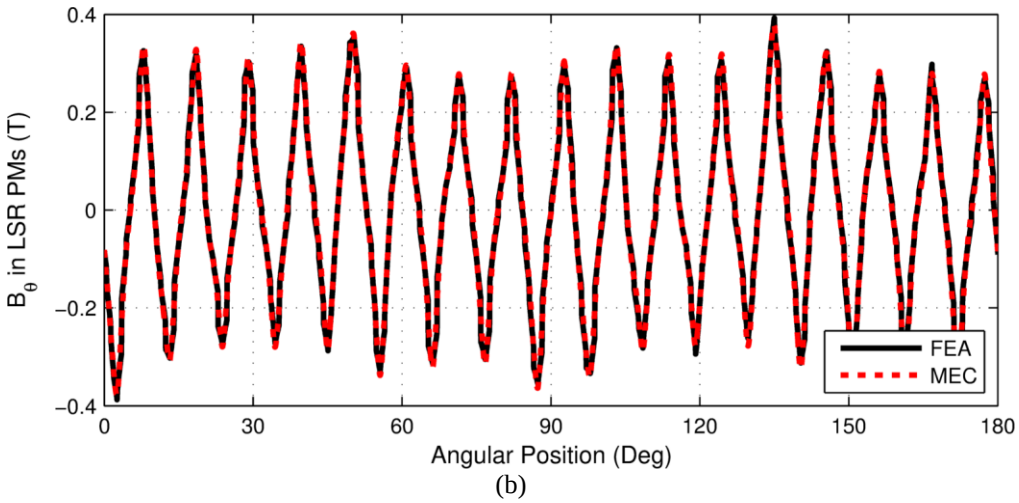


(b)

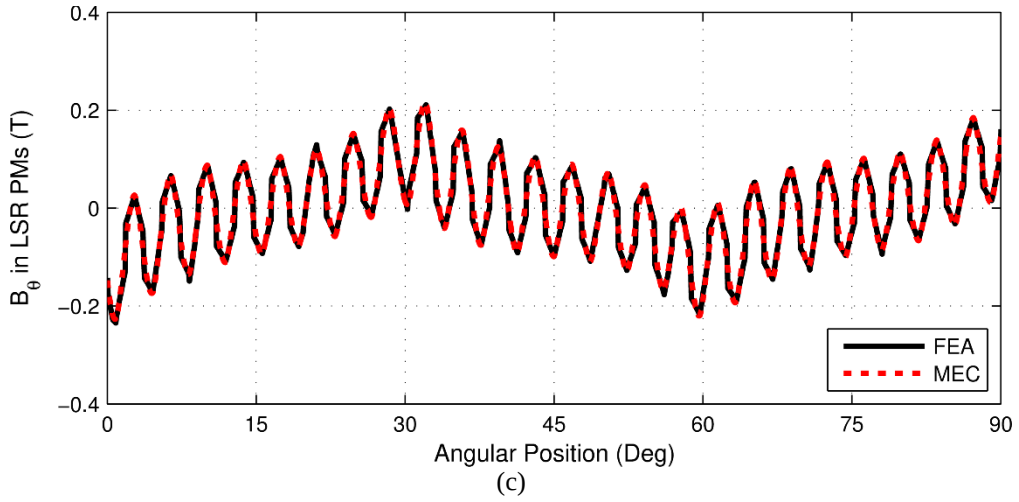


(c)

Figure 98. Tangential Flux Density Along a Circular Path in the Radial Middle of the LSR Permanent Magnets of (a) Base Design 1, (b) Base Design 2, and (c) Base Design 3

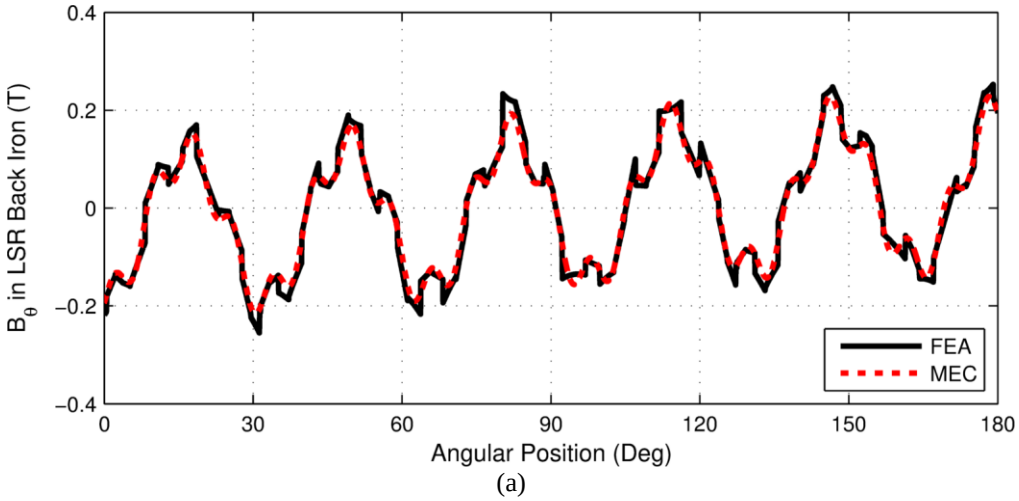


(a)

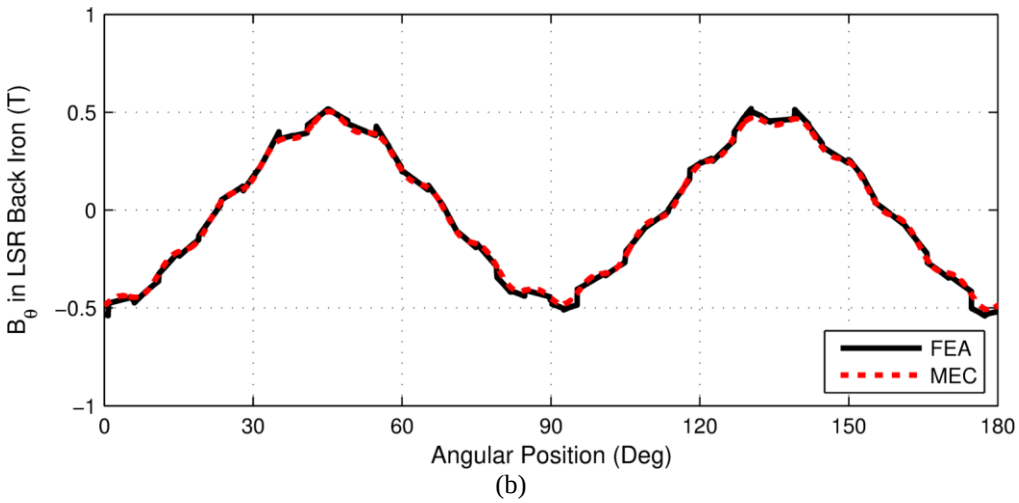


(b)

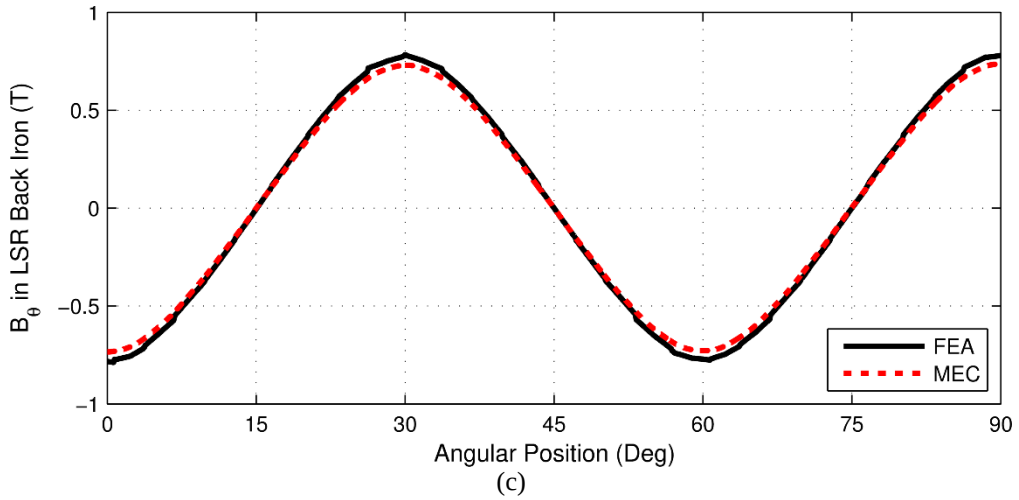


(c)

Figure 99. Tangential Flux Density Along a Circular Path in the Radial Middle of the LSR Back Iron of (a) Base Design 1, (b) Base Design 2, and (c) Base Design 3

## 8.3 Single Design Parameter Sweeps

In order to further demonstrate the accuracy of the MEC model and illustrate scenarios in which it breaks down due to the linearity assumption, the three base designs previously specified in Table 18 were used as starting points and the individual design parameters included in Table 19 were independently swept over the ranges of values specified in Table 19. For example, all other base design parameters specified in Table 18 and the $G_r$ values were fixed while the HSR pole pair count was swept from 3 to 15 in each base design. Each of the resulting design points was evaluated using a 2D MEC model with the "Fine Mesh" discretization settings specified in Table 20 and a 2D FEA model. The results of this analysis are summarized in several graphs which illustrate the variations in the MEC model's torque prediction accuracy with each of these parameters for all three base designs. Note the vertical axis scaling when analyzing these graphs, as the MEC model is extremely accurate over the full range of values for some parameters, which results in narrow vertical axis ranges for maximum resolution.

Table 19. Radial Flux Magnetic Gear Base Design Single Parameter Sweep Definitions

| Parameter | Description | Ranges of Values | Units |
|---|---|---|---|
| $T_{HSBI}$ | HSR back iron thickness | 1, 2, 3, … 40 | mm |
| $T_{HSPM}$ | HSR magnet thickness | 1, 2, 3, … 25 | mm |
| $T_{HSAG}$ | HSR air gap thickness | 0.25, 0.5, 0.75, … 5 | mm |
| $T_{Mods}$ | Modulator thickness | 1, 2, 3, … 20 | mm |
| $T_{LSAG}$ | LSR air gap thickness | 0.25, 0.5, 0.75, … 5 | mm |
| $T_{LSPM}$ | LSR magnet thickness | 1, 2, 3, … 25 | mm |
| $T_{LSBI}$ | LSR back iron thickness | 1, 2, 3, … 30 | mm |
| $P_{HS}$ | HSR pole pairs | 3, 4, 5, … 15 | |
| $\alpha_{Mods}$ | Modulators angular fill factor | 0.05, 0.1, 0.15, … 0.95 | |
| $\alpha_{HSPM}$ | HSR magnets angular fill factor | 0.1, 0.2, 0.3, … 1 | |
| $\alpha_{LSPM}$ | LSR magnets angular fill factor | 0.1, 0.2, 0.3, … 1 | |
| $R_{Out}$ | Gear active outer radius | 125, 130, 135, … 200 | mm |

Table 20. Radial Flux Magnetic Gear MEC Model Discretization Settings Used for the Single Parameter Sweep Study and the Optimization Study

| Parameter | Description | Coarse Mesh | Fine Mesh |
|---|---|---|---|
| ALM | Angular layers multiplier | 10 | 30 |
| $N_{RL,HSBI}$ | Number of radial layers in the HSR back iron | 3 | 3 |
| $RLM_{HSPM}$ | HSR magnets radial layers multiplier | 10 | 20 |
| $RLM_{HSAG}$ | HSR air gap radial layers multiplier | 10 | 20 |
| $RLM_{Mods}$ | Modulators radial layers multiplier | 10 | 20 |
| $RLM_{LSAG}$ | LSR air gap radial layers multiplier | 10 | 20 |
| $RLM_{LSPM}$ | LSR magnets radial layers multiplier | 10 | 20 |
| $N_{RL,LSBI}$ | Number of radial layers in the LSR back iron | 3 | 3 |
| $N_{RL,HSPM,min}$ | Minimum number of radial layers in the HSR magnets | 3 | 3 |
| $N_{RL,HSAG,min}$ | Minimum number of radial layers in the HSR air gap | 3 | 3 |
| $N_{RL,Mods,min}$ | Minimum number of radial layers in the modulators | 3 | 5 |
| $N_{RL,LSAG,min}$ | Minimum number of radial layers in the LSR air gap | 3 | 3 |
| $N_{RL,LSPM,min}$ | Minimum number of radial layers in the LSR magnets | 3 | 5 |

Figures 100-103 depict the variation of the MEC accuracy with the HSR back iron thickness, LSR back iron thickness, modulator radial thickness, and modulator angular fill factor, respectively. For each of these parameters, the MEC is extremely accurate over most of the range of considered values; however, when any of the associated component dimensions becomes sufficiently small (radially or tangentially thin), the ferromagnetic material deeply saturates, causing the assumption of linearity to break down and the MEC to overestimate the stall torque rating of the corresponding design. It is important to note that most of these parameter values which cause the system to become appreciably nonlinear and the model to become inaccurate are impractically small from a mechanical design and manufacturing standpoint.

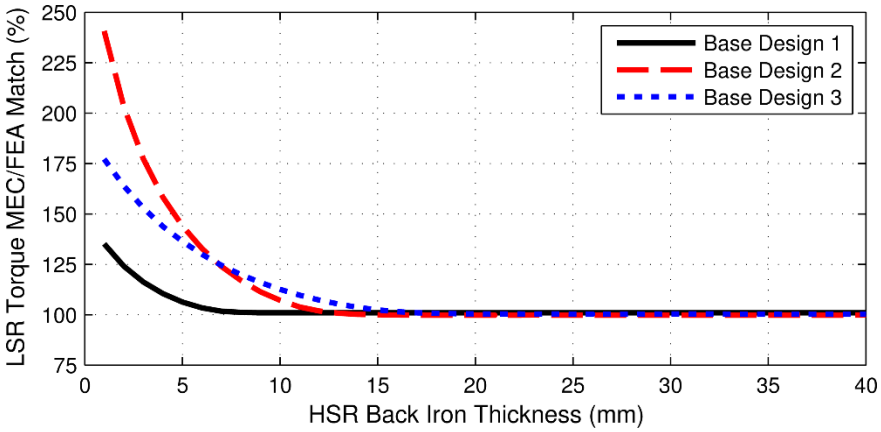


Figure 100. Variation of MEC Accuracy with HSR Back Iron Thickness for Base Designs

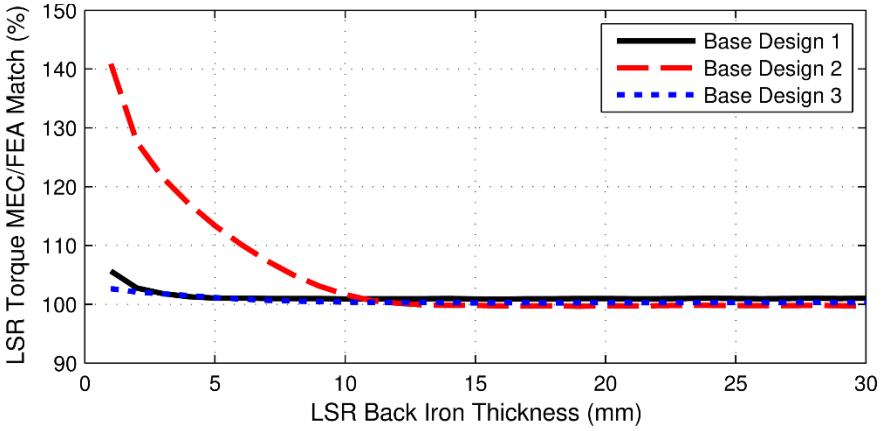


Figure 101. Variation of MEC Accuracy with LSR Back Iron Thickness for Base Designs

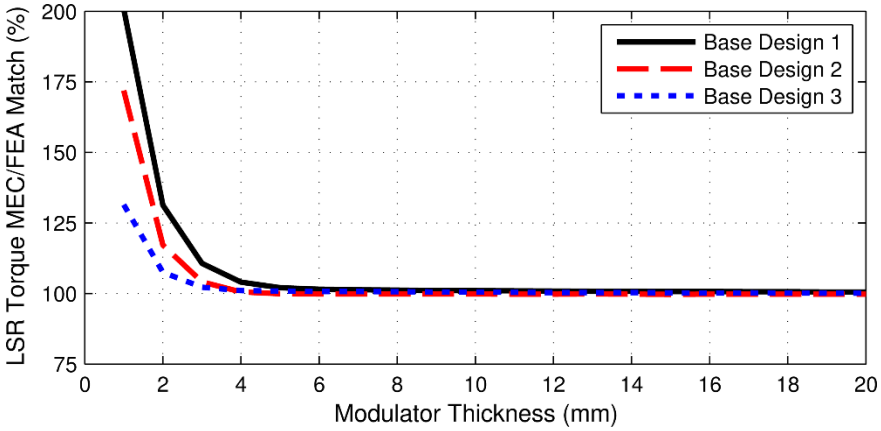


Figure 102. Variation of MEC Accuracy with Modulator Thickness for Base Designs

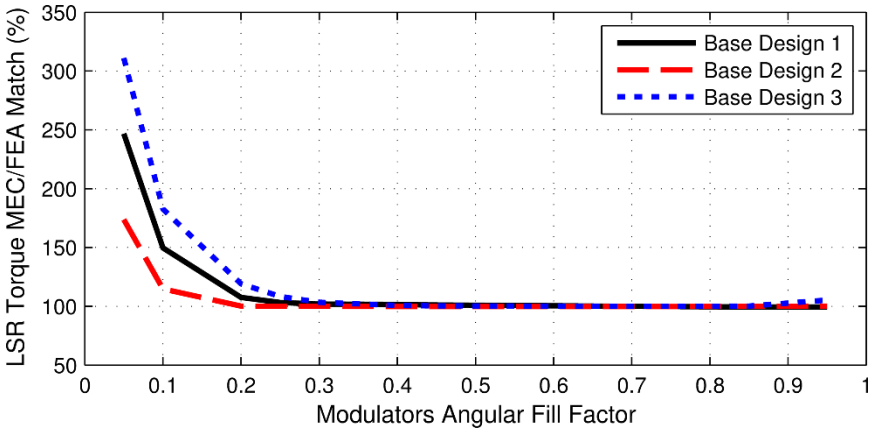


Figure 103. Variation of MEC Accuracy with Modulators Angular Fill Factor for Base Designs

Figures 104-111 illustrate the variation of the MEC accuracy with the HSR magnet thickness, LSR magnet thickness, HSR magnet angular fill factor, LSR magnet angular fill factor, HSR air gap thickness, LSR air gap thickness, HSR pole pair count, and outer radius, respectively. The MEC is extremely accurate over the full range of values considered for each of these parameters, with at most only a few percent of variation in accuracy between the extreme ends of the broad parameter value spectrums. Some of the slight fluctuations in the curves are simply due to discretization effects, but there are also some very low impact upward and downward trends in the MEC torque predictions relative to those of the FEA model. These trends are due to the effects of the parameter variations on saturation and leakage flux. Additionally, the MEC's accuracy would not be as constant with respect to the variation of key parameters if a fixed mesh with constant numbers of angular and radial layers was used instead of the scalable mesh settings specified in Table 20, which are based on the angular and radial layers multipliers developed in Section 8.1.

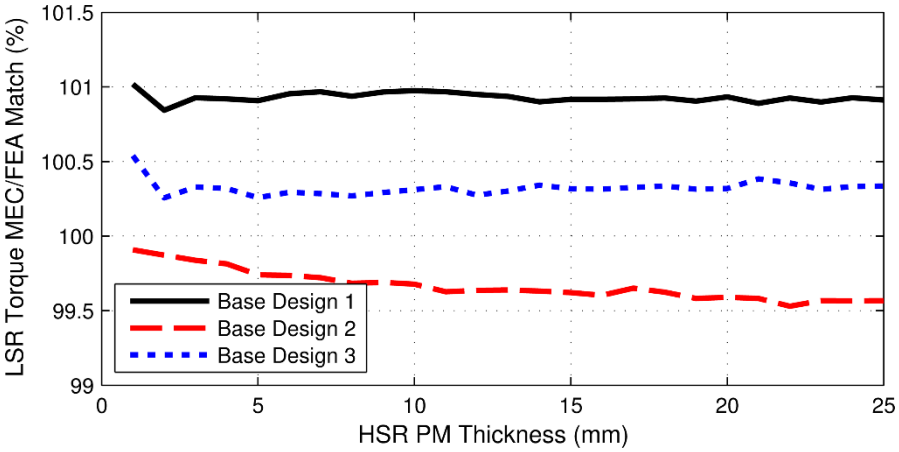


Figure 104. Variation of MEC Accuracy with HSR PM Thickness for Base Designs

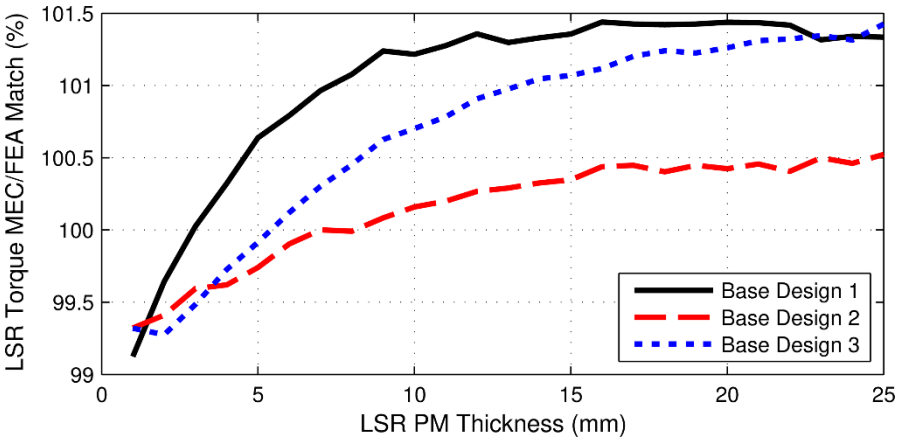


Figure 105. Variation of MEC Accuracy with LSR PM Thickness for Base Designs

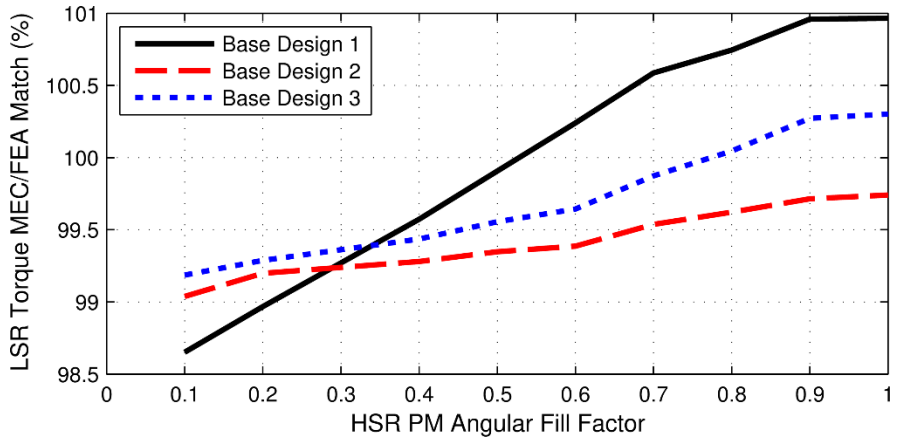


Figure 106. Variation of MEC Accuracy with HSR PM Angular Fill Factor for Base Designs

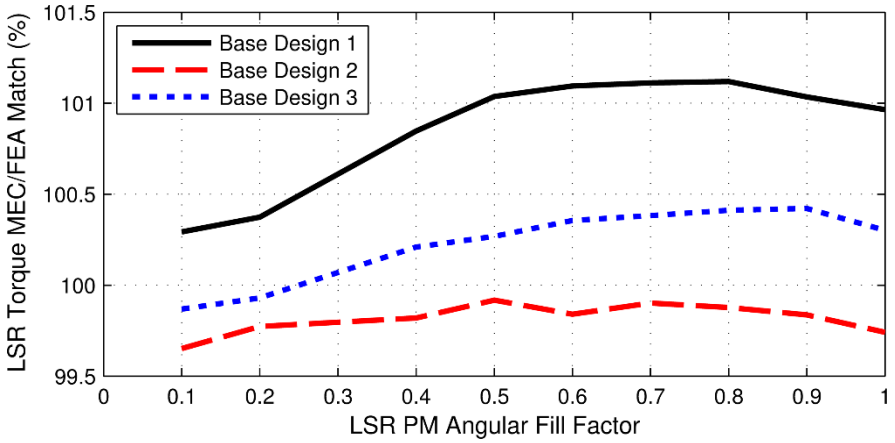


Figure 107. Variation of MEC Accuracy with LSR PM Angular Fill Factor for Base Designs

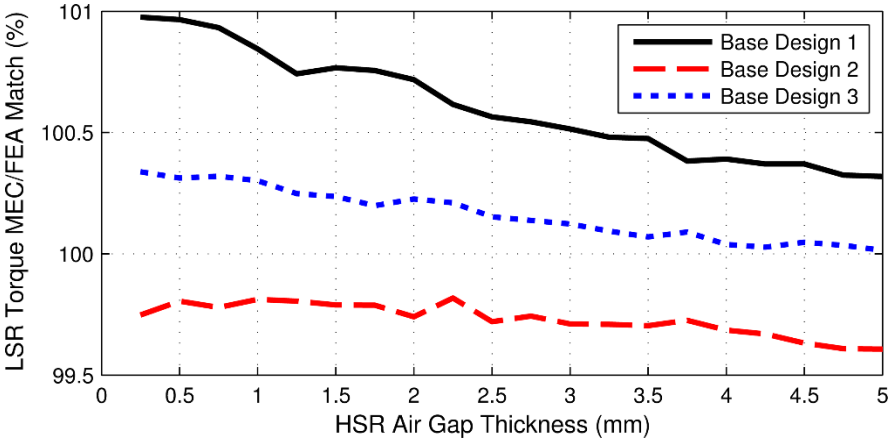


Figure 108. Variation of MEC Accuracy with HSR Air Gap Thickness for Base Designs

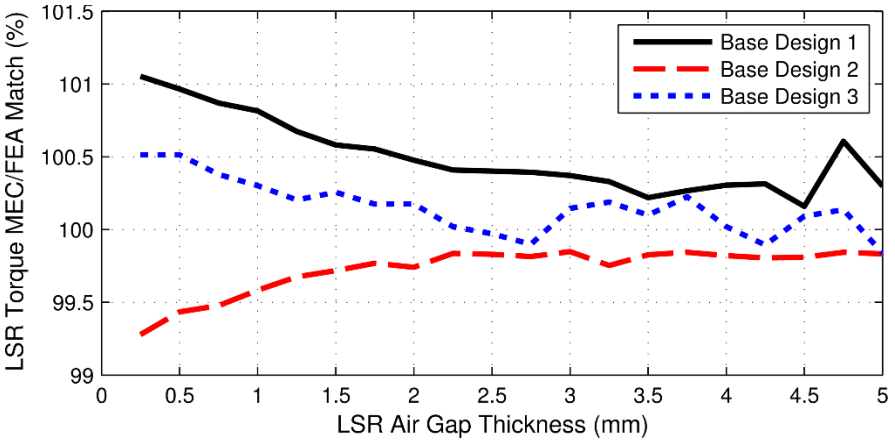


Figure 109. Variation of MEC Accuracy with LSR Air Gap Thickness for Base Designs

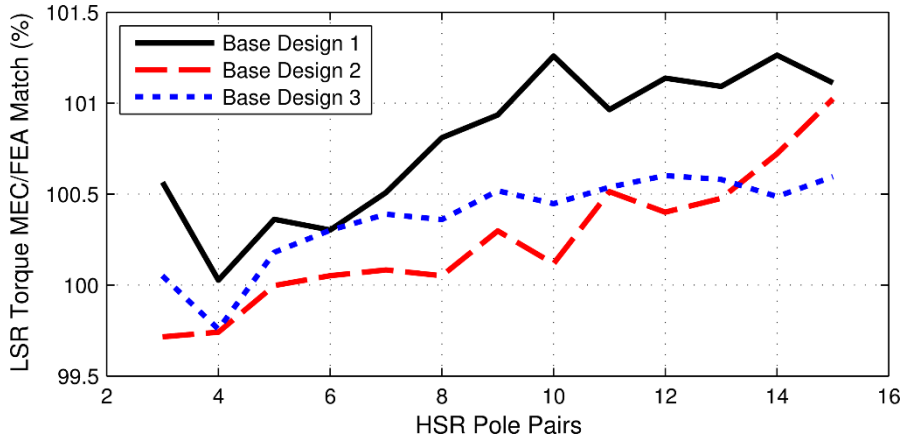


Figure 110. Variation of MEC Accuracy with HSR Pole Pairs for Base Designs

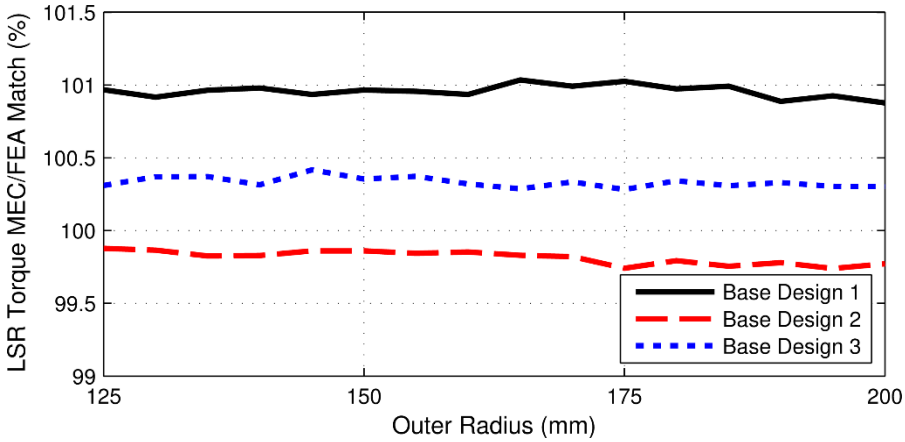


Figure 111. Variation of MEC Accuracy with Outer Radius for Base Designs

## 8.4 Design Optimization Study

The final and most important test of the MEC model as a design tool is an example optimization study. As demonstrated by the preceding graphs, saturation or an inadequately low number of radial layers can cause the MEC model to overestimate the stall torque of a given design, but an inadequately low number of angular layers can cause the MEC model to underestimate the stall torque of the same design. Thus, using insufficiently small amounts of radial and angular layers can cause these effects to roughly

cancel out for a single design or a small set of designs and result in extremely fast models with accurate stall torque predictions. However, if such a low resolution model is applied to a broader range of designs, its accuracy will typically decrease, and this may bias the results toward a certain subset of designs. In order to validate that the proposed MEC model does not suffer from these issues and that it is suitable for use as an optimization tool, several of the critical geometric gear parameters were swept over the ranges of values specified in Table 21. Each of the resulting 46,656 designs was evaluated using the 2D MEC model with both the "coarse mesh" and the "fine mesh" settings specified in Table 20, as well as a 2D nonlinear FEA model. Although the "coarse mesh" uses looser discretization settings than the "fine mesh," it still results in higher resolution reluctance networks than most of those used in other MEC studies described in the literature.

Due to strong interdependencies between the effects of different dimensions, the values of certain variables were coupled through additional derived parameters, which are included in Table 21. As discussed in Sections 5 and 6, because the LSR has more magnetic poles than the HSR, there is significantly more flux leakage between adjacent poles on the LSR than there is on the HSR. Therefore, it is prudent to concentrate most of the magnet material on the HSR. Thus, the radial thickness of the LSR magnets, $T_{LSPM}$, is determined by the radial thickness of the HSR magnets, $T_{HSPM}$, and a derived parameter, $k_{PM}$, as shown in (23), which is repeated below. Additionally, the HSR back iron thickness, $T_{HSBI}$, was sized based on the HSR permanent magnet pole arc and the derived parameter, $k_{HSBI}$, as indicated in (60), where $R_{HSPM}$ denotes the inner radius of the HSR permanent magnets. The term $k_{HSBI}$ represents the idealized ratio of the HSR permanent

flux density to the HSR back iron flux density, based on an overly simplified, single pole pair model of the magnetic flux paths in the HSR. Thus, the thickness of the HSR back iron is sized based on the HSR permanent magnet pole arc and $k_{HSBI}$, where a larger value of $k_{HSBI}$ indicates a thicker HSR back iron with lower magnetic loading. While the HSR permanent magnet pole arc dominates the necessary sizing of the HSR back iron, the sizing of the LSR back iron is impacted by the pole arcs of both the HSR and the LSR permanent magnets and is ultimately frequently dictated by practical construction considerations. Thus, the parametric optimization study uses a simple set of direct fixed LSR back iron thicknesses.

Table 21. Optimization Study Parameter Sweep Ranges

| Parameter | Description | Ranges of Values | Units |
|---|---|---|---|
| $G_r$ | Nearest integer gear ratio | 4, 8, 16 | |
| $P_{HS}$ | HSR pole pairs<br>For $G_r = 4$<br>For $G_r = 8$<br>For $G_r = 16$ | <br>4, 5, 6, … 18<br>3, 4, 5, … 13<br>3, 4, 5, … 8 | |
| $R_{Out}$ | Active outer radius | 150, 175, 200 | mm |
| $k_{HSBI}$ | HSR back iron thickness coefficient | 0.4, 0.5, 0.6 | |
| $T_{HSPM}$ | HSR magnet thickness | 3, 5, 7, … 13 | mm |
| $T_{AG}$ | Common air gap thickness | 1.5 | mm |
| $T_{Mods}$ | Modulator thickness | 11, 14, 17 | mm |
| $k_{PM}$ | LSR magnet thickness ratio | 0.5, 0.75, 1 | |
| $T_{LSBI}$ | LSR back iron thickness | 20, 25, 30 | mm |

$$T_{LSPM} = T_{HSPM} \cdot k_{PM} \tag{23}$$

$$T_{HSBI} = \left(\frac{\pi \cdot R_{HSPM}}{P_{HS}}\right) \cdot k_{HSBI} \tag{60}$$

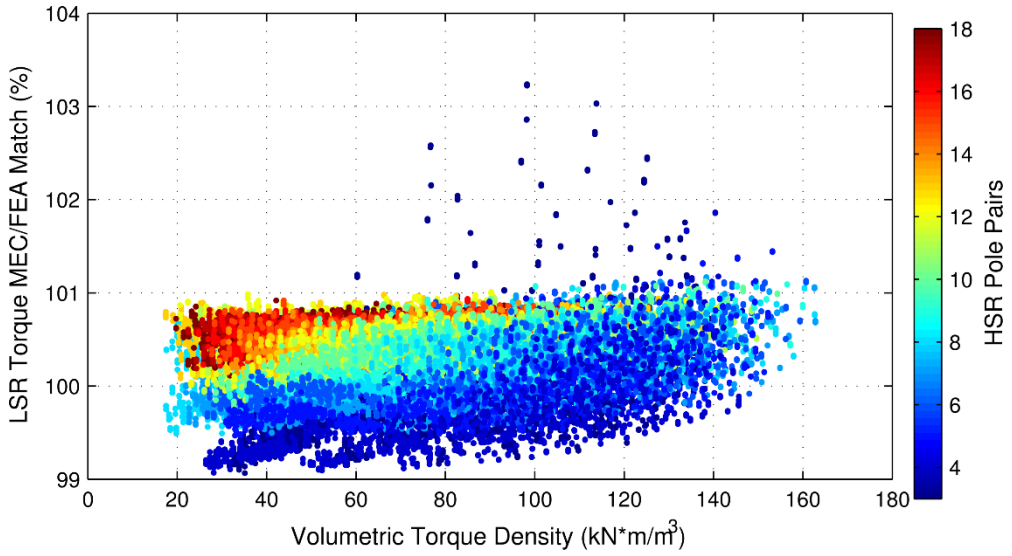


Figure 112. Fine Mesh MEC Accuracy for the Parametric Optimization Study Designs

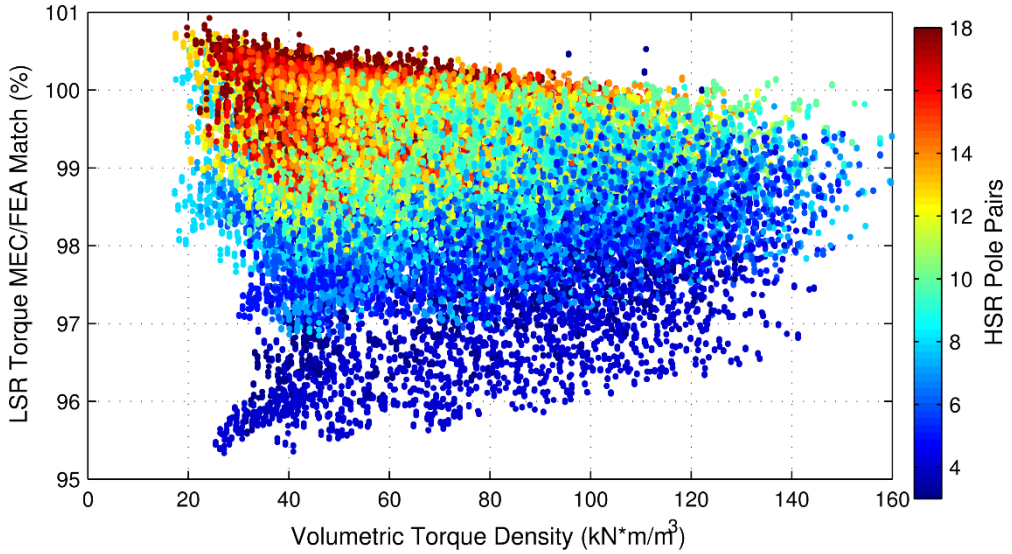


Figure 113. Coarse Mesh MEC Accuracy for the Parametric Optimization Study Designs

Figures 112 and 113 and the remaining graphs in this section summarize the results of this optimization study. The plots in Figures 112 and 113 illustrate the MEC model's accuracy, using both the fine and coarse mesh settings, over the entire parametric sweep space. Figure 112 indicates that the fine mesh MEC model torque predictions generally

match the corresponding FEA model torque predictions within roughly ±1%. The few exceptions to this extremely tight error bound are some of the designs with the minimum HSR pole pair count value of 3 and the maximum outer radius value of 200 mm, which results in the maximum HSR pole arc. The fine mesh MEC slightly overestimates the torque ratings of these few designs by as much as 3.2% because it does not account for the impact of saturation caused by the large HSR pole arc. Figure 113 demonstrates that the coarse mesh MEC model torque predictions are also fairly accurate over the full parametric sweep space, but tend to be slightly lower, with errors ranging from approximately -5% to +1%. This is primarily a result of using a smaller ALM, which, as shown in the discretization impact analysis, biases some of the torque predictions toward slightly lower values and inadvertently helps to cancel out the aforementioned worst overestimates produced by the fine mesh MEC.

Figure 114 provides a legend describing the significance of each curve in Figures 115-120, which indicate various optimization trends predicted by the FEA, coarse mesh MEC, and fine mesh MEC models for each of the three gear ratios considered in the study. In particular, the plots in Figures 115-120 show the variation of two key design quality metrics, optimal volumetric torque density and optimal PM volumetric torque density (stall torque divided by PM material volume), with three of the most interesting and impactful design parameters included in the optimization sweep, HSR pole pairs, HSR magnet thickness, and active outer radius. Volumetric torque density, one of the most common metrics in magnetic gear literature, provides a normalized description of the size (volume) of each design. As discussed in prior sections, optimization for volumetric

torque density tends to favor thicker magnets and lower pole counts. PM volumetric torque density provides a normalized characterization of the amount of magnet material required for each design and, as demonstrated in Section 6, can serve as an analogous substitute for active material cost, which is dominated by the cost of the magnets. Optimization for PM volumetric torque density tends to favor thinner magnets and higher pole counts. The results in Figures 115-120 demonstrate that both the fine and coarse mesh MEC models provide extremely accurate characterizations of these different design trends. Although the fine mesh MEC model is generally slightly more accurate, there are some limited instances in which, due to cancellation of various error sources, the coarse mesh MEC model actually produces a better match with the results given by the FEA model.

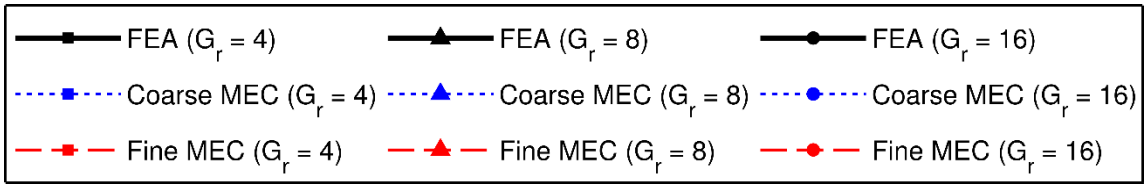


Figure 114. Legend for Design Optimization Trend Plots in Figures 115-120

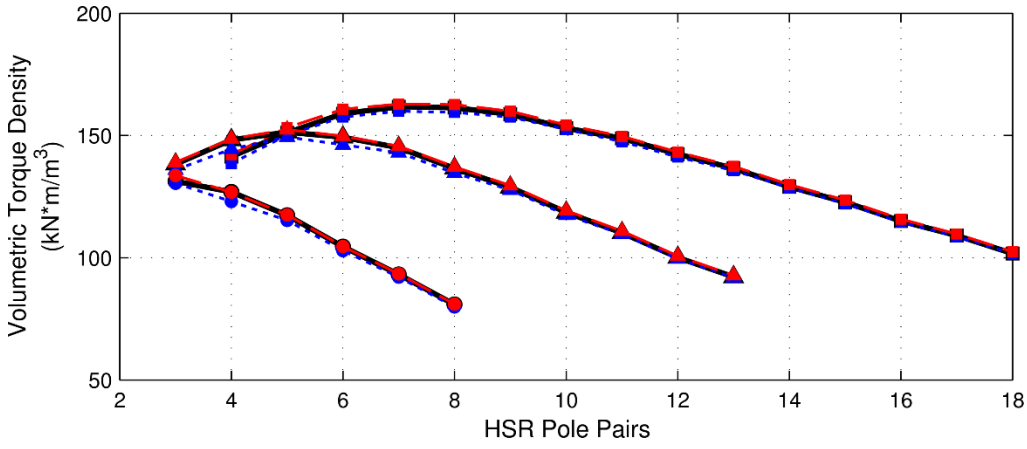


Figure 115. Variation of Maximum Volumetric Torque Density with HSR Pole Pairs

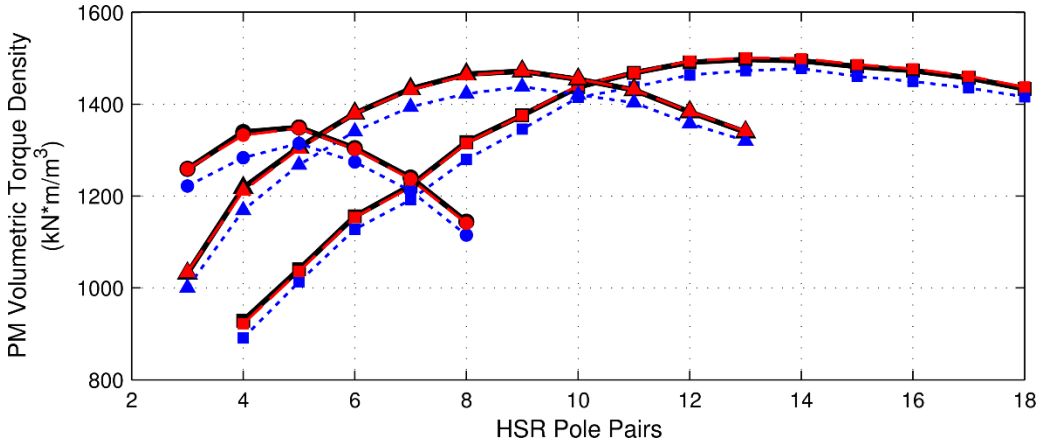


Figure 116. Variation of Maximum PM Volumetric Torque Density with HSR Pole Pairs

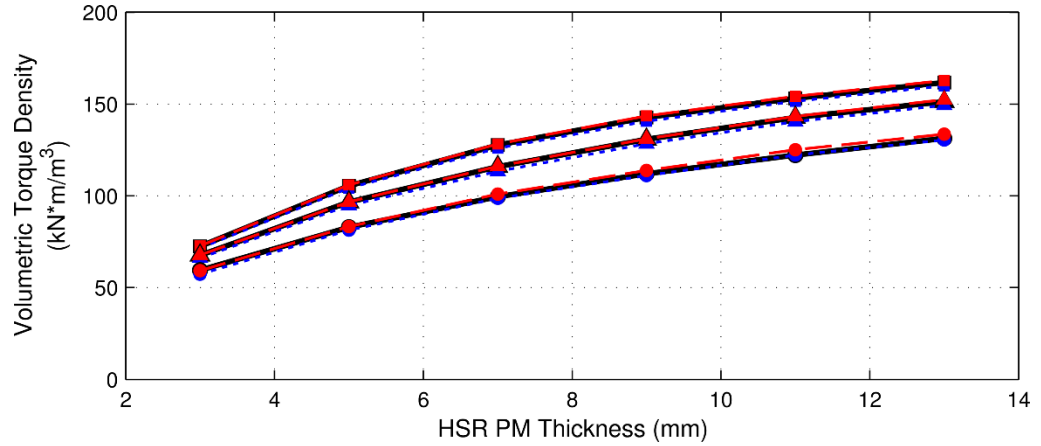


Figure 117. Variation of Maximum Volumetric Torque Density with HSR PM Thickness

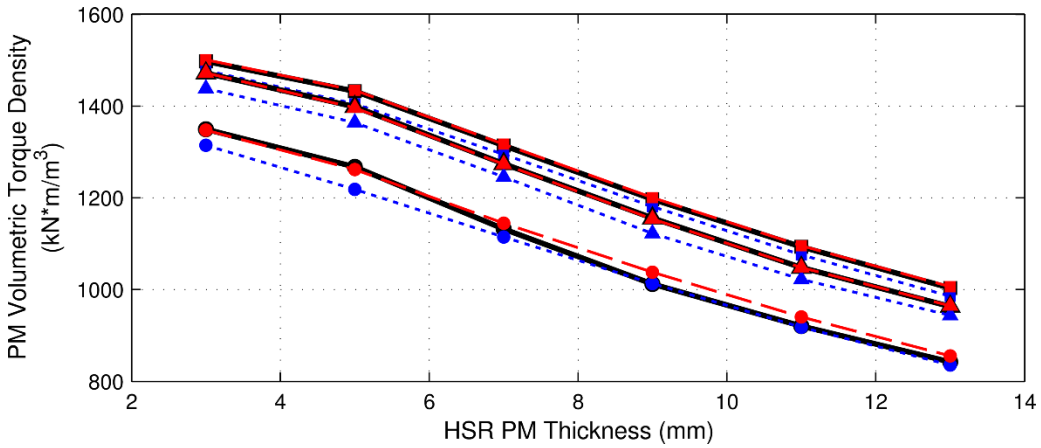


Figure 118. Variation of Maximum PM Volumetric Torque Density with HSR PM Thickness

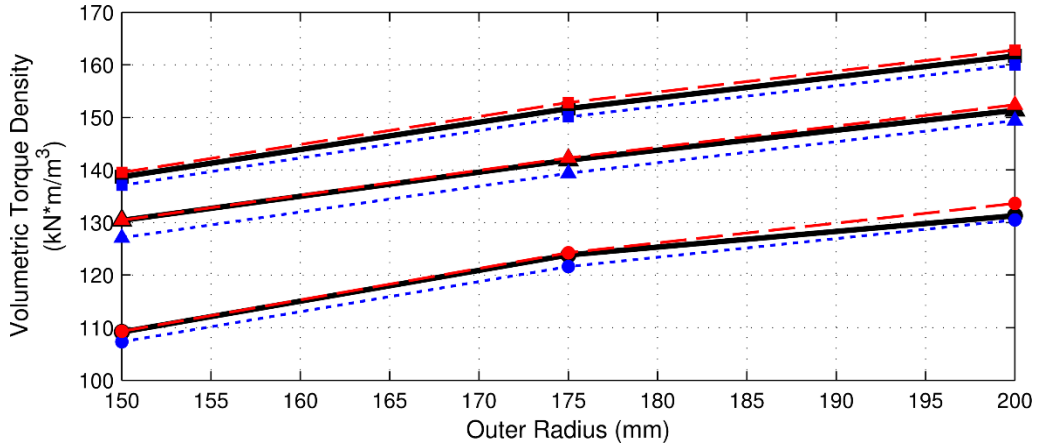


Figure 119. Variation of Maximum Volumetric Torque Density with Active Outer Radius

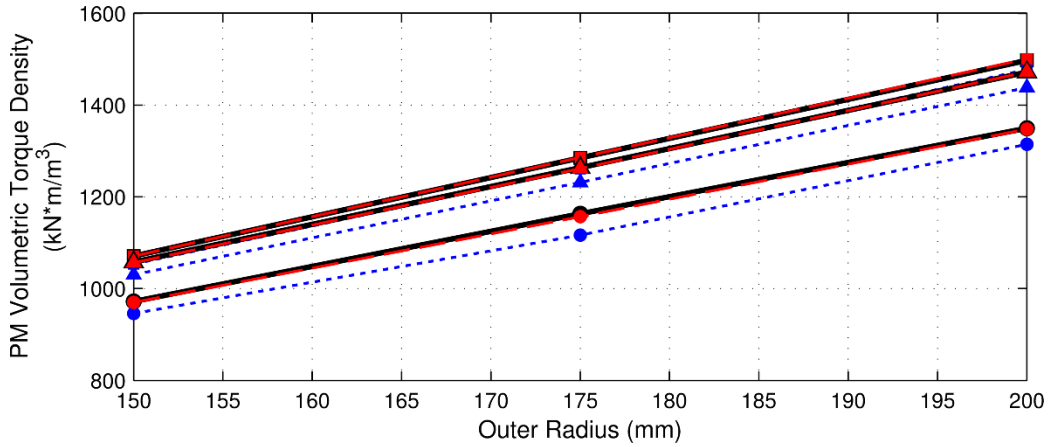


Figure 120. Variation of Maximum PM Volumetric Torque Density with Active Outer Radius

Table 22 provides some basic statistics summarizing the accuracy and speed of the coarse and fine mesh MEC models relative to the FEA model over the entire evaluated parametric design space. This data, along with the information in Figures 112-120, demonstrates that the MEC model is an extremely fast and accurate first pass analysis tool capable of tracking key electromagnetic design optimization trends. Although the fine mesh version of the MEC model is slightly more accurate, the coarse mesh MEC model

is also generally fairly accurate and appreciably faster, which might make it a better option for use in a first pass analysis. The correct mesh discretization selections will be dictated by the exact situation and analysis objectives.

Table 22. MEC Model Accuracy and Timing Statistics for Optimization Study

| Metric | Coarse MEC | Fine MEC | FEA |
|---|---|---|---|
| Minimum Percent Match | 95.3% | 99.1% | N/A |
| Maximum Percent Match | 100.9% | 103.2% | N/A |
| Average Percent Match | 98.8% | 100.3% | N/A |
| Average Absolute Match Error | 1.26% | 0.39% | N/A |
| Total Simulation Time (sec) | 5078 | 31,492 | 1,390,599 |
| Average Simulation Time (sec) | 0.11 | 0.68 | 29.8 |

The simulation times required for the MEC and FEA models depend on a plethora of different considerations, including the designs evaluated and the computers used in the analysis. The timing data in Table 22 is simply intended to provide a general indication of the relative speeds of the different models, rather than exact characterizations. A strict convergence criteria was used for the FEA model employed in this analysis to ensure extremely accurate results and a reliable set of reference data for comparison against the MEC model predictions. Based on other simulation studies, using a more typical, less strict convergence setting for the FEA model would likely yield comparable accuracy for most non-extreme design points and reduce the average simulation time for a single case to under 10 seconds. The average simulation time for both the MEC and FEA models was elevated due to the inclusion of high pole pair count designs in the optimization space, as both models require more simulation time for these designs than they do for the designs with lower pole pair counts. Regardless of these considerations, the results for this

optimization study indicate that the MEC model is exceptionally accurate and approximately 44-271 times faster than the FEA model. Some of this speedup is attributed to the linearity of the MEC model and the fact that it predetermines the orientation of the flux flow in the various flux tubes, which results in a simple system of scalar equations, while the FEA model is nonlinear and does not restrict the flux orientation in each element, but instead determines this information as part of the model solution. However, another factor in the relative simulation speed is likely the MEC model's use of predetermined mesh (flux tube) distributions which require negligible time to produce, as compared to the FEA model's adaptive mesh formation process. This suggests that a major source of the difference in speeds between the two approaches may not necessarily be an inherent difference between the MEC and FEA concepts, but rather a result of these particular embodiments of the techniques. The ambiguity of the source of this speedup is a repeated theme throughout MEC literature, which frequently pits generalized commercial FEA software against custom MEC models that simply use less elements and produce less accurate solutions. Further investigation must be done to perform a more even comparison and characterize the tradeoffs between speed and accuracy for these two methods, but these results clearly indicate that the MEC approach is an enticing and potentially situationally advantageous analysis technique.

# 9. DEVELOPMENT OF A 3D MAGNETIC EQUIVALENT CIRCUIT MODEL FOR RADIAL FLUX MAGNETIC GEARS

## 9.1 Geometry Discretization

If necessary, the 2D MEC magnetic gear model can easily be extended to a full 3D MEC model. The 3D MEC mesh is systematically formed by using the same angular and radial layers employed in the 2D MEC and further subdividing the system geometry into axial or z-coordinate layers (ZL). Each intersection of a radial layer, an angular layer, and an axial layer defines a 3D node cell. Every 3D node cell consists of two radially directed permeances, two tangentially directed permeances, and two axially directed permeances, each of which is connected to the center node of the cell and one of the cell's radial, tangential, or axial boundaries, as shown in Figure 121. The radial and tangential permeances are calculated in the same manner as for the 2D MEC, according to (33) and (34). Additionally, if the node cell corresponds to a permanent magnet, then the radially directed injected fluxes are also calculated in the same manner as for the 2D MEC, according to (35)-(43). A conceptual illustration of an axially oriented flux tube is provided in Figure 122 and the formula for the permeance of each axially directed flux tube ($\mathcal{P}_{ax}$) is given by (61). Note that each axially directed flux tube corresponds to the full radial width of its node cell, the full angular width of its node cell, and one half of the axial height of its node cell. Accordingly, as with the radial and tangential permeance expressions in (33) and (34), $R_{in}$ indicates the inner radius of the flux tube, $R_{out}$ denotes the outer radius of the flux tube, $\Delta\theta$ is the uniform angular width of the flux tube (in

radians), Δz is the uniform axial height of the flux tube, and μ is the permeability of the flux tube material.

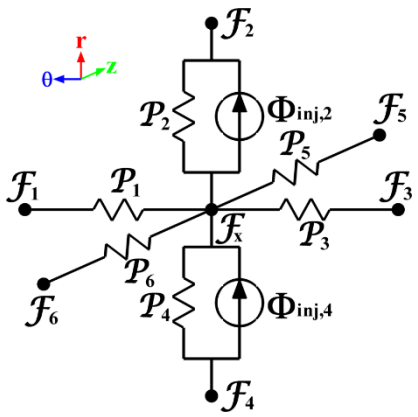


Figure 121. Annotated 3D Node Cell Schematic

$$\mathcal{P}_{ax} = \int_{R_{in}}^{R_{out}} \frac{\mu \cdot \Delta\theta \cdot r \cdot dr}{\Delta z} = \left(\frac{\mu \cdot \Delta\theta}{2 \cdot \Delta z}\right) \cdot \left(R_{out}^2 - R_{in}^2\right) \tag{61}$$

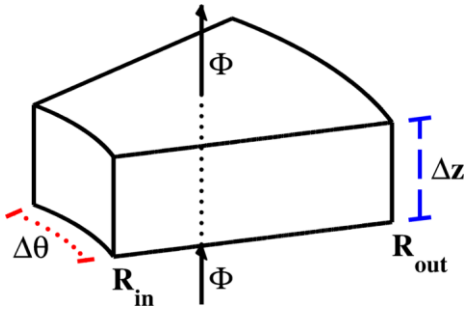


Figure 122. Conceptual Illustration of an Axially Oriented Flux Tube

## 9.2 In-Gear Permeances

Applying Gauss's law for magnetism to each 3D node cell in the full MEC, such as the one depicted in Figure 121, yields a node MMF equation of the form given in (62). This expression can be rearranged into the form of (63) which clearly demonstrates the relationship between the basic 3D MEC node MMF equation and the basic 2D MEC node

MMF equation given in (44). The first term in (63), $\Phi_{x,2D}$, is defined in (64) as the algebraic sum of all fluxes flowing out of node x due to the MMFs of nodes in the same axial layer and it is equal to the entire left side of the 2D MEC node MMF equation given in (44). The second term on the left side of (63) is simply the product of the sum of all axially directed permeances attached to the target node (node "x") and the MMF of the target node ($\mathcal{F}_x$). The remaining two terms in (63) represent the algebraic sum of the axial flux components flowing out of node x due to the axially directed permeances attached to the target node and the MMFs of the corresponding axially adjacent nodes. As is the case for the 2D MEC node MMF equation, the terms on the right side correspond to the algebraic sum of the injected flux sources flowing into the target node.

$$(\mathcal{P}_1 + \mathcal{P}_2 + \mathcal{P}_3 + \mathcal{P}_4 + \mathcal{P}_5 + \mathcal{P}_6)\cdot\mathcal{F}_x - \sum_{i=1}^{6} \mathcal{P}_i\cdot\mathcal{F}_i = -\Phi_{inj,2} + \Phi_{inj,4} \tag{62}$$

$$\Phi_{x,2D} + (\mathcal{P}_5 + \mathcal{P}_6)\cdot\mathcal{F}_x - \mathcal{P}_5\cdot\mathcal{F}_5 - \mathcal{P}_6\cdot\mathcal{F}_6 = -\Phi_{inj,2} + \Phi_{inj,4} \tag{63}$$

$$\Phi_{x,2D} = (\mathcal{P}_1 + \mathcal{P}_2 + \mathcal{P}_3 + \mathcal{P}_4)\cdot\mathcal{F}_x - \mathcal{P}_1\cdot\mathcal{F}_1 - \mathcal{P}_2\cdot\mathcal{F}_2 - \mathcal{P}_3\cdot\mathcal{F}_3 - \mathcal{P}_4\cdot\mathcal{F}_4 \tag{64}$$

The use of 3D node cells is effectively equivalent to building the full 3D MEC by stacking 2D MEC layers on top of each other and connecting corresponding nodes in adjacent 2D MEC layers (adjacent axial layers) with intermediate layers of axially directed permeances. The 3D MEC schematic snippet in Figure 123 illustrates this layering arrangement. The 3D MEC model includes both the gear geometry and a defined region of air or free space axially beyond the gear. The total number of axial layers, $N_{ZL}$, in the 3D MEC is defined in (65) as the sum of the number of axial layers in the gear, $N_{LIG}$, and the number of axial layers outside of the gear, $N_{LOG}$, which are both independent user

controlled parameters in addition to the 8 other 2D MEC mesh discretization parameters. Furthermore, because more axial resolution is generally required at the axial ends of the gear, as compared to the axial middle of the gear, the relative distribution of the total model axial height throughout the various layers is not necessarily uniform and can be directly specified as needed for different designs. Finally, in addition to the previously discussed 2D cross-sectional symmetry exhibited by certain designs, the basic radial flux magnetic gear topology always has symmetry about the z plane corresponding to the axial middle of the gear. Since this feature is true for all ideal designs, only one axial half of the gear stack is considered in this review of the 3D MEC model to reduce the necessary number of axial layers. The full 3D MEC solution information is then obtained by scaling the "half-stack" model results. This solution is exactly equivalent to that which would be obtained by including the full axial stack in the 3D model.

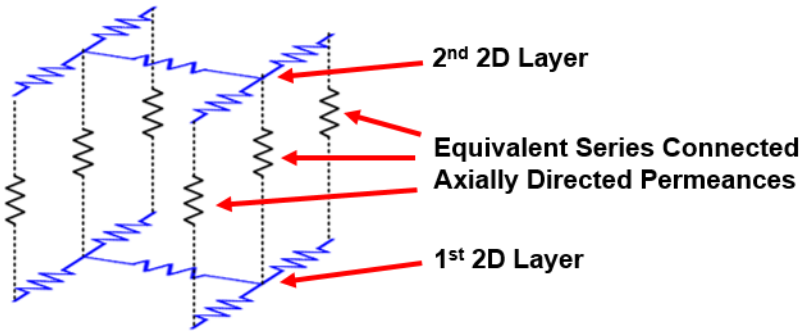


Figure 123. Construction of the 3D MEC from Axially Connected 2D MEC Layers

$$N_{ZL} = N_{LIG} + N_{LOG} \tag{65}$$

Each node in the 3D MEC corresponds to a node MMF equation of the same basic form as the one shown in (62) or (63) and there are $N_{3D}$ total nodes in a 3D MEC model, where $N_{3D}$ is the product of the number of angular layers, the total number of radial layers,

and the total number of axial layers, as indicated in (66). Thus, the resulting system of linear equations for the full 3D MEC model can be expressed in matrix form according to (67), where $\mathcal{P}_{3D}$ is the ($N_{3D}$ x $N_{3D}$) 3D system permeance matrix, $\mathcal{F}_{3D}$ is the ($N_{3D}$ x 1) column vector of unknown MMFs for each corresponding node in the 3D MEC, and $\Phi_{3D}$ is the ($N_{3D}$ x 1) column vector of the algebraic sums of the injected fluxes entering each corresponding node in the 3D MEC. The $i^{th}$ row in $\mathcal{P}_{3D}$ corresponds to the $i^{th}$ node in the MEC and contains the permeance coefficients for that node's MMF equation, such as those shown on the left side of (62). The $j^{th}$ column in $\mathcal{P}_{3D}$ also corresponds to the $j^{th}$ node in the MEC. Entry $\mathcal{P}_{3D(i,j)}$ in $\mathcal{P}_{3D}$ contains the permeance coefficient which describes the impact of the $j^{th}$ node's MMF on the $i^{th}$ node's MMF equation. Each diagonal entry $\mathcal{P}_{3D(i,i)}$ in $\mathcal{P}_{3D}$ contains the positive sum of all equivalent permeances attached directly to node i. The permeance coefficient of $\mathcal{F}_x$ in (62) is an example of what would become a diagonal entry in the matrix representation of the system of equations. Each diagonal entry indicates the impact of the corresponding node's MMF on its own node MMF equation. Each off-diagonal entry $\mathcal{P}_{3D(i,j)}$ in $\mathcal{P}_{3D}$ (entries where $i \neq j$) contains the negative value of the equivalent permeance directly connecting nodes i and j. If there is no direct connection between nodes i and j (a permeance path that does not go through another node), then the corresponding entry in $\mathcal{P}_{3D}$ is zero. The permeance coefficients of $\mathcal{F}_1$, $\mathcal{F}_2$, $\mathcal{F}_3$, $\mathcal{F}_4$, $\mathcal{F}_5$ and $\mathcal{F}_6$ in (62) are examples of what would become off-diagonal entries in the matrix representation of the system of equations.

$$N_{3D} = N_{AL} \cdot N_{RL} \cdot N_{ZL} \tag{66}$$

$$\mathcal{P}_{3D}\mathcal{F}_{3D} = \Phi_{3D} \tag{67}$$

$\mathcal{P}_{3D}$, can be constructed in a general form with its constituent submatrices as shown in (68)-(82). The arrangement of these matrices is based on the MEC model node numbering system, in which the first $N_{2D}$ rows and the first $N_{2D}$ columns in $\mathcal{P}_{3D}$ correspond to nodes in the first axial layer, and the next $N_{2D}$ rows and the next $N_{2D}$ columns correspond to nodes in the second axial layer, and so on. Within any set of $N_{2D}$ rows or columns, the first $N_{AL}$ rows or columns correspond to nodes in the first radial layer of that axial layer and next $N_{AL}$ rows or columns correspond to nodes in the second radial layer of that axial layer, and so on, as was the case for the organization of a single 2D MEC system permeance matrix, $\mathcal{P}_{2D}$.

The first three submatrices used in the construction of $\mathcal{P}_{3D}$ correspond to permeances inside the active gear geometry and are given in (68)-(70). $\mathcal{P}_{Ax,IG}$, defined in (68), is an ($N_{2D}$ x $N_{2D}$) matrix in which each diagonal entry $\mathcal{P}_{Ax,IG(i:i)}$ contains the "per-meter" value of the axial permeance connected to the $i^{th}$ node in each 2D layer, assuming that the axial flux tubes are one meter long and contained entirely in the gear (and not the air region outside of the gear). All off-diagonal entries in $\mathcal{P}_{Ax,IG}$ are zero. The ($N_{2D}$ x $N_{2D}$) axial permeance matrix, $\mathcal{P}_{IG(m:m-1)}$, corresponding to the axial permeances connecting in-gear axial layer m to in-gear axial layer m-1 can then be formed from $\mathcal{P}_{Ax,IG}$, according to (69). The scaling term used in (69) is simply the inverse of the appropriate axial path

length, which is the average of the axial height of in-gear axial layer m, $h_{IG,m}$, and the axial height of in-gear axial layer m-1, $h_{IG,m-1}$. As indicated in (70), the ($N_{2D}$ x $N_{2D}$) matrix of radial and tangential permeances corresponding to in-gear axial layer m, $\mathcal{P}_{IG(m:m)}$, is formed by simply scaling the 2D MEC in-gear system permeance matrix, $\mathcal{P}_{2D,IG}$, by the height of in-gear axial layer m. The matrix $\mathcal{P}_{2D,IG}$ is still formed according to (50) exactly as it is in a 2D MEC model, assuming a unit height.

$$\mathcal{P}_{Ax,IG} = \begin{bmatrix} \mathcal{P}_{Ax,IG(1:1)} & 0 & \cdots & 0 \\ 0 & \mathcal{P}_{Ax,IG(2:2)} & \ddots & \vdots \\ \vdots & \ddots & \ddots & 0 \\ 0 & \cdots & 0 & \mathcal{P}_{Ax,IG(N_{2D}:N_{2D})} \end{bmatrix} \tag{68}$$

$$\mathcal{P}_{IG(m:m-1)} = \mathcal{P}_{IG(m-1:m)} = \left(\frac{2}{h_{IG,m} + h_{IG,m-1}}\right) \cdot \mathcal{P}_{Ax,IG} \tag{69}$$

$$\mathcal{P}_{IG(m:m)} = h_{IG,m} \cdot \mathcal{P}_{2D,IG} \tag{70}$$

### 9.3 Out-of-Gear Permeances

There is an analogous out-of-gear permeance matrix corresponding to each of the three previously described in-gear permeance matrices. The matrix $\mathcal{P}_{Ax,OG}$, defined in (71), is an ($N_{2D}$ x $N_{2D}$) matrix in which each diagonal entry $\mathcal{P}_{Ax,OG(i:i)}$ contains the "per-meter" value of the axial permeance connected to the $i^{th}$ node in each 2D layer, assuming that the axial flux tubes are one meter long and contained entirely in the air region outside of the gear. As was the case with $\mathcal{P}_{Ax,IG}$, all off-diagonal entries in $\mathcal{P}_{Ax,OG}$ are zero. The

($N_{2D}$ x $N_{2D}$) axial permeance matrix, $\mathcal{P}_{OG(m:m-1)}$, corresponding to the axial permeances connecting out-of-gear axial layer m to out-of-gear axial layer m-1 can then be formed from $\mathcal{P}_{Ax,OG}$, according to (72). The scaling term used in (72) is the inverse of the appropriate axial path length, which is the average of the axial height of out-of-gear axial layer m, $h_{OG,m}$, and the axial height of out-of-gear axial layer m-1, $h_{OG,m-1}$. As indicated in (73), the ($N_{2D}$ x $N_{2D}$) matrix of radial and tangential permeances corresponding to out-of-gear axial layer m, $\mathcal{P}_{OG(m:m)}$, is formed by scaling the 2D MEC out-of-gear system permeance matrix, $\mathcal{P}_{2D,OG}$, by the height of out-of-gear axial layer m. $\mathcal{P}_{2D,OG}$, is formed in the same manner as $\mathcal{P}_{2D,IG}$, but all of the permeabilities used in the individual permeance calculations are set to $\mu_0$ because the flux tubes are located entirely in air.

$$\mathcal{P}_{Ax,OG} = \begin{bmatrix} \mathcal{P}_{Ax,OG(1:1)} & 0 & \cdots & 0 \\ 0 & \mathcal{P}_{Ax,OG(2:2)} & \ddots & \vdots \\ \vdots & \ddots & \ddots & 0 \\ 0 & \cdots & 0 & \mathcal{P}_{Ax,OG(N_{2D}:N_{2D})} \end{bmatrix} \tag{71}$$

$$\mathcal{P}_{OG(m:m-1)} = \mathcal{P}_{OG(m-1:m)} = \left(\frac{2}{h_{OG,m} + h_{OG,m-1}}\right) \cdot \mathcal{P}_{Ax,OG} \tag{72}$$

$$\mathcal{P}_{OG(m:m)} = h_{OG,m} \cdot \mathcal{P}_{2D,OG} \tag{73}$$

### 9.4 Boundary Permeances

All of the preceding matrices defined in (68)-(73) correspond to permeances located either entirely in the active gear region, (68)-(70), or entirely in the air region

outside of the gear, (71)-(73). However, the set of equivalent axial permeances connecting the last (top) in-gear axial layer to the first (bottom) out-of-gear axial layer, is formed by the series connection of the axial permeances corresponding to the top half of the last in-gear axial layer and the axial permeances corresponding to the bottom half of the first out-of-gear axial layer. $\mathcal{P}_{Bound}$ is an ($N_{2D}$ x $N_{2D}$) matrix, representing these boundary axial permeances. Each diagonal entry $\mathcal{P}_{Bound(i:i)}$ contains the equivalent axial permeance connecting the $i^{th}$ node in the last in-gear axial layer to the $i^{th}$ node in the first out-of-gear axial layer. As defined in (74), each diagonal entry $\mathcal{P}_{Bound(i:i)}$ is formed by the scaled series combination of the corresponding diagonal entries in $\mathcal{P}_{Ax,IG}$ and $\mathcal{P}_{Ax,OG}$ ($\mathcal{P}_{Ax,IG(i:i)}$ and $\mathcal{P}_{Ax,OG(i:i)}$). All off-diagonal entries in $\mathcal{P}_{Bound}$ are zero.

$$\mathcal{P}_{Bound(i:i)} = \left(\left(\frac{h_{IG,N_{LIG}}}{2}\right)\cdot\left(\frac{1}{\mathcal{P}_{Ax,IG(i:i)}}\right) + \left(\frac{h_{OG,1}}{2}\right)\cdot\left(\frac{1}{\mathcal{P}_{Ax,OG(i:i)}}\right)\right)^{-1} \tag{74}$$

## 9.5 Formation of the System of Equations

The portion of $\mathcal{P}_{3D}$ corresponding to the in-gear nodes is constructed according to (75)-(77). The (($N_{LIG}$·$N_{2D}$) x ($N_{LIG}$·$N_{2D}$)) matrix $\mathcal{P}_{3D,Ax,IG}$, defined in (75), contains the coefficients corresponding to axial permeances connected to in-gear nodes. Each diagonal submatrix entry $\mathcal{P}_{3D,Ax,IG(m,m)}$ in $\mathcal{P}_{3D,Ax,IG}$ contains the sum of the diagonal axial permeance matrices corresponding to axial permeances connected to nodes in the $m^{th}$ in-gear axial layer. Each individual diagonal entry $\mathcal{P}_{3D,Ax,IG(i,i)}$ in $\mathcal{P}_{3D,Ax,IG}$ contains the sum of all equivalent axial permeances connected to the $i^{th}$ in-gear node. These diagonal entries are

analogous to the permeance coefficient of $\mathcal{F}_x$ in (63). Each off-diagonal submatrix entry $\mathcal{P}_{3D,Ax,IG(m,n)}$ in $\mathcal{P}_{3D,Ax,IG}$ (entries where $m \neq n$) contains the negative diagonal axial permeance matrix corresponding to axial permeances connecting the $m^{th}$ in-gear axial layer to the $n^{th}$ in-gear axial layer. Each individual off-diagonal entry $\mathcal{P}_{3D,Ax,IG(i,j)}$ in $\mathcal{P}_{3D,Ax,IG}$ (entries where $i \neq j$) contains the negative value of the equivalent axial permeance connecting the $i^{th}$ in-gear node to the $j^{th}$ in-gear node. These off-diagonal entries are analogous to the permeance coefficients of $\mathcal{F}_5$ and $\mathcal{F}_6$ in (63). Thus, for the in-gear nodes, $\mathcal{P}_{3D,Ax,IG}$ represents the terms on the left- side of (63), excluding $\Phi_{x,2D}$. The $((N_{LIG} \cdot N_{2D}) \times (N_{LIG} \cdot N_{2D}))$ matrix $\mathcal{P}_{3D,CS,IG}$, defined in (76), contains the coefficients corresponding to permeances connected to in-gear nodes within their own cross-sectional 2D layer (radial and tangential permeances, but not axial permeances). Each diagonal submatrix entry $\mathcal{P}_{3D,CS,IG(m,m)}$ in $\mathcal{P}_{3D,CS,IG}$ is the 2D MEC system permeance matrix corresponding to the $m^{th}$ 2D (axial) in-gear layer. These diagonal submatrices are analogous to the permeance coefficients in the $\Phi_{x,2D}$ term of (63), as defined in (64). The portion of $\mathcal{P}_{3D}$ corresponding to the in-gear nodes, $\mathcal{P}_{3D,IG}$, is formed by adding these submatrices as shown in (77). Note that the first submatrix row of $\mathcal{P}_{3D,Ax,IG}$ only uses a single diagonal axial submatrix, $\mathcal{P}_{IG(1:2)}$. This is due to the previously discussed use of a "half-stack" fractional model based on the gear's symmetry about the z-plane corresponding to its axial center. This effectively imposes the necessary zero axial flux boundary condition on the axial bottom of the "half-stack" model (the axial middle of the full stack gear model). If designs without

this symmetry need to be evaluated, such as those with axial misalignment, the 3D MEC system permeance matrix can easily be adjusted, using the same basic formation process, to model the full gear stack and two air regions outside of the gear (one on each end).

$$\mathcal{P}_{3D,Ax,IG} = \begin{bmatrix} \mathcal{P}_{IG(1:2)} & -\mathcal{P}_{IG(1:2)} & 0 & \cdots & 0 \\ -\mathcal{P}_{IG(2:1)} & \mathcal{P}_{IG(2:1)} + \mathcal{P}_{IG(2:3)} & \ddots & \ddots & \vdots \\ 0 & \ddots & \ddots & \ddots & 0 \\ \vdots & \ddots & \ddots & \ddots & -\mathcal{P}_{IG(N_{LIG}-1:N_{LIG})} \\ 0 & \cdots & 0 & -\mathcal{P}_{IG(N_{LIG}:N_{LIG}-1)} & \mathcal{P}_{IG(N_{LIG}:N_{LIG}-1)} + \mathcal{P}_{Bound} \end{bmatrix} \quad (75)$$

$$\mathcal{P}_{3D,CS,IG} = \begin{bmatrix} \mathcal{P}_{IG(1:1)} & 0 & \cdots & 0 \\ 0 & \mathcal{P}_{IG(2:2)} & \ddots & \vdots \\ \vdots & \ddots & \ddots & 0 \\ 0 & \cdots & 0 & \mathcal{P}_{IG(N_{LIG}:N_{LIG})} \end{bmatrix} \quad (76)$$

$$\mathcal{P}_{3D,IG} = \mathcal{P}_{3D,Ax,IG} + \mathcal{P}_{3D,CS,IG} \quad (77)$$

Again, there is an analogous out-of-gear permeance matrix corresponding to each of the three previously described in-gear permeance matrices, and the portion of $\mathcal{P}_{3D}$ corresponding to the out-of-gear nodes is constructed according to (78)-(80). The $((N_{LOG} \cdot N_{2D}) \times (N_{LOG} \cdot N_{2D}))$ matrix $\mathcal{P}_{3D,Ax,OG}$, defined in (78), contains the coefficients corresponding to axial permeances connected to out-of-gear nodes. Each diagonal submatrix entry $\mathcal{P}_{3D,Ax,OG(m,m)}$ in $\mathcal{P}_{3D,Ax,OG}$ contains the sum of the diagonal axial

permeance matrices corresponding to axial permeances connected to nodes in the $m^{th}$ out-of-gear axial layer. Each individual diagonal entry $\mathcal{P}_{3D,Ax,OG(i,i)}$ in $\mathcal{P}_{3D,Ax,OG}$ contains the sum of all equivalent axial permeances connected to the $i^{th}$ out-of-gear node. Each off-diagonal submatrix entry $\mathcal{P}_{3D,Ax,OG(m,n)}$ in $\mathcal{P}_{3D,Ax,OG}$ (entries where $m \neq n$) contains the negative diagonal axial permeance matrix corresponding to axial permeances connecting the $m^{th}$ and $n^{th}$ out-of-gear axial layers. Each individual off-diagonal entry $\mathcal{P}_{3D,Ax,OG(i,j)}$ in $\mathcal{P}_{3D,Ax,OG}$ (entries where $i \neq j$) contains the negative value of the equivalent axial permeance connecting the $i^{th}$ and $j^{th}$ out-of-gear nodes. The $((N_{LOG} \cdot N_{2D}) \times (N_{LOG} \cdot N_{2D}))$ matrix $\mathcal{P}_{3D,CS,OG}$, defined in (79), contains the coefficients corresponding to permeances connected to out-of-gear nodes within their own cross-sectional 2D layer (radial and tangential permeances, but not axial permeances). Each diagonal submatrix entry $\mathcal{P}_{3D,CS,OG(m,m)}$ in $\mathcal{P}_{3D,CS,OG}$ is the 2D MEC system permeance matrix corresponding to the $m^{th}$ 2D (axial) out-of-gear layer. The portion of $\mathcal{P}_{3D}$ corresponding to the out-of-gear nodes, $\mathcal{P}_{3D,OG}$, is formed by adding these submatrices as shown in (80).

$$\mathcal{P}_{3D,Ax,OG} = \begin{bmatrix} \mathcal{P}_{Bound} + \mathcal{P}_{OG(1:2)} & -\mathcal{P}_{OG(1:2)} & 0 & \cdots \\ -\mathcal{P}_{OG(2:1)} & \mathcal{P}_{OG(2:1)} + \mathcal{P}_{OG(2:3)} & \ddots & \ddots \\ 0 & \ddots & \ddots & -\mathcal{P}_{OG(N_{LOG}-1:N_{LOG})} \\ \vdots & \ddots & -\mathcal{P}_{OG(N_{LOG}:N_{LOG}-1)} & \mathcal{P}_{OG(N_{LOG}:N_{LOG}-1)} \end{bmatrix} \quad (78)$$

$$\mathcal{P}_{3D,CS,OG} = \begin{bmatrix} \mathcal{P}_{OG(1:1)} & 0 & \cdots & 0 \\ 0 & \mathcal{P}_{OG(2:2)} & \ddots & \vdots \\ \vdots & \ddots & \ddots & 0 \\ 0 & \cdots & 0 & \mathcal{P}_{OG(N_{LIG}:N_{LIG})} \end{bmatrix} \tag{79}$$

$$\mathcal{P}_{3D,OG} = \mathcal{P}_{3D,Ax,OG} + \mathcal{P}_{3D,CS,OG} \tag{80}$$

The $((N_{LIG} \cdot N_{2D})$ x $(N_{LOG} \cdot N_{2D}))$ matrix $\mathcal{P}_{3D,Bound}$, defined in (81), contains the portion of the overall 3D MEC system permeance matrix corresponding solely to the boundary axial permeances connecting nodes in the top in-gear layer and the bottom out-of-gear layer. All of the entries in this matrix are zeros, except for the single submatrix $\mathcal{P}_{Bound}$ in the corner. $\mathcal{P}_{3D}$ is created by concatenating the submatrices $\mathcal{P}_{3D,Bound}$, $\mathcal{P}^{T}_{3D,Bound}$ (the transpose of $\mathcal{P}_{3D,Bound}$), $\mathcal{P}_{3D,IG}$, and $\mathcal{P}_{3D,OG}$, in the arrangement indicated by (82). $\mathcal{P}_{3D}$ is always symmetric because all permeances in the MEC are bidirectional.

$$\mathcal{P}_{3D,Bound} = \begin{bmatrix} 0 & \cdots & \cdots & 0 \\ \vdots & \ddots & \ddots & \vdots \\ 0 & \ddots & \ddots & \vdots \\ \mathcal{P}_{Bound} & 0 & \cdots & 0 \end{bmatrix} \tag{81}$$

$$\mathcal{P}_{3D} = \begin{bmatrix} \mathcal{P}_{3D,IG} & -\mathcal{P}_{3D,Bound} \\ -\mathcal{P}^{T}_{3D,Bound} & \mathcal{P}_{3D,OG} \end{bmatrix} \tag{82}$$

Each node in the 3D MEC has six adjacent nodes: one on the radial inside, one on the radial outside, one on the clockwise circumferential side, one on the counterclockwise

circumferential side, one on the axial bottom side, and one on the axial top side. The only exceptions to this rule are the nodes in the innermost radial layer, which do not have any adjacent nodes on the radial inside, the nodes in the outermost radial layer, which do not have any adjacent nodes on the radial outside, the nodes in the bottom in-gear axial layer which do not have any adjacent nodes on the axial bottom side, and the nodes in the top out-of-gear axial layer which do not have any adjacent nodes on the axial top side. In light of this observation and close inspection of the matrices defined in (68)-(82), it is evident that each row in $\mathcal{P}_{3D}$ which does not correspond to one of these boundary layers has seven non-zero entries, one for each adjacent node, as well as the diagonal entry in each row. Thus, $N_{NZ3D}$, the total number of non-zero entries in $\mathcal{P}_{3D}$, is given by (83) and the sparseness of $\mathcal{P}_{3D}$ can be calculated according to (84). This expression indicates that, as expected, 3D MEC permeance matrices are even more sparse than 2D MEC permeance matrices; therefore, the MATLAB implementation of the MEC model stores $\mathcal{P}_{3D}$ as a sparse matrix in order to dramatically reduce the requisite amount of memory used by the program.

$$N_{NZ3D} = 7 \cdot N_{AL} \cdot N_{RL} \cdot N_{ZL} - 2 \cdot N_{AL} \cdot (N_{RL} + N_{ZL}) \tag{83}$$

$$\text{Sparseness of } \mathcal{P}_{3D} = \left(1 - \frac{N_{NZ3D}}{N_{3D}^2}\right) \cdot 100\% \tag{84}$$

## 9.6 Solution of the System of Equations

The 3D MEC model is "solved" by solving the linear system of equations given in (67) for the $N_{3D}$ unknown node MMFs in the column vector $\mathcal{F}_{3D}$. As indicated in the description of the 2D MEC implementation, if the 3D MEC model has cross-sectional

symmetry, then it can be analyzed by solving the subset of equations corresponding to nodes in a symmetrical fraction of the "half-stack" model and extending that solution to the remaining symmetrical fraction(s). Additionally, the same rules for the treatment of a reference node provided in the discussion of the 2D MEC solution also apply to the 3D MEC solution. In complete "half-stack" 3D MEC models or fractional models with even symmetry, the potential of the first node is selected as the reference potential of zero. This makes the first node equation redundant, allowing the first row of $\mathcal{P}_{3D}$ and $\Phi_{3D}$ to be eliminated. Furthermore, the first column of $\mathcal{P}_{3D}$ is eliminated because the first node has zero potential, and the remaining system can be solved. However, for models with odd symmetry, it is desirable for corresponding nodes in adjacent fractions of the model to have potentials with the same magnitudes and opposite signs. This choice effectively determines the zero potential reference, which may not correspond to any of the nodes. Thus, for models with odd symmetry, the first row of $\mathcal{P}_{3D}$ and $\Phi_{3D}$ and the first column of $\mathcal{P}_{3D}$ must not be eliminated before the system is solved.

Ideally, the MEC system can be solved by inverting the appropriate part of the system permeance matrix, $\mathcal{P}_{3D}$', as shown in (85), where $\mathcal{P}_{3D}$', $\mathcal{F}_{3D}$', and $\Phi_{3D}$' represent the relevant portions of $\mathcal{P}_{3D}$, $\mathcal{F}_{3D}$, and $\Phi_{3D}$ based on the application of the preceding discussion of symmetry and the reference node. However the 3D MEC system is much larger than its corresponding 2D MEC system; therefore, it is even more infeasible to simply invert the 3D MEC system matrix due to the computational time and memory requirements. In order to mitigate these issues, the MATLAB implementation of the 3D

MEC model uses the same approach applied in the 2D MEC and solves the system by factorizing $\mathcal{P}_{3D}$' and solving the corresponding triangular systems as described in [145]. The use of sparse matrices and an optimal factorization method are even more beneficial with respect to memory requirements and simulation run times for the solution of 3D MEC models.

$$\mathcal{F}_{3D}' = (\mathcal{P}_{3D}')^{-1}\Phi_{3D}' \tag{85}$$

Once a 3D MEC model has been "solved" for the vector of node MMFs, this information can be used along with the reluctances of the flux tubes to calculate various other quantities of interest, such as the flux in any flux tube and the flux density at any position in the gear. Similarly to the 2D MEC model, the 3D MEC model also uses Maxwell stress tensors for torque calculations. In particular, the torque on the HSR, $\tau_{HSR,3D}$, and the torque on the LSR, $\tau_{LSR,3D}$, are calculated using Maxwell stress tensors according to (86) and (87), respectively. $R_{HSAG}$ and $R_{LSAG}$ represent the radii of the integration paths in the high speed air gap and low speed air gap, while $B_r$ and $B_\theta$ represent the radial and tangential components of the magnetic flux density, which are both functions of the position in the gear. The parameter $h_{Total}$ denotes the total axial height of the full stack model (including the air regions beyond both axial ends of the gear). This implementation of the 3D MEC uses a symmetrical "half-stack" model; therefore, the torques are given by integrating the Maxwell stress tensor over the full axial length of the "half stack" model (from $z = 0$ to $z = h_{Total}/2$) and then doubling that torque to account for the other half of the stack. The torque on the entire modulator structure, $\tau_{Mods,3D}$ is then calculated according (88).

$$\tau_{HSR,3D} = 2\cdot\left(\frac{r_{HSAG}^2}{\mu_0}\right)\cdot\int_0^{h_{total}/2}\int_0^{2\pi} B_r(r_{HSAG},\theta,z)\cdot B_\theta(r_{HSAG},\theta,z)\cdot d\theta\cdot dz \tag{86}$$

$$\tau_{LSR,3D} = -2\cdot\left(\frac{r_{LSAG}^2}{\mu_0}\right)\cdot\int_0^{h_{total}/2}\int_0^{2\pi} B_r(r_{LSAG},\theta,z)\cdot B_\theta(R_{LSAG},\theta,z)\cdot d\theta\cdot dz \tag{87}$$

$$\tau_{Mods,3D} = -\left(\tau_{HSR,3D} + \tau_{LSR,3D}\right) \tag{88}$$

# 10. EVALUATION OF THE RADIAL FLUX MAGNETIC GEAR 3D MAGNETIC EQUIVALENT CIRCUIT MODEL

## 10.1 Impact of Axial Discretization

The 3D MEC model developed in the previous section introduced 2 new discretization parameters, the number of axial layers in the gear, $N_{LIG}$, and the number of axial layers outside of the gear, $N_{LOG}$. Because there is more axial leakage flux in the space near the axial ends of the gear than there is in the axial middle of the gear or the out-of-gear air regions further removed from the gear, the axial ends of the gear and the portions of the air region just beyond the axial ends of the gear require the most axial resolution. In light of this consideration, rather than simply using uniform height axial layers throughout the active gear stack and the out-of-gear air region, this analysis develops and employs the axial layer height distributions described by (89)-(92). The expression in (89) gives the normalized height of the $m^{th}$ in-gear axial layer, $\bar{h}_{IG,m}$, as a function of the total number of in-gear axial layers, $N_{LIG}$, and the in-gear axial layer distribution factor, $k_{z,IG}$. Since this analysis uses a symmetrical half stack gear model, the first in-gear axial layer (m = 1) corresponds to the bottom of the half stack model, which is axially adjacent to the middle of the full gear. Layer index $m = N_{LIG}$ corresponds to the in-gear axial layer at the end of the gear stack, which is axially adjacent to the out-of-gear air region. The normalized height of the $m^{th}$ in-gear axial layer, $\bar{h}_{IG,m}$, indicates the fraction of the MEC model's total in-gear region axial height, $h_{IG}$, that corresponds to the $m^{th}$ in-gear axial layer. As this analysis uses a half stack model, the total in-gear region

axial height, $h_{IG}$, is only half of the actual full magnetic gear stack height. The actual height of the $m^{th}$ in-gear axial layer, $h_{IG,m}$, is then given by (90). Thus, the in-gear axial layer distribution is controlled by 2 scalar parameters, $N_{LIG}$ and $k_{z,IG}$. Setting, $k_{z,IG}$.= 0 yields a uniform axial layer height distribution, with each axial layer having the same axial height. Setting $k_{z,IG} > 0$ results in a non-uniform distribution, with the first in-gear axial layer having the largest axial layer height (the least axial resolution) and the last in-gear axial layer having the smallest axial layer height (the most axial resolution). Increasing the value of $k_{z,IG}$ produces an increasingly aggressive and imbalanced in-gear axial layer distribution with more axial resolution at the axial end of the gear and less axial resolution in the axial middle of the gear.

$$\bar{h}_{IG,m} = \frac{\left(N_{LIG} - (m-1)\right)^{k_{z,IG}}}{\sum_{m=1}^{N_{LIG}} m^{k_{z,IG}}} \tag{89}$$

$$h_{IG,m} = \bar{h}_{IG,m} \cdot h_{IG} \tag{90}$$

$$\bar{h}_{OG,n} = \frac{n^{k_{z,OG}}}{\sum_{n=1}^{N_{LOG}} n^{k_{z,OG}}} \tag{91}$$

$$h_{OG,n} = \bar{h}_{OG,n} \cdot h_{OG} \tag{92}$$

The analogous expression in (91) defines the normalized axial height of the $n^{th}$ out-of-gear axial layer, $\bar{h}_{OG,n}$, as a function of the total number of out-of-gear axial layers, $N_{LOG}$, and the out-of-gear axial layer distribution factor, $k_{z,OG}$. For all MEC and FEA models used in this study, the total axial height of the out-of-gear air region, $h_{OG}$, was set equal to double the full stack magnetic gear axial height. It is worth noting that this is an overly simplified approach to scaling the axial height of the out-of-gear air region, and a

more efficient tactic would likely involve determining this height as a function of relevant gear geometry parameters, such as the HSR permanent magnet pole arc and the effective air gap sizes. The first out-of-gear axial layer (n = 1) corresponds to the portion of the air region immediately adjacent to the end of the active gear stack. Out-of-gear axial layer index n = $N_{LOG}$ corresponds to the out-of-gear axial layer furthest away from the gear stack. The normalized height of the $n^{th}$ out-of-gear axial layer, $\bar{h}_{OG,n}$, denotes the fraction of the total out-of-gear air region axial height, $h_{OG}$, that corresponds to the $n^{th}$ out-of-gear axial layer. The actual height of the $n^{th}$ out-of-gear axial layer, $h_{OG,n}$, is then given by (92). Thus, much like the in-gear axial layer distribution, the out-of-gear axial layer distribution is also controlled by 2 scalar parameters, $N_{LOG}$ and $k_{z,OG}$. Setting, $k_{z,OG}$.= 0 yields a uniform axial layer height distribution, with each out-of-gear axial layer having the same axial height. Setting $k_{z,OG} > 0$ results in a non-uniform distribution, with the first out-of-gear axial layer having the smallest axial layer axial height (the most axial resolution) and the last out-of-gear axial layer having the largest axial layer height (the least axial resolution). Increasing the value of $k_{z,OG}$ produces an increasingly aggressive and imbalanced out-of-gear axial layer distribution with more axial resolution at the end of the air region closest to the end of the gear stack and less axial resolution at the end of the air region furthest away from the gear stack.

In order to examine the impact of these axial discretization parameters, the same three base designs used in the evaluation of the 2D MEC model and summarized in Table 18 were analyzed at axial stack lengths of 30 mm, 100 mm, and 300 mm with both the 3D MEC model and a 3D FEA model. For all 3D MEC model simulations, the 2D MEC

discretization parameters were fixed at the values indicated in Table 23 based on the results of the 2D MEC model evaluation. First, the effects of the in-gear axial discretization parameters, $N_{LIG}$ and $k_{z,IG}$, were characterized by sweeping these variables through the 77 combinations of values specified in the first column of Table 24 for each of the three base designs at each of the three previously listed axial stack lengths. As indicated in Table 24, the out-of-gear discretization parameters, $N_{LOG}$ and $k_{z,OG}$, were fixed at values of 4 and 0 for these simulations. Next, the effects of the out-of-gear axial discretization parameters, $N_{LOG}$ and $k_{z,OG}$, were also independently characterized by sweeping these variables through the 77 combinations of values specified in the second column of Table 24 for each of the three base designs at each of the three previously mentioned axial stack lengths. As indicated in Table 24, the in-gear discretization parameters, $N_{LIG}$ and $k_{z,IG}$, were fixed at values of 4 and 0 for these simulations.

Table 23. Radial Flux Magnetic Gear 2D MEC Discretization Settings Used for Evaluation of 3D MEC Model

| Parameter | Description | Value |
|---|---|---|
| ALM | Angular layers multiplier | 10 |
| $N_{RL,HSBI}$ | Number of radial layers in the HSR back iron | 3 |
| $RLM_{HSPM}$ | HSR magnets radial layers multiplier | 10 |
| $RLM_{HSAG}$ | HSR air gap radial layers multiplier | 10 |
| $RLM_{Mods}$ | Modulators radial layers multiplier | 10 |
| $RLM_{LSAG}$ | LSR air gap radial layers multiplier | 10 |
| $RLM_{LSPM}$ | LSR magnets radial layers multiplier | 10 |
| $N_{RL,LSBI}$ | Number of radial layers in the LSR back iron | 3 |
| $N_{RL,HSPM,min}$ | Minimum number of radial layers in the HSR magnets | 3 |
| $N_{RL,HSAG,min}$ | Minimum number of radial layers in the HSR air gap | 3 |
| $N_{RL,Mods,min}$ | Minimum number of radial layers in the modulators | 3 |
| $N_{RL,LSAG,min}$ | Minimum number of radial layers in the LSR air gap | 3 |
| $N_{RL,LSPM,min}$ | Minimum number of radial layers in the LSR magnets | 3 |

Table 24. Radial Flux Magnetic Gear 3D MEC Model Axial Layer Discretization Parameter Sweep Definitions

| Parameter | In-Gear Axial Layer Discretization Sweep Value(s) | Out-Of-Gear Axial Layer Discretization Sweep Value(s) |
|---|---|---|
| $N_{LIG}$ | 2, 3, 4, … 12 | 4 |
| $k_{z,IG}$ | 0, 0.5, 1, … 3 | 0 |
| $N_{LOG}$ | 4 | 2, 3, 4, … 12 |
| $k_{z,OG}$ | 0 | 0, 0.5, 1, … 3 |

The graphs in Figures 124-126 illustrate the results of the in-gear and out-of-gear axial layer discretization parameter sweeps for the 30 mm, 100 mm, and 300 mm stack height designs. Be sure to consider the vertical axis scaling when analyzing these graphs, as the limited impact of certain discretization parameters results in some very narrow vertical axis ranges for maximum resolution. These graphs indicate that the out-of-gear axial layers distribution plays a more important role in the model's accuracy than the in-gear axial layers distribution. This behavior is likely a result of the nature of the axial leakage flux paths. The in-gear axial leakage flux primarily travels through the highly permeable modulators and back irons, thus these portions of the axial leakage flux paths constitute relatively small parts of the overall axial leakage flux path reluctances. As a result, the in-gear axial resolution has a smaller impact on the overall characterization of the axial leakage flux. However, the out-of-gear axial leakage flux paths travel entirely through air, thus these portions of the axial leakage flux paths account for large parts of the overall path reluctances and there is significant variation in the axial leakage flux along these sections of the paths. Accordingly, the out-of-gear axial resolution has a much more dramatic effect on the overall characterization of the axial leakage flux.

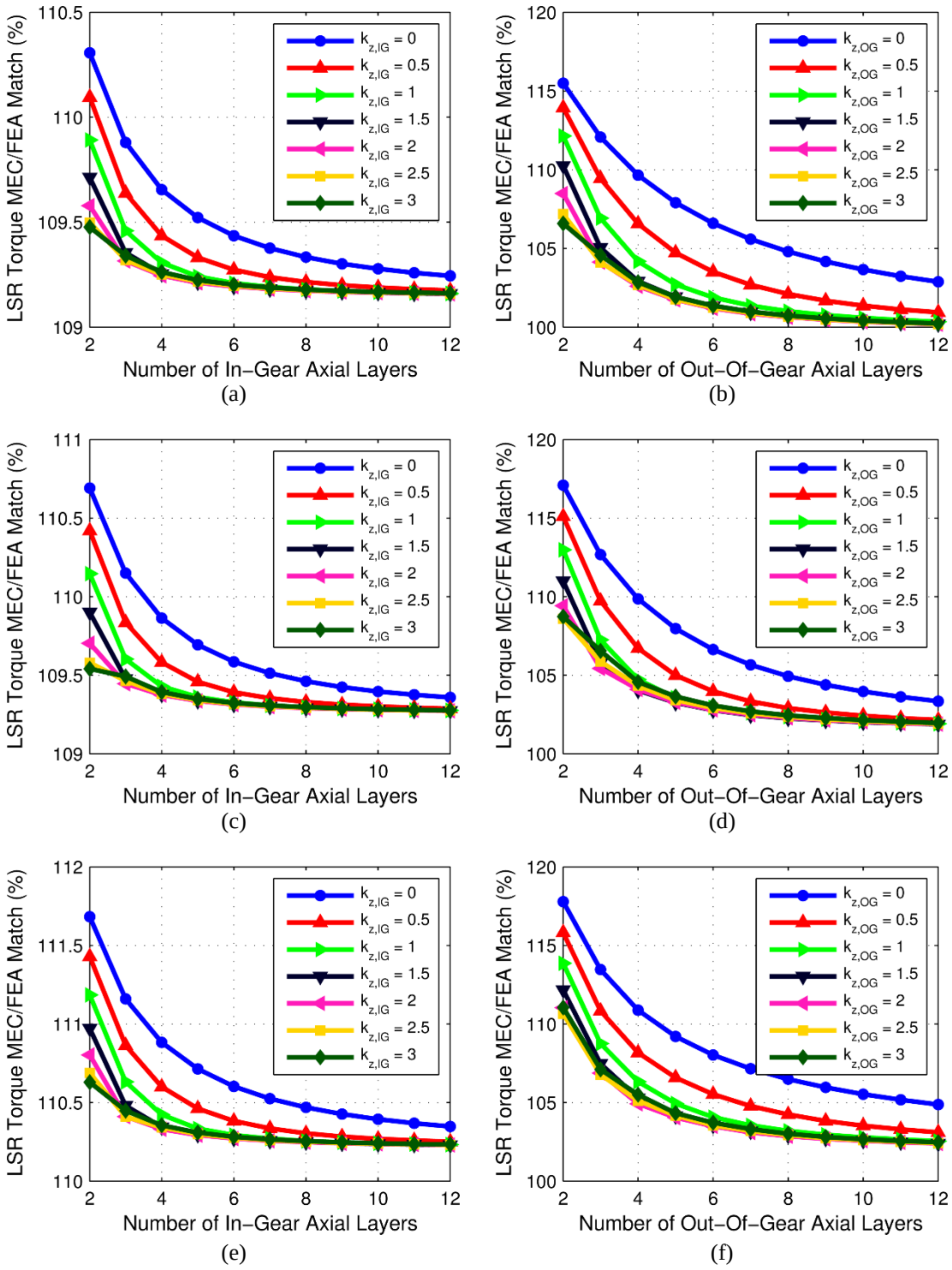


Figure 124. Variation of Radial Flux Magnetic Gear 3D MEC Accuracy at a 30 mm Stack Length for Base Design 1 with (a) In-Gear and (b) Out-of-Gear Axial Discretization Parameters, for Base Design 2 with (c) In-Gear and (d) Out-of-Gear Axial Discretization Parameters, and for Base Design 3 with (e) In-Gear and (f) Out-of-Gear Axial Discretization Parameters

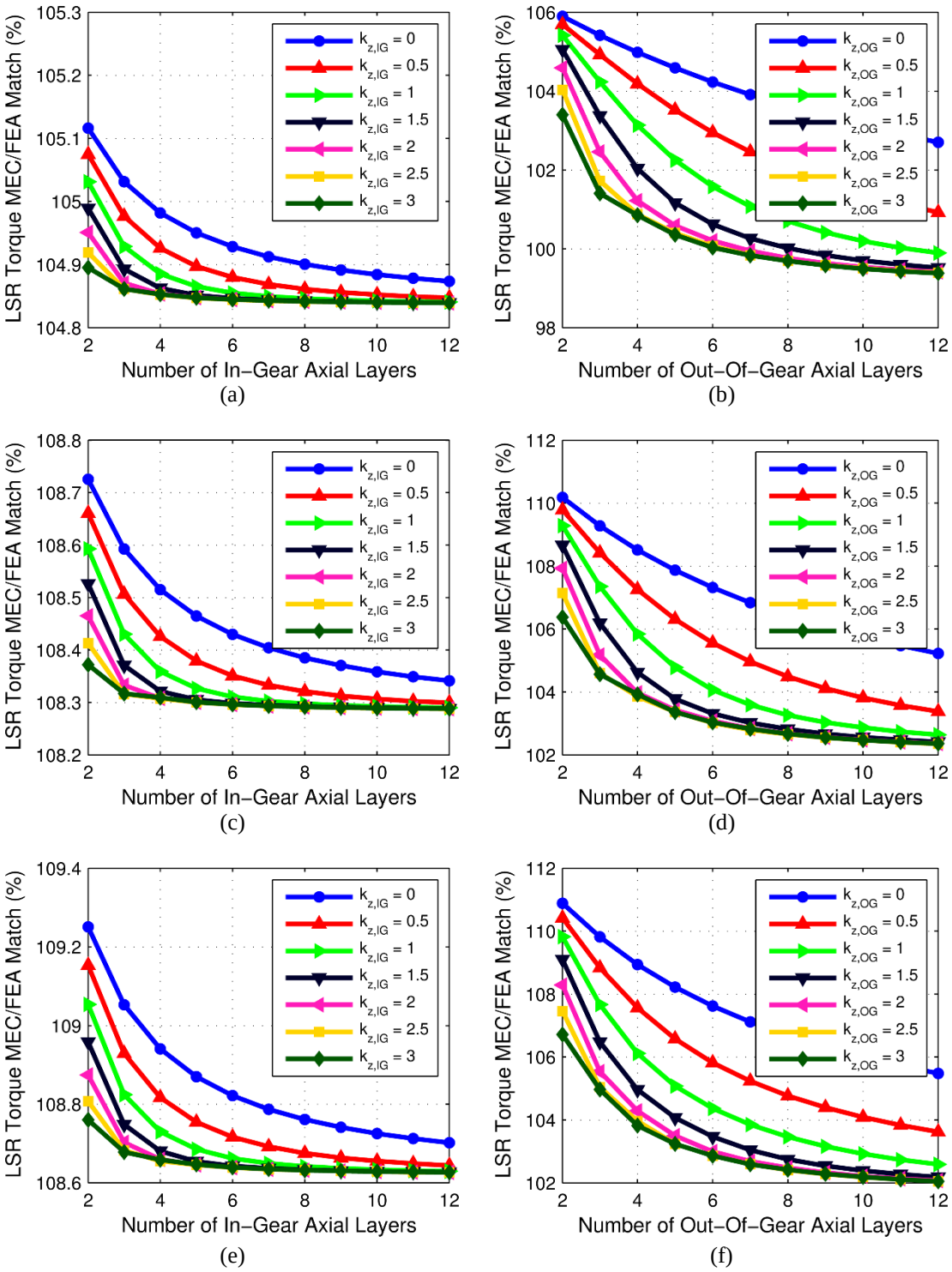


Figure 125. Variation of Radial Flux Magnetic Gear 3D MEC Accuracy at a 100 mm Stack Length for Base Design 1 with (a) In-Gear and (b) Out-of-Gear Axial Discretization Parameters, for Base Design 2 with (c) In-Gear and (d) Out-of-Gear Axial Discretization Parameters, and for Base Design 3 with (e) In-Gear and (f) Out-of-Gear Axial Discretization Parameters

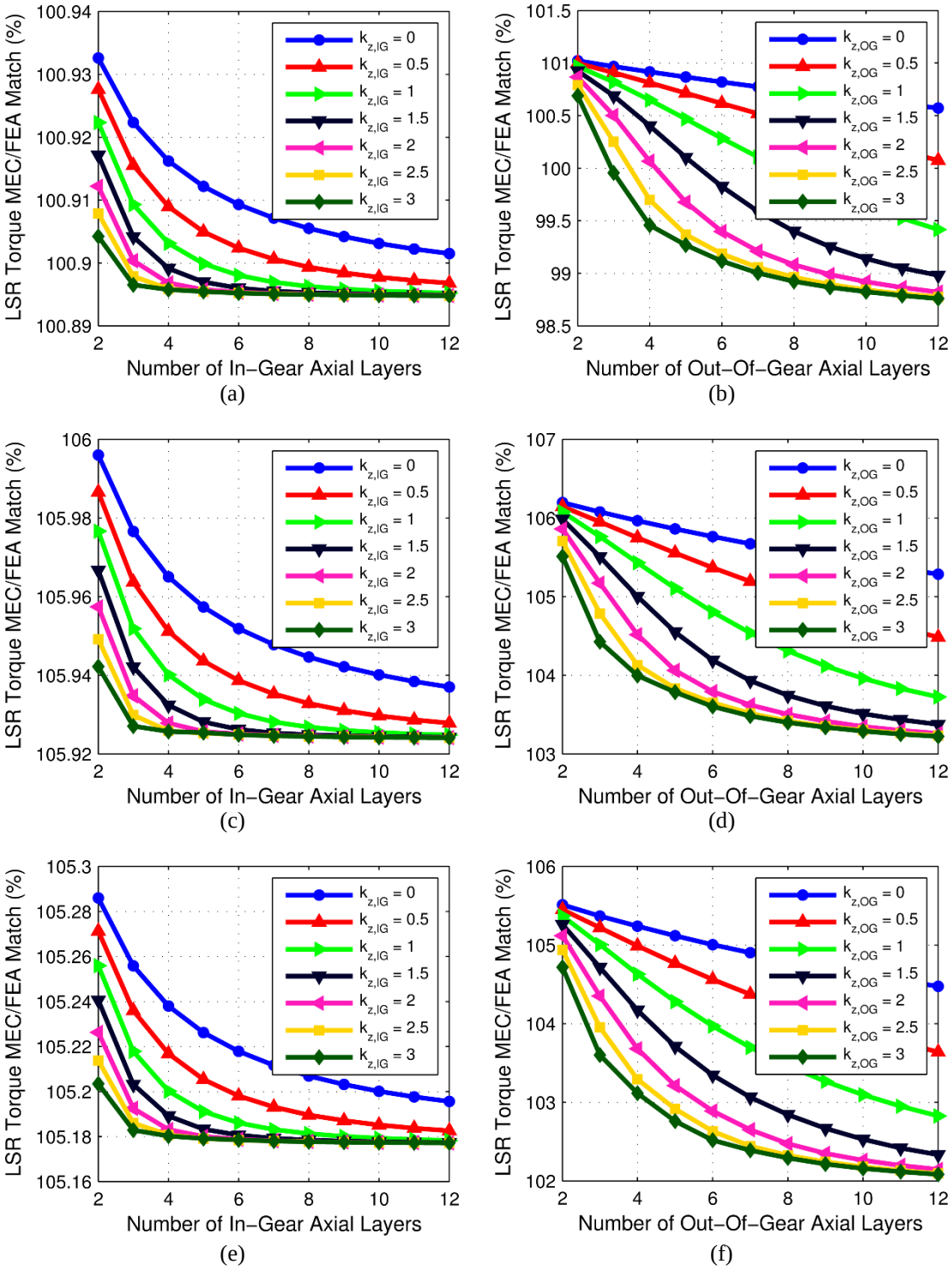


Figure 126. Variation of Radial Flux Magnetic Gear 3D MEC Accuracy at a 300 mm Stack Length for Base Design 1 with (a) In-Gear and (b) Out-of-Gear Axial Discretization Parameters, for Base Design 2 with (c) In-Gear and (d) Out-of-Gear Axial Discretization Parameters, and for Base Design 3 with (e) In-Gear and (f) Out-of-Gear Axial Discretization Parameters

The results in Figures 124-126 also demonstrate that increasing the axial resolution has a more significant effect on the MEC model's accuracy for designs with shorter axial stack lengths. This is not surprising given that 3D effects are simply more impactful for magnetic gears with shorter stack lengths. Gears with long stack lengths generally only experience appreciable axial leakage flux near the ends of the axial stacks, thus these 3D effects have a limited impact on torque transmission capabilities and their accurate characterization (through the use of increased axial resolution) plays a less significant role in the fidelity of the overall design characterization. As a result of these considerations, gears with longer stack lengths generally require less axial resolution to determine the stall torque with sufficient accuracy. This also reinforces the commonly accepted notion that if a gear's axial stack length is large enough relative to other key geometric parameters, a 2D model may provide an adequate representation of the design.

Finally, the trends in Figures 124-126 illustrate that increasing the axial layer distribution factors notably improves the model's accuracy, but with diminishing returns. This pattern occurs because increasing the distribution factors produces smaller axial layers near the end of the active gear stack, both in the gear and in the air region next to the end of the gear, but it also produces larger axial layers near the middle of the gear stack (at the bottom of the half stack model) and in the part of the air region furthest away from the gear. Increasing the distribution factors too much can cause the lack of resolution in the large range of space associated with the thick layers to outweigh the high resolution in the limited, but important range of space associated with the small layers. For excessively large distribution factors, this can even negatively affect the model's accuracy. Once the

model includes a sufficient number of axial layers, there is minimal variation in impact at the high end of the considered axial distribution factor spectrum. The exact effects of the distribution factors and the amounts of axial layers vary for the different base designs and stack lengths settings. This inconsistency suggests the need for future studies to develop a more normalized approach to controlling the axial resolution, such as the angular layers multiplier and the radial layers multipliers devised during the analysis of the 2D MEC model. However, the axial layer distribution factors clearly provide a simple, effective, and flexible means of efficiently distributing the axial layers in the 3D MEC model. It is also worth noting that the accuracy of the 3D MEC model could be further improved beyond the results shown in Figures 124-126 by using higher resolution 2D discretization settings, but this moderate performance gain would come at the expense of slower simulation times.

## 10.2 Axial Stack Length Sweeps

Next, to demonstrate the 3D MEC model's ability to track the variation of 3D effects with different axial stack heights, the three base designs were evaluated using both the 3D MEC model and a 3D FEA model at the range of axial stack heights specified in Table 25. Based on the results of the axial discretization parameters sweep study, the fixed axial discretization settings specified in Table 25 were selected for use in this analysis. Additionally, the base designs were also analyzed by using a 2D FEA model and scaling the results to the appropriate stack heights for comparison with the 3D model torque predictions.

Table 25. Radial Flux Magnetic Gear 3D MEC Model Axial Stack Length Sweep Settings

| Parameter | Values |
|---|---|
| Axial Stack Length (mm) | 20, 30, 40, … 150, 175, 200, … 500 |
| $N_{LIG}$ | 3 |
| $k_{z,IG}$ | 2 |
| $N_{LOG}$ | 10 |
| $k_{z,OG}$ | 2.5 |

Figures 127-130 illustrate the results of the axial stack length sweep study. Figure 127 provides a legend describing the significance of each curve in Figures 128-130. The graph in Figure 128 shows the LSR stall torque predicted by each of the different models for each of the different base designs at all of the evaluated axial stack lengths. The graph in Figure 129 displays the same information for a subset of the shorter stack lengths, where 3D effects are more significant, to provide a better perspective of the relative accuracies of the different models. These results demonstrate that the 3D MEC model is extremely accurate, relative to the 3D FEA model, and capable of tracking the change in stall torque of a given cross-sectional design over a wide range of axial stack lengths. Notably, the 3D MEC model is very accurate even at short stack lengths, which suffer from the most significant 3D effects. In contrast, Figures 129 and 130 clearly reveal that the 2D FEA model significantly overestimates the gear torque ratings at short stack lengths. As the stack length of a magnetic gear design increases, the 3D MEC model remains extremely accurate; however, the 2D FEA model also becomes increasingly accurate. The graph in Figure 128 demonstrates that as the stack length of a gear increases, the 2D FEA model still overestimates the torque rating; however, the difference simply becomes less significant as the gear torque rating grows with the stack length.

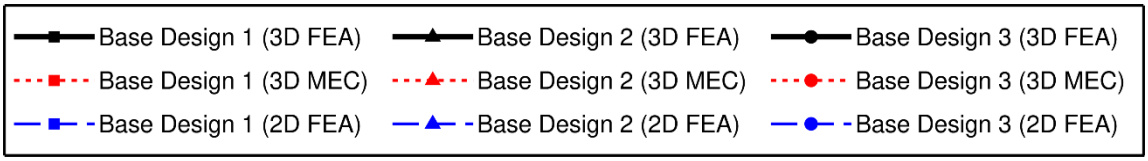


Figure 127. Legend for the Axial Stack Length Sweep Study Graphs in Figures 128-130

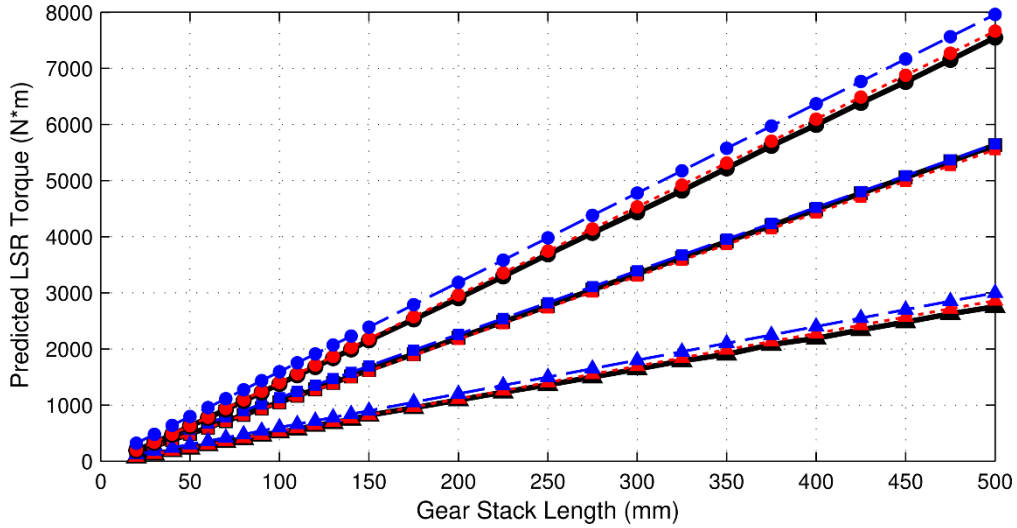


Figure 128. Base Design LSR Stall Torque Predictions by the 3D FEA, 3D MEC, and 2D FEA Models for All Evaluated Stack Lengths

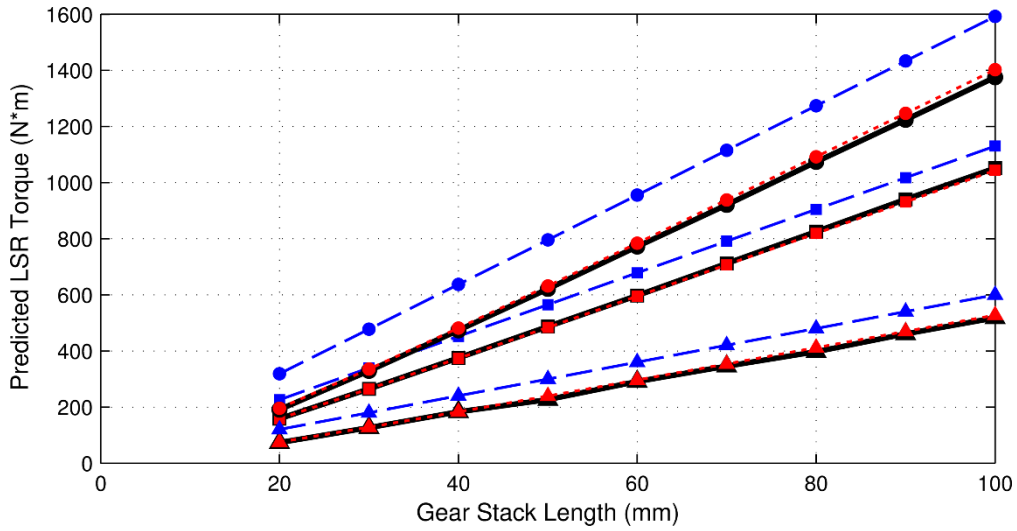


Figure 129. Base Design LSR Stall Torque Predictions by the 3D FEA, 3D MEC, and 2D FEA Models for a Subset of Shorter Stack Lengths

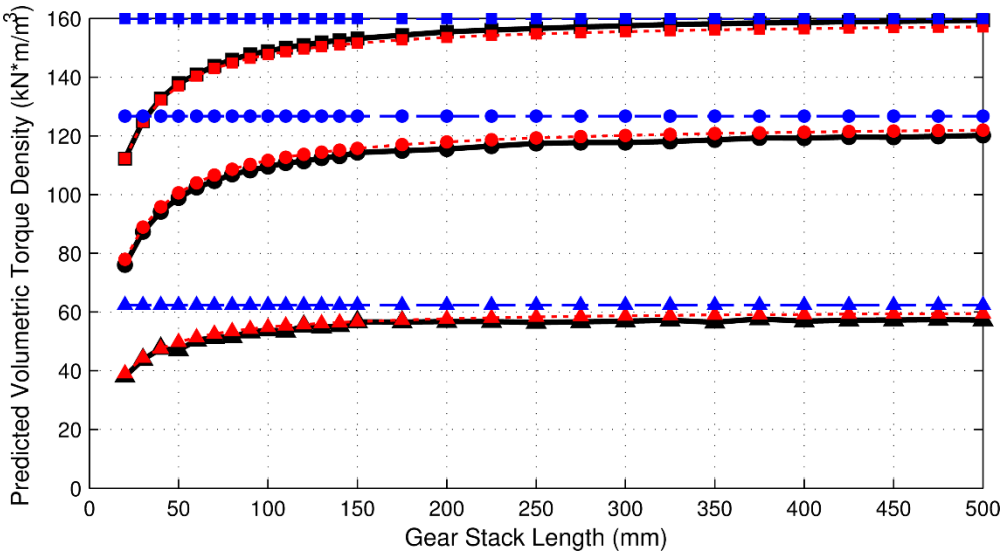


Figure 130. Base Design Volumetric Torque Density Predictions by the 3D FEA, 3D MEC, and 2D FEA Models for All Evaluated Stack Lengths

The graph in Figure 130 shows the variation of volumetric torque density with stack length for each of the three base designs, as predicted by the 3D FEA, 3D MEC, and 2D FEA models. Although this is effectively the same information as the results in Figures 128-129, volumetric torque density provides a superior natural scaling to better illustrate the changes in the relative accuracies of the different models with stack length. The 3D MEC model volumetric torque density prediction consistently matches the 3D FEA model prediction within a few percent across the full range of evaluated axial stack lengths, but the 2D FEA model significantly overestimates the volumetric torque density of each design by as much as 50% at the shorter stack lengths and gradually becomes more accurate as the stack length increases.

Not only is the 3D MEC model an accurate analysis tool, as demonstrated by the results in Figures 128-130, but it is also an extremely fast analysis tool. The axial stack length sweep study defined in Table 25 consisted of 28 different stack lengths for 3

different base designs, resulting in a total of 84 different simulation cases. The 3D FEA simulations of these 84 cases took a total of 1 day, 17 hours, 8 minutes and 9 seconds. In contrast, the 3D MEC simulations of these 84 cases took a mere total of 7 minutes and 59 seconds, with an average torque prediction match of 101.2% and an average absolute torque prediction error of 1.8% relative to the corresponding torque predictions of the nonlinear 3D FEA model. Thus, for the conditions used in this study, the 3D MEC model was approximately 309 times faster than the 3D FEA model on average. As noted in the discussion of the 2D MEC simulation speed, the simulation times required for the MEC and FEA models depend on a plethora of different considerations, including the designs evaluated, the model settings, and the computers used in the analysis. This timing data is simply intended to provide a general indication of the relative speeds of the different models, rather than exact characterizations. A strict convergence criteria was used for the FEA model employed in this analysis to ensure extremely accurate results and a reliable set of reference data for comparison against the MEC model predictions. A looser convergence setting could be used for the FEA model to make it faster, but this would also introduce more error into its torque predictions. Similarly, as previously mentioned, the 3D MEC model accuracy could be improved even more by using higher resolution 2D discretization settings, but that would also result in slower simulation times.

Finally, when comparing the relative simulation speeds of the 3D MEC and 3D FEA models, it is also important to note that the MEC model used in this analysis employed a fixed number of axial layers; therefore, its simulation run time was invariant with respect to stack length. In contrast, the 3D FEA model's simulation time increased

significantly with respect to stack length. In light of this consideration, it is clear that including large stack lengths of up to 500 mm biased the simulation times in favor of the MEC model. Furthermore, based on the results in Figures 128-130, a 3D model is not nearly as essential at the larger stack lengths as it is at the shorter stack lengths. However, even if the timing comparison is limited to only the 27 simulation cases with stack lengths of 100 mm or less, for which 3D models are clearly necessary, then the 3D MEC model was still 109 times faster than the 3D FEA model on average. Regardless of these details, the 3D MEC model is undoubtedly an extremely fast and accurate analysis tool with unmistakable advantages over standard commercial FEA models in certain situations.

# 11. SUMMARY AND CONCLUSIONS

## 11.1 Summary

Although the concept of magnetic gears dates back more than 100 years, the technology has received renewed interest over the last two decades due to the availability of high energy density rare earth permanent magnets and the development of improved topologies. Magnetic gears offer a promising alternative to their mechanical counterparts for use in certain high torque, low speed applications because their contactless operation provides a plethora of potential advantages, such as reduced maintenance, inherent overload protection (no threat of gear teeth breaking), improved reliability, decreased noise, and physical isolation between the input and output shafts. Furthermore, various magnetically geared machine (MGM) topologies integrate a magnetic gear with a low torque, high speed motor or generator to produce a single device with the compact size and cost effectiveness of mechanically geared systems and the reliability of larger direct drive machines. Despite these possible advantages, at the time of this study there are no mainstream commercial magnetic gears because significant work remains to investigate numerous practical manufacturing considerations and improve the technology's size, weight, cost, and efficiency in order to compete with conventional solutions such as mechanical gears and direct drive machines. This dissertation addresses some of these issues by describing the development of analysis and design techniques for axial and radial flux coaxial magnetic gears and magnetically geared machines, as well as the construction and evaluation of experimental prototypes of these devices.

Section 1 provides a brief overview of the history of magnetic gears, including a summary of key patents and a discussion of several important topologies. In particular, this dissertation focuses on coaxial radial and axial flux magnetic gears using surface permanent magnets, which are the most popular and promising modern magnetic gear topologies. Section 1 also includes a simplified explanation of the common fundamental operating principle of flux modulation shared by these two dual topologies. Because magnetic gears must compete against more conventional solutions, Tables 1 and 2 provide a diverse sampling of example commercial mechanical gears and direct drive machines. Although the exact capabilities of these technologies depend on several different application and case specific factors, the examples in Tables 1 and 2 indicate general ranges of reasonable values for important performance metrics, such as volumetric torque density (torque per unit volume), gravimetric torque density (torque per unit mass), and efficiency, which are used to characterize the magnetic gear designs discussed in the subsequent sections.

Section 2 introduces the various models and MATLAB controlled analysis system developed throughout the studies and used to simulate different magnetic gear designs. Most of the studies used finite element analysis (FEA) models constructed in Maxwell by ANSYS due to its tremendous parametrization capabilities; however, MagNet by Infolytica was employed for transient simulations of axial flux magnetic gears because of its ability to model multiple moving parts in 3D systems. In addition to the FEA models, the previously published radial and axial flux magnetic gear analytical models summarized in Tables 5 and 6 were also re-derived and implemented in MATLAB for

evaluation. The MATLAB controlled analysis system and infrastructure illustrated in Figure 11 was developed to systematically control and automate all of these models in order to maximize the number of design cases that could be analyzed with the given computational resources and time.

Section 3 summarizes the experimental evaluation of the first known passive axial flux magnetic gear prototype, referred to as AMTRAN (axial magnetic transmission). AMTRAN exhibited an 8:1 gear ratio and a stall torque of 40.2 N·m, corresponding to a volumetric torque density of 22.4 $kN{\cdot}m/m^3$. Although AMTRAN suffered from a low torque density and poor efficiency due to several significant design oversimplifications, such as the use of large air gaps, a single HSR pole pair, and solid, commonly sized rotor back irons, it still produced several useful outcomes. The comparison between the simulation torque predictions and the experimental results validated the accuracy of the 3D FEA models. Additionally, the process of constructing and testing the prototype provided a great deal of experience and information regarding the nature of the topology's mechanical and structural challenges.

Section 4 presents the design and evaluation of a new patent-pending compact axial flux magnetically geared machine (AFMGM) which integrates an axial flux permanent magnet generator into the radial bore of an axial flux magnetic gear. This arrangement utilizes the empty space inside of the axial gear which is unused or poorly used in the previously proposed series axial flux magnetically geared machine topology. As a result of this change, the total volume consumed by the compact AFMGM remains identical to that required for the corresponding passive axial flux gear. Additionally, the

compact topology also allows the integrated generator to inherently use a smaller outer radius than the magnetic gear, which is consistent with their natural design points since the generator is a low torque, high speed machine and the gear is high torque, low speed device. Based on the results of a parametric axial flux magnetic gear design study, a conservative prototype was designed and constructed with a 9.33:1 internal gear ratio and a stall torque of 42.2 N·m, resulting in a volumetric torque density of 7.8 kN·m/m$^3$ and corresponding to an excellent 100.2% match with value predicted by the 3D FEA model. To demonstrate that this low torque density was a function of several conservative design choices, and not an inherent property of the topology, a more competitive, but realistic alternate design was simulated using a 3D FEA model. This simulated design exhibited a stall torque of 105.9 N·m, corresponding to a torque density of 60.6 kN·m/m$^3$.

Section 5 details the design and evaluation of a large scale inner stator radial flux magnetically geared machine (IS-RFMGM) in which the integrated machine is magnetically decoupled from the magnetic gear. The conservative prototype IS-RFMGM used an internal 11.33:1 gear ratio and exhibited a 3870 N·m experimental stall torque, corresponding to a volumetric torque density of 82.8 kN·m/m$^3$ and a gravimetric torque density of 14.5 N·m/kg. Additionally, the experimental stall torque represented a 99.1% match with the simulated stall torque predicted by a 3D FEA model. This experimental stall torque is believed to be by far the largest ever achieved by any MGM prototype described in detail in the existing literature at the time of this study. Finally, during dynamic experimental testing as a generator, the IS-RFMGM prototype achieved an efficiency of nearly 90% over much of its steady-state operating range.

Section 6 employs an extensive 2D and 3D FEA parametric design study to examine the impact of using ferrite or NdFeB magnets on the active material cost, torque density, and optimal design parameters of surface permanent magnet radial flux magnetic gears. The results reveal that, under the assumed design constraints, relative to the nominal ferrite cost of $10/kg, designs with a gear ratio of ~4 require NdFeB to cost at least $93/kg before ferrite is cost competitive, while designs with gear ratios of ~8 and ~16 require NdFeB rates of $92/kg and $91/kg, respectively. Alternatively, relative to the nominal NdFeB cost of $50/kg, a ferrite design with a gear ratio of ~4 requires ferrite to cost at most $3.3/kg for ferrite to be cost competitive, while designs with gear ratios of ~8 and ~16 require a ferrite rate of $3.5/kg or less. Additionally, the plots in Figures 70-72 illustrate the minimal achievable active material cost designs for different combinations of magnet material and steel cost rates. For most historical price combination scenarios, NdFeB gear designs can achieve lower active material costs than ferrite gear designs. Furthermore, regardless of price considerations, optimal NdFeB gear designs can always achieve significantly lower sizes and masses than optimal ferrite gear designs.

Finally, Sections 7-10 describe the implementation and evaluation of generalized parametric 2D and 3D linear magnetic equivalent circuit (MEC) models for radial flux magnetic gears. Specifically, Section 7 explains the implementation of the 2D MEC model, Section 8 summarizes its evaluation, Section 9 describes the extension of the 2D MEC model to a 3D MEC model, and Section 10 evaluates the speed and accuracy of the 3D MEC model. Table 22 summarizes the accuracy and timing statistics for a 46,656 case parametric design study in which a coarse resolution 2D MEC model and a fine resolution

2D MEC model achieved average torque prediction matches of 98.8% and 100.3% with the corresponding predictions of a non-linear 2D FEA model. Furthermore, the coarse and fine resolution MEC models only required average simulation times of 0.11 seconds and 0.68 seconds per case, as compared to the average simulation time of 29.8 seconds per case required by the non-linear 2D FEA model. Similarly, the 3D MEC model achieved an average match of 101.2% with the torque predictions of corresponding nonlinear 3D FEA models for 3 different cross-sectional base designs analyzed at stack lengths ranging from 20 mm to 500 mm (resulting in a total of 84 cases). Based on the conditions used in the study, the 3D MEC model was 309 times faster than the 3D FEA model on average. Even if the study is limited to only include the 27 cases involving stack lengths of 100 mm of less, for which 3D models are essential, then the 3D MEC model was still 109 times faster than the 3D FEA model on average. These results indicate that the MEC model is a promising and potentially situationally advantageous analysis tool.

## 11.2 Conclusions and Future Work

Collectively, this dissertation provides the tools and methodology for the systematic evaluation and analysis of axial and radial flux magnetic gears and magnetically geared machines. It also offers extensive detailed characterizations of several important magnetic gear and magnetically geared machine design trends. Finally, this dissertation describes the design, construction, and evaluation of multiple ground breaking experimental prototypes to validate the simulation predictions and investigate several practical considerations important to the success and proliferation of the technology.

Despite this dissertation's contributions to the existing body of magnetic gear knowledge, a significant amount of work still remains to be done in order to advance and commercialize the technology. Detailed design studies must be performed to evaluate the possibility of using magnetic gears and magnetically geared machines for specific applications and compare them against existing solutions with respect to both engineering and financial considerations. These efforts should also include investigations of multi-stage magnetic gear designs for appropriate applications. Additionally, further optimization studies are required to properly and thoroughly compare several different competing design options with respect to a wide range of scenarios and performance metrics. Examples of such competing design options include axial flux versus radial flux magnetic gears, flux focusing versus surface permanent magnet gears, and magnetically coupled versus magnetically decoupled magnetically geared machines. All magnetic gear topologies require further investigation into the related issues of axially or radially escaping leakage flux and optimal design trends that account for structural material. Addressing these considerations is an important step toward reducing the gap between theoretically predicted and experimentally measured efficiency, as well as the gap between the active material and total material torque densities. In order to facilitate some of the aforementioned future work, the magnetic gear MEC should be extended to include the axial flux topology, as well as non-linear material modeling and transient loss analysis capabilities.

In addition to the future theoretical studies, more magnetic gear and magnetically geared machine prototypes must also be constructed and tested to investigate practical

mechanical and structural considerations and provide tangible validations or refutations of the technology's frequently touted potential advantages. In particular, the bearing configurations and the modulator support structure are two of the most important mechanical design features for any magnetic gear and both of these details require further development and improvement. Experimental work must be performed to investigate the dynamic performance and control of magnetic gears, including characterizing different magnetic gear designs' torsional stiffness and transient responses to oscillating inputs and loads, as well as developing slip detection, prevention, and recovery algorithms. Furthermore, while many studies, including this dissertation, argue that magnetic gears offer improved reliability, there is currently no known experimental evidence to support these claims. Experimental lifecycle testing of magnetic gears should be conducted to investigate these assertions and provide reliable data on the topic. Although many papers already describe limited investigations into these proposed theoretical and experimental future research topics, continued work in these areas will increase the probability of magnetic gears and magnetically geared machines reaching their full potential and developing into a key enabling technology for a plethora of different applications.

# REFERENCES


[1] K. Atallah and D. Howe, "A Novel High-Performance Magnetic Gear," *IEEE Trans. Magn.*, vol. 37, no. 4, pp. 2844-2846, Jul. 2001.

[2] K. Atallah, S. D. Calverley, and D. Howe, "Design, Analysis and Realisation of a High-Performance Magnetic Gear," *IEE Proc. Elec. Power Appl.*, vol. 151, no. 2, pp. 135-143, Mar. 2004.

[3] P. O. Rasmussen, T. O. Andersen, F. T. Jorgensen, and O. Nielsen, "Development of a High-Performance Magnetic Gear," *IEEE Trans. Ind. Appl.*, vol. 41, no. 3, pp. 764-770, May-Jun. 2005.

[4] N. W. Frank and H. A. Toliyat, "Analysis of the Concentric Planetary Magnetic Gear with Strengthened Stator and Interior Permanent Magnet Inner Rotor," *IEEE Trans. Ind. Appl.*, vol. 47, no. 4, pp. 1652-1660, Jul.-Aug. 2011.

[5] N. W. Frank, "Analysis of the Concentric Planetary Magnetic Gear," Ph.D. dissertation, Dept. Elect. and Comput. Eng., Texas A&M Univ., College Station, Tx., 2011.

[6] P. M. Tlali, R.-J. Wang, and S. Gerber, "Magnetic Gear Technologies: A Review," in *Proc. Int. Conf. Elect. Mach.*, 2014, pp. 544-550.

[7] D. J. Evans and Z. Q. Zhu, "Influence of Design Parameters on Magnetic Gear's Torque Capability," in *Proc. IEEE Int. Elect. Mach. and Drives Conf.*, 2011, pp. 1403-1408.

[8] L. Brönn, R.-J. Wang, and M. J. Kamper, "Development of a Shutter Type Magnetic Gear," in *Proc. Southern African Universities Power Eng. Conf.*, 2010, pp. 78-82.

[9] M. Venturini and F. Leonardi, "High Torque, Low Speed Joint Actuator Based on PM Brushless Motor and Magnetic Gearing," in *Conf. Rec. IEEE Ind. Appl. Soc. Annu. Meeting*, 1993, pp. 37-42.

[10] K. Atallah, J. Rens, S. Mezani, and D. Howe, "A Novel 'Pseudo' Direct-Drive Brushless Permanent Magnet Machine," *IEEE Trans. Magn.*, vol. 44, no. 11, pp. 4349-4352, Nov. 2008.

[11] P. O. Rasmussen, H. H. Mortensen, T. N. Matzen, T. M. Jahns, and H. A. Toliyat, "Motor Integrated Permanent Magnet Gear with a Wide Torque-Speed Range," in *Proc. IEEE Energy Convers. Congr. and Expo.*, 2009, pp. 1510-1518.

[12] P. O. Rasmussen, T. V. Frandsen, K. K. Jensen, and K. Jessen, "Experimental Evaluation of a Motor-Integrated Permanent-Magnet Gear," *IEEE Trans. Ind. Appl.*, vol. 49, no. 2, pp. 850-859, Mar.-Apr. 2013.

[13] T. V. Frandsen, L. Mathe, N. I. Berg, R. K. Holm, T. N. Matzen, P. O. Rasmussen, and K. K. Jensen, "Motor Integrated Permanent Magnet Gear in a Battery Electrical Vehicle," *IEEE Trans. Ind. Appl.*, vol. 51, no. 2, pp. 1516-1525, Mar.-Apr. 2015.

[14] L. Jian, K. T. Chau, and J. Z. Jiang, "A Magnetic-Geared Outer-Rotor Permanent-Magnet Brushless Machine for Wind Power Generation," *IEEE Trans. Ind. Appl.*, vol. 45, no. 3, pp. 954-962, May-Jun. 2009.

[15] S. Gerber and R. J. Wang, "Design and Evaluation of a Magnetically Geared PM Machine," *IEEE Trans. Magn.*, vol. 51, no. 8, pp. 1-10, Aug. 2015.

[16] P. M. Tlali, S. Gerber, and R. J. Wang, "Optimal Design of an Outer-Stator Magnetically Geared Permanent Magnet Machine," *IEEE Trans. Magn.*, vol. 52, no. 2, pp. 1-10, Feb. 2016.

[17] R.-J. Wang, L. Brönn, S. Gerber, and P. M. Tlali, "Design and Evaluation of a Disc-Type Magnetically Geared PM Wind Generator," in *Proc. Int. Conf. Power Eng., Energy and Electr. Drives*, 2013, pp. 1259-1264.

[18] L. Brönn, "Design and Performance Evaluation of a Magnetically Geared Axial-Flux Permanent Magnet Generator," M.S. thesis, Dept. Elect. Eng., Stellenbosch Univ., Stellenbosch, South Africa, 2012.

[19] D. J. Evans and Z. Q. Zhu, "Optimal Torque Matching of a Magnetic Gear within a Permanent Magnet Machine," in *Proc. IEEE Int. Elect. Mach. and Drives Conf.*, 2011, pp. 995-1000.

[20] L. L. Wang, J. X. Shen, P. C. K. Luk, W. Z. Fei, C. F. Wang, and H. Hao, "Development of a Magnetic-Geared Permanent-Magnet Brushless Motor," *IEEE Trans. Magn.*, vol. 45, no. 10, pp. 4578-4581, Oct. 2009.

[21] S. Du, Y. Zhang, and J. Jiang, "Research on a Novel Combined Permanent Magnet Electrical Machine," in *Proc. Int. Conf. Elect. Mach. and Syst.*, 2008, pp. 3564-3567.

[22] K. Atallah, S. Calverley, R. Clark, J. Rens, and D. Howe, "A New PM Machine Topology for Low-Speed, High-Torque Drives," in *Proc. Int. Conf. Elect. Mach.*, 2008, pp. 1-4.

[23] L. Jian, K. T. Chau, and J. Z. Jiang, "An Integrated Magnetic-Geared Permanent-Magnet In-Wheel Motor Drive for Electric Vehicles," in *Proc. IEEE Vehicle Power and Propulsion Conf.*, 2008, pp. 1-6.

[24] K. T. Chau, D. Zhang, J. Z. Jiang, C. Liu, and Y. Zhang, "Design of a Magnetic-Geared Outer-Rotor Permanent-Magnet Brushless Motor for Electric Vehicles," *IEEE Trans. Magn.*, vol. 43, no. 6, pp. 2504-2506, Jun. 2007.

[25] M. Johnson, M. C. Gardner, and H. A. Toliyat, "Design and Analysis of an Axial Flux Magnetically Geared Generator," *IEEE Trans. Ind. Appl.*, vol. 53, no. 1, pp. 97-105, Jan.-Feb. 2017.

[26] N. W. Frank and H. A. Toliyat, "Gearing Ratios of a Magnetic Gear for Wind Turbines," in *Proc. IEEE Int. Elect. Mach. and Drives Conf.*, 2009, pp. 1224-1230.

[27] K. K. Uppalapati, J. Z. Bird, D. Jia, J. Garner, and A. Zhou, "Performance of a Magnetic Gear Using Ferrite Magnets for Low Speed Ocean Power Generation," in *Proc. IEEE Energy Convers. Congr. and Expo.*, 2012, pp. 3348-3355.

[28] S. Pakdelian and H. A. Toliyat, "Trans-Rotary Magnetic Gear for Wave Energy Applicaion," in *Proc. IEEE Power and Energy Soc. Gen. Meeting*, 2012, pp. 1-4.

[29] L. Shah, A. Cruden, and B. W. Williams, "A Variable Speed Magnetic Gear Box Using Contra-Rotating Input Shafts," *IEEE Trans. Magn.*, vol. 47, no. 2, pp. 431-438, Feb. 2011.

[30] N. W. Frank and H. A. Toliyat, "Gearing Ratios of a Magnetic Gear for Marine Applications," in *Proc. IEEE Electr. Ship Technol. Symp.*, 2009, pp. 477-481.

[31] D. J. Powell, S. D. Calverley, F. de Wildt, and K. Daffey, "Design and Analysis of a Pseudo Direct-Drive Propulsion Motor," in *Proc. IET Int. Conf. Power Electron., Mach. and Drives*, 2010, pp. 1-2.

[32] W. J. McDonald, T. F. Price, and G. P. Hatch, "Wellbore Motor Having Magnetic Gear Drive," U.S. Patent 7 481 283 B2, Jan. 27, 2009.

[33] H. A. Toliyat, M. Johnson, and M. C. Gardner, "A Compact Topology for Axial Field Magnetically Geared Machines," U.S. Patent Appl. 62/239,695, Oct. 6, 2016.

[34] F. T. Jørgensen, "Design and Construction of Permanent Magnetic Gears," Ph.D. dissertation, Dept. Energy Technol., Aalborg University, Aalborg, DK, 2010.

[35] M. Calvin, "A Comparative Study between Axial and Radial Flux-Focusing Magnetic Gear Topologies and Mechanical Gearboxes," M.S. thesis, Dept. Eng. Technol., Univ. North Carolina at Charlotte, Charlotte, NC, 2015.

[36] Winsmith, "Winsmith D-90 Type DE Catalog," [Online]. Available: http://www.winsmith.com/wp-content/uploads/D90_TYPE_DE_Catalog_190I-2.pdf. Accessed: Jan. 28, 2017.

[37] Neugart, "Neugart Servo Gearheads 2003 Catalog," [Online]. Available: http://aisimem.com/downloads/NeugartCatalog2003.pdf. Accessed: Jan. 28, 2017.

[38] Stober, "Stober Servofit Precision Planetary Gearhead Catalog," [Online]. Available: https://www.industrialmagza.com/pdf/Stober/ServoFit%20Gearheads/SPG-MGZ.pdf. Accessed: Jan. 28, 2017.

[39] Bonfiglioli, "Bonfiglioli Riduttori: C-A-F-S Series," [Online]. Available: http://www.bonfiglioli.com/media/products/attachments/BR_CAT_CAFS_STD_ENG_R01_0.pdf. Accessed: Jan. 28, 2017.

[40] Varvel SpA, "Varvel RD Series Catalog," [Online]. Available: http://www.varvel.com/en/download/file/61. Accessed: Jan. 28, 2017.

[41] Harmonic Drive, "Engineering Data: CSD-2UF/2UH Units," [Online]. Available: http://harmonicdrive.de/mage/media/catalog/category/2014_11_ED_1019646_CSD_2UH_2UF_2.pdf. Accessed: Jan. 28, 2017.

[42] Harmonic Drive, "Engineering Data: CSG-2UH Units," [Online]. Available: http://harmonicdrive.de/mage/media/catalog/category/2014_12_ED_1019642_CSG_2UH.pdf. Accessed: Jan. 28, 2017.

[43] Sumitomo Drive Technologies, "Sumitomo Servo Catalogue 2005," [Online]. Available: http://www.sumitomodrive.com/uploads/product/files/file-255.pdf. Accessed: Jan. 28, 2017.

[44] Sumitomo Drive Technologies, "Sumitomo Cyclo 6000 Speed Reducers Catalog 2015," [Online]. Available: http://www.sumitomodrive.com/uploads/product/files/file-32.pdf. Accessed: Jan. 28, 2017.

[45] E. Gouda, S. Mezani, L. Baghli, and A. Rezzoug, "Comparative Study between Mechanical and Magnetic Planetary Gears," *IEEE Trans. Magn.*, vol. 47, no. 2, pp. 439-450, Feb. 2011.

[46] P. Mongeau, "High Torque Density Propulsion Motors," *Naval Eng. J.*, vol. 117, no. 4, pp. 53-57, Oct. 2005.

[47] GKN, "GKN Electric Motor and Generator Technology: Technical Datasheet," [Online]. Available: http://products.gknlandsystems.info/fileadmin/user_upload/pdf/Electrics/DS_GKN_electric_motor_technology_64_GB_1214.pdf. Accessed: Jan. 28, 2017.

[48] YASA Motors, "YASA 750 R Product Sheet," [Online]. Available: http://www.yasamotors.com/wp-content/uploads/2015/09/YASA-750-Product-Sheet.pdf. Accessed: Jan. 28, 2017.

[49] Protean Electric, "Protean Drive Specifications," [Online]. Available: http://www.proteanelectric.com/specifications/. Accessed: Jan. 28, 2017.

[50] C. G. Armstrong, "Power Transmitting Device," U.S. Patent 687 292, Nov. 26, 1901.

[51] A. H. Neuland, "Apparatus for Transmitting Power," U.S. Patent 1 171 351, Feb. 8, 1916.

[52] H. T. Faus, "Magnetic Gearing," U.S. Patent 2 243 555, May 27, 1941.

[53] H. T. Faus, "Magnetic Transmission," U.S. Patent 2 371 511, Mar. 13, 1945.

[54] G. A. Reese, "Magnetic Gearing Arrangement," U.S. Patent 3 301 091, Jan. 31, 1967.

[55] T. B. Martin Jr., "Magnetic Transmission," U.S. Patent 3 378 710, Apr. 16, 1968.

[56] H. P. Schlaeppi, "Magnetic Gears," U.S. Patent 3 382 386, May 7, 1968.

[57] S. Rand, "Magnetic Transmission System," U.S. Patent 3 523 204, Aug. 4, 1970.

[58] N. Laing, "Magnetic Transmission," U.S. Patent 3 645 650, Feb. 29, 1972.

[59] N. Laing, "Centrifugal Pump with Magnetic Drive," U.S. Patent 3 762 839, Oct. 2, 1973.

[60] M. Hetzel, "Low Friction Miniature Gear Drive for Transmitting Small Forces, and Method of Making Same," U.S. Patent 3 792 578, Feb. 19, 1974.

[61] W. J. Mabe Jr., "Magnetic Transmission," U.S. Patent 5 013 949, May 7, 1991.

[62] G. Schuesler and J. Lindner, "Magnetic Parallel Shaft Drive for Contactless Transmission of Torque - Uses Wheels with Magnets at Circumference at Least Two of Which Are Rotationally Located on Shafts," DE Patent 4 223 826 C2, May 11, 1994.

[63] G. Schuesler and J. Lindner, "Eccentric Drive Having Magnetic Torque Transmission," DE Patent 4 428 441 A1, Feb. 16, 1995.

[64] J. E. Rode, "Magnetic Gear and Gear Train Configuration," U.S. Patent 5 569 967, Oct. 29, 1996.

[65] B. Ackermann and L. Honds, "Magnetic Drive Arrangement Comprising a Plurality of Magnetically Cooperating Parts Which Are Movable Relative to One Another," U.S. Patent 5 633 555, May 27, 1997.

[66] B. Ackermann, "Magnetic Drive Arrangement," U.S. Patent 5 994 809, Nov. 30, 1999.

[67] A. Meisberger, "Magnetic Gear and Centrifuge Having a Magnetic Gear," U.S. Patent 6 440 055 B1, Aug. 27, 2002.

[68] A. G. Razzell and J. A. Cullen, "Compact Electrical Machine," U.S. Patent 6 794 781 B2, Sep. 21, 2004.

[69] E. W. Nissen, "Magnetic Transmission," U.S. Patent 7 105 968 B2, Sep. 12, 2006.

[70] R. J. Wise, "Torque Converter System and Method of Using the Same," U.S. Patent 7 145 276 B2, Dec. 5, 2006.

[71] K. K. Uppalapati, "An Investigation into the Torque Density Capabilities of Flux-Focusing Magnetic Gearboxes," Ph.D. dissertation, Dept. Elect. and Comput. Eng., Univ. North Carolina at Charlotte, Charlotte, NC, 2015.

[72] T. V. Frandsen, "Motor Integrated Permanent Magnet Gear," Ph.D. dissertation, Dept. Energy Technol., Aalborg University, Aalborg, DK, 2016.

[73] G. P. Hatch, "Recent Developments in Permanent Magnet Gear Systems and Machines," presented at the Magn. Conf., Lake Buena Vista, FL, 2010.

[74] K. Tsurumoto and S. Kikuchi, "A New Magnetic Gear Using Permanent Magnet," *IEEE Trans. Magn.*, vol. 23, no. 5, pp. 3622-3624, Sep. 1987.

[75] S. Kikuchi and K. Tsurumoto, "Design and Characteristics of a New Magnetic Worm Gear Using Permanent Magnet," *IEEE Trans. Magn.*, vol. 29, no. 6, pp. 2923-2925, Nov. 1993.

[76] F. T. Jorgensen, T. O. Andersen, and P. O. Rasmussen, "Two Dimensional Model of a Permanent Magnet Spur Gear," in *Conf. Rec. IEEE Ind. Appl. Soc. Annu. Meeting*, 2005, pp. 261-265.

[77] E. P. Furlani, "A Two-Dimensional Analysis for the Coupling of Magnetic Gears," *IEEE Trans. Magn.,* vol. 33, no. 3, pp. 2317-2321, May 1997.

[78] S. Mezani, K. Atallah, and D. Howe, "A High-Performance Axial-Field Magnetic Gear," *J. Appl. Phys.,* vol. 99, no. 8, pp. 08R303-1-08R303-3, Apr. 2006.

[79] K. Davey, T. Hutson, L. McDonald, C. Ras, R. Weinstein, D. Parks, and R. P. Sawh, "Rotating Cylinder Planetary Gear Motor," *IEEE Trans. Ind. Appl.,* vol. 52, no. 3, pp. 2253-2260, May-Jun. 2016.

[80] C. C. Huang, M. C. Tsai, D. G. Dorrell, and B. J. Lin, "Development of a Magnetic Planetary Gearbox," *IEEE Trans. Magn.,* vol. 44, no. 3, pp. 403-412, Mar. 2008.

[81] F. T. Jorgensen, T. O. Andersen, and P. O. Rasmussen, "The Cycloid Permanent Magnetic Gear," *IEEE Trans. Ind. Appl.,* vol. 44, no. 6, pp. 1659-1665, Nov.-Dec. 2008.

[82] K. Davey, L. McDonald, and T. Hutson, "Axial Flux Cycloidal Magnetic Gears," *IEEE Trans. Magn.,* vol. 50, no. 4, pp. 1-7, Apr. 2014.

[83] J. Rens, K. Atallah, S. D. Calverley, and D. Howe, "A Novel Magnetic Harmonic Gear," *IEEE Trans. Ind. Appl.,* vol. 46, no. 1, pp. 206-212, Jan.-Feb. 2010.

[84] L. Jian and K. T. Chau, "A Coaxial Magnetic Gear with Halbach Permanent-Magnet Arrays," *IEEE Trans. Energy Convers.,* vol. 25, no. 2, pp. 319-328, Jun. 2010.

[85] A. Penzkofer and K. Atallah, "Magnetic Gears for High Torque Applications," *IEEE Trans. Magn.,* vol. 50, no. 11, pp. 1-4, Nov. 2014.

[86] L. Jian, K. T. Chau, Y. Gong, J. Z. Jiang, C. Yu, and W. Li, "Comparison of Coaxial Magnetic Gears with Different Topologies," *IEEE Trans. Magn.,* vol. 45, no. 10, pp. 4526-4529, Oct. 2009.

[87] M. Johnson, M. C. Gardner, and H. A. Toliyat, "Analysis of Axial Field Magnetic Gears with Halbach Arrays," in *Proc. IEEE Int. Elect. Mach. and Drives Conf.,* 2015, pp. 108-114.

[88] K. K. Uppalapati, W. Bomela, J. Z. Bird, M. Calvin, and J. Wright, "Construction of a Low Speed Flux Focusing Magnetic Gear," in *Proc. IEEE Energy Convers. Congr. and Expo.,* 2013, pp. 2178-2184.

[89] K. Uppalapati and J. Bird, "A Flux Focusing Ferrite Magnetic Gear," in *Proc. IET Int. Conf. Power Electron., Mach. and Drives*, 2012, pp. 1-6.

[90] K. K. Uppalapati and J. Z. Bird, "An Iterative Magnetomechanical Deflection Model for a Magnetic Gear," *IEEE Trans. Magn.*, vol. 50, no. 2, pp. 245-248, 2014.

[91] K. K. Uppalapati, J. Z. Bird, J. Wright, J. Pitchard, M. Calvin, and W. Williams, "A Magnetic Gearbox with an Active Region Torque Density of 239Nm/L," in *Proc. IEEE Energy Convers. Congr. and Expo.*, 2014, pp. 1422-1428.

[92] S. Hazra, S. Bhattacharya, K. K. Uppalapati, and J. Bird, "Ocean Energy Power Take-Off Using Oscillating Paddle," in *Proc. IEEE Energy Convers. Congr. and Expo.*, 2012, pp. 407-413.

[93] V. M. Acharya, J. Z. Bird, and M. Calvin, "A Flux Focusing Axial Magnetic Gear," *IEEE Trans. Magn.*, vol. 49, no. 7, pp. 4092-4095, Jul. 2013.

[94] X. Li, K. T. Chau, M. Cheng, W. Hua, and Y. Du, "An Improved Coaxial Magnetic Gear Using Flux Focusing," in *Proc. Int. Conf. Elect. Mach. and Syst.*, 2011, pp. 1-4.

[95] X. Liu, K. T. Chau, J. Z. Jiang, and C. Yu, "Design and Analysis of Interior-Magnet Outer-Rotor Concentric Magnetic Gears," *J. Appl. Phys.*, vol. 105, no. 7, pp. 07F101-103, Apr. 2009.

[96] R. C. Holehouse, K. Atallah, and J. Wang, "Design and Realization of a Linear Magnetic Gear," *IEEE Trans. Magn.*, vol. 47, no. 10, pp. 4171-4174, Oct. 2011.

[97] R. C. Holehouse, K. Atallah, and J. Wang, "A Linear Magnetic Gear," in *Proc. Int. Conf. Elect. Mach.*, 2012, pp. 563-569.

[98] W. Li, K. T. Chau, and J. Z. Jiang, "Application of Linear Magnetic Gears for Pseudo-Direct-Drive Oceanic Wave Energy Harvesting," *IEEE Trans. Magn.*, vol. 47, no. 10, pp. 2624-2627, Oct. 2011.

[99] S. Pakdelian, N. W. Frank, and H. A. Toliyat, "Principles of the Trans-Rotary Magnetic Gear," *IEEE Trans. Magn.*, vol. 49, no. 2, pp. 883-889, Feb. 2013.

[100] S. Pakdelian and H. A. Toliyat, "Design Aspects of the Trans-Rotary Magnetic Gear," in *Proc. Annu. Conf. IEEE Ind. Electron. Soc.*, 2012, pp. 1720-1725.

[101] S. Pakdelian, N. W. Frank, and H. A. Toliyat, "Analysis and Design of the Trans-Rotary Magnetic Gear," in *Proc. IEEE Energy Convers. Congr. and Expo.*, 2012, pp. 3340-3347.

[102] T. Lubin, S. Mezani, and A. Rezzoug, "Analytical Computation of the Magnetic Field Distribution in a Magnetic Gear," *IEEE Trans. Magn.*, vol. 46, no. 7, pp. 2611-2621, Jul. 2010.

[103] T. Lubin, S. Mezani, and A. Rezzoug, "Development of a 2-D Analytical Model for the Electromagnetic Computation of Axial-Field Magnetic Gears," *IEEE Trans. Magn.*, vol. 49, no. 11, pp. 5507-5521, Nov. 2013.

[104] L. Jian and K. T. Chau, "Analytical Calculation of Magnetic Field Distribution in Coaxial Magnetic Gears," *Progress In Electromagnetics Research*, vol. 92, pp. 1-16, 2009.

[105] M. Johnson, A. Shapoury, P. Boghrat, M. Post, and H. A. Toliyat, "Analysis and Development of an Axial Flux Magnetic Gear," in *Proc. IEEE Energy Convers. Congr. and Expo.*, 2014, pp. 5893-5900.

[106] B. Czech and P. Bauer, "Wave Energy Converter Concepts: Design Challenges and Classification," *IEEE Ind. Electron. Mag.*, vol. 6, no. 2, pp. 4-16, Jun. 2012.

[107] T. Brekken, "Fundamentals of Ocean Wave Energy Conversion, Modeling, and Control," in *Proc. IEEE Int. Symp. Ind. Electron.*, 2010, pp. 3921-3966.

[108] M. A. Mueller, H. Polinder, and N. Baker, "Current and Novel Electrical Generator Technology for Wave Energy Converters," in *Proc. IEEE Int. Elect. Mach. and Drives Conf.*, 2007, pp. 1401-1406.

[109] A. Muetze and J. G. Vining, "Ocean Wave Energy Conversion - a Survey," in *Conf. Rec. IEEE Ind. Appl. Soc. Annu. Meeting*, 2006, pp. 1410-1417.

[110] N. Niguchi, K. Hirata, A. Zaini, and S. Nagai, "Proposal of an Axial-Type Magnetic-Geared Motor," in *Proc. Int. Conf. Elect. Mach.*, 2012, pp. 738-743.

[111] C. Tong, Z. Song, P. Zheng, J. Bai, and Q. Zhao, "Research on Electromagnetic Performance of an Axial Magnetic-Field-Modulated Brushless Double-Rotor Machine for Hybrid Electric Vehicles," in *Proc. Int. Conf. Elect. Mach. and Syst.*, 2014, pp. 2896-2902.

[112] W. N. Fu and S. L. Ho, "A Novel Axial-Flux Electric Machine for in-Wheel Gearless Drive in Plug-in Hybrid Electric Vehicles," in *Proc. IEEE Conf. Electromagn. Field Comput.*, 2010, pp. 1-1.

[113] S. Gerber and R. J. Wang, "Torque Capability Comparison of Two Magnetically Geared PM Machine Topologies," in *Proc. IEEE Int. Conf. Ind. Technol.*, 2013, pp. 1915-1920.

[114] Magnomatics Limited, "PDD Compact, High Torque Motors and Generators," [Online]. Available: http://www.magnomatics.com/pages/media/media.htm. Accessed: Dec. 1, 2016.

[115] S. Gerber and R. J. Wang, "Evaluation of a Prototype Magnetic Gear," in *Proc. IEEE Int. Conf. Ind. Technol.*, 2013, pp. 319-324.

[116] M. Johnson, M. C. Gardner, and H. A. Toliyat, "Design Comparison of NdFeB and Ferrite Radial Flux Magnetic Gears," in *Proc. IEEE Energy Convers. Congr. and Expo.*, 2016, pp. 1-8.

[117] S. Gerber and R. J. Wang, "Analysis of the End-Effects in Magnetic Gears and Magnetically Geared Machines," in *Proc. Int. Conf. Elect. Mach.*, 2014, pp. 396-402.

[118] T. V. Frandsen and P. O. Rasmussen, "Loss Investigation of Motor Integrated Permanent Magnet Gear," in *Proc. Int. Conf. Elect. Mach. and Syst.*, 2014, pp. 2673-2679.

[119] T. V. Frandsen and P. O. Rasmussen, "Practical Investigation of End Effect Losses in a Motor Integrated Permanent Magnet Gear," in *Proc. IEEE Energy Convers. Congr. and Expo.*, 2015, pp. 4425-4432.

[120] M. Chen, K. T. Chau, W. Li, and C. Liu, "Cost-Effectiveness Comparison of Coaxial Magnetic Gears with Different Magnet Materials," *IEEE Trans. Magn.*, vol. 50, no. 2, pp. 821-824, Feb. 2014.

[121] R. Wolf, "Recent History, Current Events, and the Future of Rare Earth and Ferrite Magnets," in *Proc. Asian Metal Rare Earth Summit*, 2013.

[122] G. Bramerdorfer, S. Silber, G. Weidenholzer, and W. Amrhein, "Comprehensive Cost Optimization Study of High-Efficiency Brushless Synchronous Machines," in *Proc. IEEE Int. Elect. Mach. and Drives Conf.*, 2013, pp. 1126-1131.

[123] P. Zhang, G. Y. Sizov, D. M. Ionel, and N. A. O. Demerdash, "Establishing the Relative Merits of Interior and Spoke-Type Permanent-Magnet Machines with Ferrite or NdFeB through Systematic Design Optimization," *IEEE Trans. Ind. Appl.*, vol. 51, no. 4, pp. 2940-2948, Jul.-Aug. 2015.

[124] J. F. H. Douglas, "The Reluctance of Some Irregular Magnetic Fields," *Trans. AIEE*, vol. XXXIV, no. 1, pp. 1067-1134, Apr. 1915.

[125] E. R. Lwithwaite, "Magnetic Equivalent Circuits for Electrical Machines," *Proc. Inst. Electr. Eng.*, vol. 114, no. 11, pp. 1805-1809, Nov. 1967.

[126] C. J. Carpenter, "Magnetic Equivalent Circuits," *Proc. Inst. Electr. Eng.*, vol. 115, no. 10, pp. 1503-1511, Oct. 1968.

[127] V. Ostovic, "A Method for Evaluation of Transient and Steady State Performance in Saturated Squirrel Cage Induction Machines," *IEEE Trans. Energy Convers.*, vol. EC-1, no. 3, pp. 190-197, Sept. 1986.

[128] V. Ostovic, "Computation of Saturated Permanent-Magnet AC Motor Performance by Means of Magnetic Circuits," *IEEE Trans. Ind. Appl.*, vol. IA-23, no. 5, pp. 836-841, Sept. 1987.

[129] V. Ostovic, "A Simplified Approach to Magnetic Equivalent-Circuit Modeling of Induction Machines," *IEEE Trans. Ind. Appl.*, vol. 24, no. 2, pp. 308-316, Mar.-Apr. 1988.

[130] V. Ostovic, "A Novel Method for Evaluation of Transient States in Saturated Electric Machines," *IEEE Trans. Ind. Appl.*, vol. 25, no. 1, pp. 96-100, Jan.-Feb. 1989.

[131] C. B. Rasmussen and E. Ritchie, "A Magnetic Equivalent Circuit Approach for Predicting PM Motor Performance," in *Conf. Rec. IEEE Ind. Appl. Soc. Annu. Meeting*, 1997, pp. 10-17 vol.1.

[132] J. Perho, "Reluctance Network for Analysing Induction Machines," Ph.D. dissertation, Dept. Elect. and Commun. Eng., Helsinki Univ. Tech., Espoo, Finland, 2002.

[133] S. D. Sudhoff, B. T. Kuhn, K. A. Corzine, and B. T. Branecky, "Magnetic Equivalent Circuit Modeling of Induction Motors," *IEEE Trans. Energy Convers.*, vol. 22, no. 2, pp. 259-270, Jun. 2007.

[134] M. Yilmaz and P. T. Krein, "Capabilities of Finite Element Analysis and Magnetic Equivalent Circuits for Electrical Machine Analysis and Design," in *Proc. IEEE Power Electron. Specialists Conf.*, 2008, pp. 4027-4033.

[135] M. Amrhein and P. T. Krein, "Magnetic Equivalent Circuit Simulations of Electrical Machines for Design Purposes," in *Proc. IEEE Elect. Ship Technol. Symp.*, 2007, pp. 254-260.

[136] M. F. Hsieh and Y. C. Hsu, "A Generalized Magnetic Circuit Modeling Approach for Design of Surface Permanent-Magnet Machines," *IEEE Trans. Ind. Electron.*, vol. 59, no. 2, pp. 779-792, Feb. 2012.

[137] C. Bruzzese, D. Zito, and A. Tessarolo, "Finite Reluctance Approach: A Systematic Method for the Construction of Magnetic Network-Based Dynamic Models of Electrical Machines," in *Proc. AEIT Annu. Conf.*, 2014, pp. 1-6.

[138] M. Amrhein and P. T. Krein, "Magnetic Equivalent Circuit Modeling of Induction Machines Design-Oriented Approach with Extension to 3-D," in *Proc. IEEE Int. Elect. Mach. and Drives Conf.*, 2007, pp. 1557-1563.

[139] M. Amrhein and P. T. Krein, "3-D Magnetic Equivalent Circuit Framework for Modeling Electromechanical Devices," *IEEE Trans. Energy Convers.*, vol. 24, no. 2, pp. 397-405, Jun. 2009.

[140] M. Amrhein and P. T. Krein, "Force Calculation in 3-D Magnetic Equivalent Circuit Networks with a Maxwell Stress Tensor," *IEEE Trans. Energy Convers.*, vol. 24, no. 3, pp. 587-593, Sept. 2009.

[141] M. Fukuoka, K. Nakamura, and O. Ichinokura, "Dynamic Analysis of Planetary-Type Magnetic Gear Based on Reluctance Network Analysis," *IEEE Trans. Magn.*, vol. 47, no. 10, pp. 2414-2417, Oct. 2011.

[142] M. Fukuoka, K. Nakamura, and O. Ichinokura, "A Method for Optimizing the Design of SPM Type Magnetic Gear Based on Reluctance Network Analysis," in *Proc. Int. Conf. Elect. Mach.*, 2012, pp. 30-35.

[143] D. Thyroff, S. Meier, and I. Hahn, "Modeling Integrated Magnetic Gears Using a Magnetic Equivalent Circuit," in *Proc. Annu. Conf. IEEE Ind. Electron. Soc.*, 2015, pp. 2904-2908.

[144] H. W. Derbas, J. M. Williams, A. C. Koenig, and S. D. Pekarek, "A Comparison of Nodal- and Mesh-Based Magnetic Equivalent Circuit Models," *IEEE Trans. Energy Convers.*, vol. 24, no. 2, pp. 388-396, Jun. 2009.

[145] T. A. Davis, "Algorithm 930: FACTORIZE: An Object-Oriented Linear System Solver for MATLAB," *ACM Trans. Math. Softw.*, vol. 39, no. 4, pp. 1-18, Jul. 2013.